Contents

Chapter 8.0 Electrical Potentials

Abelardo Ramirez

8.1 Introduction

Natural and spontaneous electrical potentials, known as self-potentials (SPs), occur within the earth because of electrochemical or mechanical activity. Self-potential anomalies have been observed in natural geothermal environments where a significant flow of hot water and steam occurs, qualitatively similar to the conditions expected in the near-field environment (NFE) of the potential nuclear-waste repository at Yucca Mountain, Nevada (Corwin and Hoover, 1979; Zohdy et al., 1973; Anderson and Johnson, 1976). Because of their potential influence on reaction processes, SPs may be significant in understanding how the NFE will evolve geochemically. In addition, SPs may generate electrical currents that may affect the performance of metallic waste containers. This chapter discusses some particular mechanisms that generate SPs in rock-water systems and provides order-of-magnitude estimates for the SPs that may be present in the NFE.

Other currents that may be present in the NFE are magnetotelluric and telluric currents; however, these currents are believed to be the result of diurnal variations, caused by solar emission, aurora, and other phenomena, in the earth's magnetic field (Telford et al., 1976). These currents are probably less significant than those caused by SPs and are outside the scope of this discussion.

8.2 Self-Potentials

Underground water is an important factor in most occurrences of SPs. Telford et al. (1976) found that SPs are associated with variations in rock properties at contact interfaces where corrosion occurs as a result of thermal and pressure gradients in underground fluids (thermoelectric and streaming potentials), and with variations in electrolytic concentrations of groundwater (electrochemical potential).

8.2.1 Streaming Potential

When two phases are placed in contact, a difference in potential between them generally develops. If one of the phases is a polar liquid, like water, its dipolar molecules will tend to be oriented in a particular direction at the interface, generating a potential difference. If there are ions or excess electrons in one or both phases, the electrical charges will tend to distribute themselves nonuniformly at the interface. The region between the two adjoining phases is always marked by a separation of electrical charges so that near, or on the surface of, phase I there is an excess charge of one sign, and the balancing charge is distributed somehow through the adjoining surface regions of phase II (Hunter, 1981). This arrangement of charges at the interface is referred to as the electrical double layer. When liquid moves through a capillary or a porous medium under a pressure gradient, the excess charges near the wall are carried along by the liquid, and their accumulation downstream causes the buildup of an electrical field, which drives an electrical current back (by ionic conduction through the liquid) against the direction of liquid flow (Hunter, 1981). The measured potential difference across the capillary is called the streaming potential.

Ishido et al. (1983) report that in rock-water systems the streaming potential coefficient increases exponentially with decreasing hydraulic radii $<10^{-6}$ m. Klavetter and Peters (1987) show that for Topopah Spring tuff (the potential repository horizon) the pore sizes range from 10^{-6} to 10^{-8} m with most of the pore volume due to the 10^{-7} m fraction. This would suggest that the streaming potential coefficient for Topopah Spring tuff will be relatively high due to its small pore sizes (although to the best of our knowledge the coefficient has not been established for welded tuff). Nourbehecht (1963) reports that the streaming potential coefficients for a wide variety of rocks ranges from about 0.3 to 30 mV/atm.

Chapter 1 shows numerical modeling results that predict a region of condensate accumulation with 100% saturation adjacent to the boiling region. Pressure gradients within this region of high saturation can cause liquid to flow very slowly within the porous medium. There will be streaming potential associated with the

liquid flow. The magnitude of the streaming potential cannot be estimated because the streaming potential coefficient for unsaturated welded tuff is not known at this time.

8.2.2 Thermoelectric Potential

Temperature gradients give rise to thermoelectric potentials in rock-water systems (Telford et al., 1976). Nourbehecht (1963) reports that the thermoelectric coefficient for rock can be as high as 1 mV/°C with average values of about 0.2 to 0.4 mV/°C. As reported in Chapter 1, these numerical modeling results show that drift wall temperatures as high as 200°C may be present in the repository and a temperature near 96°C within the condensate region. If we assume an average thermoelectric coefficient of 0.3 mV/°C and a temperature difference of 100°C, the calculated thermoelectric potential is 30 mV. Chapter 1 calculations show that the temperature gradient decreases as time after emplacement increases, which implies that the thermoelectric potential would also decrease as time after emplacement increases.

8.2.3 Electrochemical Potential

Electrochemical potentials arise when diffusion of ions occurs. This potential is attributed to two causes: (1) the difference in mobilities of various ions in solutions of different concentration (diffusion potential), and (2) the potential that develops when two electrodes are immersed in the same solution but at two different concentrations (Nernst potential). For example, when the concentrations are in the ratio of 5:1, the potential that develops is ±50 mV (Telford et al., 1976).

In regions where interconnected fluids exist across the potential field, ionic diffusion and reaction relationships will be influenced by the potential field. This effect needs to be evaluated in future work.

8.3 Summary

We have briefly described the mechanisms that are likely to be operating in the NFE, generating natural electrical potentials and currents. The electric potential

fields caused by groundwater flow, and by temperature and ionic concentration gradients will coexist in the NFE. Due to the combined effects of these fields, the resulting electric potential gradients may affect the geochemical evolution of the NFE (although this has not been evaluated to the best of our knowledge) and possibly, the performance of waste container materials. Very little information is available with which to estimate SP generation within the NFE. We have raised the possibility that SPs may be significant in the NFE and, thus, should be investigated further. In addition, SPs may be useful as a diagnostic measurement of the near-field hydrothermal environment.

8.4 References

Anderson, L. A., and G. R. Johnson (1976), "Application of the Self-Potential Method to Geothermal Exploration in Long Valley, Californaia," *Journal of Geophysical Research* 81, 1527–1532. (Readily available).

Corwin, R. F., and D. B. Hoover (1979), "The Self-Potential Method in Geothermal Exploration," *Geophysics* 44, 226–245. Readily available).

Hunter, R. J. (1981), *Zeta Potential in Colloid Science, Principles and Applications* (Academic Press, London) Chapters 1–3. (NNA.920916.0006)

Ishido, T., H. Mizuanti, and K. Baba (1983), "Streaming Potential Observations, Using Geothermal Wells and In Situ Electrokinetic Coupling Coefficients under High-Temperature," *Tectonophysics* 91(1–2), 89–104. (NNA.920506.0056)

Klavetter, E. A., and R. R. Peters (1987), *An Evaluation of the Use of Mercury Porosimetry in Calculating Hydrologic Properties of Tuffs from Yucca Mountain*, Nevada, Sandia National Laboratories, Albuquerque, NM, SAND86-0286-UC-70. (NNA.890327.0056)

Nourbehecht, B. (1963), *Irreversible Thermodynamic Effects in Inhomogeneous Media and their Applications in Certain Geoelectic Problems*, Ph.D. Thesis, Massachusetts Institute of Technology, Cambridge, MA, pp. 1, 3, and 6. (NNA.920506.0032)

Telford, W. M., L. P. Geldart, R. E. Sheriff, and D. A. Keys (1976), *Applied Geophysics* (Cambridge University Press, London). (NNA.891106.0192)

Zohdy, A. A. A. R., L. A. Anderson, and L. J. P. Muffler (1973), "Resistivity, Self-Potential, and Induced-Polarization Surveys of a Vapor Dominated Geothermal System, "*Geophysics* 38, 1130–1144. (NNA.91062.0059)

Contents

Chapter 9.0 Field Thermal Tests

W. Lin and A. Ramirez

9.1 Introduction

Understanding the movement of moisture, including liquid water, steam, and vapor, in the near-field environment (NFE) of the potential nuclear-waste repository at Yucca Mountain, Nevada is one of the goals of waste-package environment hydrologic investigations. This section discusses field tests to enhance our understanding of how thermal loading, resulting from waste package emplacement, will affect the hydrologic properties and processes of the NFE.

One of the main concerns in the NFE of a nuclear-waste repository is the quantity and quality of the water that may be present to contact the waste and waste packages (near field) and in the rock mass surrounding the repository since water can cause property changes in the altered zone. Processes that may affect the quantity and quality of the water are coupled thermal-mechanical-hydrological-chemical (TMHC) processes. The TMHC processes may involve the *in situ* pore water in the Topopah Spring tuff, water present in fractures, and/or condensate that result(s) from water mobilized by heat, as well as any introduced water (either naturally or artificially) after the emplacement of the wastes. Field and laboratory tests are conducted to: enhance our understanding of the coupled TMHC processes and to measure physical properties. This chapter discusses the field tests.

The rationales of conducting field thermal tests are to extend from laboratory tests on relatively small samples (up to 1-m, maximum), to testing of rock masses that include fractures and inhomogeneity as representative to Yucca Mountain as possible, and under test conditions as close as possible to *in situ* repository conditions. The logic of testing, i.e., increasing sample size from small to large, increasing the complexity of sample characteristics from intact to include multiple fractures and heterogeneity, and relaxing test boundary conditions from simple controlled to uncontrolled, is to evaluate the temporal and spatial scale effects, to

increase our understanding of the test results in steps, and to enhance our confidence in modeling the tests and the coupled TMHC processes to be expected in a repository. The purposes of field thermal tests are to test the coupled TMHC processes in a rock mass which is big enough to include heterogeneity, so that the test results can be used to verify model predictions and to identify important physical processes that must be included in the conceptual models. The objectives, goals, and rationales of the field tests are described in section 8.3.4.2.4.4 *Study Plan for Engineered Barrier System Field Tests* (Lin, 1995). Based on the findings and logic of that report, several field thermal tests are planned to serve different purposes (described here). The G-Tunnel test was conducted in 1988–1989, in Grouse Canyon tuff in G-Tunnel, Nevada Test Site, to improve our understanding of the thermal-hydrological processes in an underground environment and to prototype instruments and test methodologies. The Large Block Test (LBT) was designed to provide testing of the coupled TMHC processes in Topopah Spring tuff under controlled boundary conditions so that the results can be more directly compared with model calculations. Also, the LBT will provide three-dimensional (3-D) coverage of the test region with instruments. In addition, the LBT can provide a unique opportunity for investigating infiltration in a heated rock mass. The ESF Thermal Test (ESFTT) will be the first *in situ* thermal test in the potential repository horizon in Yucca Mountain. The results of the ESFTT will be used for viability analyses and license application of the repository. Although it is still in the conceptual state, the plan, if instituted, is to use the Large Scale Long Duration Test (LSLDT) to heat up a region with multiple emplacement drifts for several years so that all possible coupled TMHC processes can be tested (see section 9.5 for more details). Also planned are the Confirmation Observations of the performance of a repository. The confirmation monitoring is the only test in the true temporal and spatial scales of a repository, therefore is very critical (see section 9.6).

Basically, field thermal tests involve heating a rock mass with electrical resistor heaters and monitoring the spatial distributions and temporal variations of temperature, moisture content, concentration of certain chemical elements, and stress and displacements in the rock mass. Temperatures will be measured by using

either resistance temperature devices (RTD) or thermocouples, dependent on the temperature range to be measured and accuracy required. Moisture contents will be measured in the following means: point measurement of relative humidity will be conducted using Humicaps. Line measurement of moisture content will be done using neutron logging. Two- and three-dimensional tomographs of the moisture content will be inferred from electrical resistivity tomographs (ERT). Chemical sensors will be used to monitor concentration of some chemical elements, such as pH, conductivity, dissolved oxygen, Ca, Cl, etc. Both mechanical and optical multiple borehole extensometers (MPBXs) will be used to measure displacements. Scoping model calculations will be used to design the tests, and then model calculations with exact test configurations will be used to monitor their progress and for post-test data analyses. Chapter 1.9 presents some of the results of the model calculations. Post-test examination of the rocks are usually planned to verify some of the indirect observations by instruments during the test with direct observations. The G-Tunnel test is the only field thermal test that has been completed. The results from the G-Tunnel test are summarized in section 9.2. Recently, model analyses of the G-Tunnel test results were performed (See Chapter 1.9 for the results of those analyses). The LBT has been planned, constructed, and characterized, but instruments have not been installed. Only the pre-test characterization results of the LBT are presented here. See section 9.4 for the test design and plans for the ESFTT.

9.2 G-Tunnel Tests (*A. Ramirez*)

This discussion includes the key results and supporting data from the G-Tunnel tests in which we studied the hydrothermal perturbation of welded tuff near a horizontally oriented heater. As part of the G-Tunnel tests, we measured several parameters as a function of location and time so that we could examine the effects of heating and cooling during a thermal pulse that lasted ~195 days.

A schematic of the hydrologic environment expected to develop around a heater during thermal loading is shown in Fig. 9-1 [see Yow (1985), for additional details on the expected environmental conditions]. This figure depicts the primary

mechanisms of heat and fluid flow for an idealized example of a horizontal heater that is intersected by a near vertical fracture. The actual heater borehole was intersected by more than a dozen fractures. The rock mass consisted of matrix blocks that were bounded by fractures and the borehole wall (for blocks immediately adjacent to the heater). Under ambient conditions, the matrix blocks are partially saturated, and the fractures and borehole are essentially dry. The heater heats the borehole surface primarily via thermal radiation. As heat is conducted through the fractured rock mass, vaporization begins on the outer surfaces of the matrix blocks closest to the borehole and then proceeds in toward the center of each block. Where temperatures are in excess of saturation conditions, vigorous boiling occurs. For water vapor to flow out of the matrix blocks, gas-phase pressures must increase from the surface of the matrix block to its interior, resulting in the elevation of the boiling temperature with distance into the matrix block. Water vapor that enters the fractures is subsequently driven by gas pressure gradients (including buoyancy effects) within the fracture network. In general, vapor flow in the fractures is directed away from the center of the boiling, either radially outward or inward toward the heater hole. Vapor flow in the fractures persists until condensation conditions are encountered. Condensed water in the fractures that is not immediately imbibed by the matrix flows under gravity and capillary forces in the fractures either (1) back toward the boiling zone where it reboils, or (2) out into the condensation zone where it is eventually completely imbibed by the matrix.

9.2.1 Parameters Measured

The following parameters were measured to characterize the behavior of the rock mass within a few meters of the heater before, during, and after the thermal cycle. This discussion includes the results for a subset of the measured parameters and presents interpretations pertaining to the evolution of the NFE around a simulated waste package [for full details refer to Ramirez et al. (1991), including those reports listed in the "References" and "Bibliography of Related Reports" section].

9.2.1.1 Rock Mass Temperatures. Rock mass temperatures were used in reconstructing the thermal response of the rock and in evaluating the performance of the test equipment.

9.2.1.2 Rock Mass Gas Pressure and Atmospheric Pressure. Rock mass gas pressure and atmospheric pressure were used in reconstructing the flow regime of the air and water vapor in the rock mass.

9.2.1.3 Borehole Measurements of the Relative Dielectric Constant and Thermal Neutron Counts. Cross borehole measurements of the relative dielectric constant of the rock and single borehole measurements of thermal neutron counts were used to infer the spatial and temporal changes in the moisture content of the rock mass.

9.2.1.4 Air Humidity. Air humidity measurements in the rock mass were used to calculate the pore pressure gradients that drive the movement of liquid water within the rock mass. Changes in the moisture content and pore pressure information were used to reconstruct the flow regime of liquid water in the rock mass. The spatial variations in moisture content were used to infer the flow paths of the liquid water and to define regions that are losing or gaining water as a function of time.

9.2.1.5 Air Permeability. The air permeability measurements were used to detect changes in the permeability of the rock surrounding the heater emplacement borehole. These measurements were made along the heater borehole after all of the boreholes were drilled and sealed. The measurements were repeated after the heating sequence was completed and after the heater was removed from the borehole.

9.2.1.6 Fracture Locations and Orientations. Fracture locations and orientations were measured in all boreholes by means of a borescope and/or by borehole television surveys performed before the heater was energized. The measurements were repeated along the heater emplacement borehole after heating was completed, and these data were used to:

- Determine the effects of heating on the stability of the emplacement borehole walls.

- Interpret the changes in fracture permeability caused by the heating and cooling cycle.
- Analyze the flow regime of vapor and liquid water in the rock mass as inferred from other measurements.

9.2.1.7 Condensed Volume of Steam. The measurements of the condensed volume of steam invading the heater borehole were used to estimate the amount of gas phase humidity that flows toward the heater borehole.

9.2.2 Test Description

Sandia National Laboratories constructed the GTUF, which consists of drifts driven in welded tuff under Rainier Mesa, NTS, for the YMP (Fig. 9-2). The G-Tunnel tests were conducted in the rock mass between the small-diameter heater alcove and the rock mechanics incline.

The test included an accelerated thermal cycle to examine the effects of the heating and cooling sides of a thermal pulse. Figure 9-3 shows the test's power schedule. The initial thermal loading for the 3-m (9.8-ft) heater was ~3.3 kW (1.1 kW/m of heater length). To increase the disturbed volume of rock within the relatively short time available for prototype testing and to create sufficiently high rock temperatures to drive two-phase fluid flow, we set the initial thermal load per unit length of emplacement borehole higher than the loading expected for a typical spent fuel container (0.4–0.7 kW/m).

The duration of the heating was based on the test criteria of heating the rock mass until the boiling point isotherm moved ~0.6–0.7 m (2.0–2.3 ft) radially from the heater borehole wall. Another test criteria involved achieving emplacement heater borehole temperatures similar to those expected for the repository (235°C). The spatial extent of the heating affected a volume of rock large enough to include several fractures.

Figures 9-4 and 9-5 show the borehole layout and the measurement stations for the various instruments used. The test location within G-Tunnel is bounded by the small diameter heater alcove and the rock mechanics incline, as shown in Fig. 9-4. The heater borehole is inclined slightly upward (elevation increases from the collar

to the end of the borehole) from the rock mechanics incline. The diameter of the heater borehole is 30.5 cm (12 in.).

Twelve of the boreholes were used to monitor the rock response; all of these were nearly horizontal and were inclined slightly downward. The majority of the boreholes were orthogonal to the emplacement hole axis, which provided better coverage of the spatial variations in rock responses that occur parallel to the radius of the emplacement borehole. This arrangement allowed measurements in the direction of expected maximum thermal and hydrologic gradients. Three boreholes were drilled parallel to the heater borehole axis to monitor rock response beyond the ends of the heater.

9.2.3 Changes in Rock Mass Moisture Content

A thorough understanding of local hydrology over the package lifetime is central to understanding waste package performance. Geophysical techniques were used to monitor changes in rock moisture content during the test. The techniques chosen included neutron logging in single boreholes and high-frequency electromagnetic measurements performed between boreholes. In this section, we interpret only the neutron log results; for the electromagnetic measurement results, see Daily et al. (1989).

The neutron logging probe contains a source of high-energy neutrons and a detector for slow (thermal) neutrons. When water is present in the rock, the hydrogen in the water slows the neutrons for detection. Seven boreholes (NE-1 through NE-7) were sampled before the heater was turned on; the measurements were repeated frequently after the heater was energized to monitor temporal and spatial changes in moisture content. A paraffin shield included with the probe was sampled at the beginning and end of each logging day to verify that the tool was functioning properly.

For each borehole, we calculated the differences between the "before" and "after" measurements ("after" heating minus "before" heating) to produce a difference log. We chose to use differences rather than absolute values of moisture content because

the effects of the borehole liners and the grout within the survey boreholes are still unknown.

A spatial filter was applied to each difference log to smooth the spikes in the trace caused by the random fluctuations in the number of neutrons generated by the radioactive source in the probe. The precision for the filtered data is estimated to be ± 0.003 g/cm^3. This precision estimate means that for any one point on a difference trace that equals or exceeds ± 0.003 g/cm^3, there is a 95% probability that the difference is caused by true changes in the measurement and a 5% probability that it is caused by random fluctuations in the neutron output of the radioactive source.

Boreholes NE-2A, NE-6, and NE-7 are three coplanar boreholes located above and below the center of the heater as shown in Fig. 9-5. The data collected along these boreholes were combined and plotted as a function of radial distance to the center point of the heater assembly. The changes shown were calculated relative to preheating moisture measurements. Figures 9-6, 9-7, and 9-8 consist of two plots each that show the same data at two different scales so that the smaller changes occurring at the more distant locations can be examined.

Figures 9-6 and 9-7 show radial profiles of changes in moisture content during the drying and rewetting phases of the test. These figures also show the difference traces calculated from day 70 data (the heater was energized on day 0) and for day 301 (the last data set was collected 106 days after the heater was de-energized). The data in Fig. 9-6 were collected midway through the maximum power phase of the test. As expected, the rock closest to the heater (the shortest distance) lost substantial amounts of moisture. However, the rock near borehole NE-2A dried at a faster rate than the rock near NE-6. Fracture maps of the test region suggest that a higher concentration of fractures mapped along NE-2A may be one cause for this faster rate of drying. Also note that rock located between 1.75- and 2.25-m radii showed a small increase in moisture content as a result of the condensation of steam generated in hotter regions closer to the heater.

Between days 70 and 127 (data are not shown) the NE-2A profile showed very little additional drying when compared to Fig. 9-6, whereas the NE-6 profile showed significant additional drying. Both profiles are closely matched with the caveat that

the width of the drying region appeared to be slightly wider near NE-2A. The closely matched profiles suggest that the rock near NE-2A and NE-6 was almost completely dry because very little additional drying occurred near NE-2A during the 57 days of continued heater operation at maximum power. The radius of the dry zone achieved was ~0.7 m; this is consistent with the test objective of achieving boiling conditions within a 0.6–0.7-m radius.

The radial profile of changes in moisture content for day 301 are shown in Fig. 9-8. These data were collected during the postheating phase of the test, 106 days after the heater was de-energized. The data show relatively little change in the rock near the heater during the power rampdown and postheating phase of the test. It also shows that the rock above the heater (borehole NE-6) rewet more quickly than the rock below the heater (borehole NE-2A) for distances less than or equal to 0.5 m. This suggests that the gravity-driven flow plays a role in the rewetting process.

We gained further insights into the rewetting process by calculating changes in moisture content relative to the last day of full power heating. Figure 9-9 presents changes in moisture in borehole NE-2A, where "after" minus "before" changes are calculated relative to day 127 (i.e., the "before" data correspond to day 127, which was the day before the last day of maximum power heating). The data were obtained during the power rampdown and postheating phases of the test when the rock was cooling and rewetting. Also shown are fractures mapped along the boreholes. Note that the rock regions that show the greatest rewetting are clustered around the fractures in NE-2A. The high correlation between fracture locations and rewetting suggests that fractures play a dominant role in the rewetting process. One mechanism for rewetting along fractures may be capillary condensation of air humidity in the fractures because humid air (found in the wetter portions of the rock mass) can travel with relative ease along the fractures. Another mechanism that may be playing a role in the rewetting process is water dripping along fractures; Fig. 9-8 shows evidence consistent with this argument in that the rewetting front has penetrated more quickly above the heater (borehole NE-6) than below the heater (NE-2A).

9.2.4 Temperature Measurements

Temperature measurements were made to characterize the thermal response of the medium around the heater. There were a total of 112 thermocouples used in this test. All of these thermocouples were chromel-alumel (Type K) with an accuracy of ±1°C (1.8°F). Ten thermocouples were installed within the heated portion of the heater borehole to monitor container and borehole wall temperatures. The other 102 thermocouples were located in boreholes TC-1, TC-2, P-1, P-2, and P-3.

Figure 9-10 shows the temperatures measured in all boreholes during the last day of the maximum power phase (day 128). The temperatures are plotted as a function of the natural log of radial distance to observe the linearity or nonlinearity of the temperature profiles. Note that with the exception of the P-3 profile, all profiles are fairly linear. This indicates that the thermal conduction is the predominant heat transfer mechanism for the regions sampled. There are a few temperature values (in both P-2 and P-3) that deviate from a straight line for values of the radial distance <1 m (natural log <0). At these locations, fractures were mapped in close proximity (within a few centimeters) of the thermocouple locations. This close proximity suggests that the depressed temperature values within the boiling region are caused by fractures. At least two explanations can be postulated:

1. The fractures create more permeable flow paths for vapor to escape the system. As water is converted to vapor and allowed to escape, energy is removed from these locations. This energy is therefore not available to elevate the rock temperatures.

2. The fractures also create flow paths along which drilling water moves downward. Borehole P-3 is lower in elevation than P-2. The matrix adjacent to these fractures might have imbibed some of the drill water, thereby increasing the initial saturation near the fractures. This elevated saturation would also tend to depress the local temperature for the same reason as stated above in explanation 1.

The temperatures along borehole TC-2 are generally cooler than those in other boreholes at the same radial distance. The temperatures in P-2 are the highest among the five boreholes. Boreholes TC-1, P-1, and P-3 registered about the same temperatures. These differences in temperature are probably due to the

heterogeneous thermal properties of the rock mass. The almost linear portion of these curves at larger radial distances indicates that conduction is probably the main heat transfer mechanism. Also, the TC-2 profile shows a more shallow slope, which implies that the thermal conductivity of the rock around TC-2 is higher than at other locations.

A comparison of the P-2 and P-3 temperature profiles in Fig. 9-10 shows that the temperatures in P-3 are consistently lower than those in P-2. This is probably due to the higher temperatures measured at the top of the container. Air circulation within the heater container (i.e., hotter air rising to the top of the container) may have caused the asymmetry in temperatures.

Figure 9-11 shows the temperatures for thermocouples 86 through 89 as a function of time. These thermocouples are located below and to the side of the heater (Fig. 9-12). Thermocouples 86 and 87 show typical profiles of temperatures within the boiling region. The temperature increased quickly at the beginning of heating, then became almost linear with time. At these later times, the temperature-time plot has no obvious change of slope. A change in slope would indicate a change in the thermal conductivity and heat capacity of the rock. At later heating times, changes in slope may be attributed to the latent heat capacity of the water as the water boils or condenses in the rock mass.

Thermocouples 88 and 89 in Fig. 9-11 show very atypical temperature profiles. Note that the maximum temperature for both profiles is ~97°C. Also the profiles remained near the maximum temperature for 70 or more days even though the rest of the rock mass continued to increase in temperature during this period (maximum power phase). In addition, the slope on the left side of the flattened portions of these two profiles rapidly increased before the flattening occurred. This indicates that additional energy was being deposited at these locations. We postulate that condensed water with near-boiling temperature moved into this region from regions above the heater as illustrated by the conceptual model shown in Fig. 9-13. We recognize the possibility that this type of temperature signature is due to a heat pipe effect, but we consider this unlikely because of the rapid increase in slope observed prior to the flattening.

9.2.5 Changes in Air Permeability

Air permeability testing was conducted along sections of the heater emplacement borehole before heating and at the end of the power rampdown phase of the test. The objectives of this test were to characterize the *in situ* permeability of the fractured tuff around the heater borehole and to determine the effect of a heating and cooling cycle on rock mass permeability. A number of permeability measurements were made along packed-off sections of the borehole before the rock mass was heated and again after all heating was completed.

We used steady-state air-injection to measure the permeability. Inflatable packers were placed in preselected sections of the borehole to isolate these sections for testing. Preheating and postheating permeability values are compared in Fig. 9-14. Equivalent porous medium permeabilities along the heater borehole are also compared with mapped fracture locations. The permeabilities shown here were measured at a nominal pressure of 34 kPa (5 psi). The permeability of a 36-cm-long (14.2-in.-long) test zone varies from a minimum of 0.04 darcy (D) to a maximum of 150 D. The higher permeability value corresponds to a highly fractured zone, a few inches thick, at a depth of about 7.7 m (25.3 ft) from the collar.

A comparison of the preheating and postheating profiles in Fig. 9-14 shows that portions of the measured region had increases in gas permeability as a result of the heating cycle. Note that the greatest percentage change occurred near the center of the heater element location. This is also the portion of the borehole with the fewest fractures mapped. We postulate that the increase in permeability is due to an increase in the number of small fractures (microcracks) intercepting the heater borehole. Television surveys of the borehole showed no change in the visible fractures relative to the preheating survey. This implies that any new fractures were small enough to escape detection. Given that the lowest permeabilities were measured in the region of greatest change, increases in microfractures would have a relatively greater effect here than in regions with a higher preheating permeability. Note that the increased permeability is low when compared with the natural heterogeneity in air permeability along the borehole.

9.2.6 Steam Invading the Heater Emplacement Borehole

The thermal loading exerted by the heater dries the partially saturated rock surrounding the emplacement borehole. Vapor pressure gradients drive steam into pressure sinks such as the borehole and fractures (see Fig. 9-1). Steam may also move along the fractures toward the borehole or move outward and condense where the temperatures are sufficiently cool. The moisture entering the heater emplacement borehole was collected to provide a measure of the resistance to vapor transport toward the heater relative to the resistance to transport away from the heater as a function of time.

The moisture migrating into the heater emplacement borehole was collected using a high-temperature inflatable packer fitted to a 51-mm (2-in.) i.d. aluminum pipe. The packer sealed the borehole 50 cm (19.7 in.) outward (i.e., toward the collar) from the heater and allowed the steam to flow through the aluminum center pipe, condense, and flow to the borehole collar and into a collection device (the isolated section remained unpressurized at all times). The heater emplacement borehole had a slope of 5° downward to the collar to facilitate the collection of the condensed moisture.

Figure 9-15 presents the results from an analysis of the water collection rates during the test. Also shown for comparison is the partial pressure of water within 15 cm of the intake for the steam collection system; the partial pressure values are calculated based on relative humidity and air temperature measurements. These data show that an insignificant volume of water was collected within the first two weeks of the experiment. Thereafter, the rate of water collection reached a maximum of ~0.05 l/day, which is less than the value of ~0.5 l/day predicted by the scoping calculation. The reasons for this discrepancy are unclear at present. One possible explanation is that the packer temperature at the intake point for the system is below the dew point. This might have caused some vapor to condense, pond, and possibly drain into fractures, instead of entering the center pipe at the packer. Temperatures at some points on the packer suggest that packer surfaces could have acted as condensation points. Another possible reason for the discrepancy is that the

scoping calculations assume an infinitely long heater. This assumption would result in a substantial overestimate of the steam produced.

The water collection rate (Fig. 9-15) peaked at about day 50 and then decreased between day 50 and 90. We did not expect this decrease and have not yet explained it. Note that the partial pressure of water in the air remained approximately constant between days 50 and 128. All other conditions being equal, we expected the moisture collection rate to remain constant if the partial pressure of the air in the heater borehole remained constant. The partial pressure of water started to decrease as expected on day 128 when the power rampdown phase began.

Another unexplained aspect of the moisture collection rate is the abrupt water collection rate decrease at about day 90. This signature may be an indication of problems with the sensor; however, post-test calibration of the sensor did not indicate that the sensor was flawed.

9.2.7 Summary

The G-Tunnel tests provided valuable experience that will improve our ability to conduct the EBSFT planned for the ESF in Yucca Mountain. The results from the G-Tunnel tests indicate that many environmental conditions expected to develop around a heater in welded tuff are as described in Fig. 9-1. The test also showed us which of the applied measurement techniques performed adequately under realistic environmental conditions and which ones may need to be modified or replaced.

The G-Tunnel tests confirmed elements of the conceptual model of predicted environmental conditions. Test results confirm that a dry zone develops around the heater borehole (refer to the conceptual model in Fig. 9-13) and that the degree of drying increases with proximity to the heater. A "halo" of increased saturation develops adjacent to the dry region and migrates away from the heater as rock temperatures increase. Some of the fractures intercepting the heater borehole increase the penetration of hot-dry conditions into the rock mass. A buildup of pore gas pressure develops in rock regions where vigorous evaporation is occurring.

During the portions of the test when the heater power was gradually reduced and eventually turned off, the dry region around the heater cooled off and slowly

regained water (refer to the conceptual model in Fig. 9-16). Rewetting of the dry region occurred first in the rock above the heater and in the rock adjacent to fractures.

To explain the differences in the drying and rewetting behavior above and below the heater, we developed conceptual models that are based on the results described here and on our numerical modeling study. In general, we found that water vapor generated in a matrix block moves toward the closest fracture face (or toward the surface of the heater borehole if the block is adjacent to the borehole). Upon entering the fracture, water vapor tends to move radially outward through the fracture system until encountering condensation conditions. The heater borehole moisture collection system and the condensation on the heater packer cause some of the vapor in the fractures to move radially inward toward the heater hole. Water that condenses above the heater drains downward through the fractures. Much of this downward flow intersects the boiling zone and is reboiled, thereby slowing the upward progress of the boiling front. We observed that some of the downward flowing condensate reboiled at the lower flank of the heater, thereby stabilizing the boiling front at that location. Water that condenses below the heater drains away from the boiling zone.

Since the matrix imbibition rate is slow relative to the condensate generation and drainage rates, most of the downward-draining condensate located below the heater left the system before it could be subsequently reboiled. We also observed that the boiling zone effectively acted as an "umbrella" shielding the rock below the heater from the downward drainage of condensate generated above the heater. Rewetting of the rock above the heater and to one side of the heater was partially the result of condensate drainage in fractures. Throughout the fractured rock mass, rewetting also occurred via binary diffusion of water vapor (driven by relative humidity gradients) and via Darcy flow (driven by pressure gradients). As this water vapor reached drier rock, it condensed along the fracture faces (by capillary condensation) and was imbibed by the matrix.

Measurements of air permeability made along the heater borehole prior to heating show that the fracture system exhibits a strong heterogeneity in fracture

permeability. Measurements made after the heater was turned off show that there was an increase in air permeability as large as an order of magnitude for the rock that reached the highest temperatures.

The test also yielded some surprises in terms of environmental conditions. The temperature above the heater container was ~30°C (54°F) higher than below the container. This condition might be a consequence of hotter air accumulating at the top of the container; it may also be related to the higher moisture content below the heater borehole. The amount of steam that invaded the heater borehole is much less than that predicted by the scoping calculations. The reasons for this discrepancy are not clearly understood, but they might be a result of an inadequate system used to collect and condense the steam or an indication of invalid assumptions used in the scoping calculations.

Recently, J. Nitao used a discrete fracture model (DFM) to re-analyze the results of the G-Tunnel test. The DFM was able to predict the observed thermal hydrological processes during the G-Tunnel test. The re-analyses show that gravity drain and buoyant gas-phase convection are likely reasons why condensate buildup in the matrix was not observed in the test. Preferential drying below and wetting above the heater lends some support for the possibility that buoyant convection in the fractures is a factor driving moisture movement. Temperature predictions by all models were good, substantiating that heat transfer in the rock was primarily by thermal conduction. Because of the short duration and small spatial scale of the test, the local condensate drainage flux during the G-Tunnel test was probably much higher than that to be expected for a repository beyond the first few hundred years. The results of the analyses are presented in Chapter 1.

9.3 Large Block Test

The objectives, goals, and plans of the Large Block Test (LBT) are described in Lin (1993 ,1994). Detailed engineering plans for conducting the LBT were also completed. Originally, as described in Lin (1993), the objectives of the LBT were to conduct tests of the coupled TMHC processes in a $3 \times 3 \times 4.5$ m block of Topopah Spring tuff with

constant stress and adiabatic boundary conditions on the vertical sides. Particularly the LBT was designed to test thermally driven dryout and condensation, condensate refluxing, and the related mechanical and chemical responses of the block. The goals were to heat the large block from five heaters in a horizontal plane at about 2.75 m from the block top, with guard heaters on the sides and constant temperature controls at the top, to maintain a one-dimensional (1-D) thermal gradient in the block. The maximum temperature at the heater horizon would be about 140°C, and the temperature at the top would be about 60°C. A constant stress on the surfaces of the block would be maintained at about 4 MPa. The steady state of the temperatures would be maintained for about four to five months, then the heaters would be turned off to start a natural cooling process. The fore-mentioned instruments would be installed in boreholes in the block and on the block surfaces to have 3-D measurements of the parameters. Scoping model calculations have been performed to facilitate the test design (Lee, 1995a,b). Based on the scoping model calculations, we expected to observe a dryout region of about 2 m wide near the heater plane, a condensate zone of about 1 m thick at both above and below the dryout zone.

Due to budget constraints, we eliminated the load-retaining steel frame to maintain a constant stress of 4 Mpa and replaced it with a strap system to maintain the integrity of the block during the test. Also, we gave up the plan to have the *in situ* monitoring of chemical species. We will depend on the post-test examinations of the evidences of rock-water interaction on the fracture surfaces to evaluate the chemical part of the coupled TMHC processes. Another modification of the original test scope was that the active controls for an adiabatic boundary condition on the sides of the block (the guard heaters) was replaced by passive thermal controls, using insulation materials. This modification of the boundary control did not have much affect on the intended test. Thermal conduction calculations indicate that using insulation materials on the sides can keep the temperature distribution in most parts of the block very similar to a 1-D case. The temperature in a region of a few centimeters in thickness from the surface of the block will have significant lateral gradient. However, more sophisticated model calculations will be required when the data are analyzed to take the lateral heat flux into consideration. Currently, the

block has been isolated and all boreholes for installing instruments have been drilled. Figure 9-17 shows the boreholes in the large block. Some small blocks of the same rock type have been collected from regions adjacent to the large block for testing hydrological properties and thermal-hydrological processes in the laboratory. Some of the laboratory test results have been reported in Chapter 2. But the block has been mothballed until further notice from the Yucca Mountain Site Characterization Project.

All of the pre-test characterization of the large block has been completed. These include the bulk air permeability of the block determined by using single borehole injection before isolating the block, neutron logging to determine the initial moisture content in the block, matrix water permeability and connected porosity of cores collected during the drilling of the boreholes, the fracture distributions on the five surfaces of the block and on the surface prior to cutting the block, and video imaging in every borehole. The results of the pre-test characterization will be presented later in this section. The water permeability of one of LBT cores as a function of temperature is reported in Chapter 2.

Figure 9-18 shows the bulk air permeability of the block as a function of depth. The permeability was determined by single borehole injection before the block was isolated. The permeability varies from about 10^{-16} m^2 to more than 7×10^{-12} m^2. Intersection of fractures with the injecting borehole was the deterministic factor of the permeability variation. Because the block is highly fractured (shown later in this section), the bulk air permeability of the entire block may be more homogeneous.

Some of cores collected during the drilling were used to determine the connected porosity of the matrix. Figure 9-19 shows the matrix porosity as a function of depth. The porosity varies from about 10% to about 13.5%. The porosity of the TSw2 unit of the Topopah Spring tuff in Yucca Mountain is 12.1 ± 3.6% (Reference Information Base, YMP/93-02, Rev. 0). The matrix porosity was used to determine the water saturation from the neutron logs. Figure 9-20 shows the moisture content of the block determined by neutron logging in some of the vertical holes before and after the cutting of the block boundaries. The water saturation of the block is between 60

and 80%. This level of water saturation will provide enough moisture for creating an observable dryout zone and a condensate zone. Cutting of the block boundaries with water did not change the moisture content of the block interior.

Fractures on the five surfaces of the block were mapped carefully. Because the surfaces were cut smooth, it was possible to conduct very detailed fracture mapping. But it was difficult to determine dip on the top surface and strike and true dip of most of the fractures on the vertical surfaces. Figures 9-21 through 9-25 show the fractures on top, north, west, south, and east sides of the block, respectively. These fracture maps were combined into a 3-D physical model, which was used to project the fractures in the block to locate the instrument holes. These fracture maps and video images in each borehole will be used to infer fractures within the block, using fracture projecting software, such as Earth Vision.

Prior to cutting the block, the cleaned off ground surface was mapped in detail. After it was cut, this area became the top of the block and was subsequently mapped (see Fig. 9-21), but this data was not analyzed at the time of this report. Because the pre-cut surface was excavated, rather than cut smooth, dip measurements were made of many of the fracture surfaces. Block characterization indicates that the fracture system is similar to that observed underground in the ESF Access Drift. Figure 9-26 shows comparison plots of the fractures mapped on the top of the LBT prior to block cutting and that in the ESF. Comparison of the data from the ESF [Fig. 9-26(b)] and the LBT [Fig. 9-26(a)] shows that fractures in the LBT are similar to those observed in the ESF in the TSw2 unit (Barr et al., 1996) with the exception that the low-angle fractures mapped in the ESF are not represented in the LBT mapped features. This difference is because the data set is from the horizontal surface and therefore low-angle sets would not be observed. Low-angle fractures were observed on the sides of the LBT; however, that data set has not been analyzed and will be reported in subsequent revisions of the NFER.

It may also be apparent that the strike of the fracture set is more northerly in the LBT data set. This may be a result of several things. (1) It is quite likely that there is orientation bias in the data from the ESF, specifically the main drift is nearly north-south and therefore would not show northerly striking features that often (Yow and

Wilder, 1983). (2) There may have been rotation of the near surface block that forms the Fran Ridge. or (3) There may be a declination setting difference in the compasses used for these different mapping exercises. Based on past experience, it is judged that the orientation bias is very likely, although it is impossible to know if that is the only reason for the difference in strike. Once data is available from the ESF alcoves that are oriented east-west, the significance of orientation bias can be evaluated and perhaps a composite fracture stereoplot could be produced by normalization techniques as discussed in Wilder and Yow, 1984. If compass setting errors are the reason for the difference, subsequent analyses should resolve this since there is a set of measurements that were conducted based on surveyed block corners.

Regardless of the minor differences, from the standpoint of fracture sets, the LBT rock seems to be a good representation of the fracture system that has been observed in the ESF. The fractures are dominately in one vertical set that has north to northwesterly strikes.

A comparison of fracture spacing may be somewhat misleading since the same criteria on fracture length was not applied. However, the fracture system observed in the LBT, as inspection of Fig. 9-27 indicates, is similar to that reported from the ESF. There is about 0.75 fracture/ft (excluding short fractures so that the comparison with ESF is more appropriate) along any of the east-west grid lines and nearly 0.5 fracture/ft along the north-south grid lines (more comparable to the drift orientation). Fracture densities in the ESF are around 3-4 fractures/m, which is equivalent to 1 fracture/ft seen on the LBT map. Although the fracture density mapped on the excavated surface was about half that observed in the ESF, the number of fractures observed once the top was cut (Fig. 9-21) was comparable.

The orientation bias discussed here is also indicated in the fracture spacing data from the LBT, since there are about 50% more fractures seen in the east-west transects than in the north-south transects. Thus there would be rather different fracture distributions in the north-south line surveys (essentially equivalent to the ESF drift) than in the multi-directional survey obtained by the mapping of a flat surface in the LBT. Further studies of this bias will be conducted in the future but were not available at the time of this report.

On the basis of the fracture comparisons, it appears that the fracture system exhibited in the LBT is comparable to that observed underground. Based on the permeability measurements, the fracture system permeability is comparable. Also as mentioned, the moisture content is comparable to what is understood for the saturation conditions within the ESF, and the porosity of the rock matrix is also comparable. No assessment of the geochemical or mineralogical characteristics is available at this time. However, there is every indication that tests performed on the LBT could test the process models in an appropriate rock mass.

9.4 ESF Thermal Tests

The ESF Thermal Tests (ESFTTs) will be conducted in Alcove 5 off the ESF Main Drift. Alcove 5 is located at about the 2.827 km station of the ESF Main Drift. Figure 9-28 shows the plan view of the ESFTT facility. ESFTT consists of two tests: the Single Heater Test and the Drift Scale Test. ESFTT is in the construction state, therefore only the plans and the test designs are reported here. Detailed objectives, design, and planning of the ESFTT can be found in *Test Design, Plans, and Layout for the First ESF Thermal Test*, Rev.1, 1996, prepared by Civilian Radioactive Waste Management System Management and Operating Contractor.

9.4.1 Single Heater Test

As shown in Figure 9-28, the Single Heater Test (SHT) will be conducted on one side of the Observation Drift, at about 41 m from the ESF Main Drift. The main objectives of the SHT are to obtain rock mass thermal and mechanical properties at ambient and elevated temperatures, to evaluate rock bolt anchorage response to the heated conditions, and to observe thermal-hydrological-chemical changes in the rock mass due to the heating. Because the heated volume of the rock mass in the SHT is small (the test block covers an area of about 84 m^2), the thermal-hydrological-chemical observation will be mostly for developing *in situ* test experience. Figure 9-29 shows the layout of the SHT. The test region is the block between the Observation Drift, Thermomechanical Alcove, and Thermomechanical Alcove Extension. The

construction and drilling are completed and the instruments are being installed in the holes. The heater is scheduled to be turned on by the end of August 1996.

The 5-m-long heater will be placed in a hole (7 m long), which is drilled into the test block from the Thermomechanical Alcove. The boreholes include: (as shown in the lower portion of Fig. 9-29) four ERT holes, four neutron/RTD holes (for neutron logging and temperature measurements), two chemical holes, two hydrological holes, and two optical extensometer holes. Chemical sensors and fluid extracting devices will be mounted on Science Engineering Associates Membrane In-situ Sampling Technology (SEAMIST) in the chemical holes for monitoring chemical processes. Humicaps and gas pressure transducers will be mounted in packers in the hydrological holes for measuring relative humidity, temperature, and gas pressures. The rest of the boreholes are for mechanical, rock bolts, and temperature measurements. The power output of the heater will be about 4 kW. The rock mass will be heated by a constant power of about 4 kW for about eight months; then the heater will be turned off. Monitoring of thermal mechanical responses, temperature, moisture content, chemical concentration, etc., will be started before the heater is energized, and will continue through the heating phase and the cooling phase.

Pre-test pneumatic tests to characterize the rock mass were completed, finding the air permeability of the test region to be very heterogeneous. The air permeability varies by more than two orders of magnitude. Generally speaking, the region between the heater and the Observation Drift has lower permeability than the region on the other side of the heater, i.e., between the heater and the Thermomechanical Alcove Extension. Also, the inner portion of the block, i.e., the region near the bottom of the heater hole, seems to have greater permeability than the outer portion of the block. Apparent fracturing in a borehole has no strong correlation with the permeability in that hole.

9.4.2 Drift Scale Test

The Drift Scale Test is the second *in situ* thermal test of the ESFTT. Again, the objectives of the Drift Scale Test are described *in Test Design, Plan, and Layout for*

the First ESF Thermal Tests, as mentioned in section 9.4. The main purpose of the Drift Scale Test (DST) is to test the coupled TMHC processes in an *in situ* environment. There will be some thermal mechanical tests for the repository design and construction. The heated area and the heated period will be large and long enough for us to observe the coupled TMHC processes that are relevant to a repository. Figure 9-30 shows the schematic layout of the DST. Figure 9-30(a) shows the plan view of the DST; Figure 9-30(b) shows one of the cross sections of Fig. 9-30(a).

Heaters will be placed in the heater drift and wing heater holes (as illustrated by holes 74 to 123 and 207 to 210). The heater drift will be about 5 m in diameter. The wing heater holes will be about 10 cm in diameter and will be spaced about 1.8 m along the axis of the heater drift. The heaters in the heater drift will be MPC size canisters with heating elements mounted in them so that the temperature on the canister surfaces will be uniform. The linear power density of the heater canister will be about 1 kW/m. Rod heater elements will be placed in the wing heater holes. The power density of the wing heaters will be about 125 w/m^2 among the inner half of the wing heaters, 175 w/m^2 for the outer half of the wing heaters. The heater drift will be about 55 m in length; the tip-to-tip span of the wing heaters will be about 28 m. The heated area of the DST will be about 1540 m^2, which will be big enough for observing large-scale thermal-hydrological processes, such as heat pipe, buoyant phase convection (see Chapter 1.9 for details).

Boreholes for instruments will be drilled radially from the heater drift, from the observation drift to the heater drift, and longitudinally along the heater drift. The goal is to obtain a 3-D coverage of the test region. In addition to the types of boreholes mentioned in section 9.4.1, Rapid Estimation of K and Alpha (REKA) probes will be installed in boreholes to perform *in situ* measurement of the thermal conductivity and diffusivity of the rock mass. The heaters will be heated at constant power for at least three years, which, depending on the responses of the rock mass, may be extended to four years, and a controlled cool-down period will follow the

three- or four-year heating period. Similar to the SHT, monitoring of the responses of the rock mass will cover the pre-heat, heating, and cool-down periods.

Construction of the main (east-west) portion of the Observation drift has been completed. The other part of the Observation drift and the Heater drift will be constructed during FY 1997. Drilling of the boreholes will be started soon, and the heaters are scheduled to be turned on in late FY 1997.

9.5 Large-Scale Long Duration Test

A large-scale long duration test (LSLDT) was incorporated into the field test planning because of the challenges of scale, both temporal and spatial, that must be considered in any testing which is both accelerated in time and therefore in gradients and in limited geometric size. This test was sized geometrically and duration was determined based on numerical analyses. This test is described in *the Study Plan for Engineered Barrier System Field Tests*, as cited in section 9.1; however, current budget planning does not commit to the LSLDT. But, it is discussed here since it is an essential part of the planned testing. If used, this test would have multiple heater drifts with observation drifts located both above and below the heated drifts, as shown in Fig. 9-31. Although at least three heater drifts would be used, five would better address issues such as condensate ponding. The heater drifts would be heated for at least four years, and subsequently extended, depending on the responses of the rock mass at the end of the fourth year. The heating period would be followed by a controlled cool-down period of at least one year and a natural cool-down period, which would be dictated by the cooling of the rock mass.

It is possible that the LSLDT may be merged or combined with the Confirmation Test. The configuration of the LSLDT would be the closest simulation of a repository that can possibly be achieved. Instrumentation for the LSLDT would be similar to that in the DST, with whatever improvement that we can learn from the DST. The distribution of the instruments in the LSLDT would provide a true 3-D coverage of the test region, would be much better than the DST.

9.6 Confirmation Monitoring

Confirmation monitoring of the repository's performance will be conducted in parts of the repository that are constructed and where early emplacement of the waste has been accomplished. Instrumentation for the confirmation monitoring will be similar to that in the DST and the propsed LSLDT. Basically, monitoring will include temperature, moisture content, mechanical responses, and chemical responses of the rock mass around the emplacement drifts. The heat source will be the radioactive decay heat from the nuclear wastes. One of the criteria for designing the methodology and instrumentation for the confirmation monitoring is the long duration of the test, which can be tens or even hundreds of years. Lessons learned from the DST and the proposed LSLDT will be used to select measurement methodologies and instruments that can provide reliable long-term monitoring.

9.7 References

Daily, W., A. Ramirez, T. Ueng, and V. LaTorre (1989), "High Frequency Electromagnetic Tomography," *Proc. Nuclear Waste Isolation in the Unsaturated Zone, Focus '89* (Am. Nuc. Soc., LaGrange Park, IL), pp. 409–416. NNA.910326.0098.

Lee, K., 1995a, *Progress Report on Pre-Test Calculations for the Large Block Test,* Lawrence Livermore National Laboratory UCRL-ID-118699, Livermore, CA. MOL.19950406.0143

Lee, K., 1995b, *Second Progress Report on Pre-Test Calculations for the Large Block Test,* Lawrence Livermore National Laboratory UCRL-ID-122300, Livermore, CA. MOL.19960417.0218

Lin, W., 1993, *Scientific Investigation Plan for Large Block Testing of Coupled Thermal-Mechanical-Hydrological-Chemical Processes,* SIP-NF-02, Lawrence Livermore National Laboratory, Livermore, CA. NNA.19930419.0032

Lin, W., 1994, *Activity Plan, AP-LBT-01, Rev. 0, for Large Block Tests of Coupled Thermal-Mechanical-Hydrological-Chemical Processes* (YMP WBS Element 1.2.3.12.4), Lawrence Livermore National Laboratory, Livermore, CA. MOL.19940908.0093

Lin, W., 1995, *Study Plan for Study 8.3.4.2.4.4, Engineered Barrier System Field Tests,* US. Department of Energy, prepared by CRWMS Management and Operating Contractor/Lawrence Livermore National Laboratory, Office of Civilian Radioactive Waste Management, Washington, DC. MOL.19960425.0195

Ramirez, A., T. Buscheck, R. Carlson, W. Daily, K. Lee, W. Lin, N. Mao, T. Ueng, H. Wang, and D. Watwood, 1991, *Prototype Engineered Barrier System Field Test*

(PEBSFT) Final Report, A. Ramirez, Scientific Editor, Lawrence Livermore National Laboratory UCRL-ID-106159, Livermore, CA. NNA.19910711.0047

Ramirez, A., D. Wilder, J. Beatty, T. Buscheck, R. Carlson, W. Daily, R. LaTorre, K. Lee, W. Lin, N-H. Mao, J. Nitao, D. Towse, T-S. Ueng, and D. Watwood (1991), *Prototype Engineered Barrier System Field Tests (PEBSFT), Progress Report through November 1, 1988*, Lawrence Livermore National Laboratory, Livermore, CA, UCID-21640.

Yow, J., Jr. (1985), "Test Concept for Waste Package Environment Tests at Yucca Mountain," in the *Proc. of the 28th U.S. Symposium on Rock Mechanics*, Tucson, AZ, pp. 1035–1042; also in Lawrence Livermore National Laboratory, Livermore, CA, UCRL-95568.

Yow, J.L. Jr, and D. G. Wilder, 1983, Planning Exploratory Drilling: The Effect of Blind Zones and Level of Logging Effort, Proceedings of 24th U.S. Symposium on Rock Mechanics, College Station, TX, pp 807-812.

Wilder, D. G., and Yow, J. L. Jr, 1984, Structural Geology Report, Spent Fuel Test-Climax, Nevada Test Site, Lawrence Livermore National Laboratory UCRL-53381, Livermore, CA.

Data Tracking Information:

9.3 Large Block Test

(Data Tracking Number: LL950103004244.004)

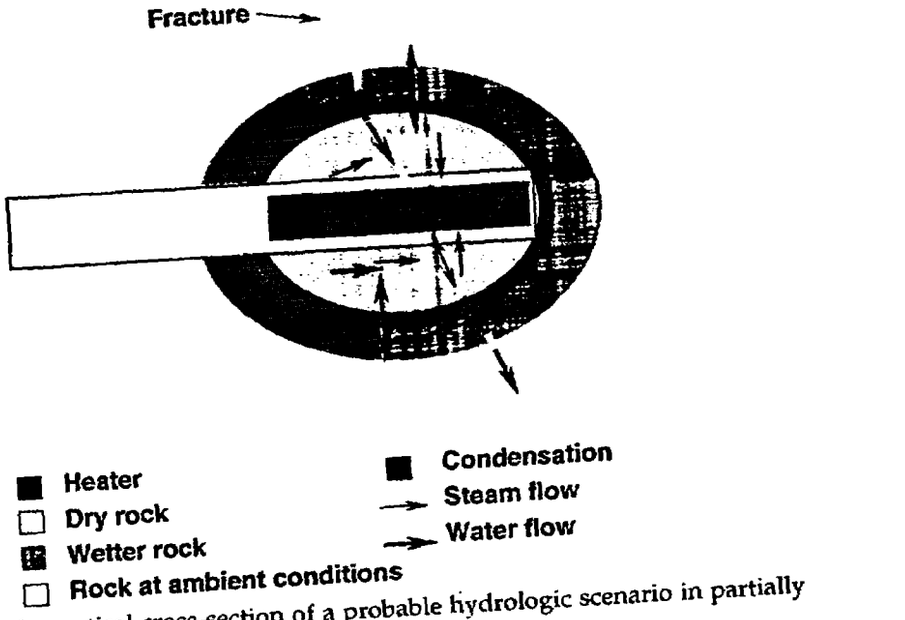

Figure 9-1. Schematic of a vertical cross-section of a probable hydrologic scenario in partially saturated welded tuff subjected to a thermal load.

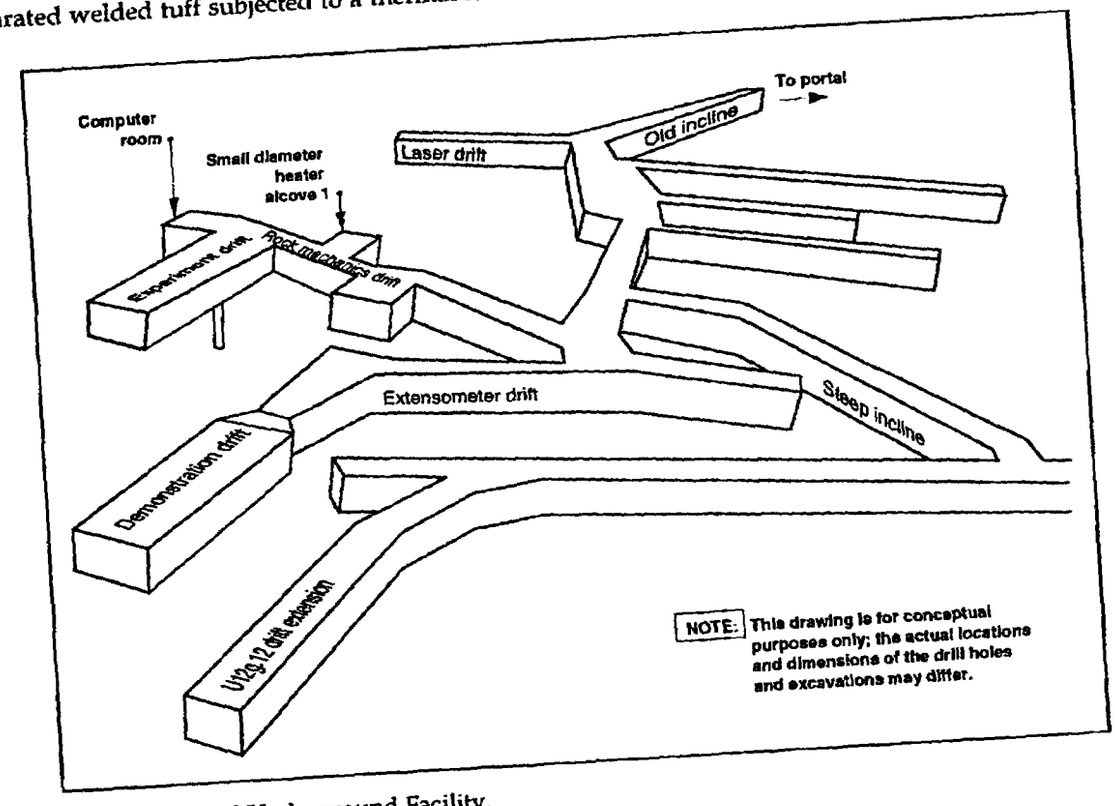

Figure 9-2. G-Tunnel Underground Facility.

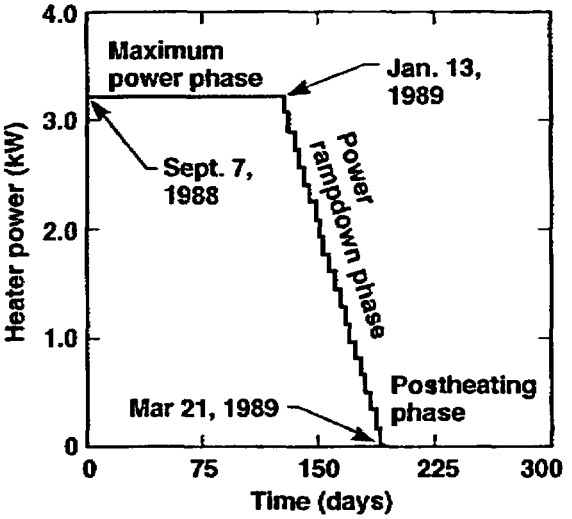

Figure 9-3. Heater power schedule used for the PEBSFT.

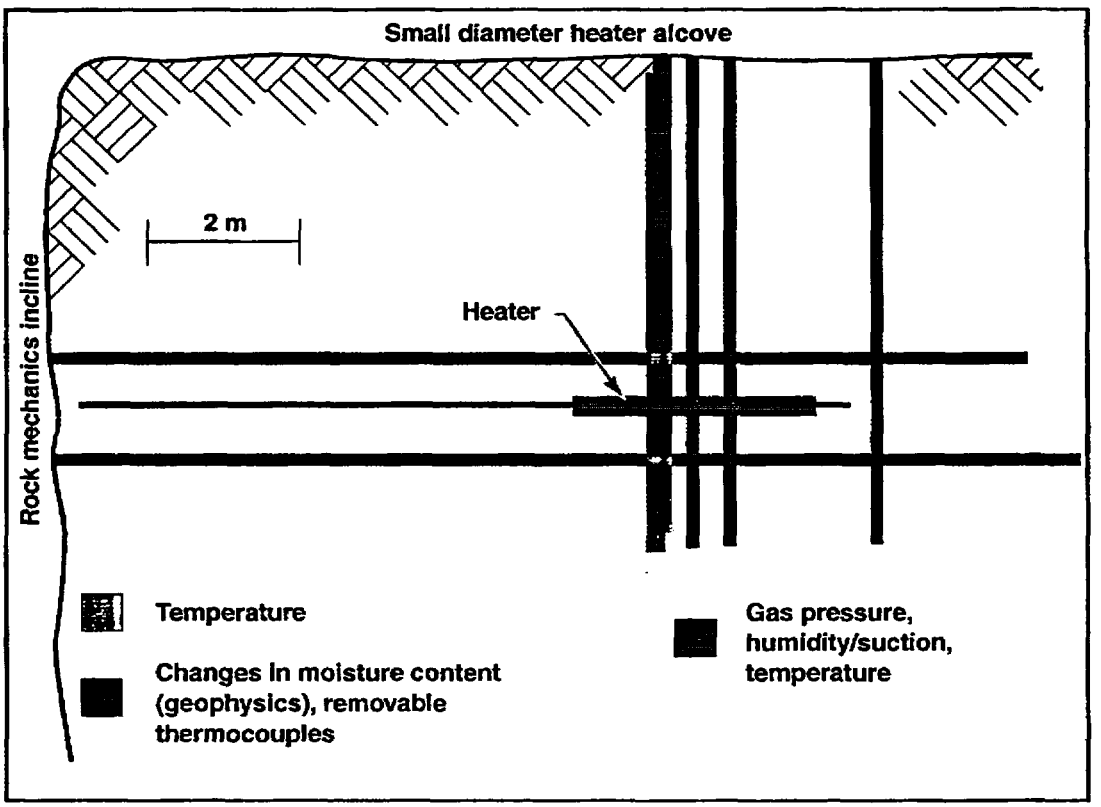

Figure 9-4. Plan view of the as-built borehole layout. The various line patterns identify the type of measurement made in each borehole. The locations of the rock mechanics incline and the small diameter heater alcove in G-Tunnel are shown for reference.

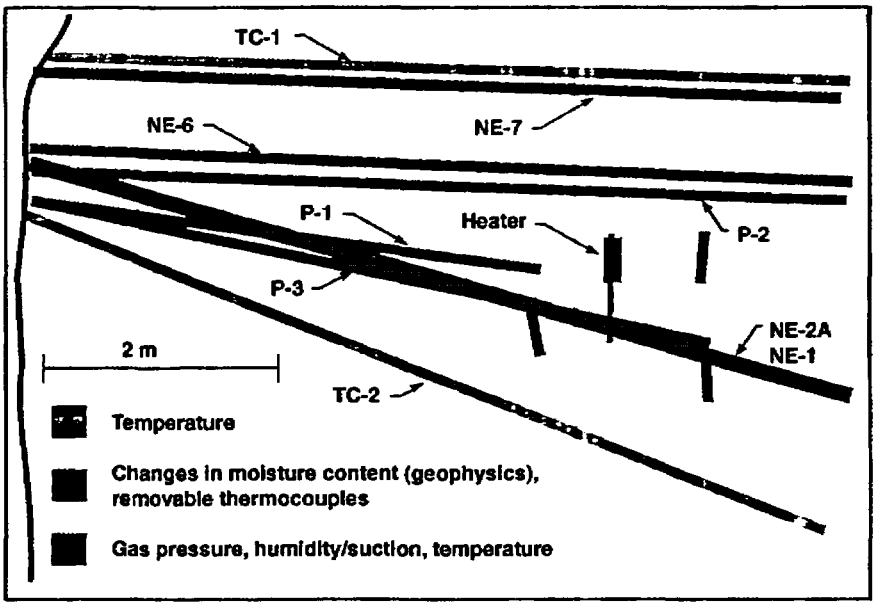

Figure 9-5. Side view of the as-built borehole layout as viewed from the rock mechanics incline. The various line patterns identify the type of measurement made in each borehole.

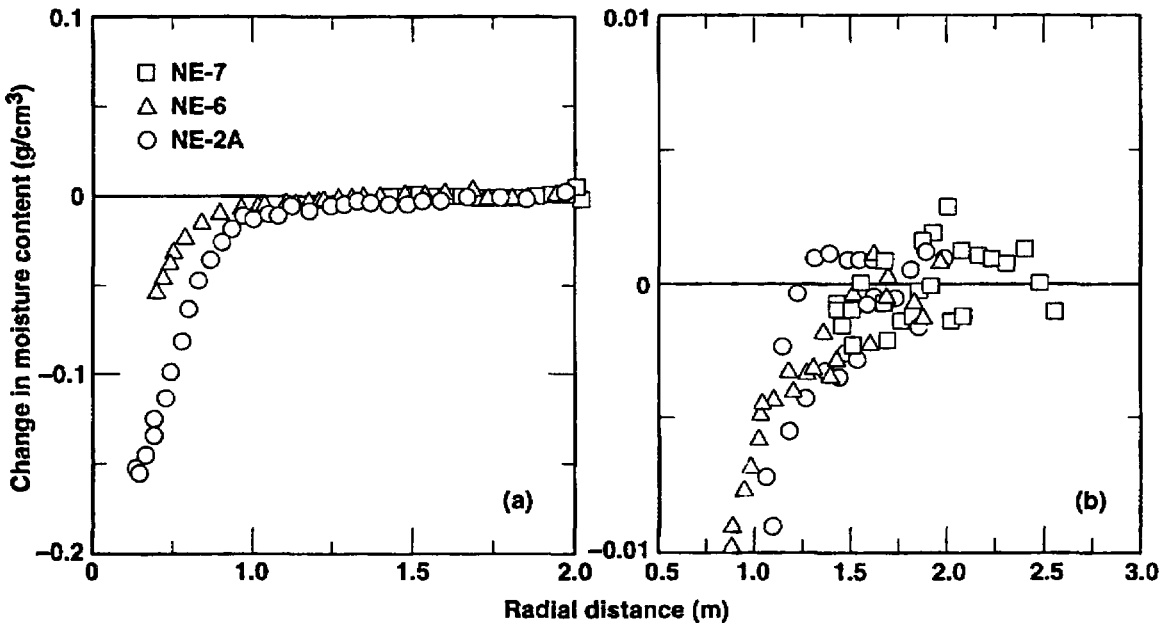

Figure 9-6. Changes in moisture content plotted against radial distance after 70 days of heating (approximately midway through the maximum power phase). A subset of the curves in (a) are shown enlarged in (b). Changes are calculated relative to preheating moisture conditions.

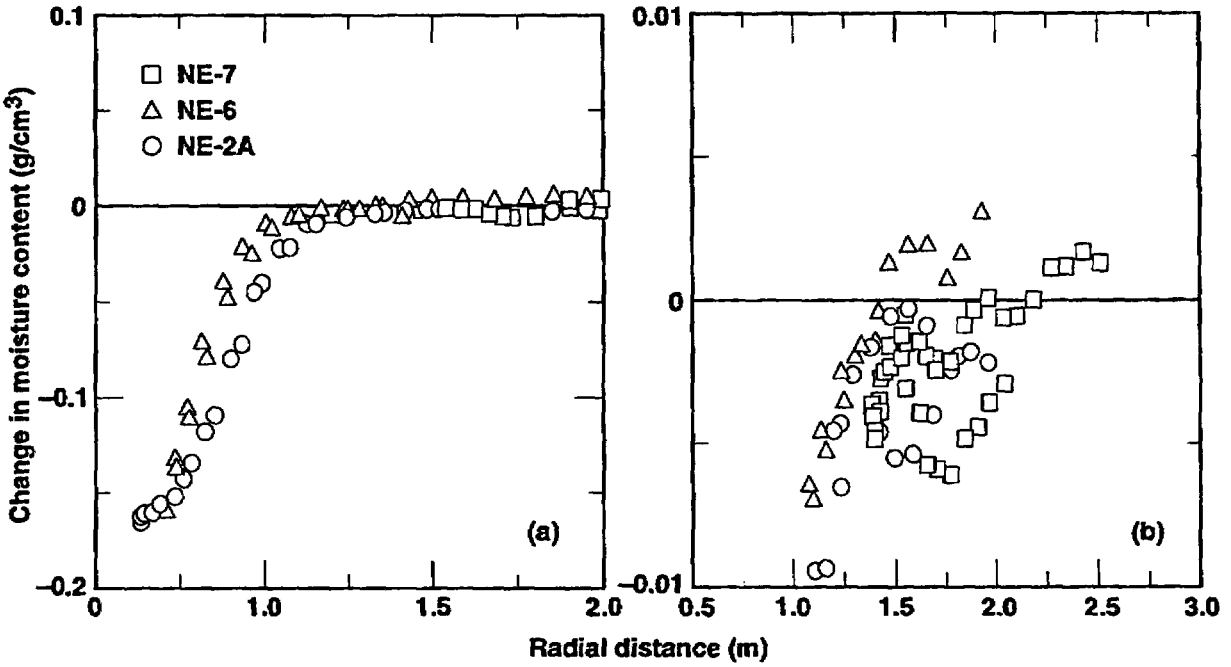

Figure 9-7. Changes in moisture content plotted against radial distance for the next to last day of maximum power heating. A subset of the curves in (a) are shown enlarged in (b). Changes are calculated relative to preheating moisture conditions.

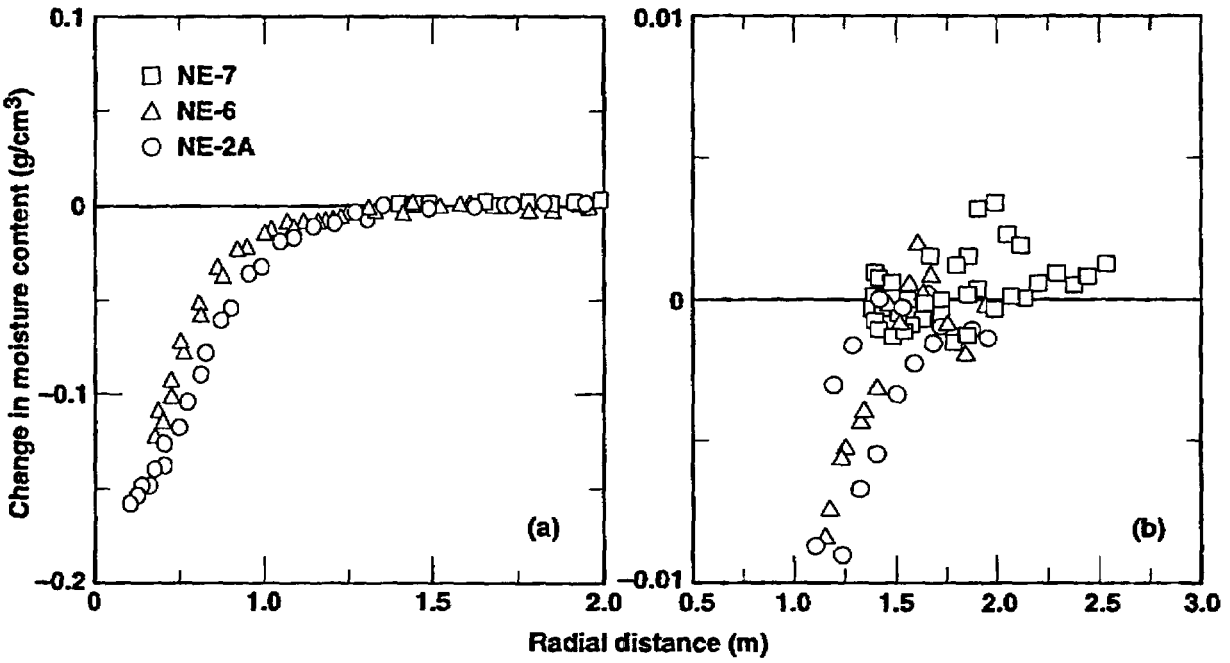

Figure 9-8. Changes in moisture content plotted against radial distance 301 days after start of heating (106 days after heater was de-energized). A subset of the curves in (a) are shown enlarged in (b). Changes are calculated relative to preheating moisture conditions.

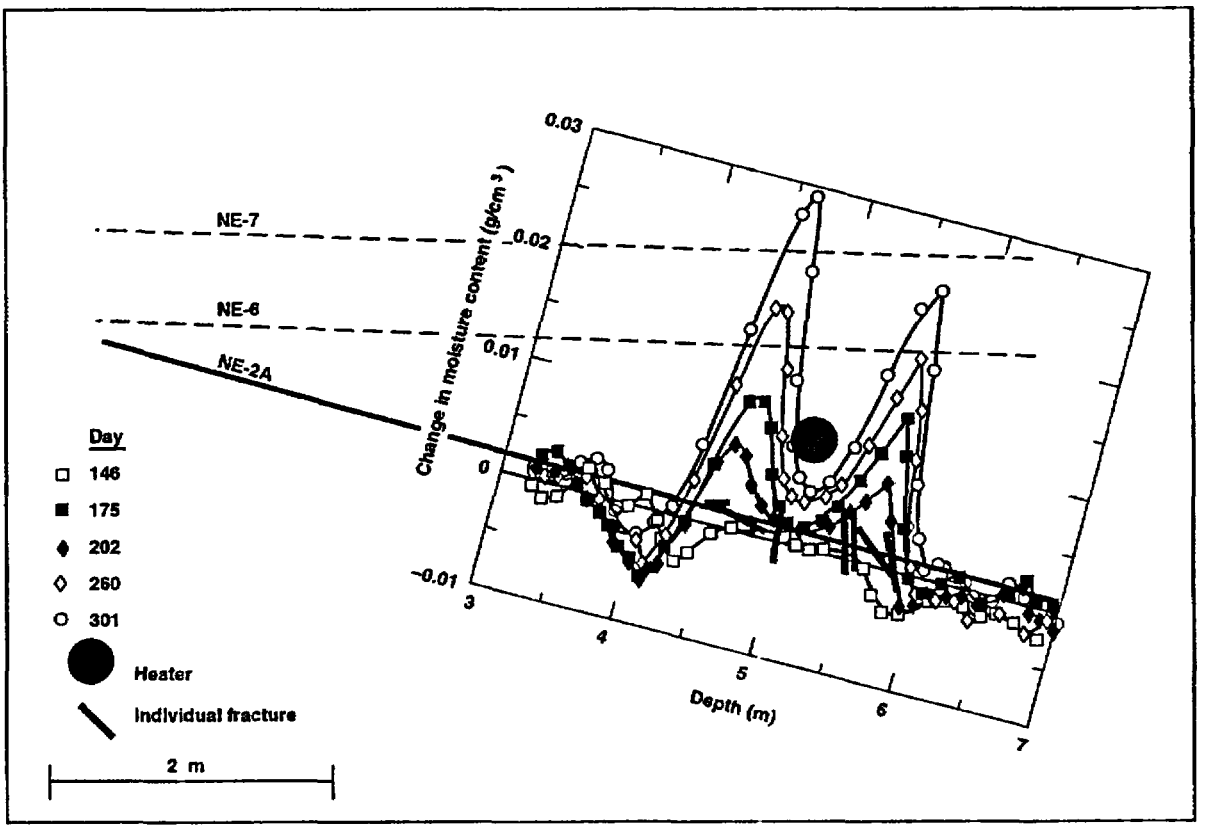

Figure 9-9. Changes in moisture content mapped along borehole NE-2A. Changes are calculated relative to the last day of full-power heating. Fractures mapped are shown for comparison.

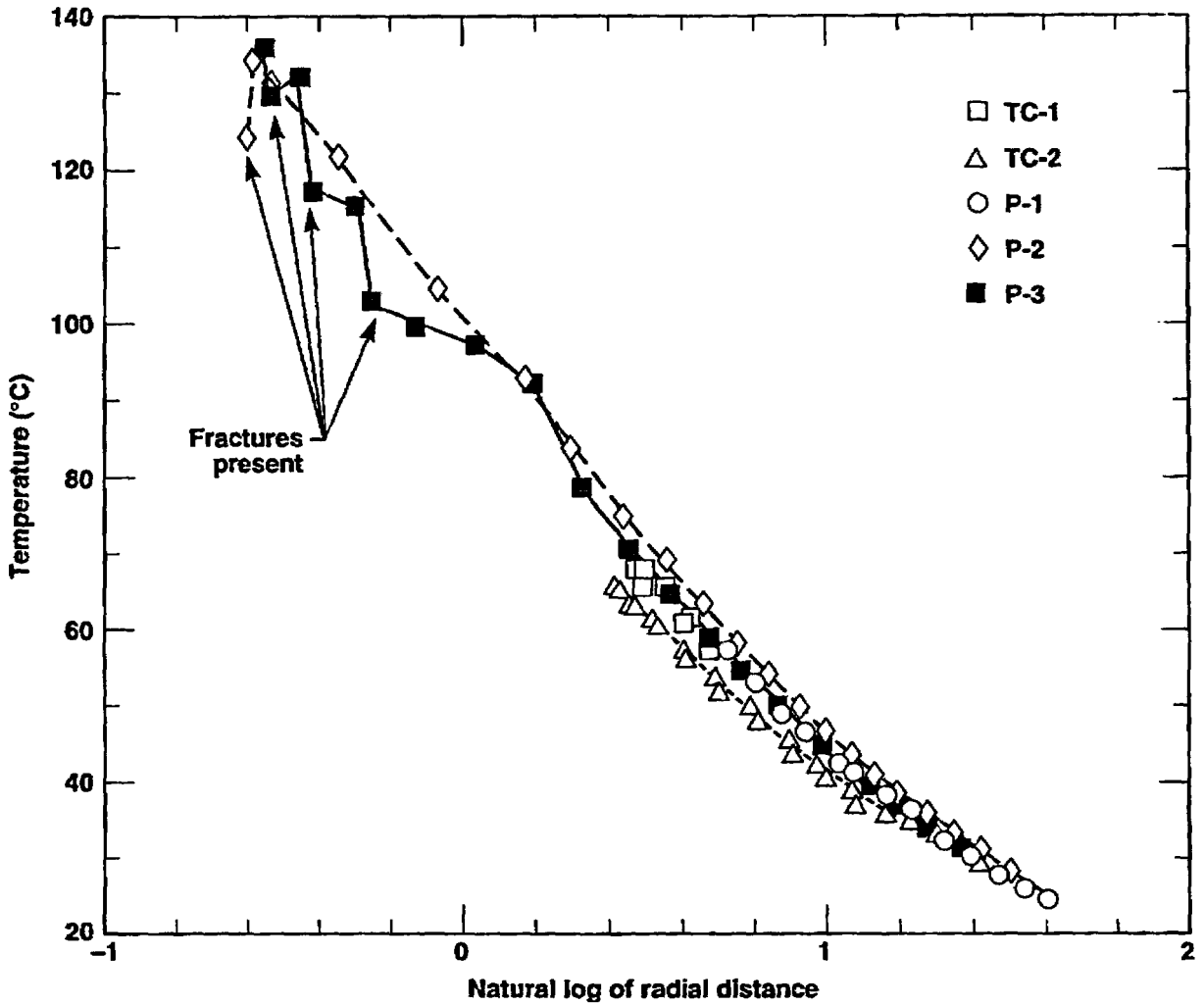

Figure 9-10. Temperatures in various boreholes measured during the last day of full-power heating.

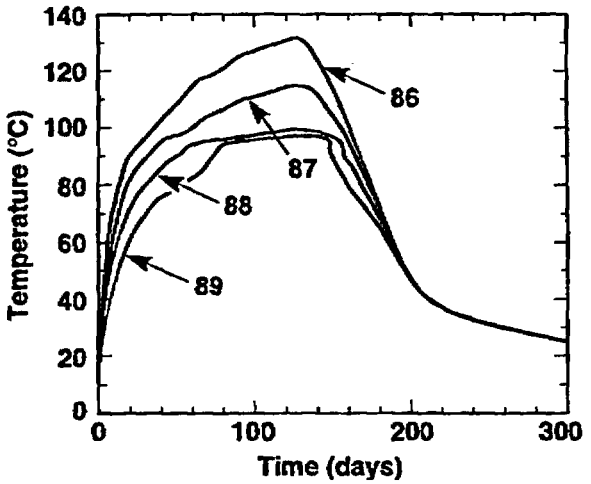

Figure 9-11. Evolution of selected temperatures in the P-3 borehole as a function of time. Thermocouples 88 and 89 show a flattening of the profiles between days 50 and 150 that may be due to the movement of condensed water in this region.

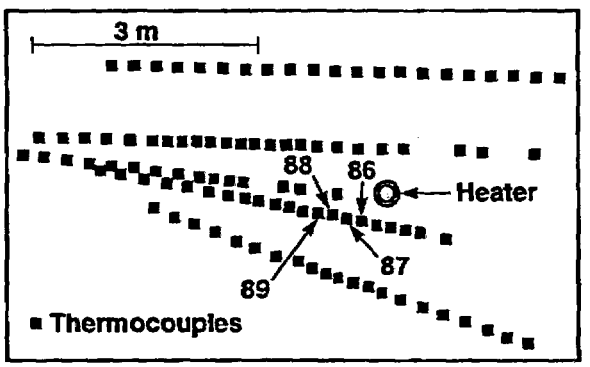

Figure 9-12. Cross-section near the heater midplane, showing thermocouple locations relative to the heater. Data for thermocouples 86 to 89 are shown in Fig. 9-11.

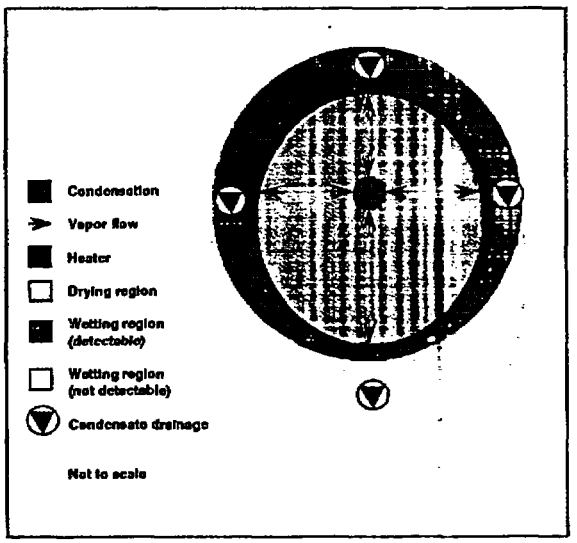

Figure 9-13. Proposed flow phenomena for a fracture perpendicular to the heater axis. The view is along the fracture plane. This conceptual model was proposed as an explanation for the atypical temperatures shown by thermocouples 88 and 89 (shown in Fig. 9-11). Also shown is the increased region of drying and wetting fronts along the fracture.

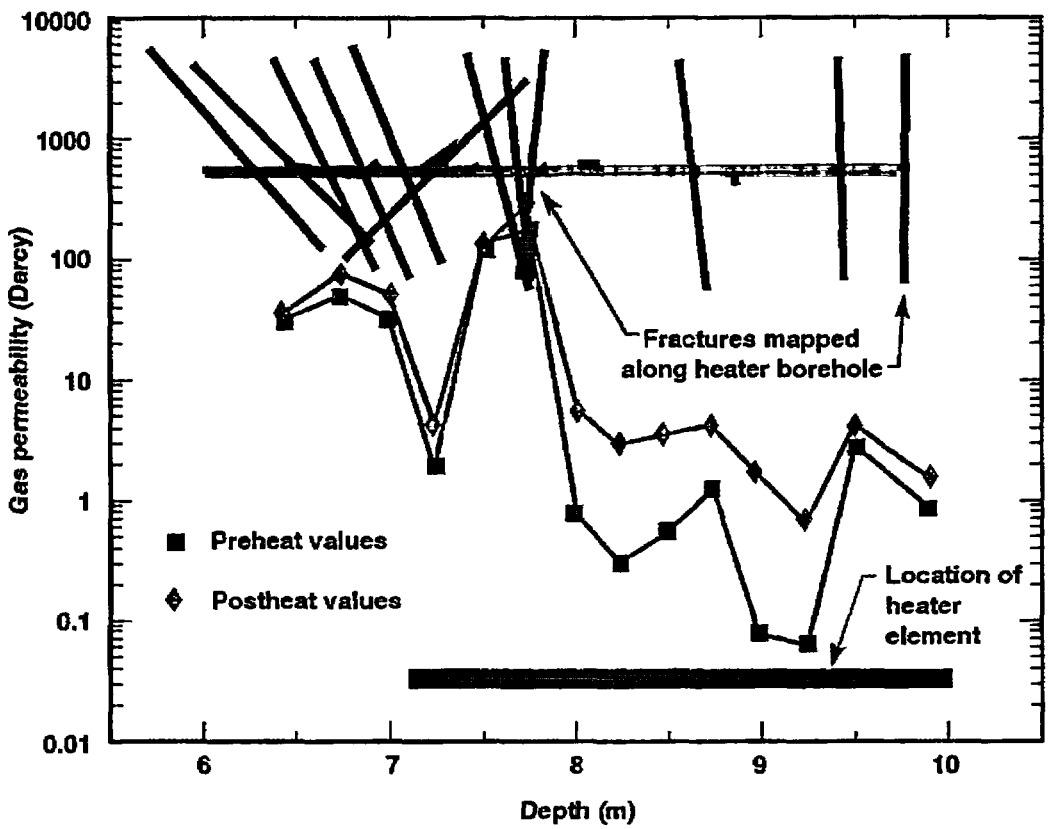

Figure 9-14. Gas permeability measurements made along the heater borehole before and after heating on the borehole.

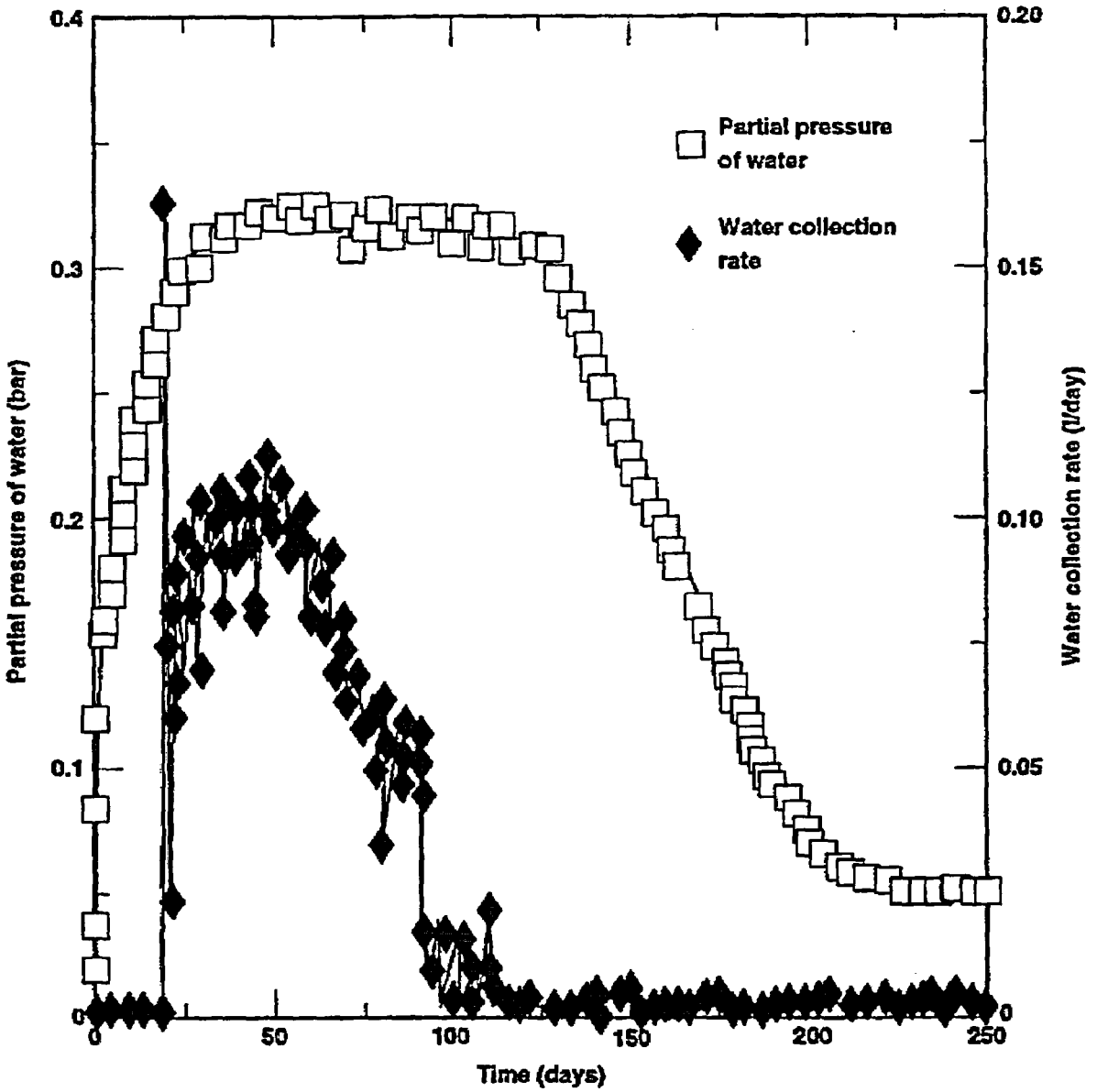

Figure 9-15. Water collection rate and partial pressure of water in the heater borehole air as a function of time.

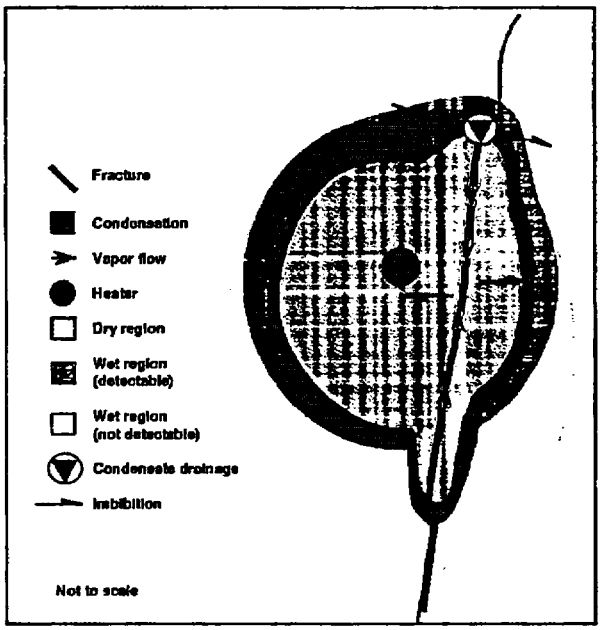

Figure 9-16. Proposed conceptual model of the mechanisms that dominate the dry region rewetting process during cooldown of the rock mass. A transect along a matrix block intersected by a fracture is shown.

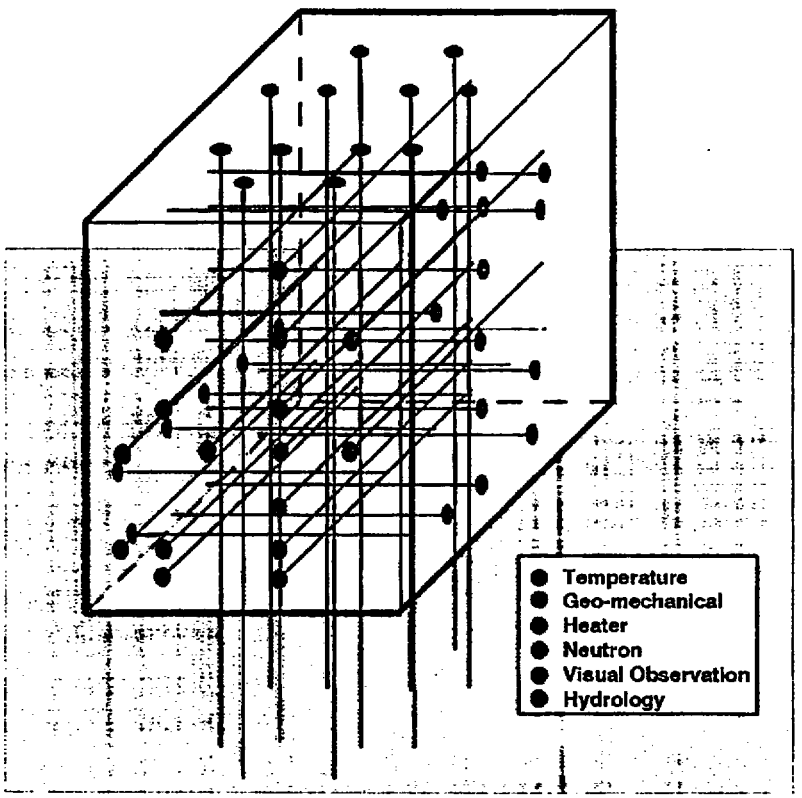

Figure 9-17. Instrument boreholes drilled in the large block for LBT.

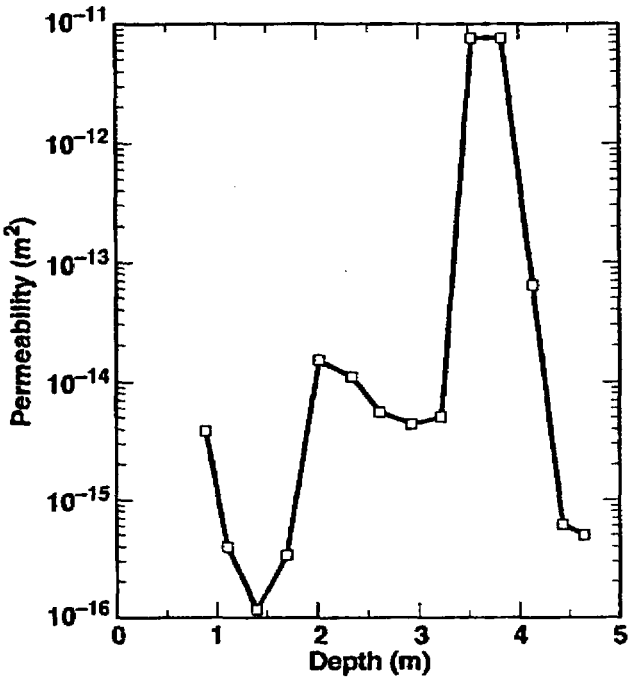

Figure 9-18. Air permeability of the large block as a function of depth measured from a single borehole air injection test in N1 hole.

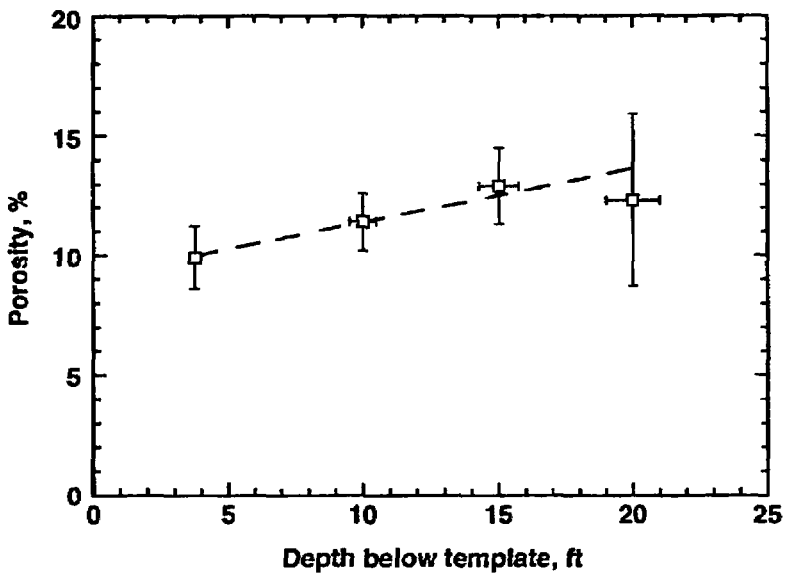

Figure 9-19. Matrix porosity of cores from the LBT as a function of depth.

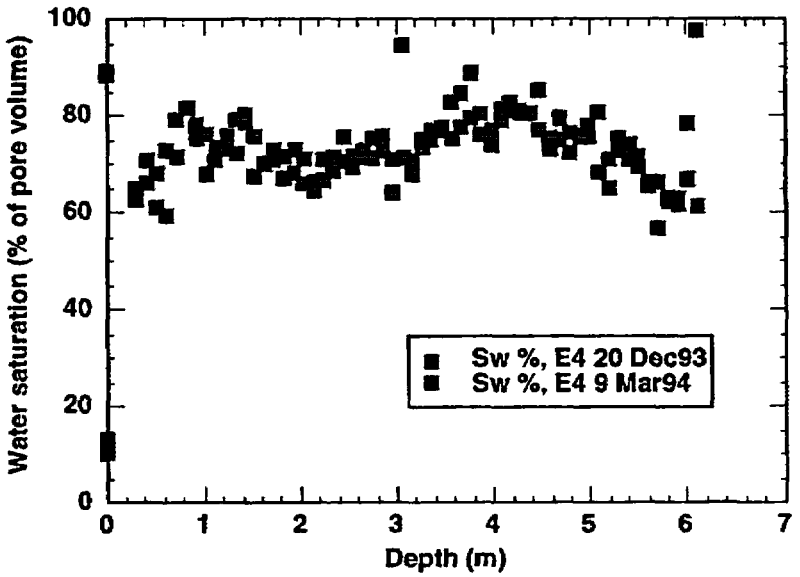

Figure 9-20. Water saturation (percent of pore volume) in a vertical hole, near the middle of the block as a function of depth, determined by neutron logging before and after the sawing.

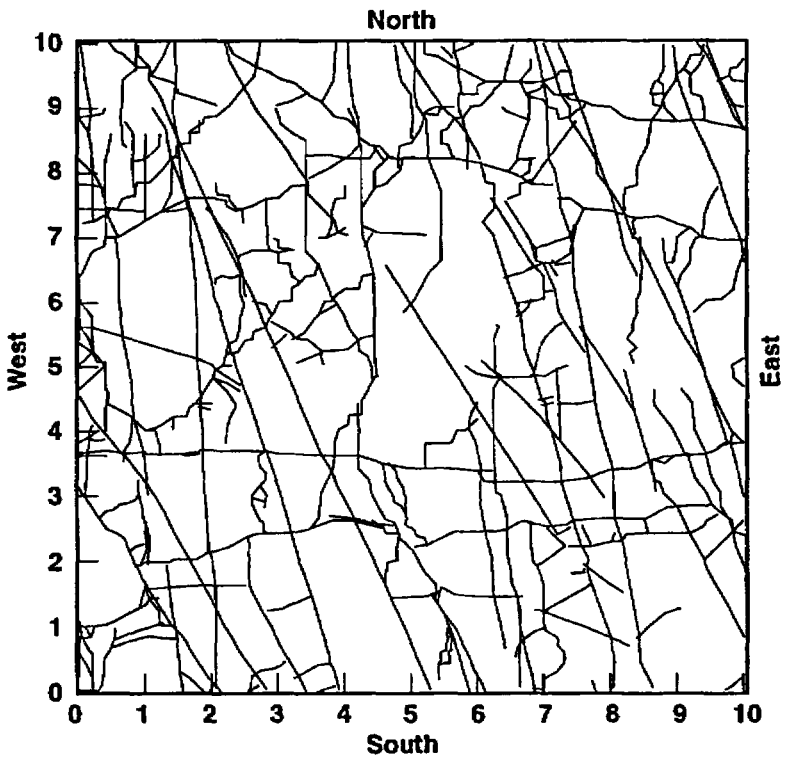

Figure 9-21. The fracture location maps on top of the block, after the top was cut smooth.

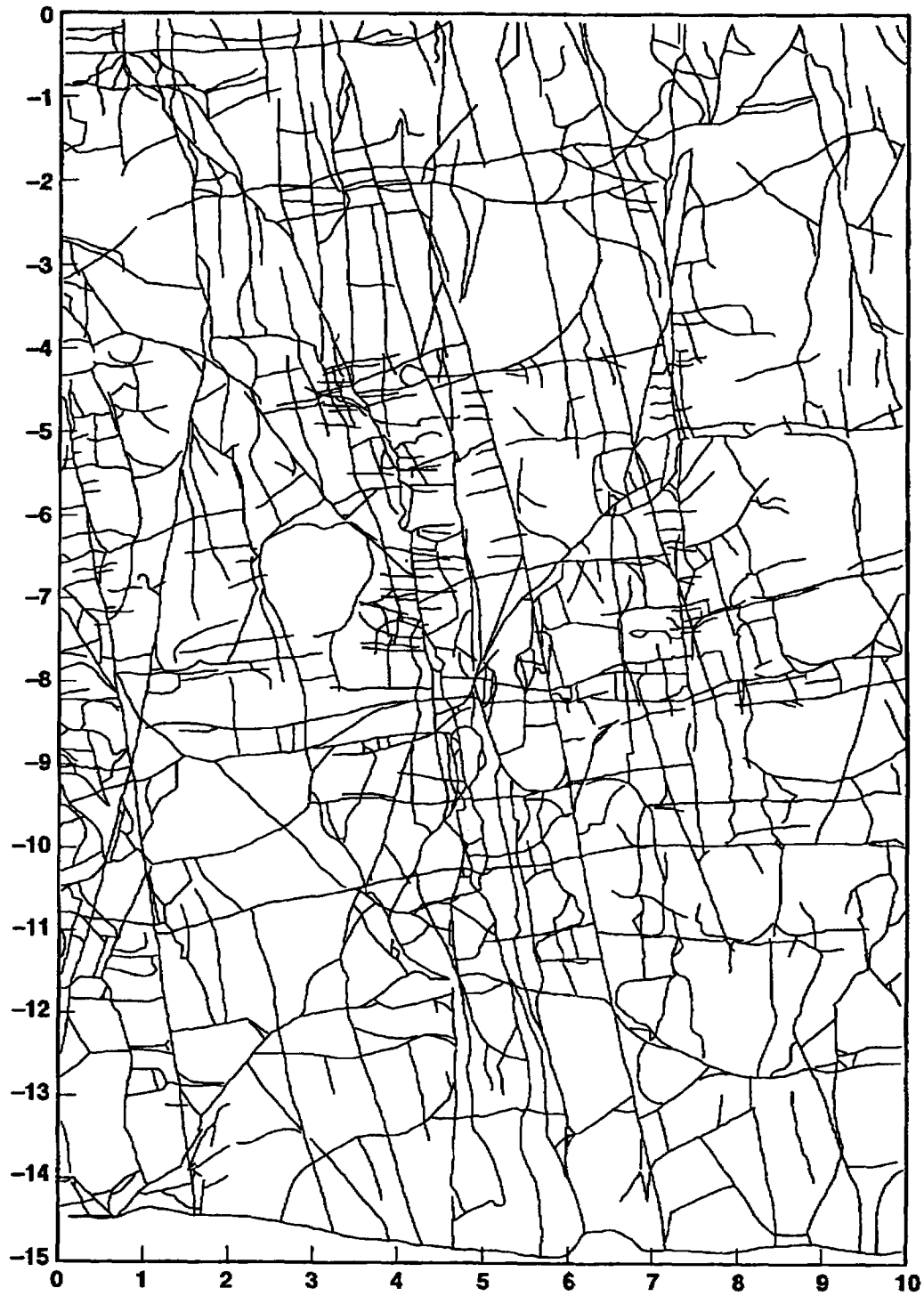

Figure 9-22. Fractures on the north face of the large block. The distance marks are in feet.

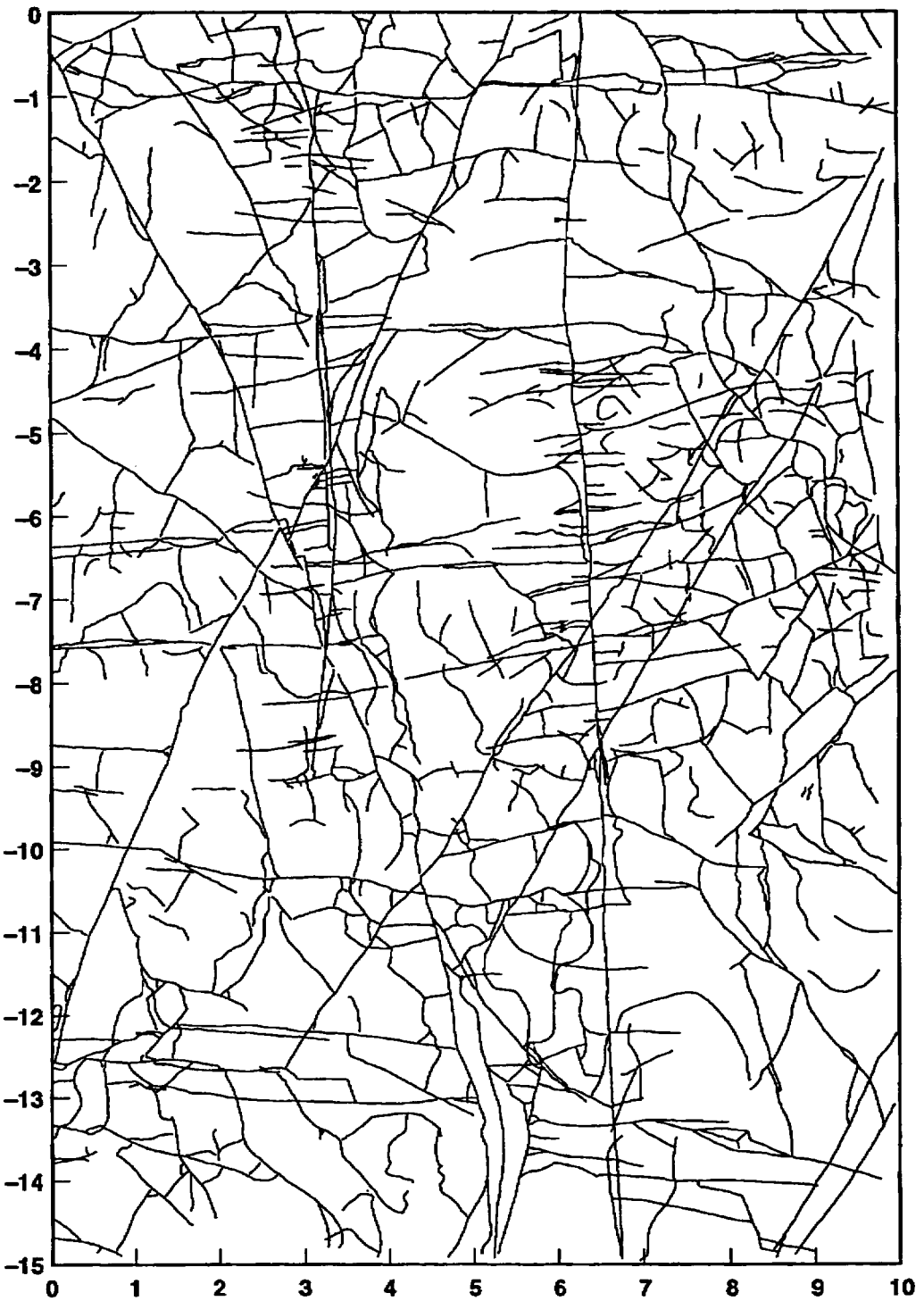

Figure 9-23. Fractures on the west face of the large block. The distance marks are in feet.

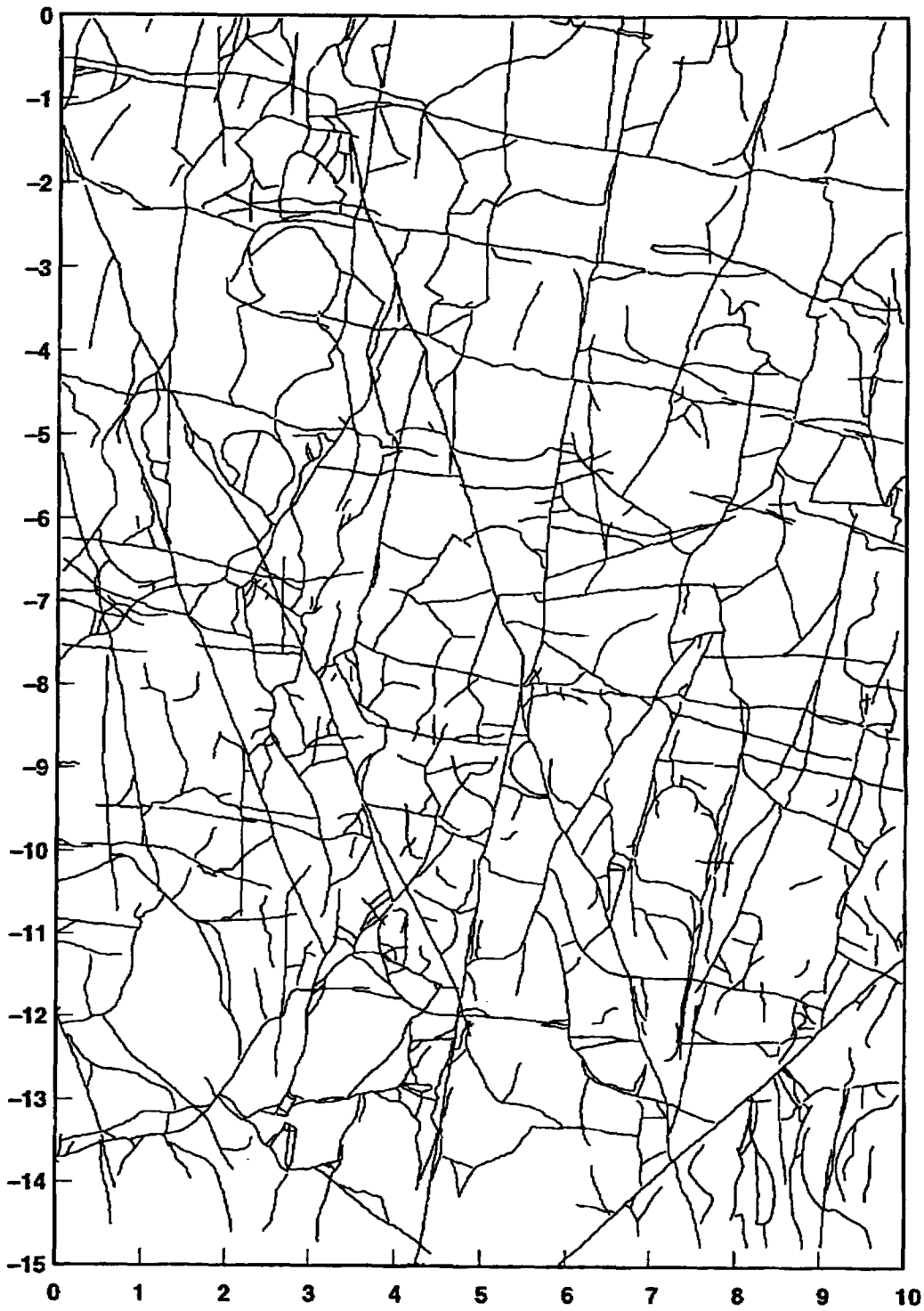

Figure 9-24. Fractures on the south face of the large block. The distance marks are in feet.

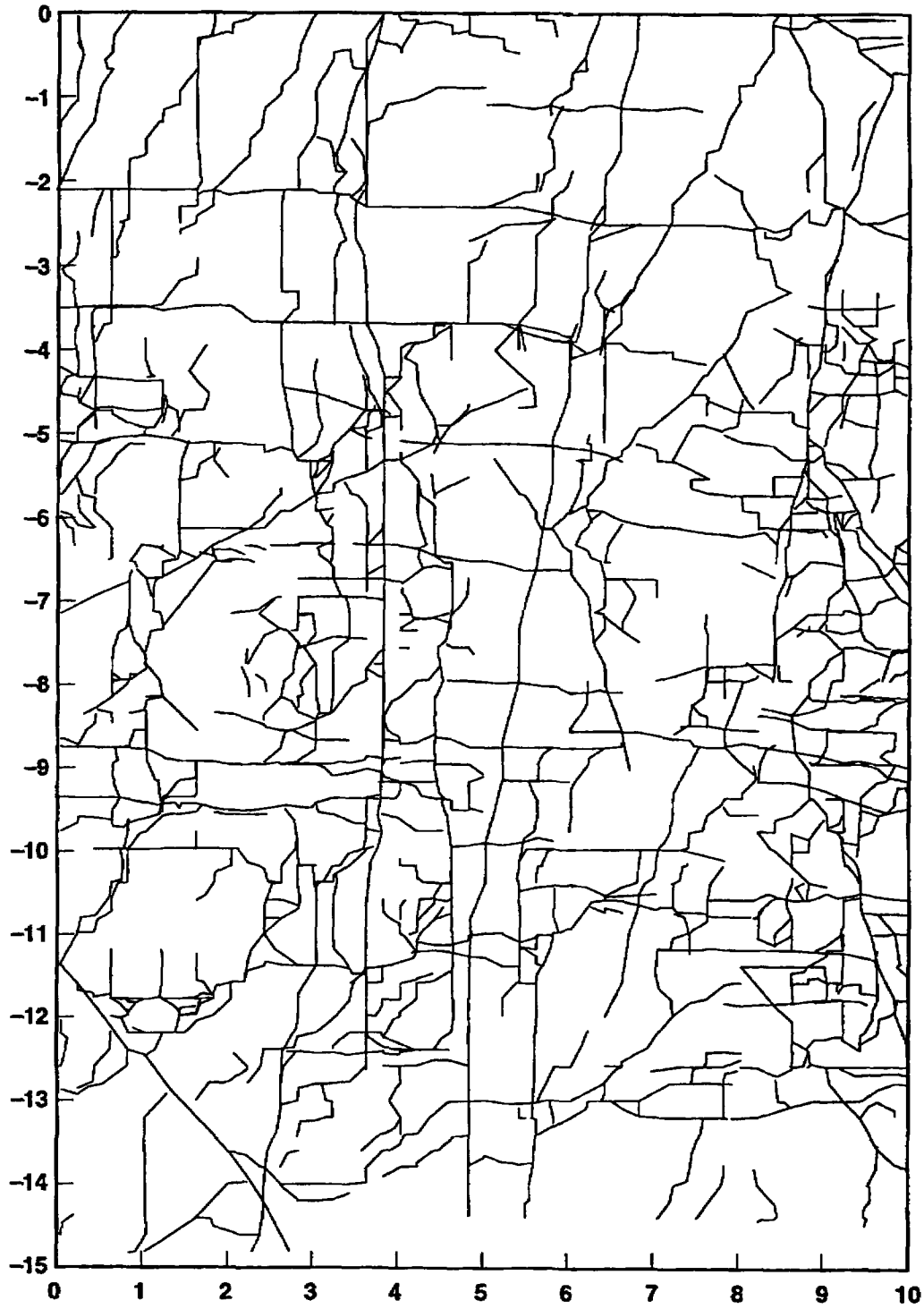

Figure 9-25. Fractures on the east face of the large block. The distance marks are in feet.

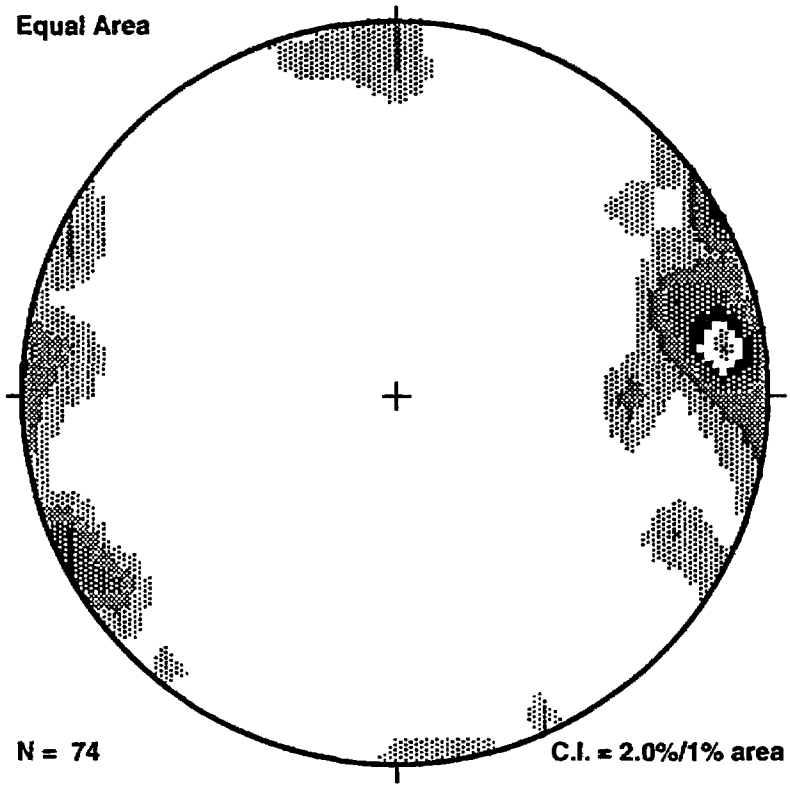

Figure 9-26a. Strike and dip of the fractures on top of the larger block, before the top was cut smooth.

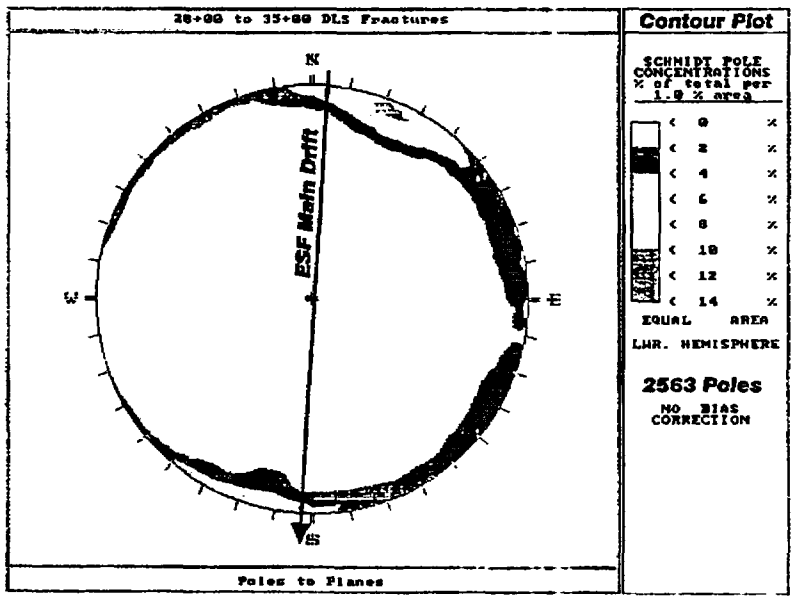

Figure 9-26b. Strike and dip plot of the fractures in the ESF main drift taken from Barr et al 1996.

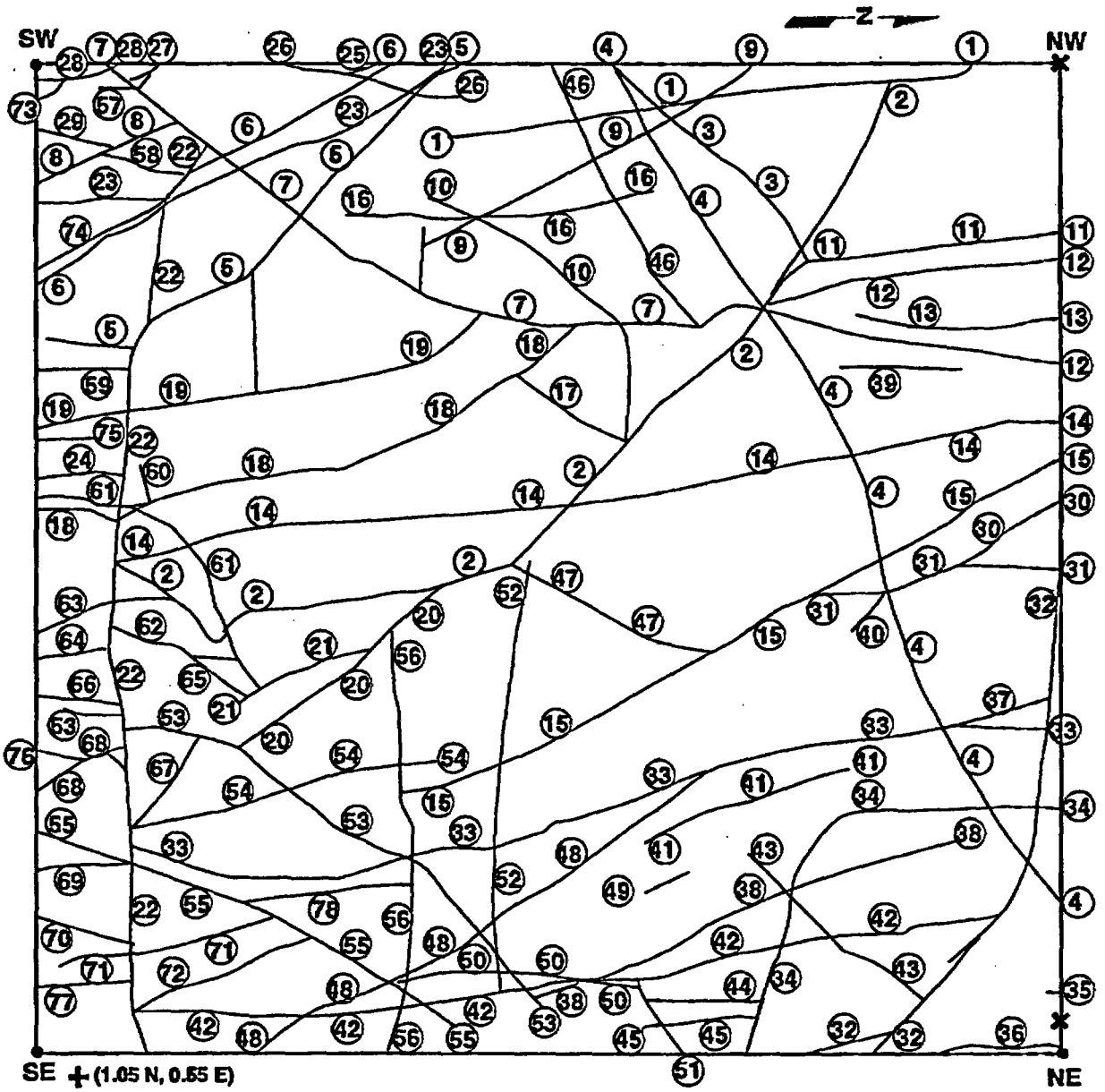

Figure 9-27. Fractures on the top of the large block before the top was cut smooth.

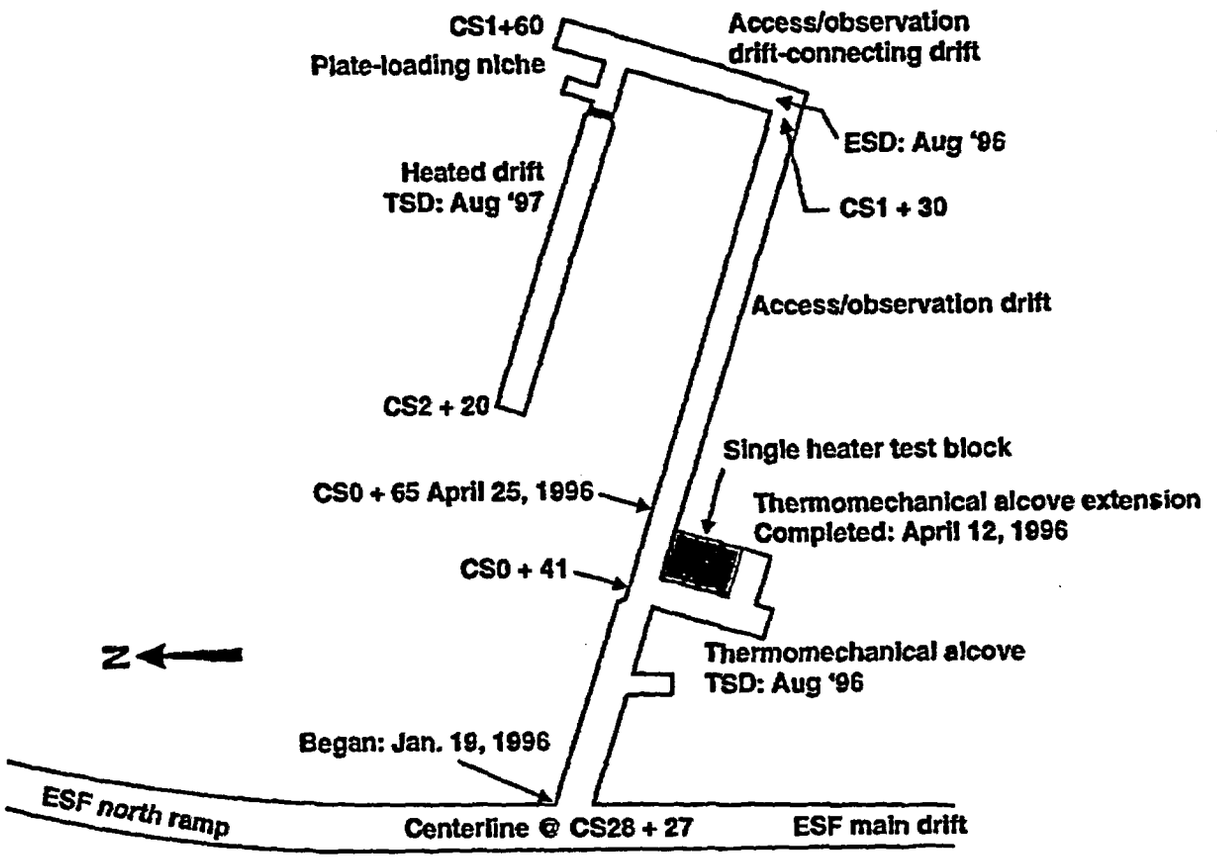

ESD: Expected excavation start date
TSD: Expected testing start date

Figure 9-28. Plan view of ESFTT facility.

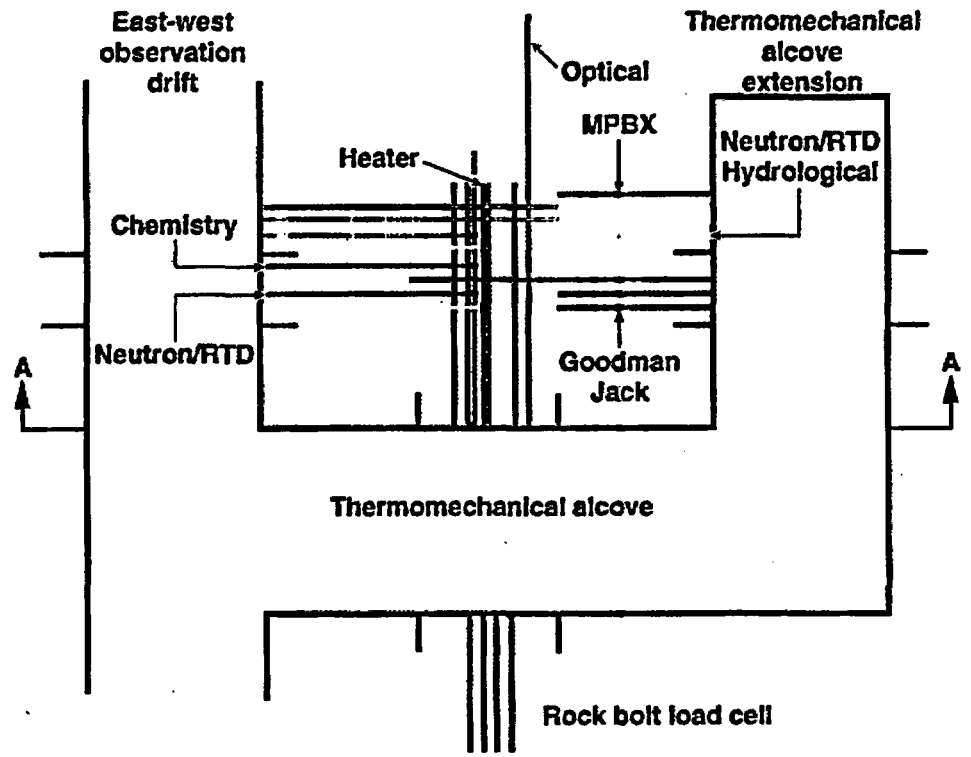

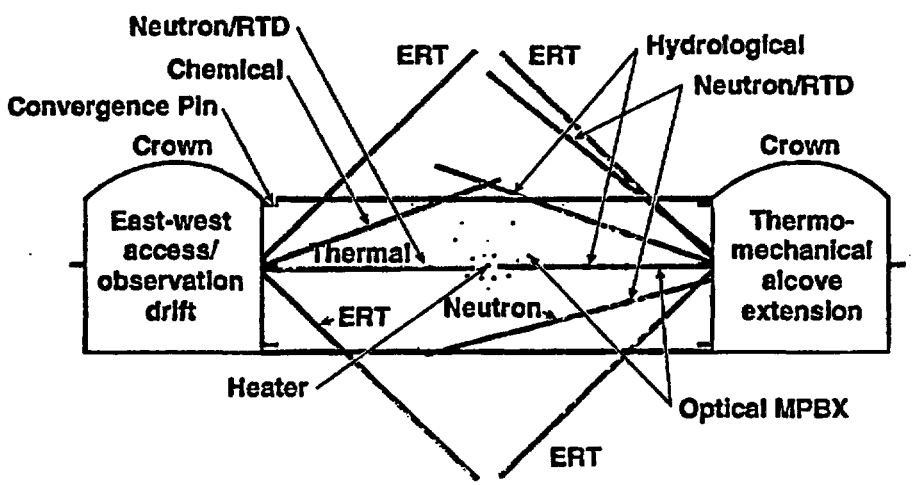

Cross-section A-A

PRELIMINARY
(Not to scale)

Figure 9-29. Layout of Single Heater Test.

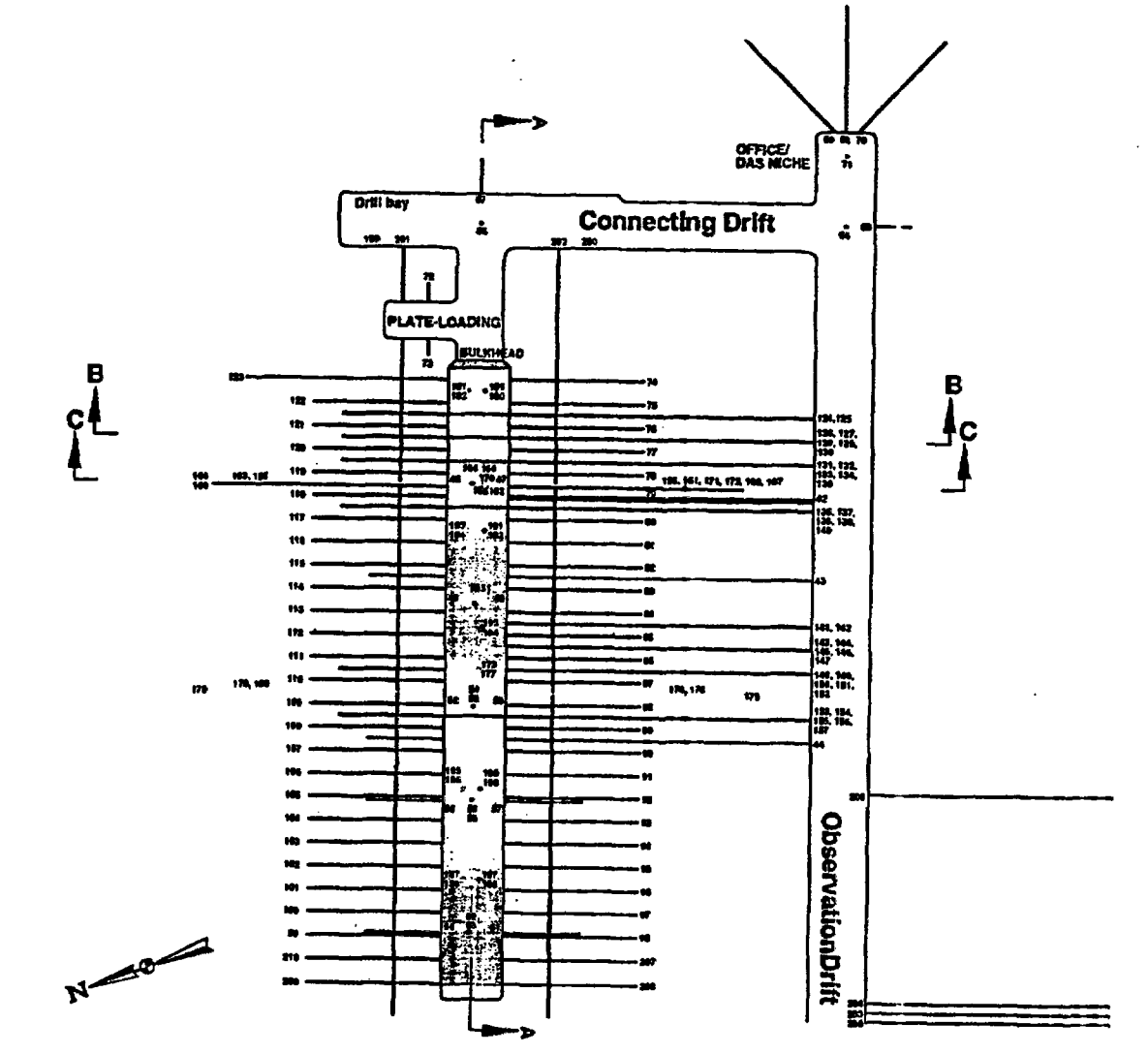

Figure 9-30a. Layout of Drift Scale Test.

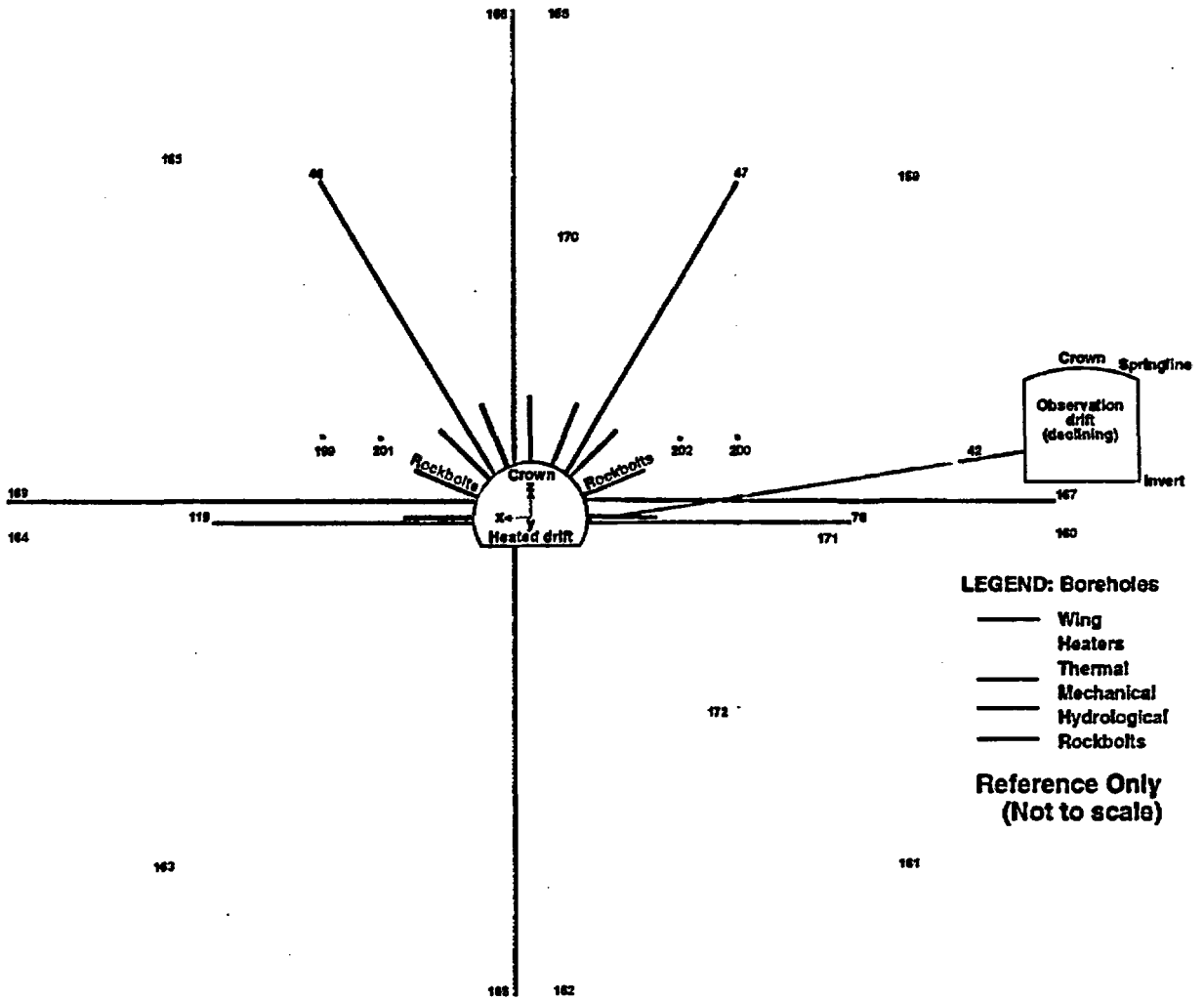

Figure 9-30b. Drift Scale Test (Cross-Section C-C).

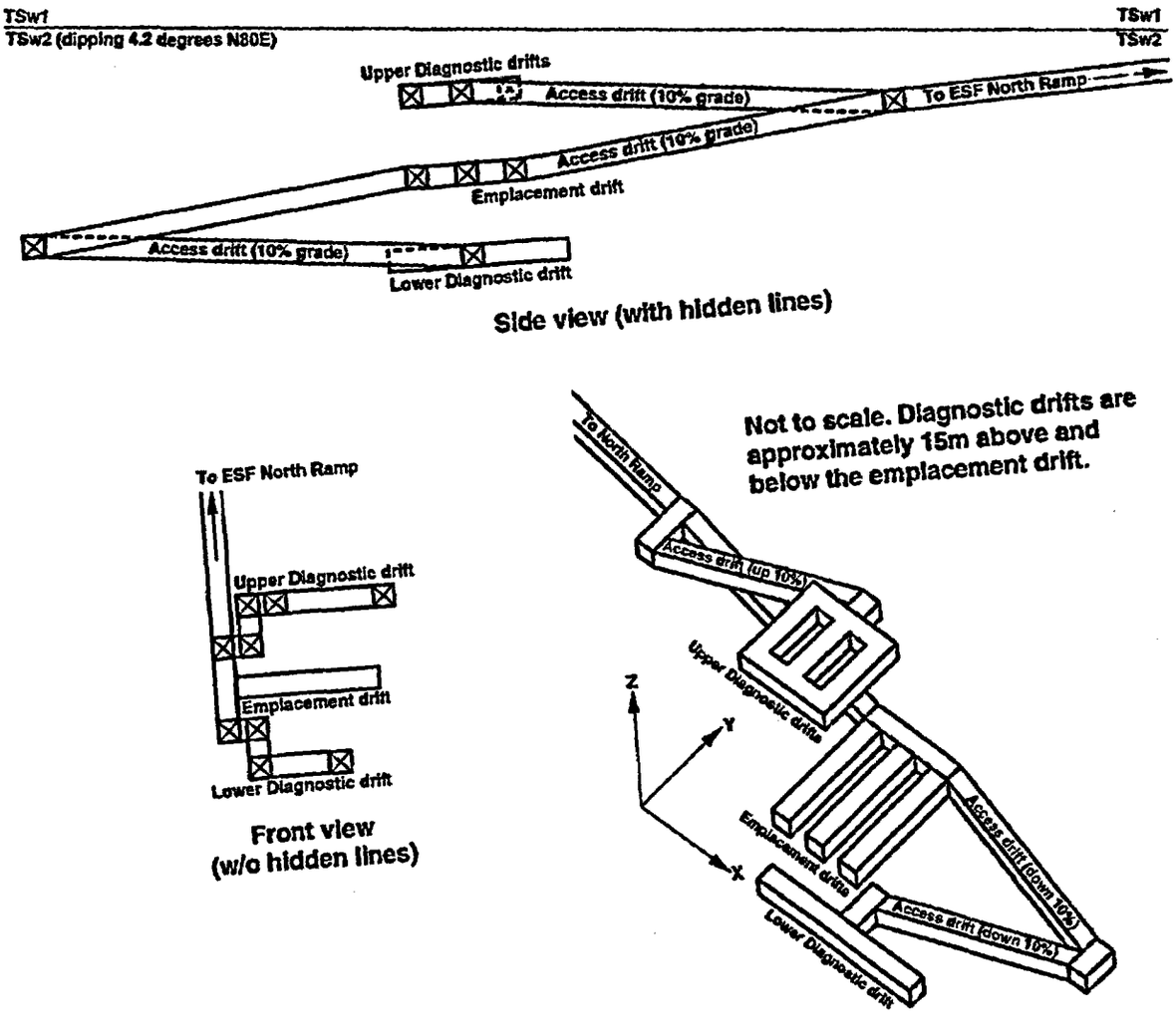

Figure 9-31. A conceptual layout for the Large Scale Long Duration Test.

Contents

Chapter 10.0 Altered Zone Environment

Introduction

The Preliminary Near-Field Environment Report (PNFER) focused attention on the environmental conditions that impact directly on the waste package container materials and on the waste form. That report pointed out that the environmental conditions for the waste packages and waste form would be very much a function of interactions between the environment and the waste, particularly the heat generated by the waste emplacement. As a result of the work that supported the PNFER, it was recognized that those same processes or interactions could potentially cause significant or fundamental property changes that could extend for considerable distances into the rock mass or natural system. However, the processes that dominated the system in the Altered Zone (AZ) were not necessarily the same as the ones that dominated either the Near-Field Environment (NFE) or even the Far-Field Environment (FFE). Therefore, a zone termed the Altered Zone was defined wherein fundamental changes to hydrologic, mineralogical, or chemical conditions may take place within the natural system, but where these conditions do not interact directly with the waste packages (rather interact with the NFE) and where changes are more significant than in the FFE where ambient conditions tend to prevail.

The environmental conditions that impact upon waste packages and radionuclides will be strongly perturbed by the heat of decay from the waste for many hundreds or thousands of years. Because of the strong thermal gradients that will exist for the first 1000 yr, the near-field or waste package environment will be dominated by kinetic effects. After the thermal pulse is transferred further into the rock mass, the rapidity of movement of the thermal isotherms slows down and equilibrium conditions begin to have more of an impact. Thus, to some degree the distinction between AZ and NFE is one of which processes dominate.

For any given emplacement scenario, the rate at which temperature changes occur depends, in general, on the distance from the heat source: the further the distance, the slower the heating rate. As just mentioned, this temperature behavior provides the basis for defining or distinguishing the NFE from the AZ. In the near-field region, hydrological processes will be dominated by water vaporization, water movement by means of gas-phase transport, and condensation in those outer regions of the NFE where temperatures are below the boiling point. Geochemical processes will be dominated by evaporation and boiling, mineral dehydration, and solid-vapor interactions. The system will be a very dynamic one in which the dryout regions will increase in size and therefore incorporate what had been zones of condensation. Because of the dynamics, coupling between hydrology and geochemistry may not be well developed (water removed before geochemical reactions changes the system in significant or fundamental ways).

In the altered zone, hydrologic processes will be dominated by an increase in water availability and increased saturation, associated with vapor condensation. There will be general elevation of temperatures several tens of degrees centigrade. The geochemical processes will be dominated by fluid-rock interactions and reactive transport. The altered zone will tend to be less dynamic than the NFE in that the residence times for water will be much longer, the dryout zone will not incorporate the condensation zones until long periods of time, if at all. Within the altered zone, these interactions will result in significant coupling between hydrological and geochemical processes, such that fluid pathways and geochemical conditions will evolve in a synergistic way.

Although the geochemical processes (e.g., recrystallizations, hydration or dehydration of mineral phases, or both; dissolution and precipitation; rock-water interaction involving water in pores and fractures; cation exchange, sorption, etc.) in both regions are the same, their impact on rock properties will be different, due to contrasts in heating and cooling rates, and in the abundance and temperature of liquid water. These differences will be expressed as differences in the magnitude and nature of chemical

and mineralogical changes, and the duration of specific processes. As a result, the repository performance will be affected differently in the two regions as a result of water-mineral interactions. For purposes of this report, the Near-Field Environment (NFE) will be considered to be those regions that acheive temperatures well above the boiling point, and the Altered Zone (AZ) will be considered to be those regions that maintain temperatures low enough to allow liquid water to exist in pores and fractures. This distinction has the advantage of focusing attention on the dominant processes that may effect performance in different regions of the repository (e.g., evaporation of water and mineral dehydration in the NFE, and rock-water interaction and the kinetics of dissolution and precipitation in the AZ). Refer to Chapter 3 for results to date of activities investigating processes in the NFE.

10.1 Mountain-Scale Unsaturated Zone (UZ) Thermal-Hydrology

The geochemical environment of the near-field, the EBS, and the altered zone will affect any liquid water that may contact the WPs, the waste-form, and any radionuclides released into the near-field and transported in the altered zone. The composition of the liquid phase will depend on the isothermal and nonisothermal flow processes and reaction history experienced by packets of mobile fluid along their respective flow paths. These packets of mobile fluid will not just be affected by coupled thermal-hydrological-geomechanical-geochemical (T-H-M-C) processes in the near field and EBS, but will also be influenced as they flow through the altered zone, which can extend more than hundreds of meters away from the repository. Intermediate flow processes, such as condensate refluxing and evaporation, can concentrate different dissolved components. Condensate may dissolve minerals from fracture walls as it drains down fractures and then precipitate those (or other) minerals as it evaporates. These changes may significantly increase or decrease fracture apertures along various intervals, thereby altering the bulk permeability distribution. Solubility and dissolution of minerals depend on temperature changes, among other things. The geochemistry of water from surface infiltration contacting WPs will vary depending on whether it drains quickly down fractures or migrates slowly in the matrix, and on whether it was affected by refluxing or buoyant gas-phase convection. It may also depend on the pathways followed by the water and on the temperature gradient along those pathways.

Changes in *RH*, liquid saturation, temperature, and the liquid-phase flow field can change hydrological properties in the unsaturated zone (UZ) such as fracture and matrix permeability, through precipitation, dissolution, or mineral alteration. Adsorptive properties of various units may be affected by temperature, liquid saturation, and compositional changes. The spatial and temporal extent of decay-heat-driven changes in temperature, liquid saturation, and *RH* in the UZ are described in Section 10.1. The temporal extent of these changes in the near field are also described in Section 1.10.5 of Chapter 1.

The zone of two-phase refluxing overlying the boiling zone (called the heat-pipe zone) is of particular interest because the liquid saturation and relative humidity *RH* remain high in this zone, increasing the likelihood of aqueous reactions and aqueous-transport processes occurring. Refluxing can also generate a very high liquid-phase flux in fractures, which can result in significant dissolution and precipitation of minerals along the fracture walls. The heat-pipe zone is typically manifested by temperatures that are very close to the nominal boiling point of water (96°C) and a liquid saturation that is very close to 100%. Vertical temperature and liquid saturation profiles are given in Section 1.10.1 to indicate where heat-pipes and related coupled T-H-M-C processes may be occurring.

Changes in temperature and the mixing of groundwater (driven by decay-heat-driven, buoyant, liquid-phase convection) could alter hydrological and adsorptive properties in the saturated zone and could thereby affect radionuclide transport in the saturated zone (SZ) [Buscheck and Nitao, 1993b]. The spatial and temporal extent of decay-heat-driven changes in temperature and in the liquid-phase flow field in the SZ are described in Section 10.2.

Fluid flow in the UZ at Yucca Mountain involves liquid- and gas-phase flow through the fractures and through the rock matrix. Under ambient conditions, the gas phase contains about 98.5% air and 1.5% water vapor. An important feature of the UZ at Yucca Mountain is its high fracture density. Moreover,

the Topopah Spring tuff (TSw2), which occurs at the potential repository depth, is one of the most densely fractured hydrostratigraphic units. This is significant because, without fractures, the rock throughout most of the UZ (including the repository horizon) would be extremely impermeable. In general, repository heat moves moisture by (1) vaporization, (2) driving water vapor from high to low gas-phase pressure, (3) condensation, and (4) gravity- or capillary-driven flow of condensate. Without fractures, the rock would be too impermeable to allow significant vaporization and movement of water vapor. The flow of condensate would also be very slow. A system of connected fractures facilitates significant decay-heat-driven fluid flow as well as natural infiltration. Enhanced gas-phase diffusion of water vapor may significantly contribute to vaporization in unfractured (relatively impermeable) rock.

Modeling and analytical studies of high-level radioactive waste isolation have demonstrated the potential importance of nonequilibrium flow processes between the fractures and the matrix [Buscheck et al., 1991; Nitao et al., 1993]. Except for regions with a perched water table or during transient recharge episodes, capillary forces cause most fractures to be drained of liquid water. Matrix permeability is extremely low for most of the hydrostratigraphic units in the UZ (including the TCw, TSw1, TSw2, TSw3, and CHnv units), so mountain-scale, liquid-phase flow and (where applicable) radionuclide transport will primarily occur in fractures rather than in the matrix. In units with intermediate matrix permeability (including the PTn and CHnv), matrix flow may also contribute to mountain-scale liquid-phase flow and transport. Liquid-phase flow in fractures may arise from three origins:

1. Ambient infiltration and percolation of rainfall and snowmelt.
2. Condensate generated under *boiling conditions*.
3. Condensate generated under *sub-boiling conditions*.

The first source arises from the ambient system; the second and third are generated by radioactive decay heat, primarily from SNF. Decay-heat-driven, buoyant vapor flow, occurring either on a sub-repository scale or on a mountain scale (Figs. 10.1.1a and b), may play an important role in generating the second and third sources of liquid water. Decay-heat-driven binary diffusion of water vapor and air (called vapor diffusion) may also play important roles in condensate generation [Buscheck and Nitao, 1994a]. A heterogeneous distribution of bulk permeability k_b can influence vapor and condensate flow under both boiling and sub-boiling conditions. Of particular concern are k_b distributions that promote the focusing of condensate flow, which could cause water to drip onto WPs [Fig. 10.1.1c] even if average behavior would indicate otherwise [Buscheck and Nitao, 1994a].

Decay heat also drives buoyant, liquid-phase convection in the SZ (Fig. 10.1.1b). Analyses of this type of flow indicate that it is likely to be the dominant means of driving radionuclide transport in the saturated zone (SZ) for tens of thousands of years [Buscheck and Nitao, 1993b; Buscheck and Nitao, 1994a]. A k_b distribution that facilitates deep convective mixing of radionuclides in the SZ would be more likely to meet a dose-based standard than a stagnant water table.

Table 10.1.1 summarizes the time and length scales involved in how repository heat influences the three major sources of fracture flow. Mountain-scale effects depend on the overall heating conditions for the entire repository. Several studies [Buscheck and Nitao, 1992; Buscheck and Nitao, 1993b; Buscheck and Nitao, 1994a] have shown that the most useful macroscopic thermal loading parameter quantifying the time-integrated heat content of the waste in the repository is the areal mass loading (AML, expressed in metric tons of uranium per acre, MTU/acre). Mountain-scale effects depend primarily on the AML of the entire repository, and they are insensitive to the details of WP emplacement, such as WP size and spacing, and spent nuclear fuel (SNF) age. These effects also depend on the distribution of thermal and hydrological properties throughout the UZ.

Sub-repository-scale (also called drift-scale) effects depend on the local heating conditions around WPs. Important factors include (1) the number of spent nuclear fuel assemblies per WP, (2) the axial spacing between WPs, (3) the lateral spacing between emplacement drifts, and (4) SNF age. In general, the number of fuel assemblies per WP is directly related to the WP size. Large WPs that contain a large number of assemblies, generally have a higher thermal output. Younger fuel has a higher thermal output than older fuel for some period of time. The local areal mass loading (LAML) depends on the WP size and spacing. For a given LAML, drift-scale effects are very different, depending on whether widely

spaced, large WPs or tightly spaced, small WPs are used. These effects also depend on the near-field distribution of thermal and hydrological properties within a few tens of meters of the WPs.

Figure 10.1.2 show the effect of decay heat on the flow of water vapor and condensate in the vicinity of an emplacement drift. Heat flow away from the WPs occurs as heat conduction, the convection of latent and sensible heat, and thermal radiation. Because of the large bulk permeability of fracture networks, gas-phase pressures in the fractures remain very close to atmospheric, even during boiling. Consequently, as temperatures reach the nominal boiling point (~96°C), boiling first occurs along fractures (Fig. 10.1.2) and proceeds into the matrix blocks. Accordingly, dry-out due to boiling is more suppressed in sparsely fractured regions (with large matrix blocks) and less suppressed in intensely fractured regions (with small matrix blocks). As boiling continues, water vapor displaces air away from the WPs and may replace it completely for sufficiently high AMLs.

Most of the water vapor reaching the fracture network is eventually driven away from the emplacement drift by higher gas-phase pressures in the boiling zone to where cooler temperatures cause it to condense along fracture walls (Fig. 10.1.2). Buoyant, gas-phase convection can cause more of the vapor flow to be driven upward to where it condenses above the dry-out zone. In general, regardless of where the condensate is generated, there are three things that can happen to it:

(1) It can drain away from the boiling zone.

(2) It can drain back toward the boiling zone.

(3) It can be imbibed by the matrix.

Because the small matrix permeability limits the rate at which the matrix can imbibe the condensate by capillary suction, it can drain for considerable distances down fractures before being completely imbibed. Below the boiling zone, condensate drainage is away from the boiling zone (Fig. 10.1.2), enhancing the dry-out rate. Above the boiling zone, condensate tends to drain back toward the boiling zone, where it reboils, thereby retarding the net rate of dry-out.

The return flow of condensate back toward the heat source causes refluxing, which is the counter-current flow of water vapor and condensate. It is important to note that refluxing does not require boiling conditions [Buscheck and Nitao, 1994a]. Heat-driven, buoyant gas-phase flow can drive refluxing under sub-boiling conditions. Under boiling conditions, refluxing results in a heat transfer mechanism (driven by the convection of latent heat) called the heat-pipe effect. Given adequately high mass flux rates of water vapor and condensate, heat pipes are capable of sustaining a given heat flux with a much flatter temperature gradient than is associated with heat conduction. Consequently, heat pipes are manifested by a flat temperature profile, with temperatures close to the nominal boiling point. Pruess and others [1984, 1990] were the first to model the heat-pipe effect in the context of thermal-hydrological performance at Yucca Mountain. Depending on the AML, these effects can occur at the sub-repository scale or on a mountain scale (Table 10.1.1).

Figure 10.1.3 shows the various decay-heat-driven processes and ambient site conditions that may significantly affect the moisture balance in the UZ. The moisture balance in the UZ (and, in particular, in the region above the repository) may play a very important role in the performance of the EBS, the natural barriers, and the total system. In general, decay heat will result in regions of dryout and condensate buildup in the UZ. Modeling studies [Buscheck and Nitao, 1993a; Buscheck and Nitao, 1993b; Buscheck and Nitao, 1994a; Buscheck et al., 1994] have indicated that decay-heat-driven changes in the saturation distribution can persist for more than 100,000 yr, even for low AMLs that never drive temperatures close to the boiling point. These effects, along with temperature changes, can alter the hydrological, geochemical, and geomechanical properties that influence fluid flow and radionuclide transport. Decay heat might drive enough water vapor out of the top of the mountain to significantly reduce the UZ moisture content for tens of thousands of years. Conversely, mountain-scale, buoyant gas-phase convection might drive enough water vapor up from the SZ (into the UZ) to *increase* the UZ moisture content for tens of thousands of years [Buscheck and Nitao, 1994a; Buscheck et al., 1994].

The important site-scale features that may significantly affect decay-heat-driven, mountain-scale, thermal-hydrological flow include:

Paintbrush vitic nonwelded tuff (PTn): This unit probably plays an important role in (1) attenuating (in space and time) episodic nonequilibruim fracture flow and (2) reducing the ambient percolation flux in the host rock (the TSw2 unit). Imbibition in the PTn serves to dampen the influence of episodic infiltration and thereby provide more time for exfiltration and lateral flow to influence the moisture balance in the PTn; all of which tend to reduce the percolation flux in the TSw2. Because it has a much lower k_b than the densely welded tuff units that lie above it (the TCw unit) and below it (the TSw1 unit), the PTn significantly influences mountain-scale gas-phase flow under both ambient and decay-heat-disturbed conditions. Analyses of mountain-scale buoyant gas-phase convection [Buscheck and Nitao, 1994a; see also Chapter 10.0 of this report] indicate that it will probably significantly limit (or cap) the upper spatial extent of large-scale gas-phase convection cells in the UZ. This could significantly affect the magnitude of moisture redistribution in the UZ by this mechanism.

Basal vitrophyre of the Topopah Spring tuff (TSw3): This unit (sometimes colloquially called the "tin basement") appears to be associated with regions of perched water, which may be the result of restricted fracture flow arising from clay fillings. If fracture and bulk permeabilty k_b are signicantly reduced in the TSw3, this would have a significant effect on condensate drainage and on mountain-scale buoyant gas-phase convection. A reduced k_b could significantly limit the lower spatial extent of large-scale gas-phase convection cells in the UZ. This could significantly affect the magnitude of moisture redistribution in the UZ by this mechanism.

Calico Hills nonwelded tuff (CHn): Both the zeolitic (CHnz) and vitric (CHnv) portions of this unit probably have a significantly lower k_b than the overlying TSw sequence. If k_b is not reduced in the TSw3, k_b values in the CHnv and CHnz are probably small enough to significantly limit the lower spatial extent of large-scale gas-phase convection cells in the UZ. This could significantly affect the magnitude of moisture redistribution in the UZ by this mechanism.

10.1.1 Models and Assumptions

10.1.1.1 V-TOUGH and NUFT Thermal-Hydrological Flow Codes. All thermal-hydrological calculations were carried out using the V-TOUGH (Vectorized Transport of Unsaturated Groundwater and Heat) code [Nitao, 1989] and NUFT (Nonisothermal Unsaturated-Saturated Flow and Transport) code [Nitao, 1993]. V-TOUGH is Lawrence Livermore National Laboratory's enhanced version of the TOUGH code, which is a member of the Mulkom family of multiphase, multicomponent codes developed at Lawrence Berkeley Laboratory [Pruess, 1987]. Both V-TOUGH and NUFT are multidimensional numerical simulators capable of modeling the coupled transport of water, vapor, air, and heat in fractured porous media. In addition to coupled multiphase heat and fluid flow, NUFT can handle multicomponent aqueous- and nonaqueous-phase species transport. NUFT is a highly efficient and robust integrated finite difference code that describes the flow of multiple phases and transport of multiple components in porous media under isothermal or nonisothermal conditions [Nitao, 1993]. NUFT solves the (nonlinear) partial differential equations for the balance of component mass and energy. NUFT has an extensive suite of linear equation solvers that allows efficient solution of practical three-dimensional problems that have tens of thousands of elements, large contrasts in element size, and sharp nonlinearities in the governing equations. For this work NUFT was configured to solve the flow and transport of air, water, and energy. V-TOUGH has been qualified for use in qualitiy affecting work. NUFT has been benchmarked against the V-TOUGH code for a wide range of problems related to decay-heat-altered nonisothermal flow and transport at Yucca Mountain; for all of the cases compared, NUFT and V-TOUGH predicted essentially identical results.

For both V-TOUGH and NUFT, the flow of fluid phases is governed by the multiphase version of Darcy's law, the diffusion of air and water vapor by Fick's law, and thermal conduction by Fourier's law. Air, water vapor, and heat are transported by fluid advection in two phases, aqueous and gaseous. Local thermodynamic equilibrium is assumed between solid and fluid phases. Water property values are calculated from steam tables. The code calculates the vaporization and condensation of water, and the resulting absorption or release of latent heat, based on local thermodynamic equilibrium.

10.1.1.2 Equivalent Continuum Model. Because of the impracticality of discretely accounting for all of the fractures at Yucca Mountain, it is often found to be necessary to account for fractures using the equivalent continuum model (ECM). The assumption of capillary-pressure and thermal equilibrium between fractures and matrix allows the fracture and matrix properties to be pore-volume-averaged into an equivalent medium. One of the objectives of lab-scale and field-scale thermal tests is to determine the validity of assumptions and approximations used in our models, including the ECM approximation. For purposes for which the existing ECM-based analyses have been used, the ECM approximation has been considered adequate. The bulk porosity ϕ_b, bulk saturation S_b, and bulk hydraulic conductivity K_b of the equivalent medium are given by the relations

$$\phi_b = \phi_f + \left(1 - \phi_f\right)\phi_m , \tag{1}$$

$$S_b = \frac{S_f\phi_f + S_m(1 - \phi_f)\phi_m}{\phi_f + (1 - \phi_f)\phi_m} , \tag{2}$$

$$K_b = K_f\phi_f + K_m\left(1 - \phi_f\right) , \tag{3}$$

where the subscripts m and f refer to the matrix and fractures, respectively. Because of the low K_m in the UZ, the value of K_b is almost completely determined by K_f and ϕ_f for most fracture spacings and permeabilities.

10.1.1.3 Thermal-Hydrological Properties. All major hydrostratigraphic units in the UZ at Yucca Mountain are included in the models. The hydrostratigraphic profile employed here has been used in several modeling studies [Buscheck et al., 1993; Buscheck and Nitao, 1992, 1993a, 1993b, 1993c, 1994a, 1994b; Buscheck et al., 1994]. The wet and dry thermal conductivity, K_{th}, data were obtained from the Reference Information Base [DOE, 1990]. We assume the steady-state liquid saturation profile obtained for a net infiltration flux (also called percolation flux) of 0 mm/yr, yielding a repository horizon saturation of 68% [Buscheck et al., 1991]. Other studies [Buscheck and Nitao, 1992; Buscheck and Nitao, 1993a; Buscheck and Nitao, 1993c] also considered the steady-state saturation profile obtained for percolation fluxes of 0.045 and 0.132 mm/yr, resulting in repository saturations of 85 and 95%, respectively. For the reference case, we used the matrix hydrological properties given in the Reference Information Base [1990] and Klavetter and Peters [1986]. We also considered the impact of more recent matrix hydrological property data reported by Pruess and Tsang [1994], which are based on measurements by Flint and others [1983].

The reference case assumed a bulk permeability, k_b, of 2.8×10^{-13} m^2 (280 millidarcy), which is equivalent to three 100-μm fractures per meter. The sensitivity of buoyant, gas-phase convection, boiling and dryout behavior to k_b was examined by considering the following values of k_b: 1.9 microdarcy (no fractures), 10 microdarcy (three 3-μm fractures per meter), 100 microdarcy (three 7-μm fractures per meter), 1 millidarcy (three 15-μm fractures per meter), 10 millidarcy (three 33-μm fractures per meter), 1 darcy (three 153-μm fractures per meter), 5 darcy (three 262-μm fractures per meter), 10 darcy (three 330-μm fractures per meter), 20 darcy (three 416-μm fractures per meter), 40 darcy (one 781-μm fracture per meter), 84 darcy (one 1000-μm fracture per meter), 168 darcy (one 1260-μm fracture per meter), 414 darcy (one 1700-μm fracture per meter), and 840 darcy (one 2150-μm fracture per meter).

10.1.1.4 Initial and Boundary Conditions. The vertical temperature distribution, T, in the models is initialized to correspond to the nominal geothermal gradient in the region. For the reference case, the repository is assumed to be at a depth of 343.1 m. The initial temperature and saturation at the repository horizon in the UZ model are 23.3°C and 68%, respectively. The atmosphere at the ground surface is represented by a constant-property boundary, with T and gas-phase pressure fixed at 13°C and 0.86 atm, respectively. The relative humidity RH at the ground surface is also fixed at a value that represents thermodynamic equilibrium with respect to the initial saturation conditions at the top of the TCw unit. Therefore, under initial (ambient) saturation and temperature conditions, there is no mass flux of water vapor between the atmosphere and upper TCw. In some previous work [e.g., Buscheck and Nitao, 1992], it was assumed that because of the large fracture permeability, buoyant convective mixing in the saturated zone (SZ) results in it acting as a heat sink. The large k_b and storativity of the SZ were also assumed to result in the water table being at a fixed depth (z = 568.1 m). For the drift-scale calculations reported here, we also assume that the water table has a fixed depth (z = 568.1 m) and a constant temperature (31°C); this causes the water table to act as a heat sink. Because this model does not explicitly model hydrothermal flow in the SZ, it is called the "UZ" model. In comparing the UZ model with the UZ-SZ model, which is described below, we found that, for the first 1000 yr, repository temperatures are insensitive to the treatment of heat flow at the water table [Buscheck and Nitao, 1993; Buscheck and Nitao, 1993c].

We conduct most of our calculations with a UZ-SZ model (which includes hydrothermal flow in the upper 1000 m of the SZ). The vertical domain of our models is a key aspect to consider when conducting mountain-scale calculations. Calculations that use a fixed-depth constant-temperature boundary at the water table substantially underpredict mountain-scale temperature rise as well as the overall magnitude of decay-heat-altered T-H effects in the UZ (see Section 10.2.1). Therefore, to adequately model the temporal and spatial extent of decay-heat-altered T-H behavior, it is essential that the lower boundary of a mountain-scale T-H model does not function as a heat sink. Moreover, it is not possible to analyze the effects of decay heat on SZ flow and transport unless the model domain include the SZ. Conductive and convective heat flow, including buoyancy flow, are modeled in the SZ. Because the RIB [DOE, 1990] lacks

thermal property and hydrological data below the PPw unit (the lowermost hydrostratigraphic unit in our UZ model), we assumed that the PPw data were applicable to the upper 1000 m of the SZ (down to the lower boundary of the UZ-SZ model). The lower boundary of the UZ-SZ model has a constant temperature of 53.5°C and a fixed pressure corresponding to the hydrostatic pressure and temperature profile of the upper 1000 m of the SZ.

For the reference-overburden case, the repository is assumed to be at a depth of 343.1 m. In Section 10.1.4, we also consider a "minimum-overburden" case (with an overburden thickness of 200 m) and a "maximum-overburden" case (with an overburden thickness of 420 m). For the reference-overburden case, the initial temperature and saturation at the repository horizon in the UZ-SZ model are 23.5°C and 68%, respectively.

For most of the calculations in Sections 10.1 and 10.2, we assume a Youngest Fuel First Spent Nuclear Fuel (SNF) receipt scenario with a 10-yr cut-off for the youngest fuel, referred to as YFF(10), and account for the emplacement of BWR waste packages (WPs), containing 40 assemblies per WP, and PWR WPs, containing 21 assemblies per WP. The waste receipt schedule was supplied by John King [1993] of the WAST organization. areal mass loadings (AMLs) of 24.2, 35.9, 55.3, 70, 83.4, 100, 110.5, and 150.0 MTU/acre were considered in our calculations.

10.1.1.5 Mountain-Scale and Sub-Repository-Scale Models. For an AML of 49.2 MTU/acre, we assumed that the heated area of the repository is 1747 acres. Note that this AML was once the reference thermal load in the Site Characterization Plan–Conceptual Design Report [SNL, 1987], which is called the SCP-CDR. For 10-yr-old SNF, this AML results in an aeal power density (APD) of 57 kW/acre. For a 1747-acre repository, the mountain-scale model represents the repository as a 3-km-diameter, 4.6-m-thick, disk-shaped heat source with a uniformly distributed thermal load. Repository areas of 559, 1118, and 3162 acres were also modeled for AMLs of 154.7, 77.3, and 27.1 MTU/acre, respectively. The model, which is similar to models used by Pruess and Tsang [1993], utilizes an axisymmetric coordinate system centered at the repository center. This model is useful for calculating temperature and saturation behavior (averaged from one emplacement drift to the next) as a function of location relative to the center (or edge) of the repository area. The assumption was also made that the thermal loading of the repository can be represented by the heat generation curve of pressurized water reactor (PWR) SNF of an average age. Calculations were made for APDs ranging from 10 to 114 kW/acre and SNF ages of 10, 20, and 30 yr with a burnup of 33,000 MWd/MTU.

Because it areally averages the thermal load, the mountain-scale model cannot represent differences in temperature and saturation behavior within (1) the pillars (i.e., the rock separating neighboring emplacement drifts), (2) the emplacement drifts, or (3) the waste packages (WPs) themselves. The drift-scale model used in this section is a two-dimensional cross-sectional model that explicitly represents the details of the WPs and emplacement drifts in the plane orthogonal to the drift axes. This model is useful in representing details of thermal-hydrological behavior at the drift (or sub-repository) scale. In particular, we are interested in how drift-scale, buoyant, gas-phase convection (which is driven by temperature differences between the drifts and pillars) affects vapor and condensate flow and thermal performance. To take advantage of symmetry, the drift-scale model assumes an infinite repository with uniformly spaced emplacement drifts. The assumption of an infinite repository area is applicable to the interior of the repository, which is not affected by cooling at the edge. This region includes most of the repository area during (at least) the first 1000 yr.

The drift-scale model assumes the 38.4-m center-to-center spacing between emplacement drifts that is found in the SCP-CDR [SNL, 1987]. The model represents a symmetry element from the symmetry plane down the center of the WP to the symmetry plane in the pillar between neighboring drifts. The thermal load is axially averaged along the axis of the drift. The WP has a cross section of 1.6×1.6 m and is located in the center of an emplacement drift that is 4.8 m high by 6.0 m wide. The drifts are assumed to remain open; therefore, heat flow from the WP surface to the drift wall occurs as thermal radiation, convection, and conduction. The drift-scale model can represent heterogeneity that occurs at the scale of the drifts. For some of our calculations, a 1.6-m-wide, high-k_b zone is oriented vertically, intersecting either the midline of the emplacement drift or the midline of the pillar separating the drifts. The k_b of this zone can be several orders of magnitude larger than k_b throughout the rest of the model (the nominal-k_b zone). The

center-to-center spacing between the high-k_b zones is 38.4 m (the same as the center-to-center drift spacing).

Heterogeneity that occurs at a larger scale is represented by a third model, which we call the cross-sectional uniform heat flow (CSUHF) model. Like the drift-scale model, the CSUHF model assumes an infinite repository, thereby enabling it to take advantage of symmetry. The CSUHF model represents an infinite series of vertical, uniformly spaced, 1.0-m-wide, high-k_b zones. We considered high-k_b zone spacings of 100 and 1000 m. For the high-k_b zones, we considered 10, 84, 414, and 840 darcy. For the nominal-k_b zones, we considered 1.9 and 100 microdarcy; 1, 10, 100, and 280 millidarcy; and 10 darcy.

Natural Infiltration	Buoyant, gas-phase convection and condensate drainage *		Boiling and condensate drainage	
	Sub-repository scale	Mountain scale	Sub-repository scale	Mountain scale
Affected by repository-heat-driven changes to the • moisture distribution • intrinsic hydrological, geochemical, and geomechanical properties	Local heating conditions Local Areal Mass Loading Waste package size Waste package spacing	Global heating conditions Areal Mass Loading Repository size Repository location	Local heating conditions Local Areal Mass Loading Waste package size Waste package spacing	Global heating conditions Areal Mass Loading Repository size Repository location
	Near-field thermo-hydrological properties	Unsaturated zone-scale thermo-hydrological properties	Near-field thermo-hydrological properties	Unsaturated zone-scale thermo-hydrological properties
	$t < 1000$ yr ** $t < 2000$ yr ***	$1000 < t < 100{,}000$ yr	$t < 50$ yr ** $t < 400$ yr *** for 27 MTU/acre $t < 1000$ yr ** for 49 MTU/acre $t < 50$ yr for 155 MTU/acre	$t < 1000$ yr $t < 100{,}000$ yr for residual effects

* Can occur under both sub-boiling and boiling conditions

** Assuming small waste packages

*** Assuming large waste packages

Table 10.1.1. The various time and length scales involved in how decay heat influences the three major sources of vapor and condensate flow.

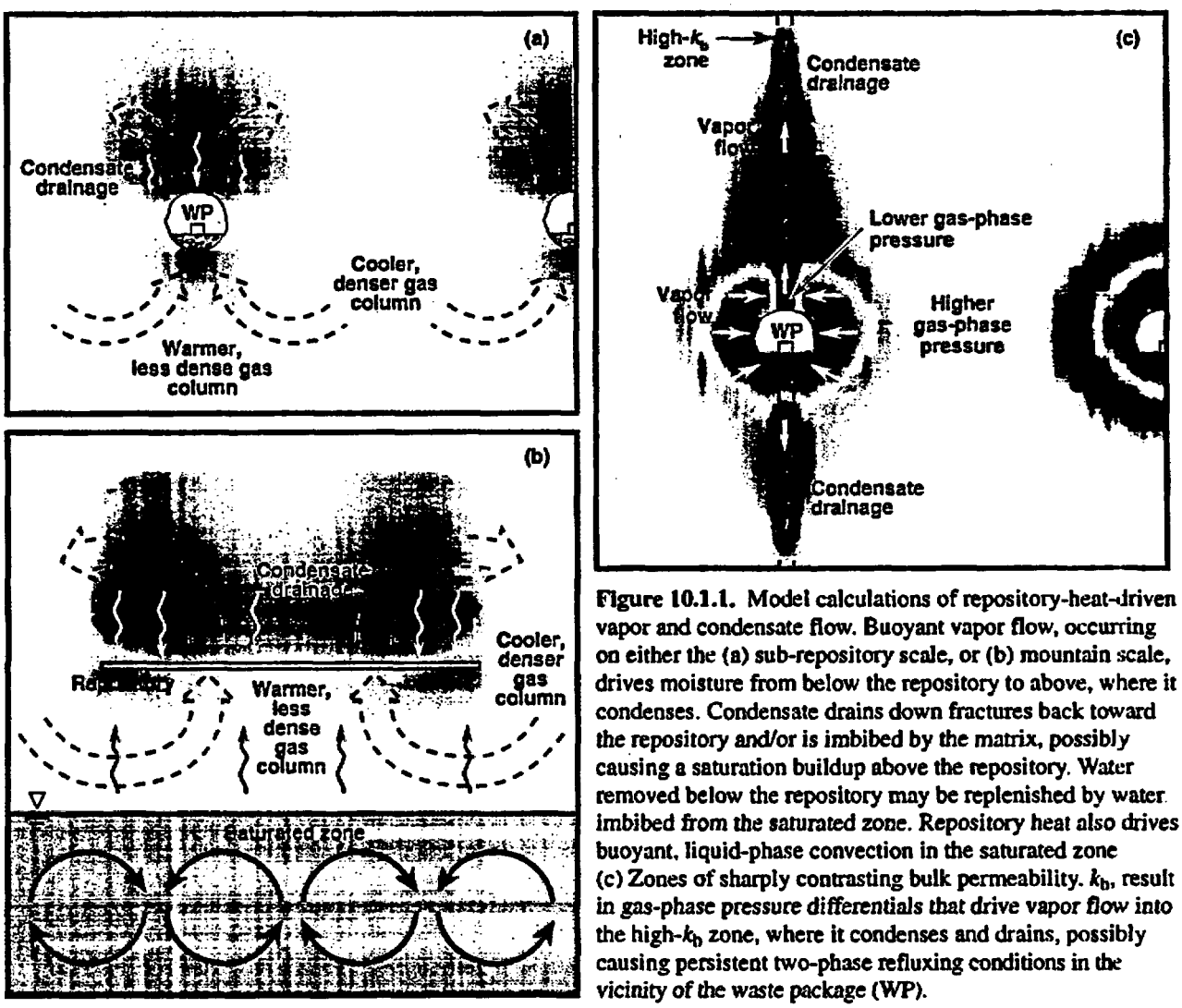

Figure 10.1.1. Model calculations of repository-heat-driven vapor and condensate flow. Buoyant vapor flow, occurring on either the (a) sub-repository scale, or (b) mountain scale, drives moisture from below the repository to above, where it condenses. Condensate drains down fractures back toward the repository and/or is imbibed by the matrix, possibly causing a saturation buildup above the repository. Water removed below the repository may be replenished by water imbibed from the saturated zone. Repository heat also drives buoyant, liquid-phase convection in the saturated zone (c) Zones of sharply contrasting bulk permeability, k_b, result in gas-phase pressure differentials that drive vapor flow into the high-k_b zone, where it condenses and drains, possibly causing persistent two-phase refluxing conditions in the vicinity of the waste package (WP).

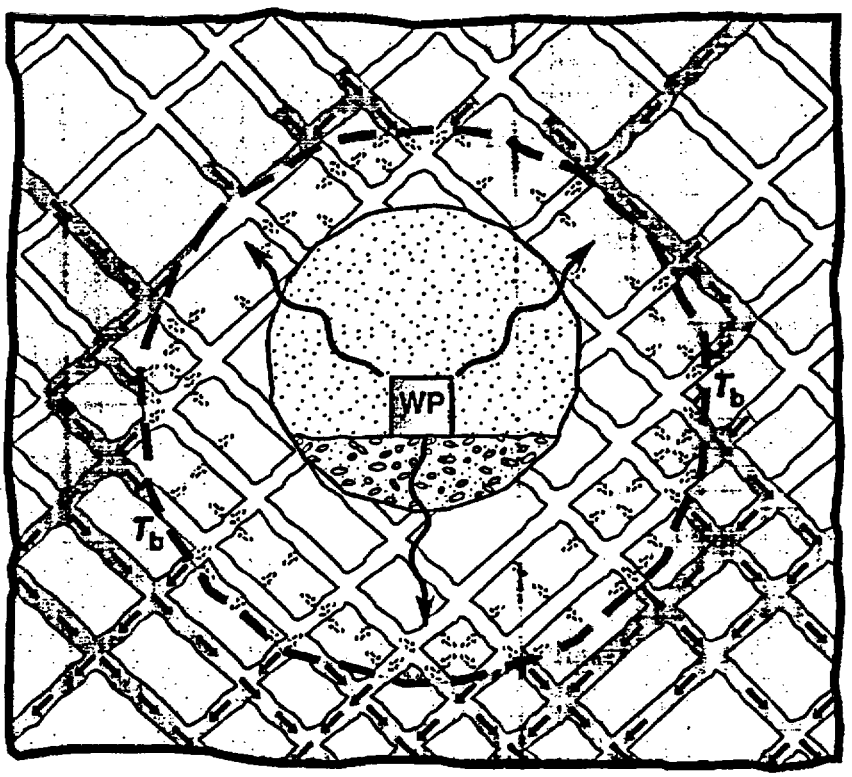

Figure 10.1.2. Schematic of hydrothermal flow near the emplacement drift. Rock dry-out occurs as boiling drives water vapor out of the rock matrix. Upon reaching the fracture network, vapor is driven away from the boiling zone to where cooler temperatures cause it to condense along fracture walls. Because the small matrix permeability limits the rate of matrix imbibition, condensate drainage persists for considerable distances down fractures.

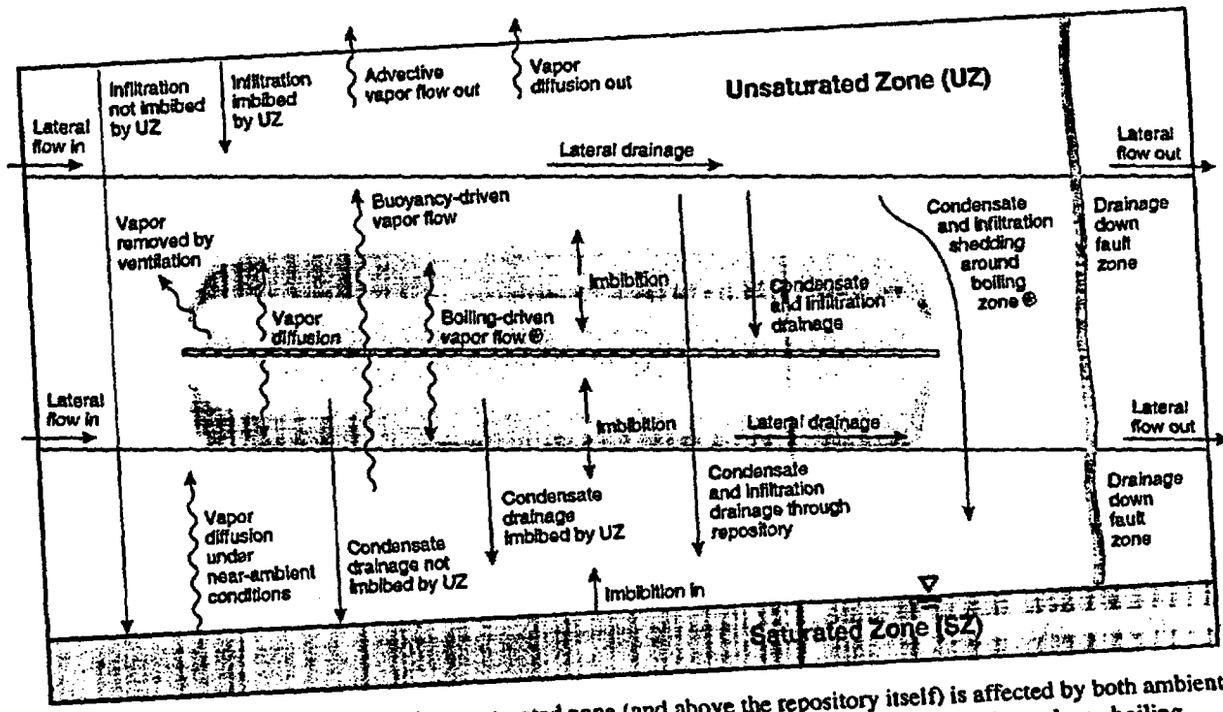

Figure 10.1.3. Moisture balance in the unsaturated zone (and above the repository itself) is affected by both ambient and decay-heat-driven processes. The two processes labeled with an asterisk (*) are applicable only to above-boiling conditions; all other processes shown can occur under both sub-boiling and above-boiling conditions.

Contents

10.1.2 Influence of Fracture Permeability Distribution

10.1.2.1 Temperature and Liquid Saturation Distribution. The vertical temperature and saturation profiles are given for three different radial distances r from the repository center (Figs. 10.1.2.1.1–10.1.2.1.5) for six different AMLs (24.2, 35.9, 55.3, 70, 83.4, and 110.5 MTU/acre). The first value of r (r = 0 m) corresponds to the center of the repository. The second value of r corresponds to the radial position that encloses 50% of the repository. This position is the "median" location in the repository that is representative of "average" conditions because half of the WPs are inside this radial position and half are outside this position. The third value of r corresponds to the radial position that encloses 95% of the repository and is a good representation of conditions at the repository edge (or perimeter) because only 5% of the WPs lie outside of this position.

Figure 10.1.2.1.1 shows the vertical temperature and saturation profiles for the 83.4-MTU/acre case at various times after emplacement. Notice that the thermal and dryout behavior are very similar for the 0 and 50% radial positions of the repository for the first thousand years, and edge-cooling effects influence at least the outer 5% of the repository during this period; the percentage of the repository that is influenced by edge-cooling effects increases with time. The flattening of the temperature profile at the nominal boiling temperature T_b (~96°C), corresponds to the two-phase flow refluxing zone (called the heat-pipe zone), which result from the countercurrent flow of water vapor away from the repository and condensate drainage back to the repository. These effects are described in more detail in other reports [Buscheck and Nitao, 1993a, 1993b, 1993c; Pruess and Tsang, 1993]. This zone is of particular interest because the liquid saturation and relative humidity RH remain high in this zone, increasing the likelihood of aqueous reactions and aqueous-transport processes occurring. Refluxing also generates a very high liquid-phase flux in fractures (see Section 1.10.6 in Chapter 1), which can result in significant dissolution and precipitation of minerals along the fracture walls.

Dryout due to boiling results in a 150- to 200-m-thick dryout zone for the inner 50% of the repository. The low liquid saturation in the dryout zone decreases the likelihood of aqueous reactions and aqueous-transport processes altering the flow and transport properties in this zone. Edge-cooling effects substantially reduce the vertical extent of dryout in the outer region of the repository. Temperatures in the outer edge of the repository only rise to 98°C, while at the center of the repository, T_{peak} = 146°C. Temperatures for the entire repository have declined to below T_b within 5000 yr; however, a zone of less-than-ambient saturations persist after that (Figs. 10.1.2.1.1g and h). The outer 5% of the repository rewets back to ambient saturation within 10,000 yr (10.1.2.1.1g), while the repository center remains below ambient saturation for more than 30,000 yr (Fig. 10.1.2.1.1h).

Figure 10.1.2.1.2 shows the vertical temperature profiles for the 35.9- and 24.2-MTU/acre cases. The mountain-scale model does not predict temperatures above T_b, indicating that averaged temperature conditions throughout the repository remain below boiling. However, as discussed later, local temperatures around the emplacement drift may be well above boiling for WPs containing a large number of SNF assemblies. Because of the absence of boiling conditions in the mountain-scale model, and because 280 millidarcy is below the threshold where mountain-scale, buoyant, gas-phase convection results in significant moisture movement, the 24.2- and 35.9-MTU/acre cases show only a minor change in saturation relative to ambient conditions. Therefore, we did not provide the vertical saturation profiles for these two cases.

Figure 10.1.2.1.3 shows the vertical temperature and saturation profiles for the 55.3-MTU/acre case. The thermal and dryout behavior are similar to that of the 83.4-MTU/acre case except that the vertical extent of boiling and dryout effects is much less. Moreover, the duration of boiling and sub-ambient liquid saturation conditions is much less for the 55.3-MTU/acre case than for the 83.4-MTU/acre case. Liquid saturation for the inner half of the repository has rewetted to ambient conditions within 30,000 yr (Fig. 10.1.2.1.3h); at the edge, liquid saturation has rewetted to ambient liquid saturation within 10,000 (Fig. 10.1.2.1.3g). There are two important observations to make about the heat-pipe zone for the 55.3-MTU/acre case: (1) the duration of refluxing conditions (i.e., high liquid-phase flux and high liquid

saturation) is nearly the same as in the higher AML cases and (2) the heat-pipe zone remains close to the repository. Both of these conditions increase the likelihood (relative to the higher AML cases) that significant decay-heat-driven alteration of flow and transport properties will occur in the vicinity of the repository. This observation also applies to the edge of a high-AML repository because edge-cooling/rewetting/shedding effects may prevent the heat-pipe zone at the repository edge from being displaced far away from the repository horizon.

Figure 10.1.2.1.4 shows the vertical temperature and saturation profiles for the 70-MTU/acre case. The thermal and dryout behavior are similar to that of the 83.4-MTU/acre case except that the vertical extent of boiling and dryout effects is halved. Moreover, the duration of boiling and sub-ambient liquid saturation conditions is somewhat less for the 70-MTU/acre case than for the 83.4-MTU/acre case [Buscheck and Nitao, 1994]. Liquid saturation for the inner half of the repository has not rewetted to ambient conditions at 30,000 yr (Fig. 10.1.2.1.4h); at the edge, liquid saturation has rewetted to ambient liquid saturation within 10,000 yr (Fig. 10.1.2.1.4g).

Figure 10.1.2.1.5 shows the vertical temperature and saturation profiles for the 110.5-MTU/acre case. The thermal and dryout performance are very similar for the 0 and 50% radial positions of the repository for the first thousand years ,and edge-cooling effects influence at least the outer 5% of the repository. The heat-pipe zone (the zone of near-boiling temperatures above the repository) has a greater length and gets 75 m closer to the ground surface than in the 83.4-MTU/acre case (compare Figs. 10.1.2.1.1 and 10.1.2.1.5). Dryout due to boiling results in a 200- to 300-m-thick dryout zone for the inner 50% of the repository. Edge-cooling effects substantially reduce the vertical extent of dryout in the outer region of the repository. Temperatures at the outer edge of the repository drop below boiling at about 2000 yr, while the center remains above T_b for more than 7000 yr. Temperatures for the entire repository have declined to below T_b within 7000 yr; however, a large zone of less-than-ambient saturations persists long after that (Figs. 10.1.2.1.5g and h). The outer 5% of the repository rewets back to ambient saturation within 30,000 yr, while the center remains below ambient saturation for more than 100,000 yr.

The spatial and temporal extent of boiling and dryout effects are substantially greater for the 110.5-MTU/acre case than for the 83.4-MTU/acre case. Likewise, the spatial and temporal extent of these effects are much greater for the 83.4-MTU/acre case than for the 70-MTU/acre case. Therefore, for relatively high AMLs, mountain-scale T-H behavior depends strongly on AML. Moreover, the heat-pipe zone is displaced further away from the repository horizon for the 110.5-MTU/acre case than for the 83.4-MTU/acre case. Edge-cooling/rewetting/shedding effects will probably have less of an impact on the edge of a 110.5-MTU/acre repository than for the edge of a 83.4-MTU/acre repository. Wide drift spacing will encourage more drift-scale condensate shedding (i.e., condensate shedding that occurs in the rock pillar between drifts), which will decrease the amount of condensate that can be displaced to the edge of the repository (see Section 1.10.6); this would lessen the contribution of edge-shedding to the liquid-phase flux at the edge of the repository, thereby lessening the impact on heat pipes at the repository edge.

10.1.2.2 Boiling-Driven and Buoyancy-Driven Vapor and Heat Flow. If the bulk permeability, k_b, of the fractured rock mass is large enough, repository heat can lead to the development of large-scale, buoyant convection cells transporting water vapor from regions below the repository to regions above. These cells also have the potential to redistribute heat within the mountain and reduce temperatures in the repository as well as in the altered zone. We conducted a mathematical analysis and a numerical modeling study [Buscheck and Nitao, 1994] to determine the conditions under which these effects may be significant.

Mountain-scale, buoyant, gas-phase convection occurs within fracture networks having a connectivity with length scale comparable to the UZ thickness and repository width (Fig. 10.1.1b). For the modeling study we used the mountain-scale, UZ-SZ model, and considered a wide range of k_b values and AMLs, including 27.1, 49.2 (the reference SCP-CDR thermal load), and 154.7 MTU/acre. We analyzed these effects for (1) a homogeneous and isotropic k_b distribution, and (2) a layered, heterogeneous k_b distribution. Because the matrix permeability is so small for most of the UZ, differences in k_b reflect differences in fracture permeability. We begin with a discussion of the mathematical analysis.

As repository heat propagates into the rock, a column of warmer, less-dense gas develops that encompasses the repository area (see Fig. 10.1.1b). The result is that gas-phase pressures, especially those

at the lowest portion of the column, are lowered relative to those at the same depth in the cooler, denser column of gas outside the repository footprint. Consequently, gas from outside the repository footprint is drawn into the region below the repository and flows upward through the repository, in a fashion similar to the updraft in a chimney. Buoyant, gas-phase convection cells develop as the warmer, less-dense column of gas within the repository footprint is displaced by the cooler, denser gas from outside the repository footprint. As the initially cooler gas is heated, its relative humidity is lowered, causing it to evaporate water from the rock matrix below the repository. This warm moist air is convected upward to where it cools above the repository, generating condensate that drains down fractures back toward the repository and/or is imbibed by the matrix, causing a saturation buildup above the repository. Because water removed below the repository may be replenished by water imbibed from the SZ, this process can result in a net buildup of liquid water in the UZ. For large enough k_b, mountain-scale, buoyant, vapor flow can dominate moisture movement on the order of 100,000 yr (see Table 10.1.1).

Under sub-boiling conditions, this phenomenon always occurs and is significant unless the k_b is very small. Under boiling conditions, steam generation causes a gas pressure buildup that can dominate the buoyancy forces, thereby suppressing large-scale buoyant convection cells. For either large k_b, or as boiling diminishes, the gas pressure buildup may not be sufficient to suppress buoyancy, and convection cells form. As these cells develop, they can transport steam (or moist air) from below the repository to the condensation zone above.

For buoyant convection cells to dominate over the boiling-generated, gas-phase pressure buildup, k_b must be larger than a threshold bulk permeability for moisture movement, $k_b > k_b^{buy}$, where k_b^{buy} is given by

$$k_b^{hyd} = \frac{q_H}{h_{fg}\rho_s}\,\frac{L_b}{L}\,\frac{T_{amb}}{\Delta T_{av}}\,\frac{\mu_g}{\rho_{g,amb}g} \tag{4}$$

where

q_H is the instantaneous areal heat load (W/m^2),

h_{fg} is latent heat of vaporization (J/kg),

ρ_s is steam density (kg/m^3),

$\rho_{g,amb}$ is mean gas-phase density under ambient conditions (kg/m^3),

L_b is thickness of the boiling zone around the repository (m),

L is thickness of the thermally perturbed zone (m),

T_{amb} is the mean ambient unsaturated zone temperature (K),

ΔT_{av} is the mean vertical change in temperature from ambient (K),

μ_g is gas-phase viscosity (kg/m-s), and

g is gravity acceleration (m/s^2).

Large-scale, buoyant convection cells will reduce repository temperatures when gas-phase convective heat flow through the repository domain is significant compared to the areally averaged heat load. This condition occurs when k_b is sufficiently large, that is, $k_b > k_b^{th}$, where the threshold bulk permeabilityf for thermal effects, k_b^{th}, is given by

$$k_b^{th} = \frac{q_H}{h_g\rho_g}\,\frac{T_{amb}}{\Delta T_{av}}\,\frac{\mu_g}{\rho_{g,amb}g} \tag{5}$$

Here, h_g is specific enthalpy of the gas phase (J/kg), and ρ_g is the gas-phase density (kg/m^3). Because q_H is a function of time, the threshold permeabilities are functions of time. Effective values of q_H, averaged over time, should be applied in making estimates of k_b^{hyd} and k_b^{th}.

The critical bulk permeabilities, k_b^{buy} and k_b^{th}, are proportional to the repository heat load, q_H, and inversely proportional to the average increase in temperature, ΔT_{av}. The latter term depends on q_H and is approximately proportional to q_H under sub-boiling conditions so that increasing q_H only weakly affects

k_b^{in}. Therefore, under sub-boiling conditions, the likelihood of buoyant, gas-phase convection impacting repository temperatures is relatively insensitive to AML. Note that k_b^{uyu} is not applicable to sub-boiling conditions. Under above-boiling conditions, the term ΔT_{av} depends weakly on q_H because most of the energy goes toward latent heat of boiling. Therefore, under boiling conditions, the critical bulk permeabilities, k_b^{uyu} and k_b^{in}, are approximately proportional to q_H. Because higher AMLs increase the critical bulk permeabilities for both moisture and heat flow, the likelihood of buoyant, gas-phase convection cells dominating moisture and heat flow is reduced.

Because $\rho_s h_{fg} \approx \rho_g h_g$, the following approximate relationship holds:

$$k_b^{hyd} \approx \frac{L_b}{L} k_b^{th} \tag{6}$$

and, therefore,

$$k_b^{hyd} < k_b^{th} \tag{7}$$

Values of k_b that are large enough for large-scale, buoyant convection to affect repository temperatures will also be large enough to affect the large-scale movement of water vapor produced by boiling. Conversely, if k_b is small enough for the large-scale movement of water vapor to be negligible, then large-scale, buoyant convection cells will not be significant enough to reduce repository temperatures. Although this method of analysis is approximate, it gives a good order-of-magnitude estimate of critical bulk permeabilities that have been verified by numerical simulations.

As an example, we consider a repository with $q_H = 14.1$ W/m^2, which is equivalent to an APD of 57 kW/acre. We use $T_{amb} = 300$°K and $\Delta T_{av} = 50$°K. Values for ρ_s, h_g, and h_{fg} were taken at conditions for saturated water vapor at a temperature of 95°C. The values for the lengths were $L = 400$ m and $L_b = 20$ m. We then obtain $k_b^{hyd} = 0.7$ darcy, and $k_b^{th} = 14$ darcy.

Buscheck and Nitao [1993b] found that mountain-scale, buoyant, gas-phase convection does not influence temperatures at the repository center until after they peak. Depending on the AML and k_b, the cooling effect of mountain-scale, buoyant, gas-phase convection can substantially reduce the duration of the boiling period, t_{bp}, in the repository. Depending on the proximity to the outer edge of the repository, edge-cooling effects can also substantially reduce t_{bp}. The details of how edge-cooling effects influence t_{bp} throughout the repository are described later in this section [Buscheck et al., 1994].

Influence of Buoyant Gas-Phase Convection on the Duration of Boiling Conditions in the Repository Rock

Figure 10.1.2.2.1 shows the area-weighted boiling period duration, t_{bp}, as a function of k_b for the 49.2- and 154.7-MTU/acre cases. Because t_{bp} is the boiling period duration averaged over the entire repository area, and the mountain-scale model assumes a uniform AML, t_{bp} effectively represents conditions in the repository rock at an average location in the repository. For $k_b < k_b^{in}$, t_{bp} is insensitive to k_b. For an AML of 154.7 MTU/acre, k_b^{in} is about 5 darcy, while for 49.2 MTU/acre, it is about 1 darcy. For $k_b > k_b^{in}$, t_{bp} decreases with increasing k_b. The cooling effect of mountain-scale, buoyant, gas-phase convection increases with proximity to the edge of the repository.

Relative to the 1-millidarcy case, increasing k_b to 1 darcy only reduces t_{bp} by 2.4% for an AML of 154.7 MTU/acre, while for 49.2 MTU/acre, it is reduced by 19.7% (Fig. 10.1.2.2.1). Increasing k_b to 5 darcy reduces t_{bp} by 11.4% for an AML of 154.7 MTU/acre, while for 49.2 MTU/acre, the reduction is 48.9%. Consistent with Equation (5), boiling behavior for the 49.2-MTU/acre repository was found to be more sensitive to mountain-scale, buoyant, gas-phase convection than for the 154.7-MTU/acre repository. The boiling-generated, gas-phase pressure buildup increases with AML, and it opposes the tendency for thermal buoyancy for some period of time [Buscheck and Nitao, 1993b].

Figures 10.1.2.2.2a-c show the duration of the boiling period, t_{bp}, as a function of repository location for the 110.5-, 83.4-, and 55.3-MTU/acre cases and all of the values of k_b considered. The influence of edge cooling is evident. Mountain-scale, buoyant, gas-phase convection begins to significantly reduce repository temperatures for $k_b > 1$ darcy. For $k_b \leq 1$ darcy, t_{bp} is insensitive to k_b. Notice that the sensitivity of t_{bp} to k_b increases with decreasing AML.

Figure 10.1.2.2.2d shows the area-weighted boiling period duration, t_{bp}, for various k_b values as a function of AML. For the 280-millidarcy cases, t_{bp} is 5450, 3390, and 1420 yr for AMLs of 110.5, 83.4, and 55.3 MTU/acre, respectively. The cooling effect that mountain-scale, buoyant, gas-phase convection has on t_{bp} increases with decreasing AML. Accordingly, the 110.5-MTU/acre case is least sensitive to this effect.

Influence of Buoyant Gas-Phase Convection on Mountain-Scale Moisture Redistribution

We compared the net buildup of liquid water above the repository, ΔV_l, for a wide range of AML and values of k_b analyzed by Buscheck and others [1994] (Fig. 10.1.2.2.3). For the high-k_b, high-AML cases (10, 40, and 84 darcy; 83.4 and 110.5 MTU/acre), a very early peak in ΔV_l occurs at 500 to 800 yr (Figs. 10.1.2.2.3c–e), coinciding with the maximum extent of boiling conditions. After the initial peak, ΔV_l declines for the high-k_b, high-AML cases, with a trough occurring at 3000 yr, coinciding with the maximum vertical extent of dry-out. For 110.5 MTU/acre, ΔV_l declines to below zero (Figs. 10.1.2.2.3d and e). For 83.4 MTU/acre, the trough is less pronounced as ΔV_l stays well above zero (Figs. 10.1.2.2.3c–e). After the trough occurs in the 83.4- and 110.5-MTU/acre cases, the increase in ΔV_l resumes until a second peak in ΔV_l occurs at around 20,000 to 30,000 yr. For the 55.3-MTU/acre case, there is no trough, and the increase in ΔV_l is uninterrupted (Figs. 10.1.2.2.3a–e). For 10, 40, and 84 darcy, the 55.3-, 83.4-, and 110.5-MTU/acre cases undergo the same initial rate of increase in ΔV_l until 500 yr, when the 110.5-MTU/acre case reaches its initial peak, and 800 yr, when the 83.4-MTU/acre case reaches its initial peak (Figs. 10.1.2.2.3c–e). This initial peak is related to the interaction of the heat-pipe effect and mountain-scale, buoyant, gas-phase convection.

It can be seen that ΔV_l is always greater in the 55.3- and 83.4-MTU/acre cases than in the 110-MTU/acre case. We plot the maximum ΔV_l (called ΔV_l^{max}) for all of the AMLs and values of k_b considered (Fig. 10.1.2.2.3f). For 55.3 MTU/acre, ΔV_l^{max} is 1.5, 1.3, 2.4, 2.6, and 2.5 times greater than in the 110.5-MTU/acre case for 280 millidarcy and 1, 10, 40, and 84 darcy, respectively. For 83.4 MTU/acre, ΔV_l^{max} is 1.5, 1.7, 1.4, 1.4, and 1.5 times greater than in the 110.5-MTU/acre case for 280 millidarcy and 1, 10, 40, and 84 darcy, respectively. To the first order, for intermediate to high AMLs, ΔV_l^{max} is proportional to the repository area if k_b is large enough ($k_b > 1$–10 millidarcy) for unthrottled advective dryout to dominate (see Section 1.8.5).

If the large-scale connected k_b is small enough, mountain-scale, buoyant, gas-phase convection does not result in a liquid water buildup above the repository. For intermediate k_b ($k_b < 110$ darcy), for which buoyant gas-phase convection does not dominate vapor flow, the cumulative effects of vapor flow and condensate buildup depend on the magnitude of boiling effects. Because low AMLs generate less boiling-driven dryout, there is less net liquid water buildup than the high AMLs, which generate more boiling-driven dryout. Because buoyant gas-phase convection governs dryout effects for high enough k_b ($k_b > 40$ darcy), ΔV_l^{max} is proportional to the repository area. Although buoyancy forces are less per unit area (of repository) for a low-AML repository than for a high-AML repository, these forces are integrated over the larger area of the low-AML repository, which results in the roughly the same overall magnitude of buoyancy-driven dryout and condensate buildup effects.

We also compared the net buildup of liquid water above the repository, ΔV_l, for all of the AMLs and values of k_b considered by Buscheck and Nitao [1994]. For an AML of 27.1 MTU/acre and $k_b < 280$ millidarcy, mountain-scale, buoyant, gas-phase convection results in a very small net change to the liquid saturation distribution (Fig. 10.1.2.2.4b); however, significant refluxing occurs, with buoyant vapor flow being balanced by condensate drainage and imbibition. For $k_b > 280$ millidarcy, condensate drainage and imbibition cannot keep up with buoyant vapor flow, and regions of net dryout below the repository and condensate buildup above develop and persist for tens of thousands of years. With the ECM, we cannot

determine whether the resulting condensate flux results in nonequilibrium fracture flow down to the repository horizon (and possibly down to the water table). However, the potential for nonequilibrium condensate drainage exists even for situations that do not result in a net redistribution of liquid saturation. *In situ* thermal tests that are of sufficient size and duration are needed to determine the potential for mountain-scale, buoyant, vapor flow to drive nonequilibrium condensate drainage in the vicinity of WPs [Buscheck et al., 1993a; Buscheck et al., 1993b; Buscheck and Nitao, 1995].

For an AML of 27.1 MTU/acre, ΔV_l increases gradually until it peaks, and declines even more gradually (Fig. 10.1.2.2.4a). A substantial ΔV_l persists well beyond 100,000 yr for the high-k_b cases. The peak ΔV_l occurs at 20,000, 20,000, 30,000, 40,000, and 40,000 yr for the 168-, 84-, 40-, 20-, and 10-darcy cases, respectively (Figs. 10.1.2.2.4a and b). For the 280-millidarcy case (Fig. 10.1.2.2.4b), the peak occurs beyond 100,000 yr. For $k_b \geq 10$ darcy, the maximum ΔV_l (called ΔV_l^{max}) increases nearly linearly with k_b. Because it cannot represent nonequilibrium fracture-matrix flow, the ECM probably underpredicts the condensate drainage flux and, consequently, may overpredict ΔV_l. However, ΔV_l is a useful indicator of the overall magnitude of condensate drainage and buildup effects. The slope of the ΔV_l vs t curve is indicative of the overall rate of condensate generation that arises from mountain-scale, buoyant, vapor flow. For high AMLs, it is indicative of the competition between vapor flow driven by the gas-pressure buildup due to boiling and vapor flow driven by thermal buoyancy.

For an AML of 49.2 MTU/acre, ΔV_l increases gradually until it peaks, and declines even more gradually (Fig. 10.1.2.2.4c). A substantial ΔV_l persists well beyond 100,000 yr for the high-k_b cases. The peak ΔV_l occurs at 20,000, 15,000, 15,000, 10,000, 6600, 5000, and 1300 yr for the 168-, 84-, 40-, 20-, 10-, 5-, and 1-darcy cases, respectively (Figs. 10.1.2.2.4c and d). For the 280- and 10-millidarcy cases, the ΔV_l peak occurs at 1000 yr (Fig. 10.1.2.2.4d). For AMLs of 27.1 and 49.2 MTU/acre, ΔV_l is never less than zero.

For an AML of 154.7 MTU/acre, the high-k_b cases ($k_b > 5$ darcy) show two peaks in the ΔV_l curve, with an early peak occurring at 300 to 500 yr and a late peak occurring beyond 20,000 yr (Fig. 10.1.2.2.4e). For the 1-darcy case, the early and late peaks occur at 900 and 20,000 yr, respectively (Fig. 10.1.2.2.4f). The early peak approximately coincides with the maximum vertical extent of boiling conditions and is related to the interaction of the heat-pipe effect and mountain-scale, buoyant, gas-phase convection. After the initial peak, ΔV_l quickly declines for the high-k_b cases, with a trough occurring at 3000 yr, coinciding with the maximum vertical extent of dryout. For the 40-, 84-, and 168-darcy cases, ΔV_l declines to below zero. After the trough occurs, ΔV_l resumes a gradual increase until a late peak occurs. This peak occurs at 60,000, 50,000, 50,000, and 25,000 yr for the 168-, 84-, 40-, and 5-darcy cases, respectively. For 10 millidarcy $< k_b <$ 1 darcy, there is no early peak in ΔV_l and a late peak occurs at 20,000 yr (Fig. 10.1.2.2.4f). For $k_b \leq$ 10 millidarcy, after a brief early period with very small positive values, ΔV_l is always negative (Fig. 10.1.2.2.4f). Therefore, if the large-scale connected k_b is small enough, mountain-scale, buoyant, gas-phase convection does not result in a liquid water buildup above the repository for the 154.7-MTU/acre case.

Figure 10.1.2.2.5 shows the ΔV_l^{max} as a function of k_b for AMLs of 27.1, 49.2, and 154.7 MTU/acre. Notice that the shape of this curve varies significantly among the various AML cases. For an AML of 154.7 MTU/acre, the slope of the curve is nearly constant, with ΔV_l^{max} increasing gradually with k_b. The dependence of ΔV_l^{max} on k_b is very nonlinear for AMLs of 27.1 and 49.2 MTU/acre. For small k_b, the slope is very shallow. For an AML of 49.2 MTU/acre, the slope increases abruptly at $k_b = 1$ darcy, while for 27.1 MTU/acre, it increases abruptly at 10 darcy.

Over the range of 1 millidarcy to 168 darcy, the following observations can be made from Fig. 10.1.2.2.5. Where the impact of mountain-scale, buoyant, gas-phase convection is greatest, low-to-intermediate AMLs result in the largest ΔV_l^{max}. For intermediate k_b (280 millidarcy to 1 darcy), where the impact of mountain-scale, buoyant, gas-phase convection is relatively moderate, ΔV_l^{max} for the various AML cases generally varies by less than a factor of 2.

It is likely that the k_b distribution at Yucca Mountain will be highly variable. Some of that variability will be random, while some may be correlated with discrete hydrological features such as fault zones or hydrostratigraphic units like the nonwelded vitric tuff units (PTn and CHnv). If the k_b distribution spans a significant fraction of the range shown in Fig. 10.1.2.2.5 (including regions in which $k_b > 10$ darcy), then mountain-scale hydrothermal behavior will be more variable for low-to-intermediate AMLs than for high

AMLs. If the k_b distribution only spans the lower end of the k_b range ($k_b < 1$ darcy), then mountain-scale hydrothermal behavior will be less variable for all AMLs.

Because the ECM cannot represent nonequilibrium fracture-matrix flow, it underpredicts the condensate drainage flux and, consequently, overpredicts ΔV_l. However, ΔV_l is a useful indicator (or surrogate) of the overall magnitude of condensate drainage flux and saturation buildup effects. The slope of the ΔV_l vs t curve is indicative of the overall rate of condensate generation that arises from mountain-scale, buoyant vapor flow. For high AMLs, it is indicative of the competition between vapor flow driven by the gas-pressure buildup due to boiling, and vapor flow driven by thermal buoyancy.

The purpose of these mountain-scale calculations is to illustrate the general sensitivity of large-scale T-H behavior to a wide range of conditions through the use of macroscopic parameters such as t_{bp}, ΔV_l, and ΔV_l^{max}. Moreover, these parameters are indicative of the magnitude of liquid-phase flux (particularly occurring in fractures) that may give rise to aqueous reactions and aqueous-transport processes that can alter the flow and transport properties in fractures. Any attempt to make specific inferences of this behavior on WP performance and radionuclide transport would require a far more detailed look at the spatial distribution of the decay-heat-driven changes to temperatures, liquid saturations, and vapor and liquid fluxes (as is done in Section 1.10.5 of Chapter 1) than can be addressed with the mountain-scale models alone.

10.1.2.3 Influence of Layered Heterogeneous Bulk Permeability Distribution on Buoyancy-Driven Vapor and Heat Flow. We also considered cases in which the k_b distribution varies vertically, which results in a layered heterogeneous k_b distribution. This is applicable in light of recent data analysis [Bodvarsson et al., 1996], which indicates considerable layering of k_b. In particular, it appears that k_b may be far smaller in the nonwelded vitric units (PTn and CHnv) and the nonwelded zeolitized unit (CHnz) than in the welded units (TCw, TSw1, TSw2, and TSw3). For AMLs of 27.1 and 154.7 MTU/acre, we considered four k_b distributions:

(1) k_b = 84 darcy everywhere.

(2) k_b = 320 millidarcy in the PTn; otherwise, k_b = 84 darcy.

(3) k_b = 280 millidarcy in the CHn; otherwise, k_b = 84 darcy.

(4) k_b = 320 millidarcy in the PTn and 280 millidarcy in the CHn; otherwise, k_b = 84 darcy.

Figure 10.1.2.3.1 shows the net buildup of liquid water above the repository, ΔV_l, for these four cases. For the 27.1-MTU/acre repository, a reduced k_b in the PTn reduces ΔV_l by half (Fig. 10.1.2.3.1a). For the uniform-k_b case, mountain-scale, buoyant, gas-phase convection behaves as though it is in an "open" system with respect to the ground surface. In this open system, the gas-phase velocity vectors are orthogonal to the ground surface in the vicinity of the ground surface. Buoyant vapor flow results in a substantial increase in liquid saturation from the repository horizon all the way to the ground surface. When k_b in the PTn is reduced, this unit functions as a gas-phase flow barrier or "vapor cap." Consequently, the direction of gas-phase flow below the PTn/TSw1 contact becomes tangential to this contact rather than crossing it. The PTn effectively isolates the buoyant, gas-phase, convection cells from the ground surface, thereby causing the convective system to be "closed" with respect to the ground surface. The resulting decrease in the gas-phase flow velocities causes an overall reduction in ΔV_l (Fig. 10.1.2.3.1a).

For the 154.7-MTU/acre repository, a reduced k_b in the PTn has a much different effect on ΔV_l (Fig. 10.1.2.3.1b). As in the 27.1-MTU/acre case, the reduced k_b in the PTn causes the buoyant convective system to be closed with respect to the ground surface, reducing the magnitude of gas-phase flow. The resulting decrease in the gas-phase flow velocities reduces the initial peak in ΔV_l by 40% (Fig. 10.1.2.3.1b). Recall that for the high-k_b cases (Fig. 10.1.2.2.3d,e and 10.1.2.2.4e), we observed an initial peak in ΔV_l at about 300 to 500 yr, followed by a steep decline (and trough) in the ΔV_l curve. The steep decline arises from buoyant convection driving water vapor to the ground surface. Figure 10.1.2.3.1b clearly indicates that an open convective system driven by a high-AML repository results in a substantial loss of water vapor to the atmosphere. However, an open convective system driven by a low-AML repository does not result in such a loss. The key difference is that boiling in the high-AML case drives most of the moisture buildup to the upper 100 m of the unsaturated zone (UZ), while for the low-AML case, the moisture

buildup is spread over the upper 340 m of the UZ. Proximity of the moisture buildup to the ground surface, and larger gas-phase velocities, facilitate the loss of moisture to the atmosphere for the high-AML case. When the PTn acts as a vapor cap, the loss of moisture to the atmosphere is impeded, trapping much of the moisture convected to the upper UZ. Consequently, the trough in the ΔV_1 curve is less pronounced, and the following increase in ΔV_1 is steeper (Fig. 10.1.2.3.1b).

For the 154.7-MTU/acre repository, the reduced k_b in the PTn causes the second peak in the ΔV_1 curve to occur much earlier (15,000 yr) than in the uniform-k_b case (50,000 yr). The earlier occurrence of the second peak is caused by the gas-phase diffusive loss of moisture to the atmosphere. Note that the value assumed for the effective diffusion factor, τ_{eff} ($\tau_{eff} = 0.2$), may be low compared to experimental values measured by soil physicists (see Section 10.1.3.2). A larger value of τ_{eff} would result in a larger diffusive loss of moisture to the atmosphere and an overall reduction in ΔV_1.

For the 27.1-MTU/acre repository, a reduced k_b in the CHn reduces ΔV_1 by half, which is almost identical to the effect that a reduced-k_b PTn has on ΔV_1 (Fig. 10.1.2.3.1a). The reduction in k_b in the CHn impedes buoyant flow through it, effectively decoupling it from the mountain-scale, buoyant convective system. The resulting reduction in the vertical extent of the buoyant convective system has the effect of reducing the gas-phase velocities and the quantity of water that can be vaporized and convected from below the repository to above, where it condenses. Reducing k_b in both the PTn and CHn reduces ΔV_1 by another factor of 2 relative to the case with the reduced k_b in the PTn (Fig. 10.1.2.3.1a).

For the 154.7-MTU/acre repository, a reduced k_b in the CHn reduces ΔV_1 by nearly half (Fig. 10.1.2.3.1b), which is similar to the effect shown for the 27.1-MTU/acre repository (Fig. 10.1.2.3.1a). Reducing k_b in both the PTn and CHn reduces ΔV_1 by nearly half relative to the case with the reduced k_b in the PTn (Fig. 10.1.2.3.1a). Figure 10.1.2.3.2 shows the impact that a reduced k_b in the PTn and CHn has on the boiling period duration, t_{bp}. The reduction in gas-phase velocities decreases the overall convective cooling effect, thereby increasing t_{bp}, particularly at the outer repository area.

10.1.2.4 Sub-Repository-Scale, Boiling-Driven and Buoyancy-Driven Vapor and Heat Flow. Sub-repository-scale (or drift-scale), buoyant, gas-phase convection occurs within fracture networks having a connectivity with length-scale comparable to the distance between the hot and cold regions of the repository (see Fig. 10.1.1a). Buoyant, gas-phase convection cells develop as the warmer, less-dense column of gas within the footprint of the waste packages (WPs) is displaced by the cooler, denser column of gas in the adjacent areas. As the initially cooler gas is heated up, its relative humidity is lowered, causing it to evaporate water from the rock matrix below hot regions of the repository. This warm moist air is convected upward to where it cools above the WPs. This generates condensate that drains down fractures back toward the repository and/or is imbibed by the matrix, causing a saturation buildup above the WPs. High AMLs result in a large zone of above-boiling temperatures, which suppresses the effects of sub-repository-scale, buoyant vapor flow [Buscheck and Nitao, 1993]. Sub-repository-scale, buoyant, gas-phase convection continues as long as significant temperature differences persist within the repository. It can dominate moisture movement for up to 1000 yr for the drift spacing described in the SCP–CDR [SNL, 1987].

More recently, there has been considerable momentum toward the use of larger WPs contains more fuel assemblies, and therefore have a higher thermal output per WP. Larger drift spacing, which is consistent with the use of larger WPs, will result in temperature differences within the repository persisting longer. Consequently, the effects of sub-repository-scale, buoyant vapor flow (if important) will also be more persistent, possibly lasting thousands of years [Buscheck et al., 1994].

Buscheck and others [1994] analyzed sub-repository-scale performance for large WPs containing either 21 PWR or 40 BWR spent nuclear fuel (SNF) assemblies with a center-to-center WP spacing of 12 m. These calculations also apply to a 12-PWR/21-BWR SNF emplacement scenario with a center-to-center WP spacing of 6.86 m. An important observation from that study concerns the substantial difference between thermal-hydrological performance predicted by mountain-scale models and that predicted by drift-scale models. For an AML of 24.2 MTU/acre, the repository-scale model predicts a peak temperature, T_{peak}, of 65°C, while the drift-scale model predicts T_{peak} of up to 172°C on the WP surface and 144°C in the rock adjacent the drift. While the repository-scale model predicts no boiling period, the drift-scale model predicts a boiling period duration, t_{bp}, of 180 to 200 yr in the rock and 300 to 350 yr on

the WP surface. Similarly, the repository-scale model predicts no boiling period for an AML of 35.9 MTU/acre, while the drift-scale model predicts t_{bp} of 960 to 1010 yr in the rock and 1110 to 1160 yr on the WP surface.

Another important observation about sub-repository-scale performance is that T_{peak} varies modestly for AMLs ranging from 24.2 to 55.3 MTU/acre [Buscheck et al. 1994]. Because it occurs so early (12 to 25 yr), T_{peak} is insensitive to whether the distance to the adjacent emplacement drift is 43.4 m or 99.0 m. For the high-AML cases, the drift spacing is small enough to cause T_{peak} to be sensitive to drift spacing. Consequently, T_{peak} is significantly greater for the 110.5-MTU/acre case than for the 83.4-MTU/acre case [Buscheck et al. 1994].

The boiling-period duration t_{bp} is insensitive to sub-repository-scale, buoyant, gas-phase convection for both the low- and high-AML cases (24.2, 35.9, and 110.5 MTU/acre). For intermediate-AML cases (55.3 and 83.4 MTU/acre), t_{bp} is modestly sensitive. For high AMLs, the extent of dryout is insensitive to sub-repository-scale, buoyant, gas-phase convection. For low AMLs, the extent of moisture movement (i.e., dryout and condensate buildup) is very dependent on the magnitude of sub-repository-scale, buoyant, gas-phase convection.

Some have equated the term "sub-boiling repository" with a repository system for which the hydrological impact of heat is insignificant. Some also define a "sub-boiling repository" to be one in which the average repository temperature is below the boiling point. Our analyses show that boiling conditions can persist around an emplacement drift even if the average repository temperature is well below boiling. Moreover, if buoyant, gas-phase convection is found to be significant, it can drive substantial vapor and condensate fluxes (over a very extensive region of the UZ) whether or not boiling ever occurs. Buoyancy-driven T-H effects can extend from the water table all the way to the ground surface, possibly resulting in coupled T-H-C processes that alter the flow and transport properties over a comparable region. On the other hand, if buoyant, gas-phase convection is found to be insignificant, a boiling period of sufficiently limited duration may be shown to generate condensate fluxes that result in coupled T-H-C processes that alter flow and transport properties over a much smaller region. The absence of local boiling conditions is not, in itself, an adequate indicator of whether repository heat drives significant vapor and condensate flow. Average repository temperatures are an even poorer indicator of whether decay-heat-driven alteration of flow and transport properties have a negligible effect on the performance of a low-AML repository. Diagnosing whether sub-boiling conditions can be equated with the absence of significant decay-heat-driven effects will require *in situ* thermal tests that are of sufficient size and duration [Buscheck et al., 1993a, 1993b; Buscheck and Nitao, 1995].

10.1.2.5 Heterogeneity-Enhanced Heat-Pipe Behavior. Refluxing, or the heat-pipe effect, is important to consider because it can affect coupled T-H-M-C processes (that may alter flow and transport properties) in two ways. First, refluxing maintains local temperatures near the boiling point, making it more difficult to dry the rock out. Consequently, the liquid saturation and relative humidity *RH* remain high, increasing the likelihood of aqueous reactions and aqueous-transport processes occurring. Second, refluxing can generate a very high liquid-phase flux in fractures, which can results in significant dissolution and precipitation of minerals along the fracture walls.

To investigate the impact of heterogeneity on the focusing of vapor flow and condensate drainage (and how that focusing affects the development of heat pipes in the near field and altered zone), we used a cross-sectional drift-scale model and a cross-sectional uniform heat flow (CSUHF) model [Buscheck and Nitao, 1994]. Both models are used to investigate the effect of lateral variability of k_b. In particular, we consider the situation in which k_b in vertically contiguous high-k_b zones is much larger than k_b throughout the rest of the fractured rock (the nominal-k_b zones). These models specifically address how focused condensate drainage might arise from gas-phase focusing. Recent analytical work by Nitao and Bradford [1996] addresses how focused condensate drainage might arise from liquid-phase focusing.

The degree of vapor flow focusing into the high-k_b zone, and the resulting duration of refluxing at the repository horizon (as well as in the altered zone in general), depends on three factors. First, k_b in the nominally fractured zone must be large enough not to significantly throttle the rate of vapor generation due to boiling (or due to evaporation under sub-boiling conditions). Second, a large contrast in k_b between the high- and nominal-k_b zones results in a gas-phase pressure differential between these zones

that preferentially drives vapor flow into the high-k_b zone (Fig. 10.1.1c). If enough vapor enters and condenses in the high-k_b zone, the return condensate flux will be large enough to maintain refluxing at the repository horizon, possibly resulting in water dripping onto WPs. Third, there must be sufficient spacing between the high-k_b zones to drive enough water vapor into these zones to result in the local condensate drainage flux being substantially greater than the mean condensate flux. Effectively, the high-k_b zones are competing for a finite quantity of vapor flow and condensate generation. Consequently, there is a trade-off between the duration of refluxing and the number of locations where it can occur in the repository. If there are too many such zones, there will be insufficient condensate focusing to cause persistent refluxing at the repository horizon. The degree of focusing necessary to cause persistent refluxing limits the number of locations where it can occur. Therefore, it is unlikely that refluxing can dominate the overall thermal behavior in the repository (or throughout the altered zone).

Figure 10.1.2.5.1 shows the effect of focused vapor and condensate flow on the normalized liquid saturation, S_l, distribution [see Eq. (8)] in the vicinity of an emplacement drift containing 30-yr-old SNF with an AML of 154.7 MTU/acre for two cases of a heterogeneous k_b distribution. The normalized liquid saturation, $\bar{S}_l$, which is given by

$$\bar{S}_l = \frac{S_l}{S_{l,\text{init}}} \tag{8}$$

where S_l is the current liquid saturation and $S_{l,\text{init}}$ is the initial (or ambient) liquid saturation. For both cases, 1.6-m-wide, 84-darcy, high-k_b zones alternate with 36.8-m-wide, 10-millidarcy, nominal-k_b zones. For the first case of k_b heterogeneity (Figs. 10.1.2.5.1a–c), the high-k_b zones are vertically aligned along the axis of the emplacement drifts. For the second case of k_b heterogeneity (Figs. 10.1.2.5.1d–f), the high-k_b zones are vertically aligned along the midline of the pillar separating emplacement drifts. For the first case, we also considered an AML of 49.2 MTU/acre for 10-yr-old SNF (Figs. 10.1.2.5.2a–c) and 20-yr-old SNF (Figs. 10.1.2.5.2d–e).

For the first case of k_b heterogeneity, the gas-phase pressure differential between the high- and nominal-k_b zones drives water vapor back toward the drift and into the high-k_b zone (Figs. 10.1.2.5.1a and b). Water vapor flows up the high-k_b zone until it condenses and drains back down. In effect, the emplacement drift functions as a manifold that enhances the gas-phase communication between the high- and nominal-k_b zones. If enough water vapor enters and condenses in this zone, the condensate drainage flux will be large enough to maintain refluxing in the repository. The resulting heat-pipe effect enables the temperature at the top of the drift to remain at the boiling point, causing a depression in the dryout zone (Figs. 10.1.2.5.1a). In spite of persistent refluxing, the temperatures along most of the remainder of the drift wall, the air in the drift, and the WP itself are well above boiling. Therefore, although liquid water may be dripping in the drift, *RH* around the WP can still be low. This situation creates very large gradients in temperature, liquid saturation and *RH*, all of which need to be considered in assessing the potential for coupled T-H-M-C processes.

The heat-pipe zone attracts heat flow (mainly by conduction) from the neighboring, nominal-k_b rock. In effect, the heat-pipe zone functions as a "cooling fin" that is manifested by an elongated region of liquid saturation buildup (Fig. 10.1.2.5.1). The process of gas-phase focusing into the heat-pipe zone develops more quickly than the process of attracting heat from the neighboring rock. Within 8.5 yr, enough heat is being conducted into the heat-pipe zone for the 154.7-MTU/acre case to overwhelm the heat pipe, causing the top of the drift to begin to dry out. Although the top of the drift has dried out, focused vapor and condensate flow continues to cause refluxing in the high-k_b zone, resulting in a depression in the upper dryout zone (Fig. 10.1.2.5.1b). Preferential heat conduction into the high-k_b zone continues to dry it out, and the manifestation of focused vapor and condensate flow on the dryout zone gradually diminishes, until at 200 yr, it is no longer evident (Fig. 10.1.2.5.1c). Thereafter, the dryout zone continues to develop as though the rock had a homogeneous k_b of 3.5 darcy, which is the bulk average of rock comprised of a 1.6-m-wide, 84-darcy zone and a 36.8-m-wide, 10-millidarcy zone.

For the second case of k_b heterogeneity, the duration of refluxing at the repository horizon (Figs. 10.1.2.5.1d and e) is considerably longer (40 yr) than in the first case (Fig. 10.1.2.5.1a). However, the ramifications of refluxing on WP performance are beneficial for the second case rather than deleterious as in the first case of k_b heterogeneity. Instead of potentially contributing to liquid contact on the WP, the refluxing zone in the pillar provides a conduit for condensate drainage through the repository horizon. This shedding of condensate around the emplacement drift may benefit WP performance by mitigating the buildup of condensate above the repository horizon. The refluxing zone continues to completely penetrate through the dryout zone at 30 yr (Fig. 10.1.2.5.1d). As in the preceding example, the refluxing zone functions as a cooling fin that preferentially attracts heat flow from the neighboring rock. However, when the refluxing zone is not coincident with the heat sources (the WPs), as it is in the pillar, it takes longer for preferential heat flow to overwhelm the refluxing zone and begin to dry it out (Fig. 10.1.2.5.1e). Consequently, heat pipes further away from the WP heat sources are more likely to persist longer than heat pipes that are closer. Similarly, heat pipes that are closer to cold WPs in a thermal design which the WPs are thermally isolated from one another (such as occurs in the ACD rev 00 design) will be more persistent than those close to hot WPs. This variability in the likelihood and/or duration of heat pipes could lead to a highly heterogeneous distribution of decay-heat-driven alteration in the near field and altered zone.

At 200 yr, the manifestation of focused vapor and condensate flow on the dryout zone is no longer evident, and the two cases have nearly identical dryout zones (Figs. 10.1.2.5.1c and f). Thereafter, the dryout zone continues to develop as though the rock had a homogeneous k_b of 3.5 darcy.

For 10-yr-old SNF and an AML of 49.2 MTU/acre, refluxing persists at the top of the drift for 65 yr (Fig. 10.1.2.5.2a), which is considerably longer than the 8.5-yr duration of refluxing for the 154.7-MTU/acre case (Fig. 10.1.2.5.1a). Focused vapor and condensate flow continue to cause a depression in the upper dryout front (Figs. 10.1.2.5.2b and c) for 1000 yr. It is important to note that this case is only able to generate marginal boiling conditions; consequently, there is insufficient heat to coalesce the dryout zones between neighboring drifts. Moreover, the local heat flux from the WP is at best only sufficient to drive the rewetting front in the high-k_b zone 1.5 m away from the top of the drift (Fig. 10.1.2.5.2b). After boiling ceases, condensate drainage in the high-k_b zone rewets the top of the drift (Fig. 10.1.2.5.2c). However, the liquid saturation is less than the critical saturation for a mobile liquid phase in the fractures; consequently, the equivalent continuum model (ECM) predicts matrix-dominated condensate drainage at 1000 yr (Fig. 10.1.2.5.2c). With the ECM, we cannot determine whether this condensate flux results in nonequilibrium fracture flow and dripping onto WPs.

We also analyzed a 49.2-MTU/acre case, with the subtle difference that it contains 20-yr-old SNF rather than the 10-yr-old SNF in the previous example. In past studies, we found that long-term, mountain-scale, thermal-hydrological behavior primarily depends on AML and is less sensitive to SNF age. However, at the drift scale, sub-to-marginal boiling conditions result in thermal-hydrological behavior that is extremely sensitive to SNF age. For 20-yr-old SNF and an AML of 49.2 MTU/acre, refluxing (with a mobile liquid phase in the fractures) persists at the top of the drift for at least 1575 yr (Figs. 10.1.2.5.2d and e; note that 1575 yr is not shown). This thermal load generates marginal boiling conditions, which last only 160 yr, and is insufficient to coalesce the dryout zones between neighboring drifts. There is also not enough heat to overwhelm the heat pipe and dry out the rock at the top of the drift. At 2534 yr, the liquid saturation in the high-k_b zone is quite high relative to ambient conditions (Fig. 10.1.2.5.2f), although it is less than the critical saturation for a mobile liquid phase in the fractures. However, with the ECM, we cannot determine whether this condensate flux results in nonequilibrium fracture flow and dripping onto WPs. The effect of gravity-driven refluxing is evident in Figs. 10.1.2.5.2e and f. Notice that, although focused condensate drainage ceases below the repository horizon, it continues above. The condensate buildup in the high-k_b zone persists for more than 5000 yr. It is important to note that decay heat continues to generate a significant condensate flux well after boiling has stopped. Consequently, decay-heat-driven coupled T-H-M-C processes may alter flow and transport properties for a considerable period even for a low-AML repository. To diagnose the potential for these coupled T-H-M-C effects to alter flow and transport properties, *in situ* thermal tests that are of sufficient size and duration are required[Buscheck et al., 1993a, 1993b; Buscheck and Nitao, 1995].

Figure 10.1.2.5.3 shows the temperature history at various locations in the emplacement drift, including the WP surface, for AMLs of 49.2, 77.4, and 154.7 MTU/acre. This example is similar to the first case of k_b heterogeneity described above with one difference; for the high-k_b zone, k_b = 414 darcy rather than 84 darcy. We made this change to further enhance the degree of gas-phase focusing and the resulting duration of refluxing in the vicinity of the drift. For all three examples, focused vapor and condensate flow causes refluxing to persist in the high-k_b zone at the top of the drift. As long as refluxing persists at the top of the drift, it prevents the temperature there from exceeding the boiling point. For the 10-yr-old SNF, 49.2-MTU/acre case, refluxing persists at the top of the drift for more than 2000 yr, long after boiling has ceased (Fig. 10.1.2.5.3a). For the 30-yr-old SNF, 77.4-MTU/acre case, refluxing persists at the top of the drift for 150 yr (Fig. 10.1.2.5.3b), while for the 154.7-MTU/acre case, refluxing persists for 30 yr (Fig. 10.1.2.5.3c). During the time that refluxing prevented the temperature in the high-k_b zone from exceeding the boiling point, temperatures throughout the rest of drift were well above boiling. For example, the temperature at the upper corner of the drift (only 2.8 m away from the high-k_b zone) managed to climb to 105, 111, and 144°C for the 49.2-, 77.4-, and 154.7-MTU/acre cases, respectively (Fig. 10.1.2.5.3). The corresponding WP surface temperatures were 121, 128, and 176°C (Fig. 10.1.2.5.3).

Based on experience with geothermal reservoirs, some have suggested that heat-pipe zones, spaced every 100 m, have the potential of convecting enough heat away from the repository to prevent its temperature from rising above the boiling point. However, we found in these examples, covering a wide range of AMLs, that the heat-pipe zone could not prevent the temperature at a location only 2.8 m away from exceeding the boiling point. Convection-dominated heat flow occurs in the heat-pipe zone, while in the neighboring rock, heat flow primarily occurs as heat conduction. Heat must be conducted from the heat sources (the WPs) to the heat-pipe zone in order for that zone to significantly influence repository temperatures. Heat cannot be conducted in relatively low thermal conductivity rock unless a significant temperature gradient is established, thereby causing temperatures away from the heat-pipe zone to be elevated above the boiling point.

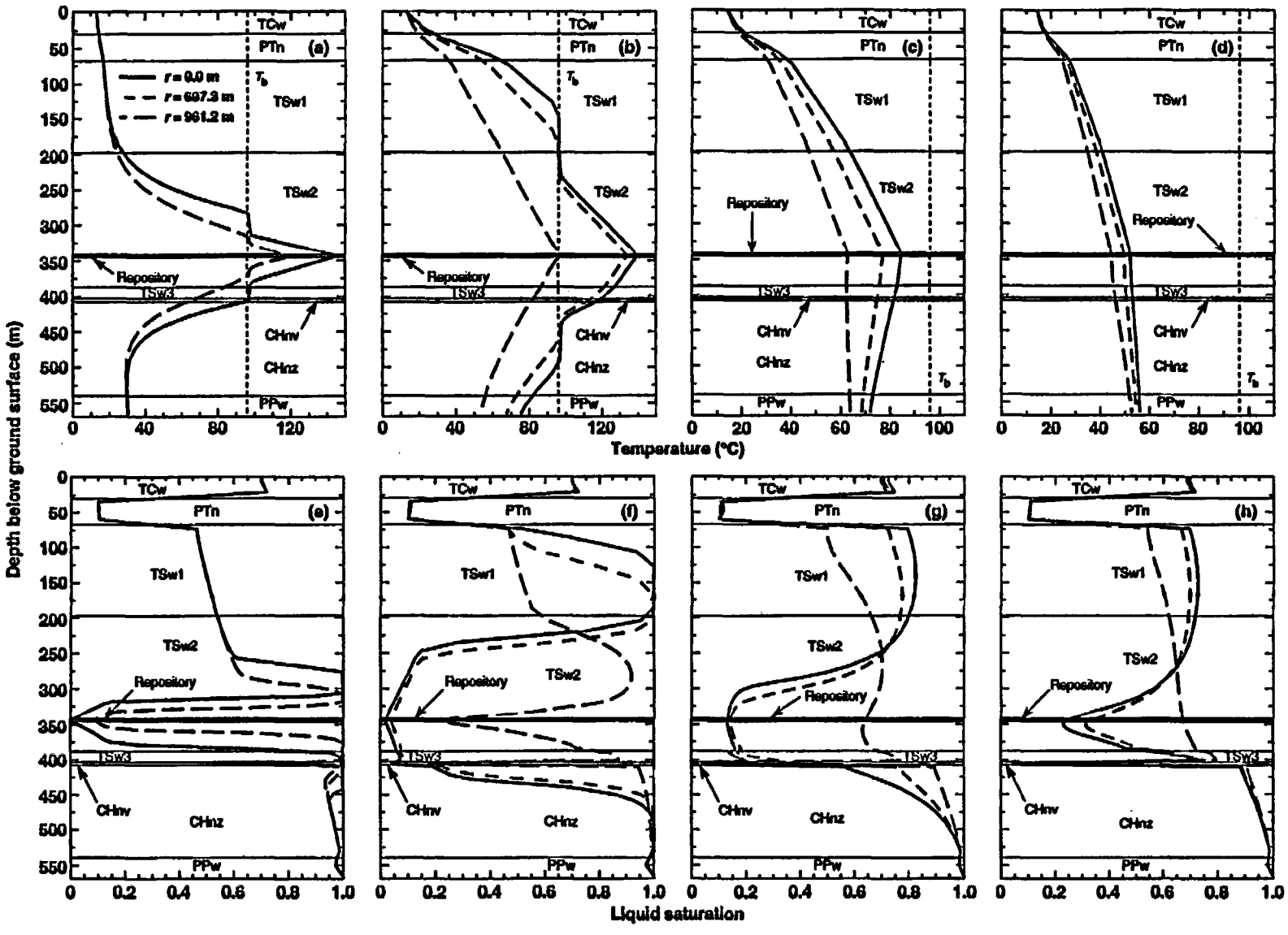

Figure 10.1.2.1.1. Vertical temperature profiles at various radial distances, r, for AML = 83.4 MTU/acre at (a) t = 100 yr, (b) t = 1000 yr, (c) t = 10,000 yr, and (d) t = 33,000 yr. Note different temperature scales. Vertical liquid saturation profiles are also plotted at (e) t = 100 yr, (f) t = 1000 yr, (g) t = 10,000 yr, and (h) t = 33,000 yr. Matrix properties for the TSw1 and TSw2 are based on Klavetter and Peters (1986). Binary gas-phase tortuosity factor τ_{eff} = 0.2 for all units.

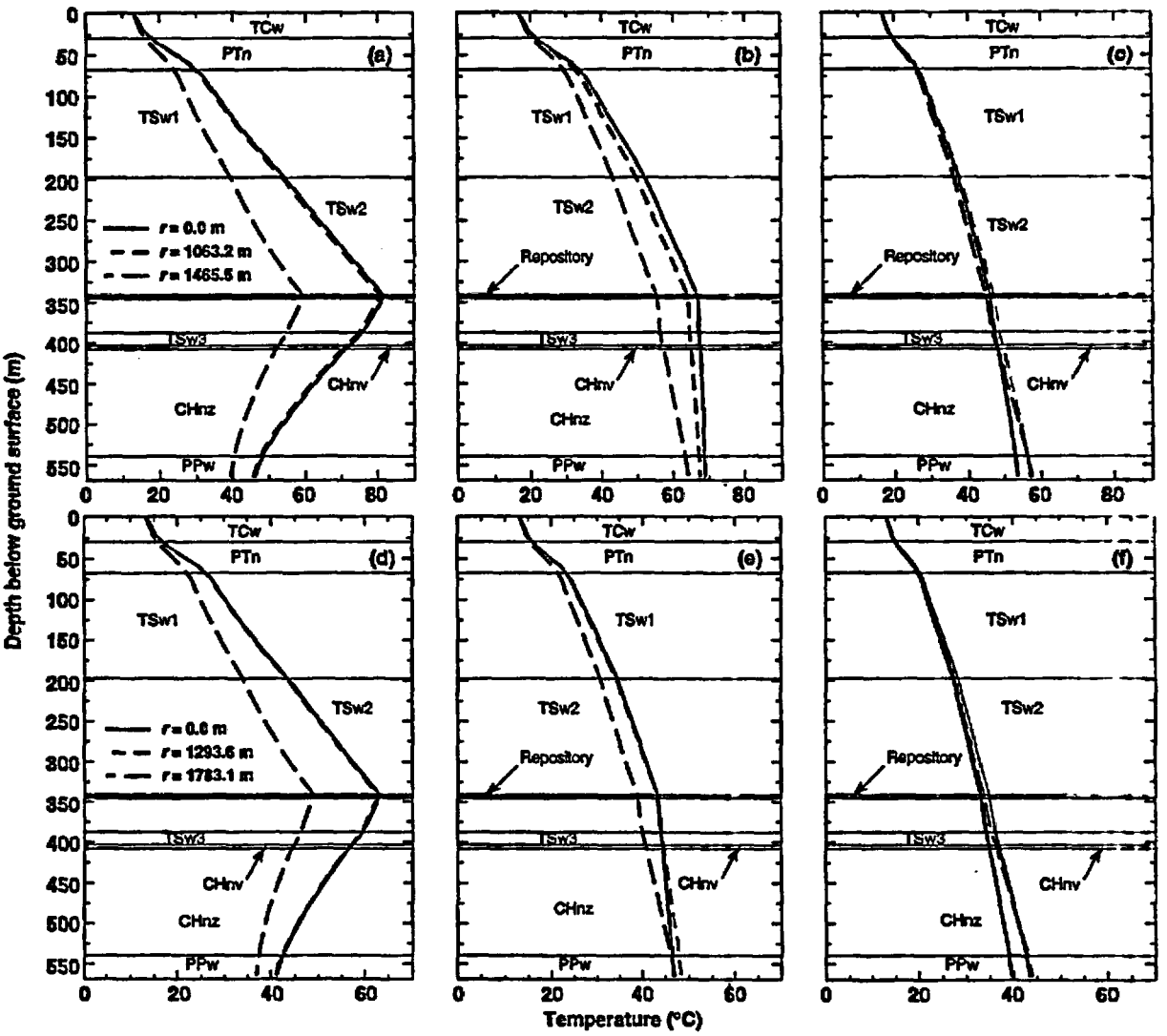

Figure 10.1.2.1.2. Vertical temperature profiles at various radial distances, r, from the repository centerline for an AML of 35.9 MTU/acre at (a) $t = 1000$ yr, (b) $t = 10{,}000$ yr, and (c) $t = 32{,}000$ yr. Vertical temperatures profiles for an AML of 24.2 MTU/acre are also plotted at (d) $t = 1000$ yr, (e) $t = 10{,}000$ yr, and (f) $t = 32{,}000$ yr. Note different temperature scales.

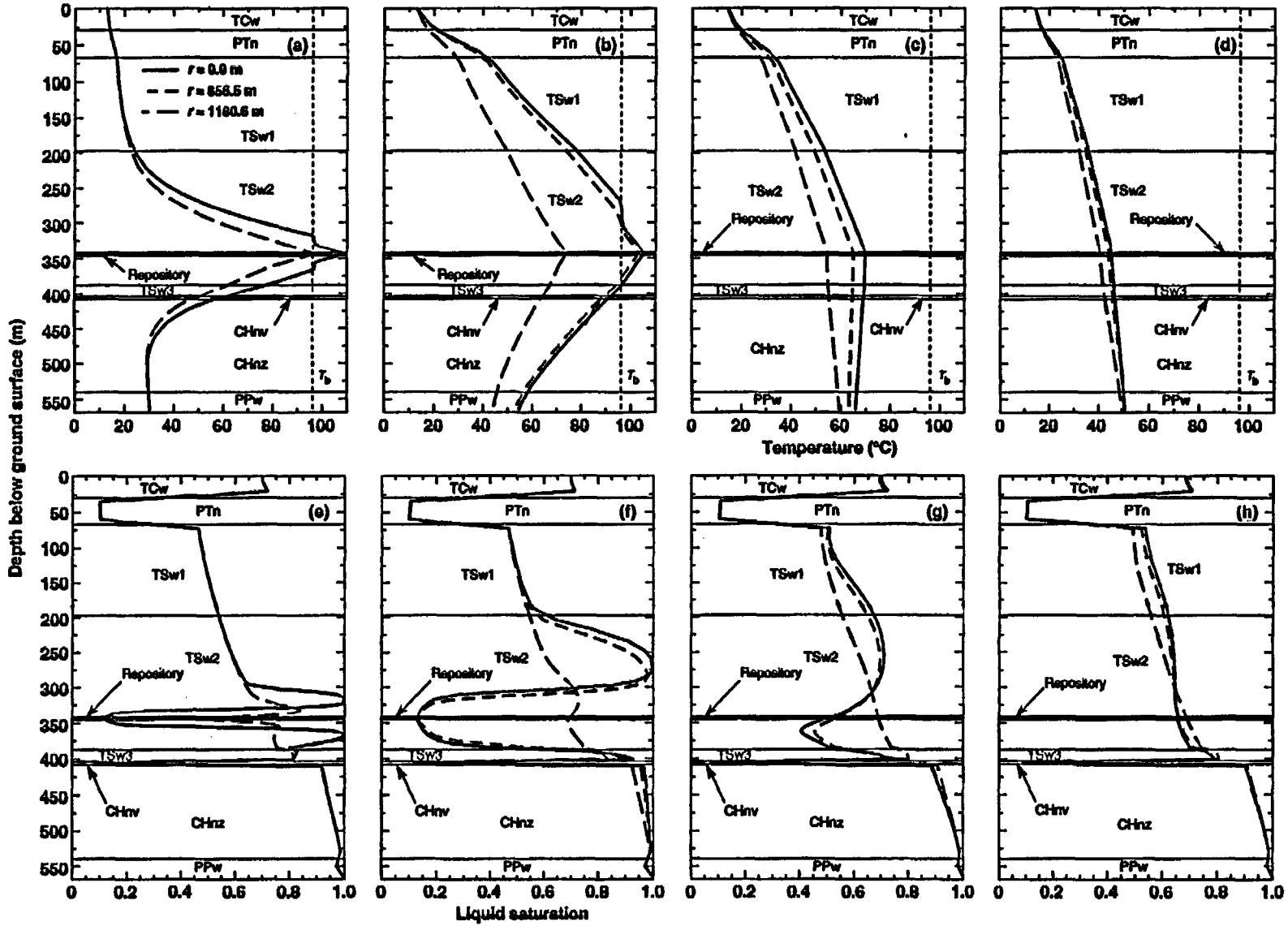

Figure 10.1.2.1.3. Vertical temperature profiles at various radial distances, r, for AML = 55.3 MTU/acre at (a) t = 100 yr, (b) t = 1000 yr, (c) t = 10,000 yr, and (d) t = 33,000 yr. Vertical liquid saturation profiles are also plotted at (e) t = 100 yr, (f) t = 1000 yr, (g) t = 10,000 yr, and (h) t = 33,000 yr. Matrix properties for the TSw1 and TSw2 are based on Klavetter and Peters (1986). Binary gas-phase tortuosity factor $\tau_{eff} = 0.2$ for all units.

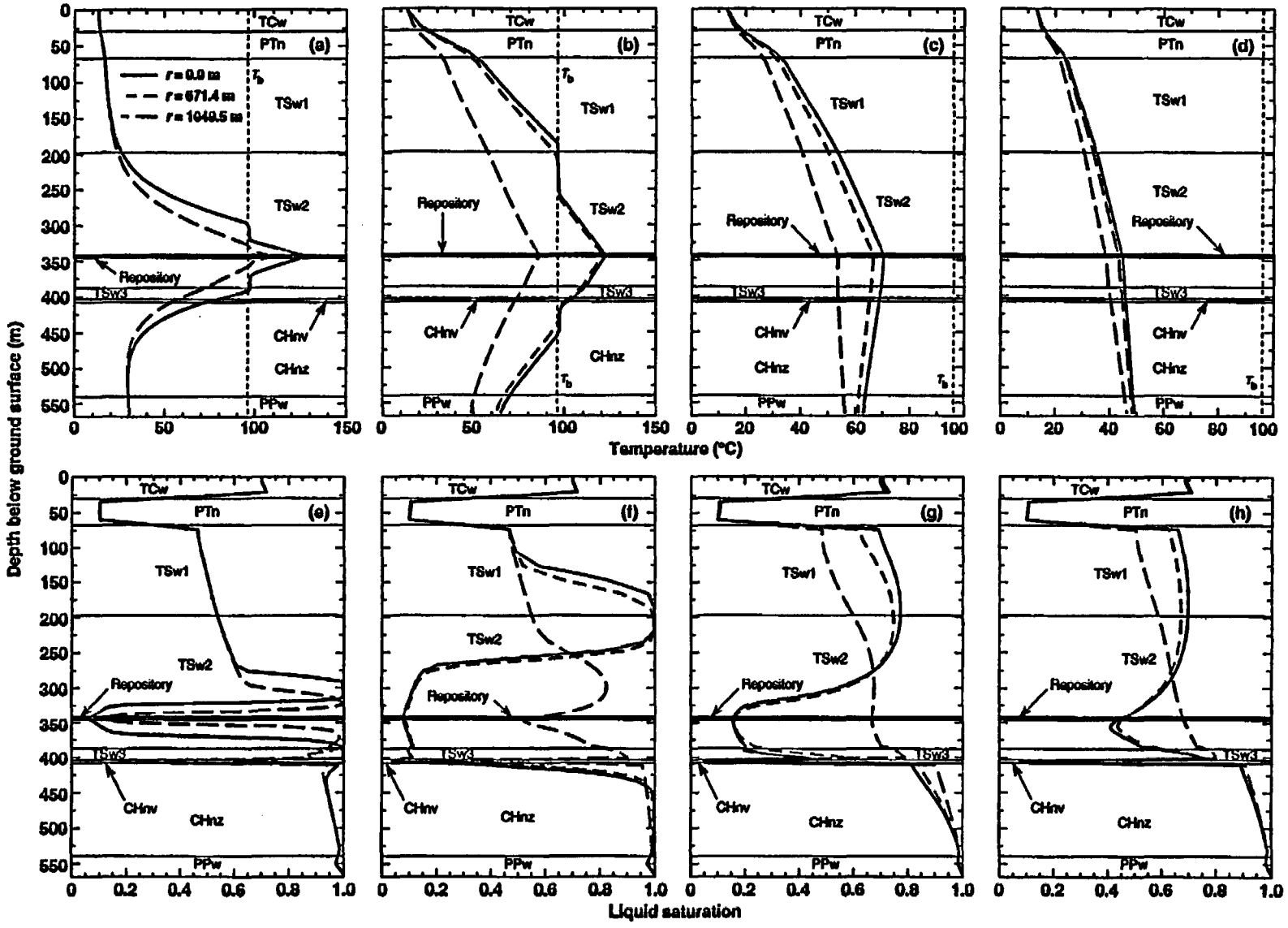

Figure 10.1.2.1.4. Vertical temperature profiles at various radial distances, r, for AML = 70.0 MTU/acre at (a) t = 100 yr, (b) t = 1000 yr, (c) t = 10,000 yr, and (d) t = 32,750 yr. Note different temperature scales. Vertical liquid saturation profiles are also plotted at (e) t = 100 yr, (f) t = 1000 yr, (g) t = 10,000 yr, and (h) t = 32,750 yr. Matrix properties for the TSw1 and TSw2 are based on Klavetter and Peters (1986). Binary gas-phase tortuosity factor $\tau_{eff} = 0.2$ for all units.

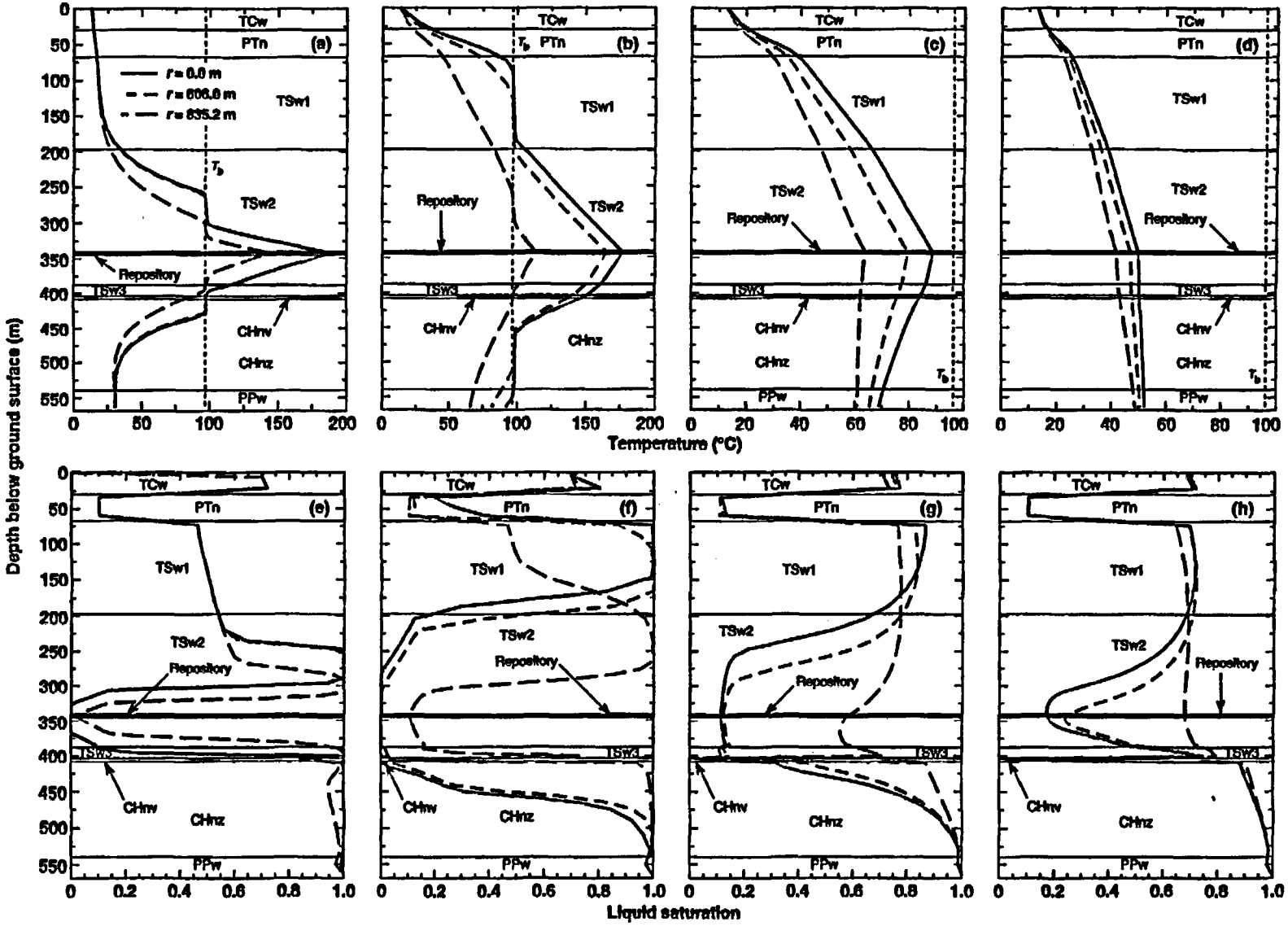

Figure 10.1.2.1.5. Vertical temperature profiles at various radial distances, r, for AML = 110.5 MTU/acre at (a) t = 100 yr, (b) t = 1000 yr, (c) t = 10,000 yr, and (d) t = 36,000 yr. Note different temperature scales. Vertical liquid saturation profiles are also plotted at (e) t = 100 yr, (f) t = 1000 yr, (g) t = 10,000 yr, and (h) t = 36,000 yr. Matrix properties for the TSw1 and TSw2 are based on Klavetter and Peters (1986). Binary gas-phase tortuosity factor $\tau_{eff} = 0.2$ for all units.

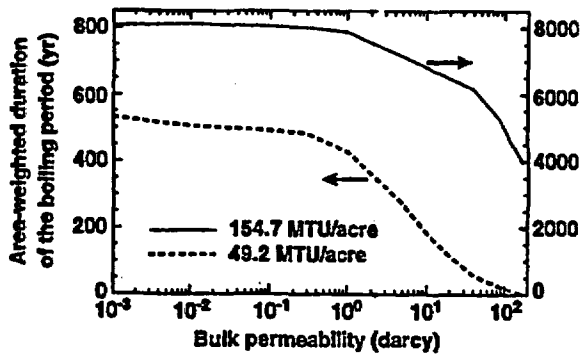

Figure 10.1.2.2.1. Area-weighted duration of the boiling period as a function of bulk permeability for AMLs of 49.2 and 154.7 MTU/acre. Note that the time scales differ by a factor of 10.

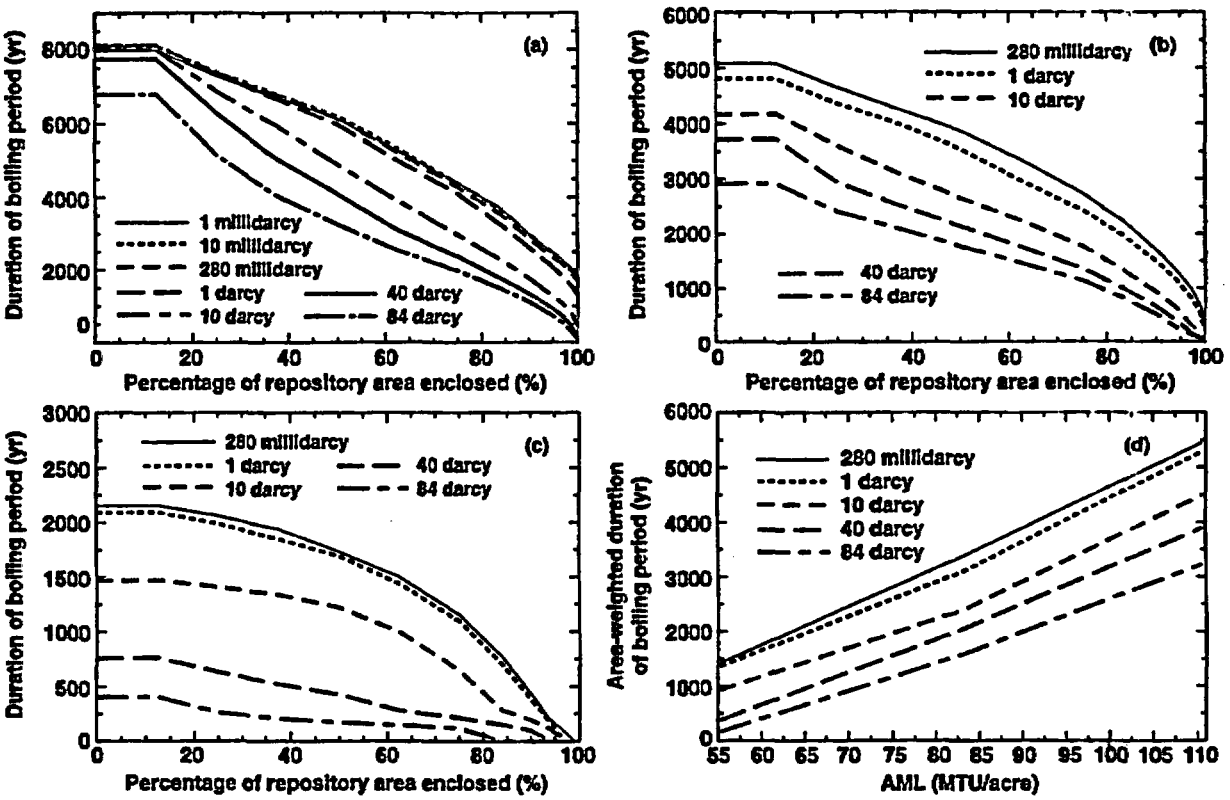

Figure 10.1.2.2.2. Duration of the boiling period at various repository locations for AMLs of (a) 110.5, (b) 83.4, and (c) 55.3 MTU/acre. The locations are identified as the percentage of the repository area enclosed, with 0% corresponding to the repository center, and 100% corresponding to the outer perimeter. (d) Area-weighted duration of the boiling period as a function of AML.

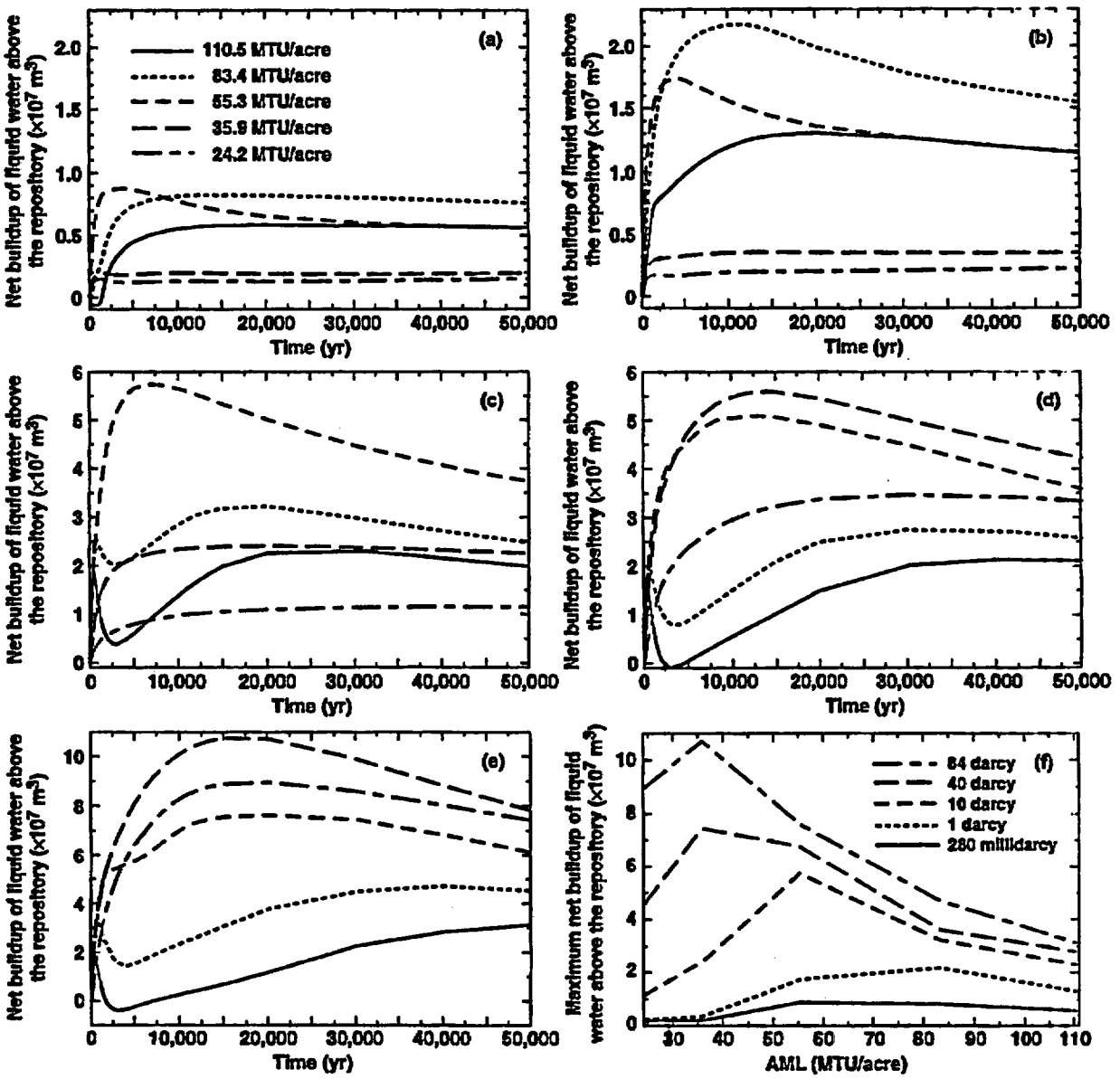

Figure 10.1.2.2.3. Net buildup of liquid water above the repository vs time for various AMLs and k_b values of (a) 280 millidarcy and (b) 1, (c) 10, (d) 40, and (e) 84 darcy. (f) Maximum net buildup of liquid water above the repository as a function of AML for various values of k_b.

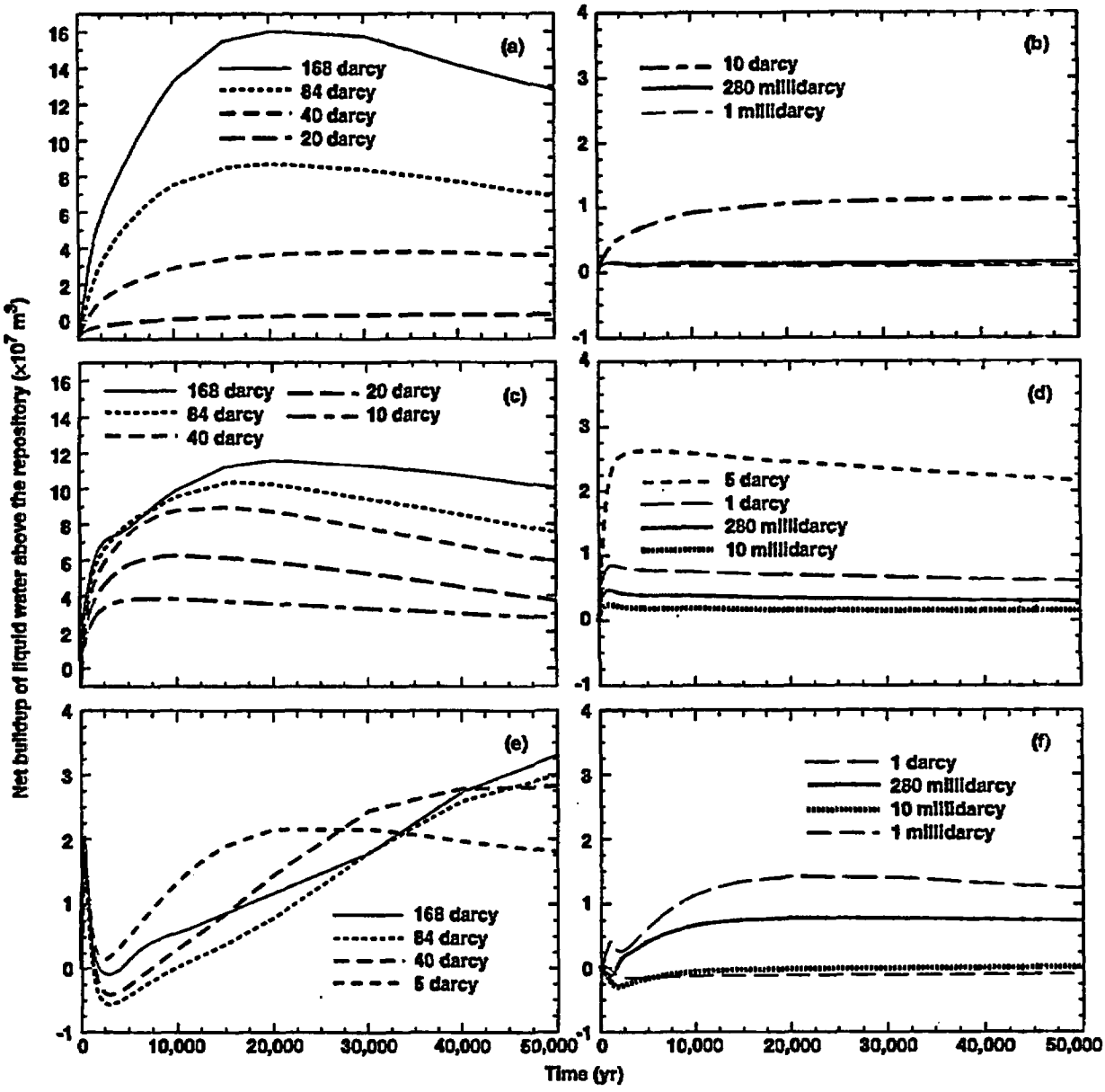

Figure 10.1.2.2.4. Net buildup of liquid water above the repository for various values of k_b and AMLs of 27.1 MTU/acre (a and b), 49.2 MTU/acre (c and d), and 154.7 MTU/acre (e and f).

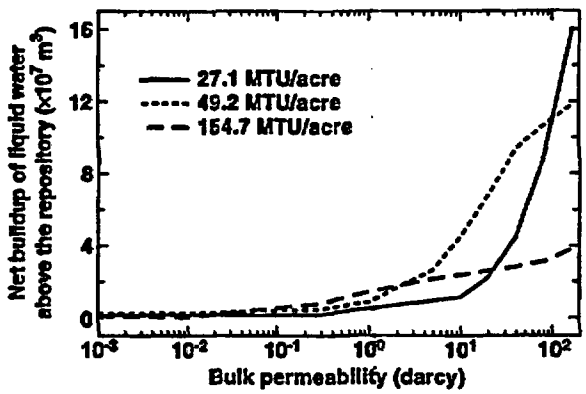

Figure 10.1.2.2.5. Maximum net buildup of liquid water above the repository as a function of bulk permeability for various AMLs.

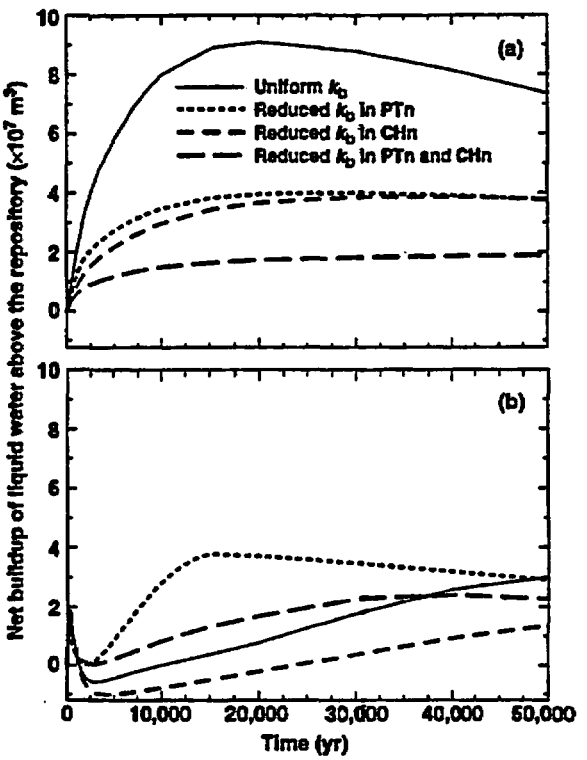

Figure 10.1.2.3.1. Net buildup of liquid water above the repository for various vertical k_b distributions and AMLs of (a) 27.1, and (b) 154.7 MTU/acre. Uniform k_b = 84 darcy. The value of k_b in the PTn is reduced to 320 millidarcy, and in the CHn, to 280 millidarcy.

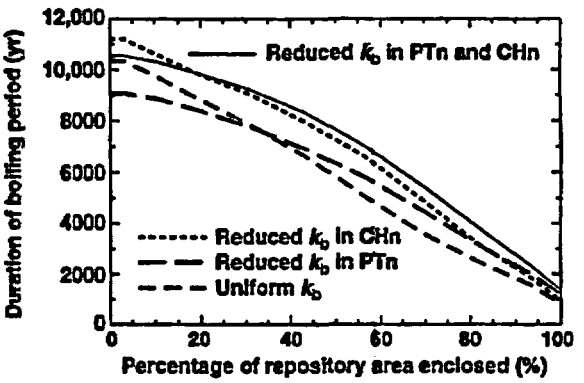

Figure 10.1.2.3.2. Duration of the boiling period at various repository locations for various vertical k_b distributions and an AML of 154.7 MTU/acre. Uniform k_b = 84 darcy. The value of k_b in the PTn is reduced to 320 millidarcy, and in the CHn, to 280 millidarcy. The repository locations are identified as the percentage of the repository area enclosed, with 0% corresponding to the repository center, and 100% corresponding to the outer perimeter.

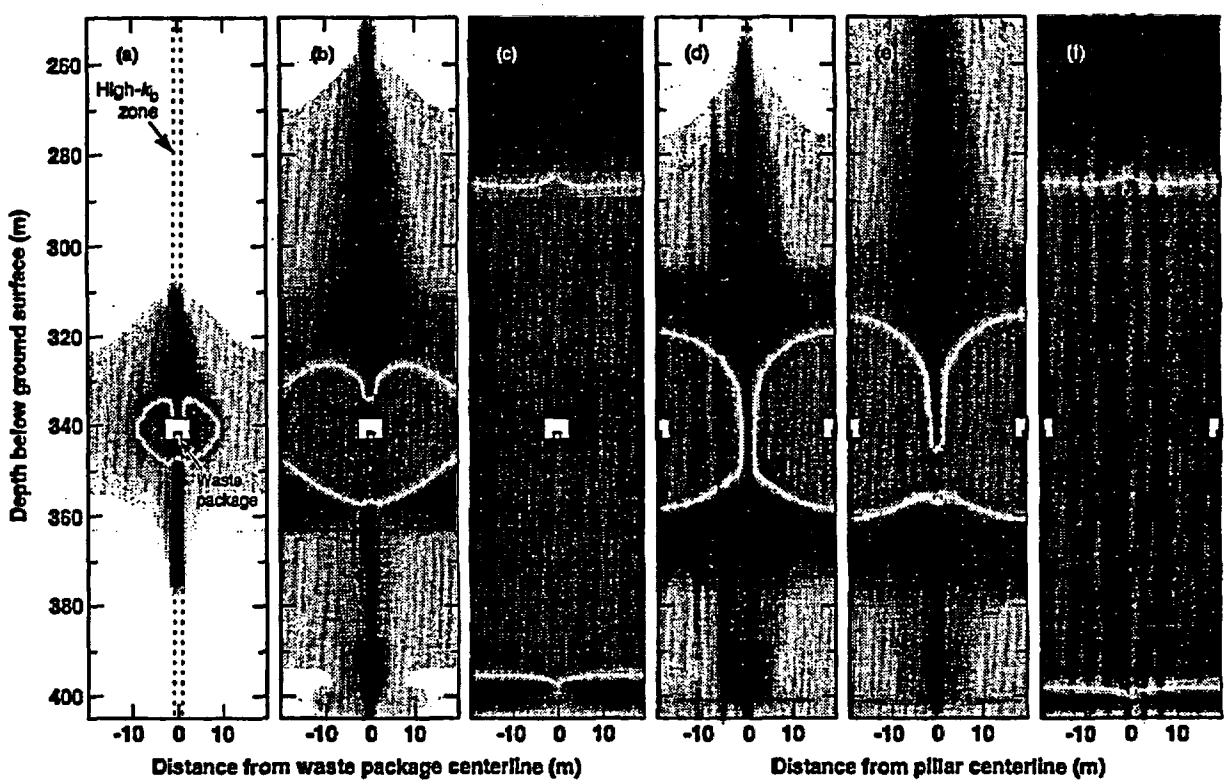

Figure 10.1.2.5.1. Dimensionless liquid saturation distribution orthogonal to an emplacement drift containing 30-yr-old SNF, for an AML of 154.7 MTU/acre and and APD of 114 kW/acre. Within the 1.6-m-wide, high-k_b zone, k_b = 84 darcy; otherwise k_b = 10 millidarcy. Distributions are shown at time t of (a) 8, (b) 30, (c) 200 yr for a k_b distribution in which the high-k_b zone intersects the center of the emplacement drift. Distributions are also shown at time t of (d) 30, (e) 40, and (f) t = 200 yr for a k_b distribution in which the high-k_b zone intersects the center of the pillar separating the emplacement drifts. The medium-shaded area surrounding the drift corresponds to a region that is drier than ambient saturation (dry-out zone). The dark-shaded areas correspond to regions that are wetter than ambient saturation (condensation zones). The lighter shading surrounding the dark-shaded area corresponds to a decreasing buildup in saturation (outer edges of condensation zones). No shading indicates no change in saturation. Note that the transition from drier to wetter conditions is shown as a white ring at early time which becomes a white band at later time.

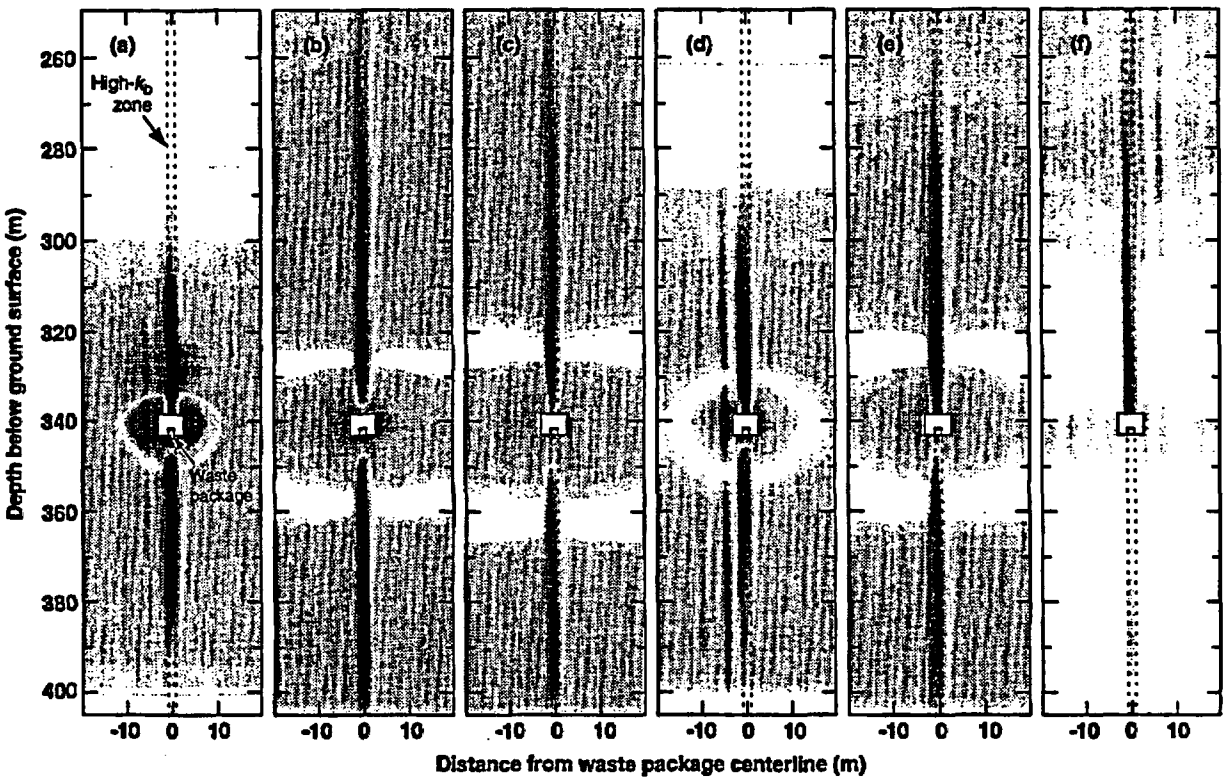

Figure 10.1.2.5.2. Dimensionless liquid saturation distribution orthogonal to an emplacement drift containing SNF, for an AML of 49.2 MTU/acre. Within the 1.6-m-wide, high-k_b zone, k_b = 84 darcy; otherwise k_b = 10 millidarcy. Distributions are shown at time t of (a) 62, (b) 663, (c) 1000 yr for 10-yr-old SNF and an APD of 57 kW/acre. Distributions are also shown at time t of (d) 159, (e) 661, and (f) 2534 yr for 20-yr-old SNF and an APD of 43.7 kW/acre. The medium-shaded area surrounding the drift corresponds to a region that is drier than ambient saturation (dry-out zone). The dark-shaded areas correspond to regions that are wetter than ambient saturation (condensation zones). The lighter shading surrounding the dark-shaded area corresponds to a decreasing buildup in saturation (outer edges of condensation zones). No shading indicates no change in saturation. Note that the transition from drier to wetter conditions is shown as a white ring at early time which becomes a white band at later time.

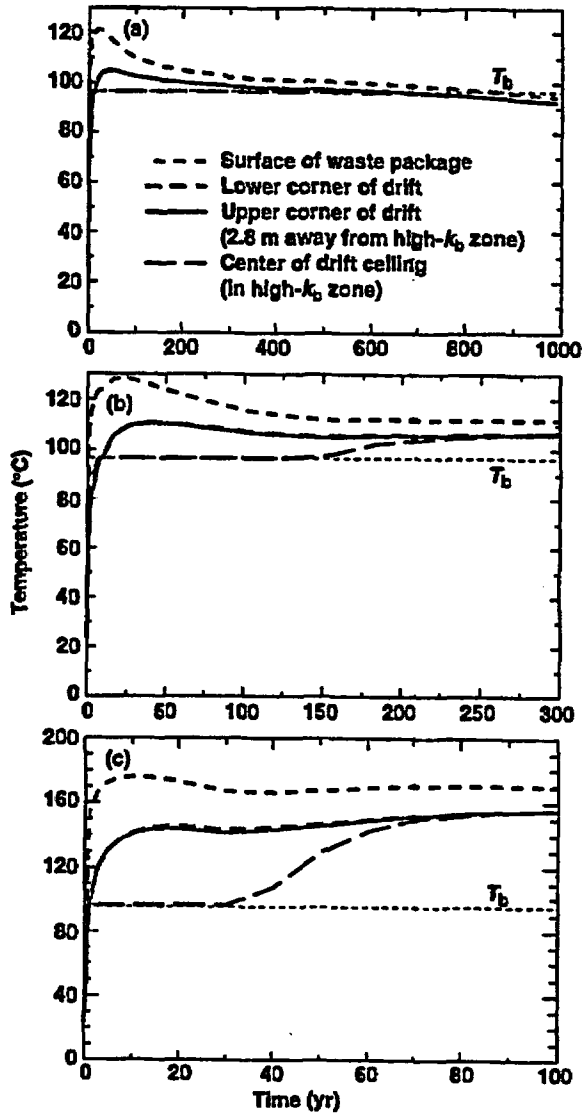

Figure 10.1.2.5.3. Temperature history at various locations in the emplacement drift for (a) 10-yr-old SNF, an APD of 57 kW/acre, and an AML of 49.2 MTU/acre, (b) 30-yr-old SNF, an APD of 57 kW/acre, and an AML of 77.4 MTU/acre, and (c) 30-yr-old SNF, an APD of 114 kW/acre, and an AML of 154.7 MTU/acre. Vertically oriented, 1.6-m-wide, 414-darcy zones are separated by 36.8-m-wide, 10-millidarcy zones.

Content

10.1.3 Influence of Matrix Hydrological Property Distribution

10.1.3.1 Boiling-Driven Vapor and Heat Flow. The mountain-scale analysis in the preceding section (Section 10.1.2), which focused on the influence of the fracture permeability distribution on thermal-hydrological (T-H) behavior, assumed the matrix hydrological data from the RIB [DOE, 1990] and Klavetter and Peters [1986]. In this section, we investigate the sensitivity of mountain-scale T-H behavior to more recently obtained matrix property data for the TSw1 and TSw2 units. As in the preceding section (Section 10.1.2), a zero ambient percolation flux is assumed. Because more recent assessments of the ambient percolation flux [Bodvarsson et al., 1996] indicate the likelihood of greater than zero net infiltration (resulting in a nonzero ambient percolation flux in the host rock), the calculations reported in this section probably overpredict the spatial and temporal extent of less-than-ambient liquid saturation and relative humidity *RH* conditions in the UZ, in general, and in the repository rock, in particular. Nonetheless, a quantitative understanding about the influence of matrix hydrological properties on dryout and rewetting behavior can be obtained from the wide range of cases that are presented in this section.

Much of the following information is presented as tables of temperature *T* and relative humidity *RH* at various locations in the repository rock. This information is provided to facilitate evaluating the likelihood of aqueous reactions and aqueous-transport processes giving rise to significant alteration of flow and transport properties. These processes depend on *T* and *RH*. For example, low *RH* (which corresponds to low liquid saturation and generally lower liquid-phase flux) reduces the likelihood of many of these processes generating significant effects; where these processes may be significant, the rate at which aqueous reactions occur depends on *T*.

The temporal extent of *RH* reduction in the repository rock (which is provided in the tables) is also a good indication of the spatial extent of *RH* reduction in the altered zone in general. Long-duration *RH* reduction in the repository rock requires that *RH* be reduced over a very large spatial extent. Vertical liquid saturation profiles are provided to help interpret the spatial extent of reduced *RH* conditions in the altered zone. Liquid saturations well below ambient correspond to low *RH*. Liquid saturations that are moderately below ambient correspond to intermediate-to-high *RH*; liquid saturations that are close to ambient correspond to *RH* = 98–99%.

Vertical temperature profiles are also provided to facilitate evaluating the impact of T on the likelihood of aqueous reactions and aqueous-transport processes giving rise to significant alteration of flow and transport properties. The zone of two-phase refluxing overlying the boiling zone (called the heat-pipe zone) is of particular interest because the liquid saturation and relative humidity *RH* remain high in this zone, increasing the likelihood of aqueous reactions and aqueous-transport processes occurring. Refluxing can also generate a very high liquid-phase flux in fractures, which can result in significant dissolution and precipitation of minerals along the fracture walls. The heat-pipe zone is typically manifested by temperatures that are very close to the nominal boiling point of water (96°C) and a liquid saturation that is very close to 100%.

Table 10.1.3.1.1 summarizes the time required to attain the indicated relative humidity *RH* in the rock at various repository locations and the temperature *T* at which that value of *RH* is attained for the "reference" case based on the RIB [1990] and Klavetter and Peters [1986] data for AMLs of 55.3, 110.5, and 150 MTU/acre. We repeated the mountain-scale calculations for the five sets of matrix properties for the Topopah Spring welded tuff (Table 10.1.3.1.2) that are reported in Pruess and Tsang [1994], which based on measurements by Flint and others [1993]. For zero percolation flux, the initial liquid saturation at the repository horizon is calculated to be 68, 76, 78, 74, 66, and 64% for the six cases in Table 10.1.3.1.2, respectively. In order to result in nearly the same initial liquid water content in the TSw1 and TSw2, a porosity (ϕ_m) of 0.11 was assumed for the three cases that yielded lower initial liquid saturation $S_{\ell,\text{init}}$ (reference case, LBL-USGS-3.4, and LBL-USGS-3.3) and $\phi_m = 0.10$ for the three cases that yielded higher $S_{\ell,\text{init}}$ (LBL-USGS-3.5, LBL-USGS-3.2, and LBL-USGS-3.1/3.6). Although these six cases have different

values of saturated matrix permeability, k_m, they all share the same bulk permeability k_b of 280 millidarcy.

For AMLs of 55.3, 110.5, and 150 MTU/acre, and for the five sets of LBL-USGS matrix property data, Tables 10.1.3.1.3–10.1.3.1.3–5 summarize *RH* and *T* in the rock at the same repository locations reported in Table 10.1.3.1.1 for the reference-case properties. Figures 10.1.3.1.1–10.1.3.1.6 give the vertical temperature and liquid saturation profiles for these six matrix-property cases and an AML of 110.5 MTU/acre. To show the influence of edge-cooling/rewetting/shedding effects on T-H behavior, vertical profiles are given at three repository locations, including: (1) $r = 0.0$ m, which is at the center of the repository, (2) $r = 606.0$ m, which is the "median" repository location that encloses 50% of the repository (i.e., 50% of the repository lies between that location and the repository edge), and (3) $r = 835.2$ m, which encloses 95% of the repository (i.e., only 5% of the repository area lies outside of that location).

For all matrix-property cases, similar thermal and dryout behavior occur over the inner half of the repository, particularly during the first 1000 yr; thereafter, edge-cooling/rewetting effects cause the 50% repository location to have slightly cooler temperatures and a slightly less extensive dryout zone than the center of the repository. For the 95% repository location, edge-cooling/rewetting/shedding effects significantly reduce temperatures and reduce both the vertical extent and magnitude of rock dryout. (Note that Section 1.10.6 of Chapter 1 also discusses the influence of edge-cooling/rewetting/shedding effects on mountain-scale and drift-scale T-H behavior.)

For AML = 110.5 MTU/acre, the five LBL-USGS matrix property cases fall into four categories with respect to the rate at which the repository rock rewets to humid ambient *RH*:

- **Fast rewetting rate:** LBL-USGS-3.2 results in much faster rewetting to ambient *RH* than the reference case (compare Tables 10.1.3.1.1b and 10.1.3.1.4a). Consequently, when a given *RH* is attained *T*, is substantially higher for LBL-USGS-3.2 than in the reference case. For example, *T* at the repository center is 96°C when *RH* = 70% as compared with 68°C in the reference case. The spatial extent of dryout is much less for the LBL-USGS-3.2 matrix-property case than for the reference matrix-property case (compare Figs. 10.1.3.1.1 and 10.1.3.1.2). The reduced vertical extent of dryout reduces the magnitude of the temperature increase in the above-boiling region for LBL-USGS-3.2. For the sub-boiling region and at later time ($t > 1000$ yr), the vertical temperature profiles are very similar for these two cases.
- **Medium rewetting rate:** LBL-USGS-3.5 rewets at nearly the same rate as the reference case (compare Tables 10.1.3.1.1b and 10.1.3.1.4b). Consequently, there is a similar relationship between *T* and *RH* in the rock. The spatial extent of dryout is slightly less for the LBL-USGS-3.5 matrix-property case than for the reference matrix-property case (compare Figs. 10.1.3.1.1 and 10.1.3.1.3). The slightly reduced vertical extent of dryout reduces the magnitude of the temperature increase in the above-boiling region for the LBL-USGS-3.5 case. For the sub-boiling region and at later time ($t > 1000$ yr), the vertical temperature profiles are very similar for these two cases.
- **Slow rewetting rate:** LBL-USGS-3.1/3.6 and LBL-USGS-3.4 have very similar rewetting rates that are much slower than the reference case in the inner 75% of the repository (compare Tables 10.1.3.1.1b and 10.1.3.1.4c-d). For the outer 10% of the repository, these three cases have similar rewetting rates (compare Tables 10.1.3.1.1b and 10.1.3.1.4c-d). These three matrix-property cases have similar spatial extents of dryout and have similar spatial temperature distributions (compare Figs. 10.1.3.1.1, 10.1.3.1.4, and 10.1.3.1.5).
- **Very slow rewetting rate:** LBL-USGS-3.3 has a much slower rewetting rate than all of the other cases, except at the outer 3% of the repository where rewetting is moderately slower (compare Table 10.1.3.1.4e with Tables 10.1.3.1.1b and 10.1.3.1.4a-d). The spatial extent of dryout is about the same for the LBL-USGS-3.3 matrix-property case and the reference matrix-property case, while slower rewetting in LBL-USGS-3.3 allows the dryout zone to remain broad for a longer duration (compare Figs. 10.1.3.1.1 and 10.1.3.1.6).

For all six matrix property cases, the outer 3% of the repository has a similar *T* versus *RH* relationship. Regardless of case, the outer 3% of the 110.5-MTU/acre repository is relatively hot (106°C) at

the time that *RH* returns to 70%. Except for LBL-USGS-3.2, the inner 75% of the repository has cooled to relatively low *T* (49-76°C) at the time that *RH* = 70%.

For AML = 55.3 MTU/acre, the five LBL-USGS matrix property cases fall into four categories with respect to the rate at which the repository rock rewets to humid (ambient) *RH*:

Fast rewetting rate: LBL-USGS-3.2 results in much faster rewetting to ambient *RH* than the reference case (compare Tables 10.1.3.1.1a and 10.1.3.1.3a)

Medium rewetting rate: LBL-USGS-3.5 rewets to ambient *RH* at about the same rate as the reference case (compare Tables 10.1.3.1.1a and 10.1.3.1.3b).

Slow rewetting rate: LBL-USGS-31/3.6 and LBL-USGS-3.4 rewet somewhat more slowly to ambient *RH* than the reference case (compare Table 10.1.3.1.1 with Tables 10.1.3.1.3c and 10.1.3.1.3d).

Very slow rewetting rate: LBL-USGS-3.3 rewets much more slowly to ambient *RH* than the reference case (compare Tables 10.1.3.1.1a and 10.1.3.1.3e).

Regardless of the rewetting rate, relatively warm conditions prevail for the 55.3-MTU/acre cases, (105 to 107°C) at the time that *RH* = 70%. With the exception of LBL-USGS-3.2, there is not a great degree of variability in the relationship between *T* and *RH* in the repository rock.

For AML = 150 MTU/acre, the five LBL-USGS matrix property cases fall into four categories with respect to the rate at which the repository rock rewets to ambient *RH*:

Fast rewetting rate: LBL-USGS-3.2 results in much faster rewetting than the reference case (compare Table 10.1.3.1.1c and 10.1.3.1.5a). Consequently, *T* is much greater with respect to *RH*. For example *T* at the center of the repository is 97°C when *RH* = 70% as compared with 68°C in the reference case.

Medium rewetting rate: LBL-USGS-3.5 results in nearly the same rewetting rate as the reference case (compare Table 10.1.3.1.1c and 10.1.3.1.5b); consequently, there is a similar relationship between *T* and *RH*.

Slow rewetting rate: LBL-USGS-3.1/3.6 and LBL-USGS-3.4 result in very similar rewetting rates that are substantially slower than the reference case in the inner 75% of the repository (compare Tables 10.1.3.1.5c and 10.1.3.1.5d with Table 10.1.3.1.1c). For the outer 10% of the repository, these three cases have similar rewetting rates.

Very slow rewetting rate: LBL-USGS-3.3 has a much slower rewetting rate throughout the entire repository (compare Table 10.1.3.1.5e with Tables 10.1.3.1.5a-d and 10.1.3.1.1c).

Rewetting to *RH* = 90% and 95% is very slow for the 150-MTU/acre cases (except for the LBL-USGS-3.2 case). Unlike the 55.3- and 110.5-MTU/acre cases, the slower rewetting rates for 150-MTU/acre LBL-USGS-3.1/3.6, LBL-USGS-3.4, and LBL-USGS-3.3 cases allow *T* at the outer 3% of the repository to decrease to relatively low *T* (83-90°C) when *RH* = 70%. With the exception of LBL-USGS-3.2, the inner 75% of the repository has decreased to relatively low temperatures (51-70°C) at the time that *RH* = 70%, and to 40-59°C at the time that *RH* = 80%.

Dryout behavior is the net result of processes that drive water vapor away from the repository and the processes that cause water to return to the repository. Processes that drive water (both gas- and liquid-phase) away from the repository (and dryout zone) include:

- Molecular diffusion of water vapor from regions of high mole fraction of water vapor to regions of low mass fraction, which is called binary gas-phase diffusion (Section 10.1.3.2).
- Advective gas-phase transport of water vapor from regions of vaporization to regions of condensation driven by:
  - Gas-phase pressure buildup from the generation of steam (Section 10.1.2.2).
  - Buoyant gas-phase convection (Section 10.1.2.2).
- Advective liquid-phase flow consisting of:
  - Condensate shedding down the flanks of the dryout zone.
  - Condensate drainage below the dryout zone.

Processes that return water to the repository (and dryout zone) include:

- Binary gas-phase diffusion of air and water vapor (Section 10.1.3.2).
- Buoyant gas-phase convection of water vapor (Section 10.1.2.2).
- Advective liquid-phase flow consisting of:
  - Ambient percolation flux (Section 1.10.6 of Chapter 1).
  - Condensate drainage above the dryout zone.
  - Matrix imbibition, occurring from regions of high matric potential (wetter areas) to regions of low matric potential (drier areas). This is the focus of this section.

Buoyant gas-phase convection causes rock dryout to occur primarily below the repository and can enhance the buildup of condensate above the dryout zone, thereby increasing the return condensate flux above the dryout zone. Buoyant gas-phase convection can also enhance the rate of vaporization. If k_b is large enough (> 1-10 darcy), this mechanism can be important whether or not boiling occurs. Gas-phase convection driven by boiling conditions can suppress the impact of buoyant gas-phase convection. In general, rewetting is the result of both liquid-phase transport of moisture (called liquid-phase rewetting) and gas-phase transport of moisture (called gas-phase rewetting) back to the dryout zone.

Some of the properties listed in Table 10.1.3.1.2 have stronger influence on the noted differences in rewetting behavior than other listed properties. Liquid-phase rewetting by matrix imbibition increases with increasing $k_{m,sat}$ and increasing m, and with decreasing α. The fact that $k_{m,sat}$ for LBL-USGS-3.2 is two orders of magnitude larger than for the other property sets is the primary reason it has such a high rewetting rate. The other five matrix-property sets have values of $k_{m,sat}$ that vary by a factor of five; differences between these sets arise from differences in their respective values of the van Genuchten curve-fitting parameters α and m.

Gas-phase rewetting is primarily affected by (1) τ_{eff} and (2) the influence of k_b in determining the magnitude of buoyant gas-phase convection. As will be discussed in the following section (Section 1.10.3.2), the van Genuchten curve-fitting parameters α and m also affect binary gas-phase diffusion (Table 10.1.3.1.2). A comparison of Table 10.1.3.1.3c with 10.1.3.1.3d, Table 10.1.3.1.4c with 10.1.3.1.4d, and Table 10.1.3.1.5c with 10.1.3.1.5d, shows that the rewetting rates are almost identical for the LBL-USGS-3.1/3.6 and LBL-USGS-3.4 property sets. Because these two property sets have the same value of α, the fivefold difference in their respective values of $k_{m,sat}$ is offset by the small difference in the van Genuchten curve-fitting parameter m (0.29 versus 0.25). LBL-USGS-3.3 has the lowest overall rewetting rate because it has the largest α and the second-smallest m of the six matrix-property sets (Table 10.1.3.1.2).

Table 10.1.3.1.1

Time required to attain the indicated relative humidity *RH* at various repository locations and the temperature at which that value of *RH* is attained for 22.5-yr-old SNF, gas-phase diffusion tortousity factor, τ_{eff} = 0.2, k_b = 280 millidarcy, and assuming the matrix properties from Klavetter and Peters (1986) for the TSw1 and TSw2 units. The locations are identified as the percentage of the repository area enclosed, with 0% corresponding to the repository center, and 100% corresponding to the edge.

Table 10.1.3.1.1a: AML = 55.3 MTU/acre

Percentage of repository area enclosed (%)	Time required to attain the indicated *RH* (yr)				Temperature at which the indicated *RH* is attained (°C)			
	70%	80%	90%	95%	70%	80%	90%	95%
50	670	1660	3330	4630	107	97	80	72
75	410	940	1610	2280	107	99	89	81
90	NA	200	380	490	NA	103	97	94
97	NA	NA	NA	NA	NA	NA	NA	NA

Table 10.1.3.1.1b: AML = 110.5 MTU/acre

Percentage of repository area enclosed (%)	Time required to attain the indicated *RH* (yr)				Temperature at which the indicated *RH* is attained (°C)			
	70%	80%	90%	95%	70%	80%	90%	95%
50	15,960	27,910	40,990	49,980	68	54	45	42
75	9540	15,520	24,950	32,590	76	64	53	48
90	3190	4890	7460	9890	93	82	73	68
97	1410	1810	2360	2890	106	101	93	88

Table 10.1.3.1.1c: AML = 150 MTU/acre

Percentage of repository area enclosed (%)	Time required to attain the indicated *RH* (yr)				Temperature at which the indicated *RH* is attained (°C)			
	70%	80%	90%	95%	70%	80%	90%	95%
50	20,630	34,850	50,920	64,150	68	52	45	41
75	16,400	24,520	32,700	43,360	70	59	51	46
90	8660	12,090	16,520	19,780	81	72	64	59
97	4330	6020	8180	10,060	93	84	77	72

Table 10.1.3.1.2: Matrix hydrological property data for the TSw1 and TSw2 units.

Sample Name	S_r	ϕ_m	$k_{m,sat}$ (m^2)	α (10^{-5} Pa^{-1})	m
Reference Case	0.08	0.11	1.9×10^{-18}	0.058	0.4438
LBL-USGS-3.2	0.0	0.10	4.0×10^{-16}	0.125	0.18
LBL-USGS-3.5	0.0	0.10	5.0×10^{-18}	0.133	0.25
LBL-USGS-3.1/3.6	0.0	0.10	1.0×10^{-18}	0.067	0.29
LBL-USGS-3.4	0.0	0.11	5.0×10^{-18}	0.067	0.25
LBL-USGS-3.3	0.0	0.11	4.0×10^{-18}	0.2	0.22

The properties listed are S_r, α, and m (the three van Genuchten characteristic curve-fitting parameters), matrix porosity (ϕ_m), and saturated matrix permeability ($k_{m,sat}$).

Table 10.1.3.1.3: AML = 55.3 MTU/acre

Time required to attain the indicated relative humidity *RH* at various repository locations and the temperature at which that value of *RH* is attained for 22.5-yr-old SNF, gas-phase diffusion tortousity factor τ_{eff} = 0.2, and k_b = 280 millidarcy. The locations are identified as the percentage of the repository area enclosed, with 0% corresponding to the repository center, and 100% corresponding to the edge

Table 10.1.3.1.3a: Matrix properties for LBL-USGS sample 3.2 in the TSw1 and TSw2 units.

Percentage of repository area enclosed (%)	Time required to attain the indicated *RH* (yr)				Temperature at which the indicated *RH* is attained (°C)			
	70%	80%	90%	95%	70%	80%	90%	95%
50	NA	750	1240	1480	NA	103	99	97
75	NA	280	700	870	NA	103	100	98
90	NA	NA	160	210	NA	NA	100	98
97	NA	NA	NA	NA	NA	NA	NA	NA

Table 10.1.3.1.3b: Matrix properties for LBL-USGS sample 3.5 in the TSw1 and TSw2 units.

Percentage of repository areaq enclosed (%)	Time required to attain the indicated *RH* (yr)				Temperature at which the indicated *RH* is attained (°C)			
	70%	80%	90%	95%	70%	80%	90%	95%
50	490	1570	2520	3490	107	98	87	79
75	290	900	1350	1700	107	100	93	87
90	NA	190	330	400	NA	103	98	96
97	NA	NA	NA	NA	NA	NA	NA	NA

Table 10.1.3.1.3c: Matrix properties for LBL-USGS sample 3.1 and LBL-USGS 3.6 in the TSw1 and TSw2 units.

Percentage of repository area enclosed (%)	Time required to attain the indicated *RH* (yr)				Temperature at which the indicated *RH* is attained (°C)			
	70%	80%	90%	95%	70%	80%	90%	95%
50	690	2240	7170	12,050	107	90	65	57
75	430	1270	3340	5930	107	95	72	63
90	NA	220	450	640	NA	102	95	91
97	NA	NA	NA	NA	NA	NA	NA	NA

Table 10.1.3.1.3d: Matrix properties for LBL-USGS sample 3.4 in the TSw1 and TSw2 units.

Percentage of repository area enclosed (%)	Time required to attain the indicated *RH* (yr)				Temperature at which the indicated *RH* is attained (°C)			
	70%	80%	90%	95%	70%	80%	90%	95%
50	870	2390	6660	10,600	106	89	67	59
75	510	1330	3210	5300	106	94	73	65
90	130	270	580	880	107	101	93	87
97	NA	NA	NA	NA	NA	NA	NA	NA

Table 10.1.3.1.3e: Matrix properties for LBL-USGS sample 3.3 in the TSw1 and TSw2 units.

Percentage of repository area enclosed (%)	Time required to attain the indicated *RH* (yr)				Temperature at which the indicated *RH* is attained (°C)			
	70%	80%	90%	95%	70%	80%	90%	95%
50	960	3180	14,200	29,100	105	81	54	43
75	580	1790	7430	15,050	106	87	60	50
90	140	320	910	1910	107	99	86	72
97	NA	NA	NA	NA	NA	NA	NA	NA

Table 10.1.3.1.4: AML = 110.5 MTU/acre

Time required to attain the indicated relative humidity *RH* at various repository locations and the temperature at which that value of *RH* is attained for 22.5-yr-old SNF, gas-phase diffusion tortousity factor τ_{eff} = 0.2,and k_b = 280 millidarcy. The locations are identified as the percentage of the repository area enclosed, with 0% corresponding to the repository center, and 100% corresponding to the edge.

Table 10.1.3.1.4a: Matrix properties for LBL-USGS sample 3.2 in the TSw1 and TSw2 units.

Percentage of repository area enclosed (%)	Time required to attain the indicated *RH* (yr)				Temperature at which the indicated *RH* is attained (°C)			
	70%	80%	90%	95%	70%	80%	90%	95%
50	5970	6410	7060	8740	96	93	90	85
75	3480	3830	4170	4800	100	98	95	91
90	1760	2070	2440	2640	106	102	99	97
97	840	1120	1450	1720	107	103	100	98

Table 10.1.3.1.4b: Matrix properties for LBL-USGS sample 3.5 in the TSw1 and TSw2 units.

Percentage of repository area enclosed (%)	Time required to attain the indicated *RH* (yr)				Temperature at which the indicated *RH* is attained (°C)			
	70%	80%	90%	95%	70%	80%	90%	95%
50	22,280	28,530	34,780	42,390	59	54	48	45
75	9580	12,710	17,200	23,350	75	68	61	55
90	2720	3680	4920	6760	97	89	82	75
97	1160	1530	1920	2290	107	103	98	93

Table 10.1.3.1.4c: Matrix properties for LBL-USGS samples 3.1 and 3.6 in the TSw1 and TSw2 units.

Percentage of repository area enclosed (%)	Time required to attain the indicated *RH* (yr)				Temperature at which the indicated *RH* is attained (°C)			
	70%	80%	90%	95%	70%	80%	90%	95%
50	31,570	48,790	72,310	94,690	51	42	37	34
75	16,160	30,080	45,930	58,990	63	49	41	38
90	3450	6560	12,010	18,980	91	76	64	54
97	1130	1620	2260	2820	107	102	94	88

Table 10.1.3.1.4d: Matrix properties for LBL-USGS sample 3.4 in the TSw1 and TSw2 units.

Percentage of repository area enclosed (%)	Time required to attain the indicated *RH* (yr)				Temperature at which the indicated *RH* is attained (°C)			
	70%	80%	90%	95%	70%	80%	90%	95%
50	31,290	47,260	71,840	93,860	51	43	37	34
75	16,470	29,220	44,140	57,350	62	50	42	38
90	3940	7260	12,780	19,080	87	74	62	54
97	1330	1830	2510	3490	107	100	91	83

Table 10.1.3.1.4e: Matrix properties for LBL-USGS sample 3.3 in the TSw1 and TSw2 units.

Percentage of repository area enclosed (%)	Time required to attain the indicated *RH* (yr)				Temperature at which the indicated *RH* is attained (°C)			
	70%	80%	90%	95%	70%	80%	90%	95%
50	33,940	61,360	119,890	185,850	49	38	32	31
75	19,730	39,340	78,500	112,770	57	44	35	33
90	4770	11,340	26,180	39,140	83	65	49	42
97	1350	1990	3410	5360	107	98	84	74

Table 10.1.3.1.5: AML = 150 MTU/acre

Time required to attain the indicated relative humidity *RH* at various repository locations and the temperature at which that value of *RH* is attained for 22.5-yr-old SNF, gas-phase diffusion tortousity factor $\tau_{eff} = 0.2$, and $k_b = 280$ millidarcy. The locations are identified as the percentage of the repository area enclosed, with 0% corresponding to the repository center, and 100% corresponding to the edge.

Table 10.1.3.1.5a: Matrix properties for LBL-USGS sample 3.2 in the TSw1 and TSw2 units.

Percentage of repository area enclosed (%)	Time required to attain the indicated *RH* (yr)				Temperature at which the indicated *RH* is attained (°C)			
	70%	80%	90%	95%	70%	80%	90%	95%
50	8960	9600	10,840	12,030	97	95	91	87
75	5690	6180	6830	8170	101	98	96	91
90	2980	3510	4060	4400	105	102	98	96
97	2020	2300	2650	2940	107	103	100	98

Table 10.1.3.1.5b: Matrix properties for LBL-USGS sample 3.5 in the TSw1 and TSw2 units.

Percentage of repository area enclosed (%)	Time required to attain the indicated *RH* (yr)				Temperature at which the indicated *RH* is attained (°C)			
	70%	80%	90%	95%	70%	80%	90%	95%
50	31,240	38,690	46,850	54,100	54	49	45	43
75	18,750	23,780	28,990	35,380	66	59	54	49
90	7740	9930	12,830	17,520	83	77	70	62
97	3480	4420	5820	8020	98	91	84	77

Table 10.1.3.1.5c: Matrix properties for LBL-USGS samples 3.1 and 3.6 in the TSw1 and TSw2 units.

Percentage of repository area enclosed (%)	Time required to attain the indicated *RH* (yr)				Temperature at which the indicated *RH* is attained (°C)			
	70%	80%	90%	95%	70%	80%	90%	95%
50	36,740	54,710	76,450	103,600	50	42	38	35
75	29,790	46,930	67,180	81,860	52	43	38	36
90	13,140	23,350	36,290	47,780	70	55	45	41
97	4630	7810	13,500	21,390	90	77	65	55

Table 10.1.3.1.5d: Matrix properties for LBL-USGS sample 3.4 in the TSw1 and TSw2 units.

Percentage of repository area enclosed (%)	Time required to attain the indicated *RH* (yr)				Temperature at which the indicated *RH* is attained (°C)			
	70%	80%	90%	95%	70%	80%	90%	95%
50	36,240	53,670	77,150	106,290	51	43	38	35
75	28,920	44,800	65,090	79,720	53	44	39	36
90	13,070	22,110	34,020	44,680	70	57	47	42
97	4970	7960	12,920	19,230	88	77	66	57

Table 10.1.3.1.5e: Matrix properties for LBL-USGS sample 3.3 in the TSw1 and TSw2 units.

Percentage of repository area enclosed (%)	Time required to attain the indicated *RH* (yr)				Temperature at which the indicated *RH* is attained (°C)			
	70%	80%	90%	95%	70%	80%	90%	95%
50	38,530	67,740	136,540	224,430	49	40	34	32
75	31,910	56,830	111,490	171,140	51	40	34	33
90	16,730	32,050	60,180	86,980	63	48	38	35
97	6120	11,790	23,940	36,410	83	68	52	44

10.1.3.2 Influence of Vapor Diffusion.

Gas-Phase Diffusion of Water Vapor

Transport of water vapor in the gas phase takes place by two mechanisms: (1) advective transport from movement of the gas phase, and (2) diffusive transport by the process of molecular diffusion. The binary diffusive mass flux of a component in a gas phase is governed by Fick's law, which for a porous medium takes the form

$$q = -\phi S_g \rho_g \tau \eta D \nabla \omega \qquad (8)$$

where ϕ is porosity, S_g is gas-phase saturation, ρ_g is gas density, τ is the tortuosity factor, η is the diffusion enhancement factor, D is the binary diffusion coefficient, and ω is the mass fraction of the component. The tortuosity factor, τ, is the reciprocal of the tortuosity and takes into account the increased path length within the porous medium. Its value is always less than or equal to unity.

The diffusion enhancement factor, η, which appears in Equation (8), can be taken to be unity for a noncondensible component or isothermal conditions. For diffusion of a condensible component, such as water vapor, driven by a thermal gradient, the diffusive flux is enhanced, so that η is greater than unity. The well-known paper by Philip and de Vries (1967) gives an explanation for this enhancement. Normally, diffusive transport of water vapor is obstructed by liquid water that blocks pore throats; consequently, diffusion is reduced at higher liquid saturations. However, the thermal gradient sets up a vapor pressure gradient in the gas phase which causes water to evaporate from a blockage and diffuse in the gas phase to a cooler blockage, where it condenses. The process continues as the water evaporates on the other side of the blockage. The mechanism whereby liquid water flows through a blockage is the pressure difference caused by the difference in meniscus curvature between the two sides.

Another phenomenon further increases diffusive fluxes under nonisothermal conditions. The gas-phase thermal conductivity is much less than that in the liquid and solid phases, so that the temperature gradient in the gas phase between liquid blockages is greater than the average temperature gradient of the bulk porous medium. The resulting increase in water vapor concentration gradients within the gas phase further increases diffusive fluxes compared to isothermal systems.

The diffusion enhancement factor is a function of liquid saturation and appears to increase significantly at sufficiently large saturations when blockages can occur, which is consistent with the above theory. The diffusion enhancement factor, η, appears to have been measured only for soils. Cass and others (1984) obtained values of η for sand that ranged from unity at 0% liquid saturation (i.e., no enhancement) to 12 at 80% liquid saturation. The value of η appears to decrease with increasing temperature. The maximum value of η decreased by almost 50% as temperature was increased from 3.5 to 32.5°C. This trend can be explained by the theory of Philip and de Vries. At greater temperatures, the higher latent heat carried by diffusive transport enhances heat transfer across the gas phase between blockages. The resulting decrease in gas-phase temperature gradients reduces the vapor-pressure gradients that drive diffusive transport.

The values of η are not directly input to the V-TOUGH code. Instead, V-TOUGH requires an effective gas-phase diffusion factor, τ_{eff}, which combines η with the tortuosity factor, τ, as follows:

$$\tau_{eff} = \eta\tau \qquad (9)$$

V-TOUGH treats τ_{eff} as a constant. If we take τ to be 0.2, and consider the upper value of 12 measured for η by Cass, we would get a value of 2.4 for τ_{eff}. For the 154.7-MTU/acre, 280-millidarcy case, we considered three values of τ_{eff}: 0.2, 1, and 2. Note that, unless specified otherwise, our calculations assume a value of 0.2 for τ_{eff}. Increasing τ_{eff} from 0.2 to 1 (thereby increasing gas-phase diffusion) results in a minor cooling effect (Fig. 10.1.3.2.1a). This cooling effect, which arises because of the increased transport of latent heat away from the repository, reduces the area-weighted boiling period duration, t_{bp}, from 7984 to 7622 yr. Increasing τ_{eff} from 0.2 to 1 also has a minor drying effect, modestly reducing the net

buildup of liquid water above the repository, ΔV_l (Fig. 10.1.3.2.1c). The maximum value of ΔV_l is only reduced by 3.2%.

As in past studies [Buscheck and Nitao, 1994], when analyzing dryout and rewetting behavior, we use the term, normalized liquid saturation, S_l, which is given by Eq.(8). The rewetting behavior of various AMLs is examined by comparing the duration of time that S_l in the repository is below 90% of ambient as a function of repository location [Buscheck et al., 1994]. Because $S_l = 0.9$ when S_l has been restored to 90% of ambient, we call this time $t(S_l = 0.9)$. The area-weighted value of $t(S_l = 0.9)$ for the entire repository is called $\bar{t}\,(\bar{S}_l = 0.9)$, which is essentially the mean rewetting time for the repository.

Figure 10.1.3.2.1b utilizes $t(S_l = 0.9)$ to illustrate rewetting behavior as a function of repository location for a range of τ_{eff}. Notice that the drying effect that results from enhanced gas-phase diffusion of water vapor increases the duration of time that most of the repository is below ambient saturation. For the inner 25% of the repository, $t(S_l = 0.9)$ is reduced somewhat (Fig. 10.1.3.2.1b) because of the reduction of t_{bp} (Fig. 10.1.3.2.1a). Because temperatures decrease with vertical distance from the repository horizon, gas-phase diffusion drives water vapor vertically away from the repository. Because temperatures also decrease with increasing radial distance, gas-phase diffusion also drives water vapor radially away from the repository. Notice that the enhanced dryout effect is greatest at the outer repository area, where temperature gradients drive water vapor radially as well as vertically away from the repository. Increasing τ_{eff} from 0.2 to 1 has the effect of increasing $t(S_l = 0.9)$ for the outer 75% of the repository. Consequently, $\bar{t}\,(\bar{S}_l = 0.9)$ is increased from 63,440 to 68,720 yr for the entire repository.

Increasing τ_{eff} from 0.2 to 2 results in a more substantial cooling effect, reducing t_{bp} from 7980 to 7320 yr (Fig. 10.1.3.2.1a). The greatest cooling effect occurs at the repository center (where the highest temperatures occur) and decreases with increasing distance from the repository center. At the repository edge, the cooling effect is minor. Increasing τ_{eff} from 0.2 to 2 also has a drying effect, reducing the maximum value of ΔV_l by 9.7% (Fig. 10.1.3.2.1c). The drying effect also increases $t(S_l = 0.9)$ for the outer 80% of the repository (Fig. 10.1.3.2.1b). Consequently, $\bar{t}\,(S_l = 0.9)$ is increased from 63,440 to 77,420 yr for the entire repository. In general, for the range of τ_{eff} considered, enhanced gas-phase diffusion results in a minor cooling effect and a minor drying effect. We plan to consider larger values of τ_{eff} and a larger range of AMLs in examining the influence of enhanced gas-phase diffusion.

Role of Vapor Diffusion in Dryout

The mole fraction of water vapor is considerably greater at the repository in response to higher temperatures there. The mole fraction n_v of water vapor under conditions of local thermodynamic equilibrium within the rock is a function of liquid saturation S_l, absolute temperature, T, and gas-phase pressure, P_g, and is given by the formula

$$n_v = [P_{sat}(T) / P_g] \exp[\psi M_w / (\rho_l RT)] \qquad (11)$$

which is a generalization of Kelvin's law to porous media. Here, $P_{sat}(T)$ is the saturation pressure, $\psi = \psi(S_l, T)$ is matric potential, M_w is molecular weight of water, ρ_l is the density of liquid water, and R is the universal gas constant. Note that $\psi < 0$; therefore, the greater the magnitude of ψ, the greater the vapor-pressure lowering effect. Note that the matric potential is a function of S_l and T. For ambient liquid saturation conditions at the repository horizon ($S_l \approx 60$–90%), the absolute value of ψ is sufficiently small such that the exponential term is essentially unity. Only at very low S_l does value of ψ become large enough for the exponential factor to have a significant effect on n_v.

As temperatures rise in the repository, the equilibrium amount of water vapor in the gas phase increases because of the increase in $P_{sat}(T)$. As temperatures reach the boiling point of water, P_{sat} approaches P_g and the mole fraction of water vapor approaches unity (i.e., the gas phase becomes 100% water vapor). The water in the rock near the fractures also starts to boil, causing the gas-phase pressure in the fractures and the rock matrix to rise, which leads to the advective transport of water vapor as long as steam is being generated. Gas-phase advection is likely to be the dominant mechanism transporting water vapor from the boiling zone to the condensation zone except for a rock mass where k_b is sufficiently small

(k_b < 1-10 millidarcy) to substantially throttle gas-phase advection and the rate of boiling. Beyond the condensation zone, vapor diffusion is the dominant mechanism of vapor movement except where k_b is sufficiently large (k_b > 1-10 darcy) for buoyant gas-phase convection to dominate. Because temperatures in the vicinity of the condensation zone are close to the boiling point, the water vapor mole fraction according to Eq. (11) is nearly unity, whereas for the region farther away from the repository (i.e., beyond the condensation zone), the temperatures are cooler and the mole fractions are much less (approximately 2% at ambient conditions). This gradient in mole fraction leads to diffusive fluxes that transport water vapor away from the condensation zone. Diffusive vapor fluxes can dominate over convective vapor fluxes around the repository if the vapor generation rate is very low or if temperatures are close to, but below, the boiling point.

Role of Vapor Diffusion in Rewetting

As the repository heat generation decays, water vapor continues to diffuse away from the repository because of the higher temperatures there. This diffusion of water vapor contributes to latent heat transport, thereby enhancing cooling of the repository. If S_l in the dryout zone is very low, the matric potential will be substantially higher than in the surrounding wetter rock. The exponential factor in Eq. (11) reduces the value of n_v in the dryout zone, and as temperatures decline, the value of n_v in the dryout zone will become smaller than that in the wetter rock away from the repository, even though temperatures are somewhat greater in the dryout zone. Thus, vapor diffusion can occur from cooler to hotter regions that have lower S_l. In general, water vapor diffuses away from the repository until repository temperatures have decreased enough so that the temperature effect (that drives water vapor away from the repository) in Eq. (11) can no longer overcompensate for the vapor-pressure lowering effect (that drives water vapor back towards the repository). This "vapor-pressure lowering" effect on n_v is significant only at lower S_l, which, for TSw2 tuff, occurs for S_l < 20-30%. Consequently, vapor diffusion will only significantly contribute to rewetting the dryout zone for S_l < 20-30%. For S_l > 20-30%, rewetting of the dryout zone will be dominated by liquid-phase advection driven by matric potential gradients and gravity. Note that the range of liquid saturation over which vapor-pressure lowering is not important depends strongly on the shape of the curve of matric potential versus S_l. The length of the time period during which diffusive vapor transport dominates rewetting behavior depends on:

- How dry the dryout zone becomes.
- The range of S_l that is associated with high matric potential.
- How quickly repository rock temperatures decline.

The longer that the dryout zone remains dry, the higher the value of S_l limit for which vapor-pressure lowering dominates rewetting behavior. The faster repository temperatures decrease while still in the high-matric-potential (i.e., dry) regime, the longer the duration of significant gas-phase diffusion of water vapor back to the dryout zone.

Influence of Enhanced Vapor Diffusion on Temperature and Relative Humidity in the Repository Rock

In the preceding section (Section 10.1.3.1), we presented the results of mountain-scale calculations for AMLs of 55.3, 110.5, and 150 MTU/acre, for six different sets of matrix properties for the TSw1 and TSw2 (Table 10.1.3.1.2), including five sets of matrix property data that are reported by Pruess and Tsang [1994], which are based on measurements by Flint and others [1993] and the reference matrix properties from the RIB [DOE, 1990]. Those calculations assumed a nominal value of gas-phase diffusion tortuosity factor (τ_{eff} = 0.2). From Eq. (9) we see that τ_{eff} is the product of the tortuosity factor τ and the vapor diffusion enhancement factor η. In this section we consider the possibility of "enhanced" binary gas-phase diffusion (τ_{eff} = 2.0) for the two high AML cases (AML = 110.5 and 150 MTU/acre). As discussed in Section 10.1.3.1, the value of matrix porosity, ϕ_m, was adjusted in order to yield roughly the same initial liquid water content in the TSw1 and TSw2. Accordingly, a value of ϕ_m = 0.11 was assumed for the three cases that yielded lower initial liquid saturation $S_{l,init}$ (the reference case with the RIB values, LBL-USGS-3.4, and LBL-USGS-3.3), and a value of ϕ_m = 0.10 was assumed for the three cases that yielded higher initial $S_{l,init}$ (LBL-USGS-3.5, LBL-USGS-3.2, and LBL-USGS-3.1/3.6).

Table 10.1.3.2.1 summarizes the time required to attain the indicated relative humidity *RH* in the rock at various repository locations and the temperature *T* at which that value of *RH* is attained for the "reference" matrix-property case based on the RIB [DOE, 1990] and Klavetter and Peters [1986] for AMLs of 110.5 and 150 MTU/acre and for $\tau_{eff} = 2.0$. For the five sets of LBL-USGS matrix-property data and AMLs of 110.5 and 150 MTU/acre, Tables 10.1.3.2.2 and 10.1.3.2.3 summarize the same *RH* and *T* information given in Table 10.1.3.2.1. Note that, although these cases have different values of saturated matrix permeability $k_{m,sat}$, they all share the same bulk permeability $k_b = 280$ millidarcy.

For AML = 110.5 MTU/acre, the five LBL-USGS matrix property cases fall into four categories with respect to the rate at which the repository rock rewets to (humid) ambient *RH*:

Fast rewetting rate: LBL-USGS-3.2 results in much faster rewetting to ambient *RH* than the reference case (compare Tables 10.1.3.2.1a and 10.1.3.2.2a). Consequently, when a given *RH* is attained, *T* is substantially higher for LBL-USGS-3.2 than in the reference case. For example, *T* at the repository center is 87°C when *RH* = 70% as compared with 70°C in the reference case. For LBL-USGS-3.2, enhanced binary gas-phase diffusion results in slower rewetting (compare Table 10.1.3.2.2a with 10.1.3.1.4a). Because $k_{m,sat}$ for LBL-USGS-3.2 is two orders of magnitude larger than in any of the other cases; advective liquid-phase rewetting (by matrix imbibition) proceeds much more quickly. This faster liquid-phase rewetting increases S_l to above the S_l range associated with the high matric-potential regime. This allows the vapor-pressure lowering in Eq. (11) to cease to be important at a time when there is still a steep temperature gradient away from the repository. Therefore, throughout the period that gas-phase diffusion is important, the temperature effect in Eq. (11) dominates over the vapor-pressure-lowering effect. Consequently, for LBL-USGS-3.2, the primary contribution of enhanced vapor diffusion is to enhance drying, while having little effect on gas-phase rewetting.

Medium rewetting rate: LBL-USGS-3.5 results in about the same rewetting rate as the reference case (compare Tables 10.1.3.2.1a and 10.1.3.2.2b). For LBL-USGS-3.5, enhanced vapor diffusion slightly increases the rewetting rate (relative to the nominal diffusion case) for the inner 75% of the repository, and slightly decreases the rewetting rate for the outer 25% (compare Table 10.1.3.2.2b with Table 10.1.3.1.4b).

Slow rewetting rate: LBL-USGS-3.1/3.6 and LBL-USGS-3.4 result in similar rewetting rates (to each other) that, for *RH* > 80%, are slower than the reference case in the inner 75% of the repository (compare Tables 10.1.3.2.1a, 10.1.3.2.2c, and 10.1.3.2.2d). For the outer 10% of the repository, these three cases have similar rewetting rates for *RH* < 80%. For the outer 10% of the repository and *RH* > 80%, these cases rewet more slowly than the reference case. A comparison of Tables 10.1.3.2.2c and d with Tables 10.1.3.1.4c and d shows that enhanced vapor diffusion increases the rewetting rate for the inner 75% of the repository and for *RH* < 95%, while it decreases the rewetting rate for the outer 10% of the repository. Because liquid-phase rewetting is slower for the inner 75% of LBL-USGS-3.1/3.6 and LBL-USGS-3.4 than in the reference case, the temperature gradient away from the repository becomes relatively shallow while the repository rock is still relatively dry; consequently, the temperature effect in Eq. (11) can no longer offset the vapor-pressure-lowering effect and vapor diffusion contributes to rewetting longer than in the reference case. In general, enhanced vapor diffusion increases the rewetting rate more substantially for LBL-USGS-3.1/3.6 and LBL-USGS-3.4 than for the reference case.

Very slow rewetting rate: LBL-USGS-3.3 results in slower rewetting rate than all of the other matrix-property sets (compare Table 10.1.3.2.2e with Tables 10.1.3.2.1a and 10.1.3.2.2a-d). A comparison of Table 10.1.3.2.2e with Table 10.1.3.1.4e shows that enhanced vapor diffusion increases the rewetting rate for the inner 75% of the repository, and slightly decreases the rewetting rate for the outer 25%. Because the advective liquid-phase rewetting rate is much slower for the inner 75% of USGS-LBL-3.3 than in the other cases, repository rock temperatures decline more quickly with respect to liquid saturation. Consequently, for LBL-USGS-3.3, the vapor-pressure-lowering effect significantly influences rewetting much longer than in the other cases, and enhanced vapor diffusion enhances rewetting more substantially than in the other cases.

For 110.5 MTU/acre and for the inner 75% of the repository, LBL-USGS-3.1/3.6, LBL-USGS-3.4, and LBL-USGS-3.3 have similar relationships between *T* and *RH*. In general, with the exception of LBL-USGS-3.2, there is not a great degree of variability in the relationship between *T* and *RH*. For all six matrix property cases, the outer 3% of the repository has a similar *T* versus *RH* relationship. Regardless of case, the outer 3% of the 110.5-MTU/acre repository is relatively hot (103 to 107°C at the time that *RH* = 70% is attained). With the exception of LBL-USGS-3.2, the inner 75% of the repository has cooled to relatively low temperatures (61 to 72°C) at the time that *RH* = 70% is attained.

For AML = 150 MTU/acre, the five LBL-USGS matrix property cases fall into four categories with respect to the rate at which the repository rock rewets to (humid) ambient *RH*:

Fast rewetting rate: LBL-USGS-3.2 results in much faster rewetting than the reference case (compare Tables 10.1.3.2.1b and 10.1.3.2.3a). Consequently, temperatures are significantly greater with respect to *RH*. For LBL-USGS-3.2, enhanced vapor diffusion results in slower rewetting than the nominal diffusion case (compare Table 10.1.3.2.3a with Table 10.1.3.1.5a). During the time that the temperature gradient away from the repository is still relatively steep, faster advective liquid-phase rewetting increases S_l to above the S_l range where vapor-pressure lowering is important. Throughout the period that gas-phase diffusion is important, the temperature effect in Eq. (11) dominates over the vapor-pressure-lowering effect. Consequently, for LBL-USGS-3.2, the primary contribution of enhanced vapor diffusion is to enhance drying, while having little effect on gas-phase rewetting.

Medium rewetting rate: LBL-USGS-3.5 results in nearly the same rewetting rate as the reference case (compare Tables 10.1.3.2.1b and 10.1.3.2.3b).

Slow rewetting rate: LBL-USGS-3.1/3.6 and LBL-USGS-3.4 result in similar rewetting rates (to each other) that are much slower than in the reference case (compare Tables 10.1.3.2.3c and d with Table 10.1.3.2.1b). A comparison of Tables 10.1.3.2.3c and d with Tables 10.1.3.1.5c and d of Section 10.1.3.1 shows that enhanced vapor diffusion increases the rewetting rate for the inner 50% of the repository and *RH* < 90%. For the outer 10% of the repository, enhanced vapor diffusion decreases the rewetting rate, particularly for *RH* > 80%.

Very slow rewetting rate: LBL-USGS-3.3 has a slower rewetting rate at any given repository location than any of the other cases (compare Table 10.1.3.2.3e with Table 10.1.3.2.1b and Tables 10.1.3.2.3a-d). A comparison of Table 10.1.3.2.3e with Table 10.1.3.1.5e shows that enhanced vapor diffusion increases the rewetting rate for the inner 75% of the repository, and substantially decreases the rewetting rate for the outer 3%. Because the advective liquid-phase rewetting rate is slower for the inner 75% of USGS-LBL-3.3 than in the other cases, repository temperatures decline quickly with respect to liquid saturation. Consequently, the vapor-pressure-lowering effect significantly impacts rewetting longer than in the other cases, and enhanced vapor diffusion enhances rewetting more substantially for LBL-USGS-3.3 than in any of the other cases.

Unlike the 110.5-MTU/acre case, the slower rewetting rates for LBL-USGS-3.1/3.6, LBL-USGS-3.4, and LBL-USGS-3.3 at 150 MTU/acre allow the outer 3% to decline to somewhat lower *T* (74 -81°C) as *RH* = 70% is attained. With the exception of LBL-USGS-3.2, the inner 75% of the repository has declined to relatively low temperatures (61-71°C) as *RH* = 70% is attained. With the exception of LBL-USGS-3.2, the inner 75% of the repository has declined to even lower *T* (49-61°C) as *RH* = 80% is attained.

In general, enhanced vapor diffusion enhances rewetting rate only where the advective liquid-phase rewetting rate is relatively slow to begin with (i.e., the cases with slow liquid-phase rewetting rates and at the center of the repository). Enhanced vapor diffusion reduces the overall rewetting rate where the advective liquid-phase rewetting rate is fastest (i.e., LBL-USGS-3.2 and at the edge of the repository). Therefore, enhanced vapor diffusion (if it actually exists) may be thought to function as somewhat of an "equalizer" of thermal-hydrological conditions in the repository rock, countering some of the effects of heating variability and natural system heterogeneity. For the LBL-USGS-3.3 properties, 150 MTU/acre and τ_{eff} = 0.2 (Table 10.1.3.1.5e), as *RH* = 70% is attained, temperatures range from 49 to 83°C from the 50 to 97% repository location (resulting in a 34°C spread), while for τ_{eff} = 2.0 (Table 10.1.3.2.3e), the temperature range is only 63 to 74°C.

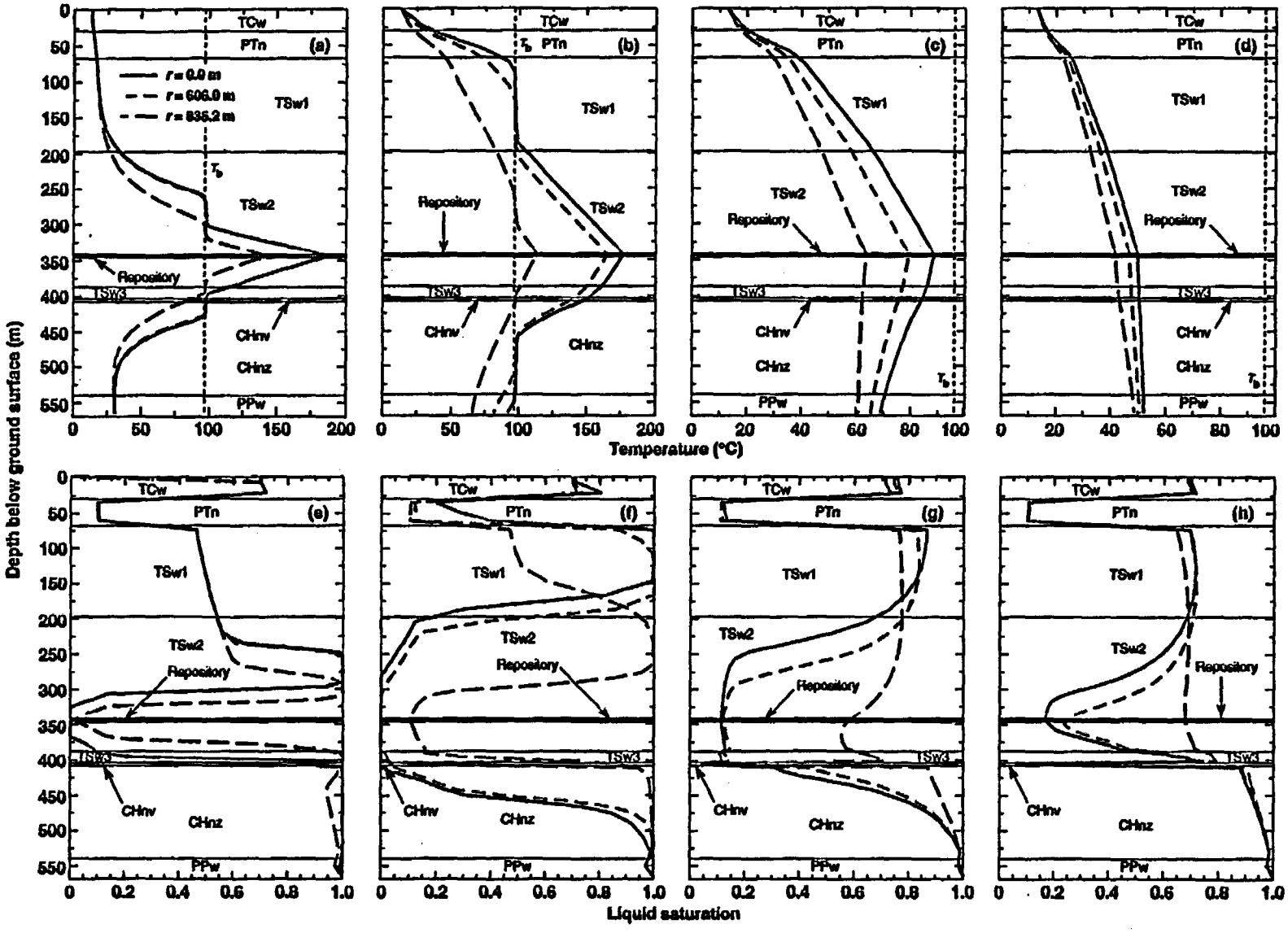

Figure 10.1.3.1.1. Vertical temperature profiles at various radial distances, r, for AML = 110.5 MTU/acre at (a) t = 100 yr, (b) t = 1000 yr, (c) t = 10,000 yr, and (d) t = 36,000 yr. Note different temperature scales. Vertical liquid saturation profiles are also plotted at (e) t = 100 yr, (f) t = 1000 yr, (g) t = 10,000 yr, and (h) t = 36,000 yr. Matrix properties for the TSw1 and TSw2 are based on Klavetter and Peters (1986). Binary gas-phase tortuosity factor $\tau_{eff} = 0.2$ for all units.

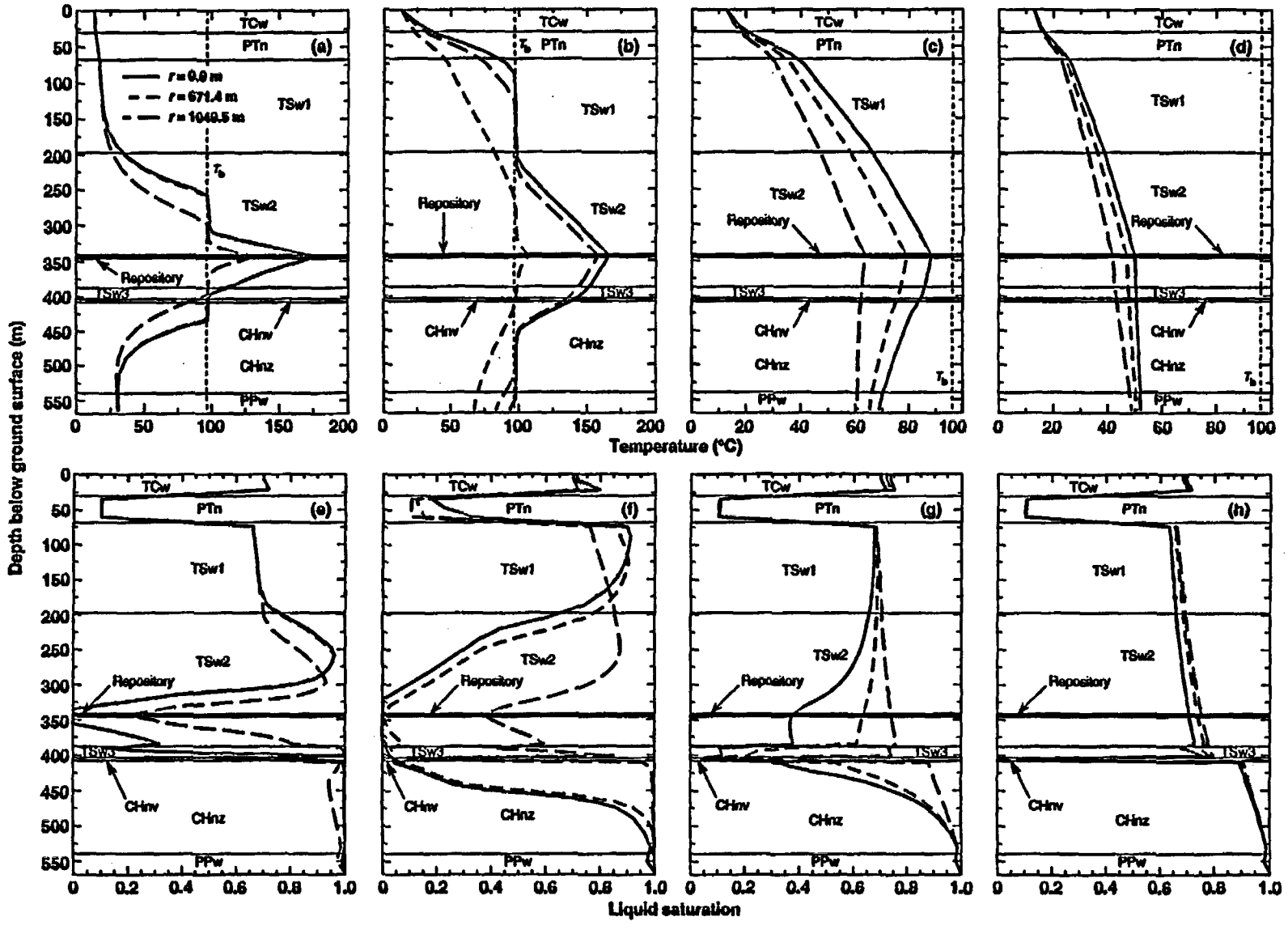

Figure 10.1.3.1.2. Vertical temperature profiles at various radial distances, r, for AML = 110.5 MTU/acre at (a) t = 100 yr, (b) t = 1000 yr, (c) t = 10,000 yr, and (d) t = 36,250 yr. Note different temperature scales. Vertical liquid saturation profiles are also plotted at (e) t = 100 yr, (f) t = 1000 yr, (g) t = 10,000 yr, and (h) t = 36,250 yr. Matrix properties for the TSw1 and TSw2 are based on LBL-USGS sample 3.2. Binary gas-phase tortuosity factor τ_{eff} = 0.2 for all units.

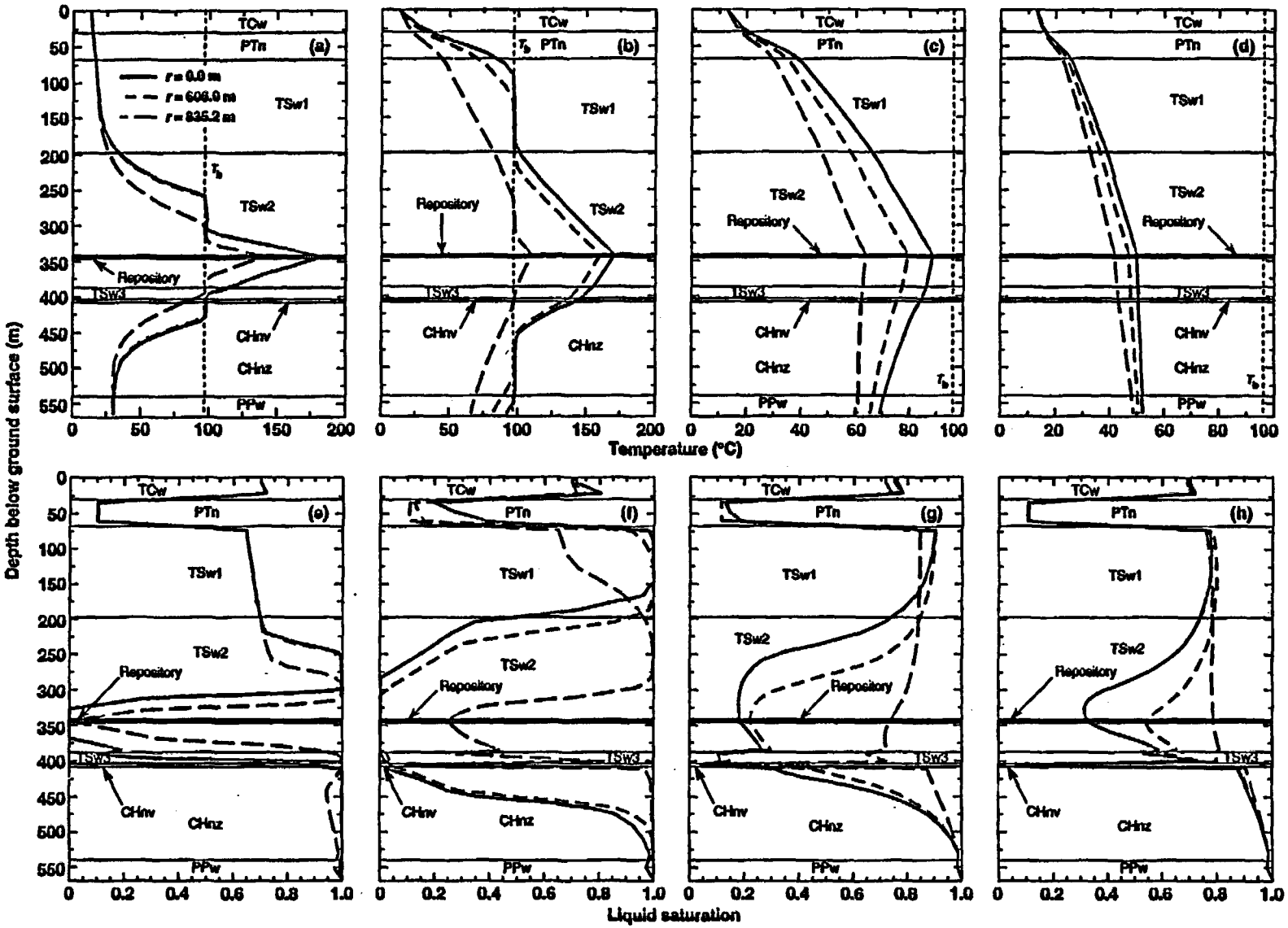

Figure 10.1.3.1.3. Vertical temperature profiles at various radial distances, r, for AML = 110.5 MTU/acre at (a) t = 100 yr, (b) t = 1000 yr, (c) t = 10,000 yr, and (d) t = 35,730 yr. Note different temperature scales. Vertical liquid saturation profiles are also plotted at (e) t = 100 yr, (f) t = 1000 yr, (g) t = 10,000 yr, and (h) t = 35,730 yr. Matrix properties for the TSw1 and TSw2 are based on LBL-USGS sample 3.5. Binary gas-phase tortuosity factor τ_{eff} = 0.2 for all units.

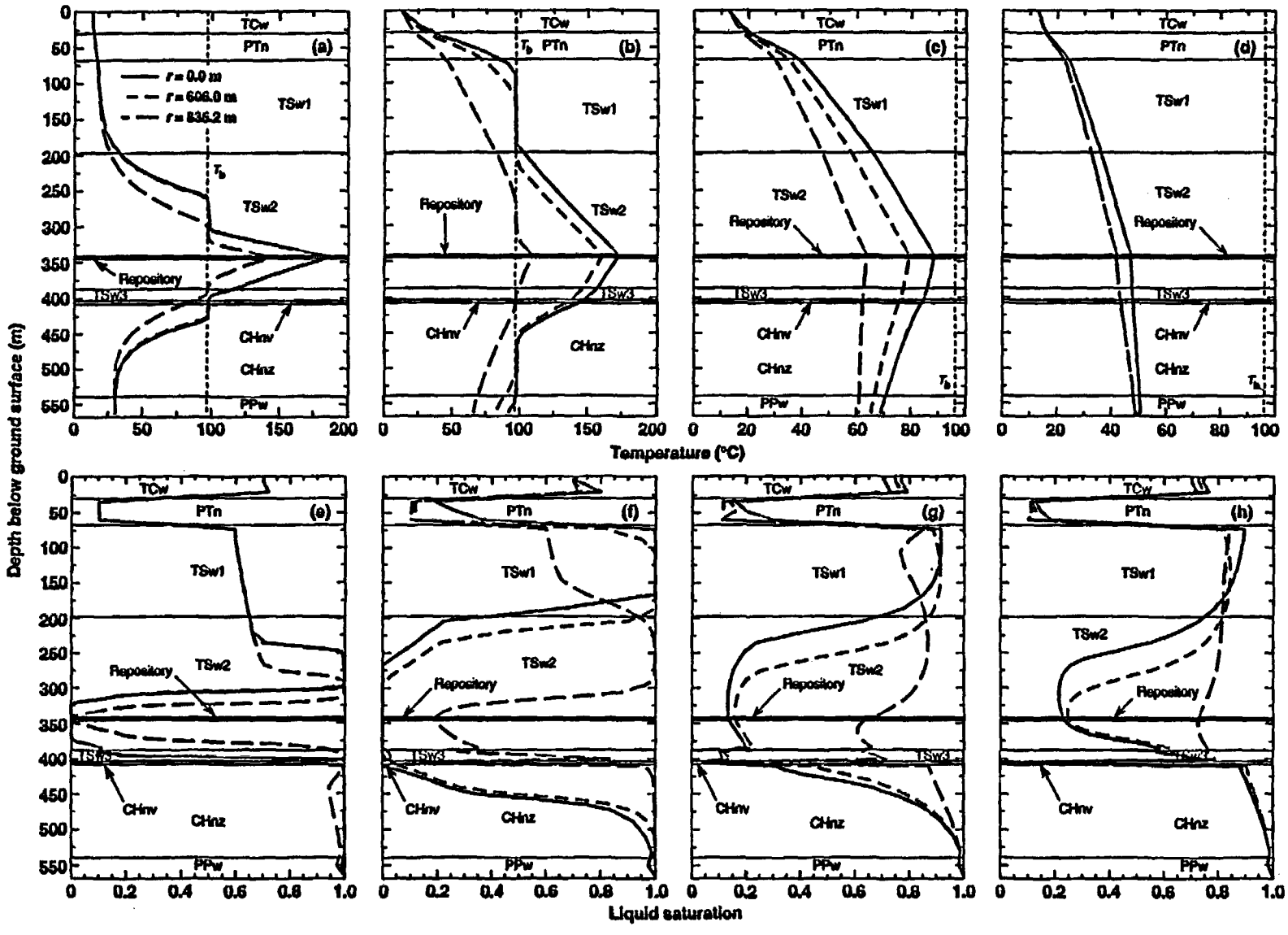

Figure 10.1.3.1.4. Vertical temperature profiles at various radial distances, r, for AML =110.5 MTU/acre at (a) t = 100 yr, (b) t = 1000 yr, (c) t = 10,000 yr, and (d) t = 35,400 yr. Note different temperature scales. Vertical liquid saturation profiles are also plotted at (e) t = 100 yr, (f) t = 1000 yr, (g) t = 10,000 yr, and (h) t = 35,400 yr. Matrix properties for the TSw1 and TSw2 are based on LBL-USGS sample 3.1/3.6. Binary gas-phase tortuosity factor τ_{eff} = 0.2 for all units.

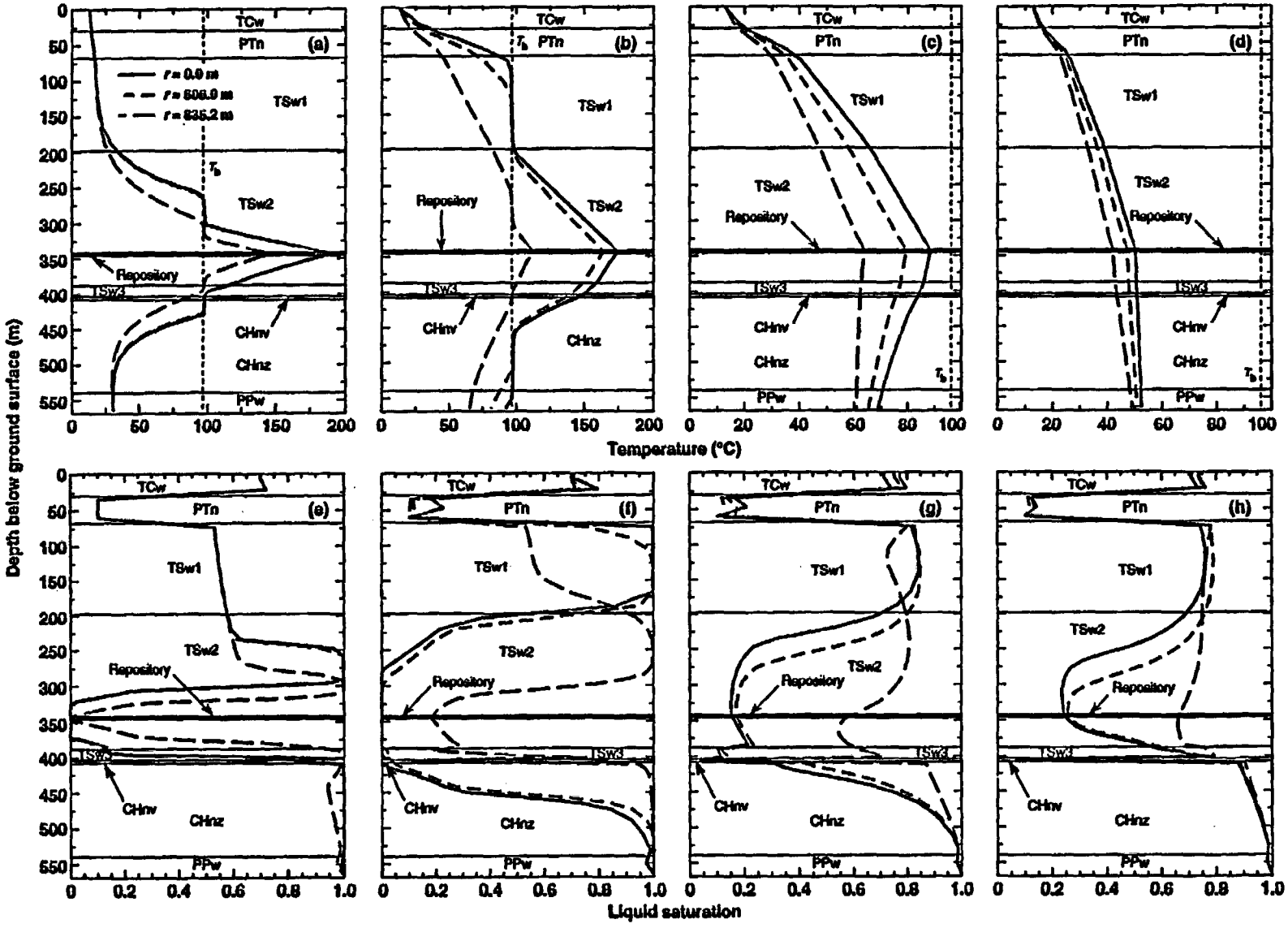

Figure 10.1.3.1.5. Vertical temperature profiles at various radial distances, r, for AML = 110.5 MTU/acre at (a) t = 100 yr, (b) t = 1000 yr, (c) t = 10,000 yr, and (d) t = 35,150 yr. Note different temperature scales. Vertical liquid saturation profiles are also plotted at (e) t = 100 yr, (f) t = 1000 yr, (g) t = 10,000 yr, and (h) t = 35,150 yr. Matrix properties for the TSw1 and TSw2 are based on LBL-USGS sample 3.4. Binary gas-phase tortuosity factor τ_{eff} = 0.2 for all units.

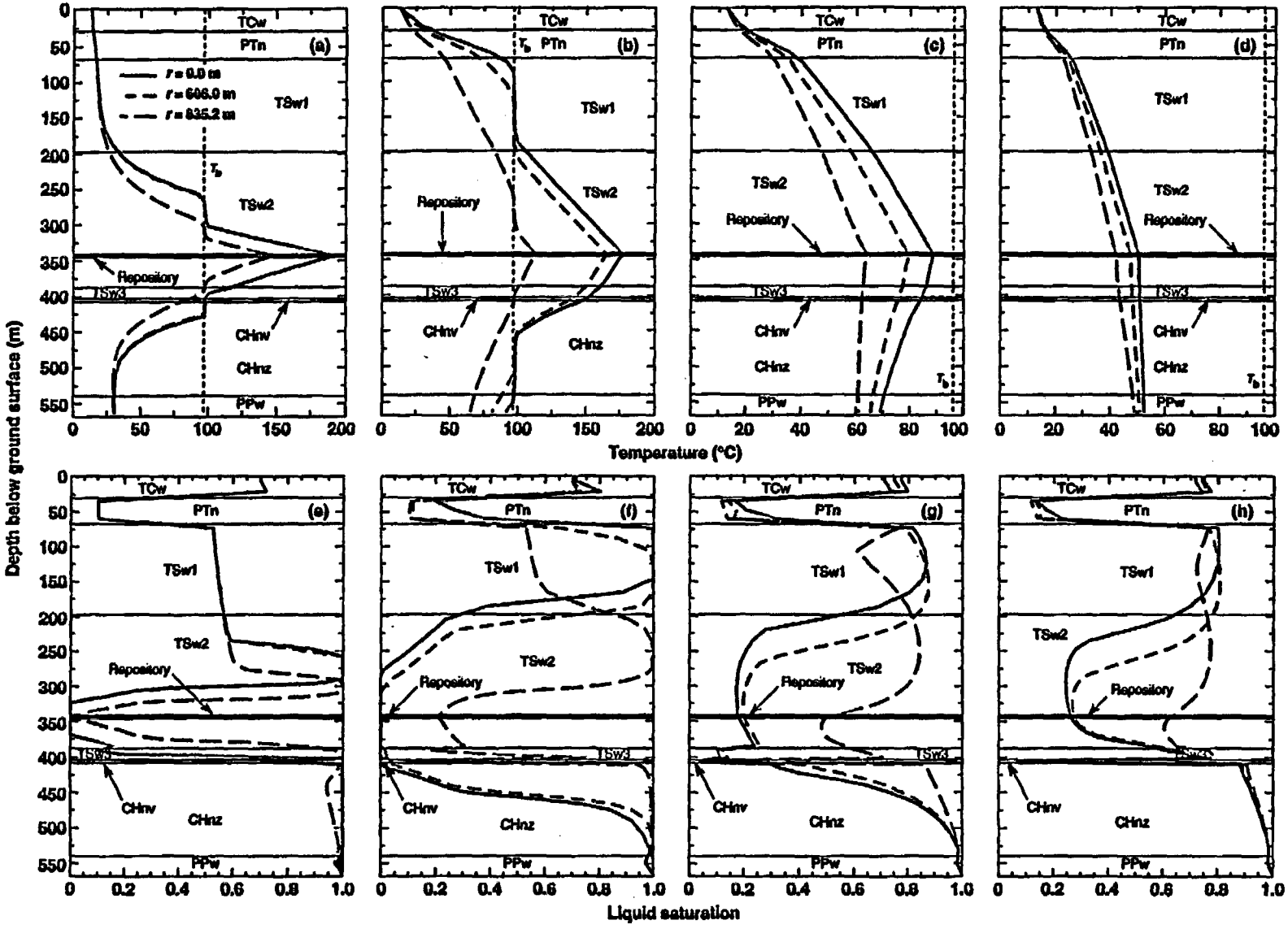

Figure 10.1.3.1.6. Vertical temperature profiles at various radial distances, r, for AML = 110.5 MTU/acre at (a) t = 100 yr, (b) t = 1000 yr, (c) t = 10,000 yr, and (d) t = 34,630 yr. Note different temperature scales. Vertical liquid saturation profiles are also plotted at (e) t = 100 yr, (f) t = 1000 yr, (g) t = 10,000 yr, and (h) t = 34,630 yr. Matrix properties for the TSw1 and TSw2 are based on LBL-USGS sample 3.3. Binary gas-phase tortuosity factor τ_{eff} = 0.2 for all units.

Table 10.1.3.2.1

Time required to attain the indicated relative humidity *RH* at various repository locations and the temperature at which that value of *RH* is attained for 22.5-yr-old SNF, gas-phase diffusion tortousity factor, τ_{eff} = 2.0, k_b = 280 millidarcy, and assuming the matrix properties from Klavetter and Peters (1986) for the TSw1 and TSw2 units. The locations are identified as the percentage of the repository area enclosed, with 0% corresponding to the repository center, and 100% corresponding to the edge.

Table 10.1.3.2.1a: AML = 110.5 MTU/acre

Percentage of repository area enclosed (%)	Time required to attain the indicated *RH* (yr)				Temperature at which the indicated *RH* is attained (°C)			
	70%	80%	90%	95%	70%	80%	90%	95%
50	14,260	23,850	42,270	59,750	70	57	44	38
75	10,180	17,870	33,350	47,150	72	59	46	41
90	3920	7730	16,040	26,640	85	71	57	48
97	1490	2240	4490	8130	104	93	76	65

Table 10.1.3.2.1b: AML = 150 MTU/acre

Percentage of repository area enclosed (%)	Time required to attain the indicated *RH* (yr)				Temperature at which the indicated *RH* is attained (°C)			
	70%	80%	90%	95%	70%	80%	90%	95%
50	19,470	29,380	48,260	64,180	69	56	45	41
75	15,390	23,380	36,100	45,900	71	59	48	44
90	9610	14,520	23,170	29,140	76	66	55	50
97	5310	8420	13,500	18,330	84	74	64	57

Table 10.1.3.2.2: AML = 110.5 MTU/acre

Time required to attain the indicated relative humidity *RH* at various repository locations and the temperature at which that value of *RH* is attained for 22.5-yr-old SNF, gas-phase diffusion tortousity factor $\tau_{eff_g} = 2.0$, and $k_b = 280$ millidarcy. The locations are identified as the percentage of the repository area enclosed, with 0% corresponding to the repository center, and 100% corresponding to the edge.

Table 10.1.3.2.2a: Matrix properties for LBL-USGS sample 3.2 in the TSw1 and TSw2 units.

Percentage of repository area enclosed (%)	Time required to attain the indicated *RH* (yr)				Temperature at which the indicated *RH* is attained (°C)			
	70%	80%	90%	95%	70%	80%	90%	95%
50	7590	9440	12,060	16,690	87	81	74	66
75	4000	4880	6490	8670	95	89	83	76
90	1860	2280	2760	3760	105	99	94	85
97	870	1170	1520	1800	107	103	99	97

Table 10.1.3.2.2b: Matrix properties for LBL-USGS sample 3.5 in the TSw1 and TSw2 units.

Percentage of repository area enclosed (%)	Time required to attain the indicated *RH* (yr)				Temperature at which the indicated *RH* is attained (°C)			
	70%	80%	90%	95%	70%	80%	90%	95%
50	14,610	23,000	36,210	46,260	69	57	47	42
75	9340	14,790	24,090	30,120	75	64	53	48
90	3080	5490	10,040	14,690	92	78	67	59
97	1190	1680	2560	4160	106	100	89	78

Table 10.1.3.2.2c: Matrix properties for LBL-USGS samples 3.1 and 3.6 in the TSw1 and TSw2 units.

Percentage of repository area enclosed (%)	Time required to attain the indicated *RH* (yr)				Temperature at which the indicated *RH* is attained (°C)			
	70%	80%	90%	95%	70%	80%	90%	95%
50	17,290	30,120	61,960	99,580	63	49	38	34
75	11,690	22,050	44,490	69,530	68	53	41	36
90	4070	9370	22,480	36,080	84	66	50	42
97	1220	1930	5290	12,620	106	97	72	57

Table 10.1.3.2.2d: Matrix properties for LBL-USGS sample 3.4 in the TSw1 and TSw2 units.

Percentage of repository area enclosed (%)	Time required to attain the indicated *RH* (yr)				Temperature at which the indicated *RH* is attained (°C)			
	70%	80%	90%	95%	70%	80%	90%	95%
50	17,640	30,050	60,100	102,350	62	49	38	34
75	12,320	22,860	45,340	73,170	66	52	40	36
90	4950	10,870	25,310	39,660	79	63	47	40
97	1510	2520	8360	17,600	104	90	64	51

Table 10.1.3.2.2e: Matrix properties for LBL-USGS sample 3.3 in the TSw1 and TSw2 units.

Percentage of repository area enclosed (%)	Time required to attain the indicated *RH* (yr)				Temperature at which the indicated *RH* is attained (°C)			
	70%	80%	90%	95%	70%	80%	90%	95%
50	17,940	30,420	68,620	149,230	61	48	37	31
75	12,980	24,460	52,390	103,200	65	51	38	33
90	5800	13,010	32,010	59,600	75	60	43	36
97	1620	3240	13,740	29,650	103	83	55	43

Table 10.1.3.2.3: AML = 150 MTU/acre

Time required to attain the indicated relative humidity *RH* at various repository locations and the temperature at which that value of *RH* is attained for 22.5-yr-old SNF, gas-phase diffusion tortousity factor $\tau_{eff.} = 2.0$, and $k_b = 280$ millidarcy. The locations are identified as the percentage of the repository area enclosed, with 0% corresponding to the repository center, and 100% corresponding to the edge.

Table 10.1.3.2.3a: Matrix properties for LBL-USGS sample 3.2 in the TSw1 and TSw2 units.

Percentage of repository area enclosed (%)	Time required to attain the indicated *RH* (yr)				Temperature at which the indicated *RH* is attained (°C)			
	70%	80%	90%	95%	70%	80%	90%	95%
50	11,790	13,940	17,810	22,390	86	80	72	65
75	7260	8640	10,930	13,650	93	88	81	74
90	3570	4260	5670	7200	101	96	89	83
97	2120	2490	2990	4020	106	102	97	90

Table 10.1.3.2.3b: Matrix properties for LBL-USGS sample 3.5 in the TSw1 and TSw2 units.

Percentage of repository area enclosed (%)	Time required to attain the indicated *RH* (yr)				Temperature at which the indicated *RH* is attained (°C)			
	70%	80%	90%	95%	70%	80%	90%	95%
50	20,720	30,360	44,280	55,940	67	56	47	43
75	15,270	22,040	30,860	39,420	71	61	52	47
90	8750	12,680	18,420	25,440	79	70	60	53
97	4250	6690	10,440	14,050	90	79	70	63

Table 10.1.3.2.3c: Matrix properties for LBL-USGS samples 3.1 and 3.6 in the TSw1 and TSw2 units.

Percentage of repository area enclosed (%)	Time required to attain the indicated *RH* (yr)				Temperature at which the indicated *RH* is attained (°C)			
	70%	80%	90%	95%	70%	80%	90%	95%
50	24,020	38,160	72,900	119,100	61	49	38	34
75	18,990	31,390	58,600	89,100	63	50	40	35
90	11,590	19,780	36,860	53,670	71	57	45	39
97	5910	10,810	21,280	32,270	81	68	53	45

Table 10.1.3.2.3d: Matrix properties for LBL-USGS sample 3.4 in the TSw1 and TSw2 units.

Percentage of repository area enclosed (%)	Time required to attain the indicated *RH* (yr)				Temperature at which the indicated *RH* is attained (°C)			
	70%	80%	90%	95%	70%	80%	90%	95%
50	25,430	38,420	73,620	129,110	64	51	39	34
75	19,590	31,890	59,570	95,320	62	50	40	35
90	12,540	21,500	39,160	59,060	69	56	44	38
97	6970	12,400	24,890	37,160	77	65	51	43

Table 10.1.3.2.3e: Matrix properties for LBL-USGS sample 3.3 in the TSw1 and TSw2 units.

Percentage of repository area enclosed (%)	Time required to attain the indicated *RH* (yr)				Temperature at which the indicated *RH* is attained (°C)			
	70%	80%	90%	95%	70%	80%	90%	95%
50	25,830	38,820	84,630	204,630	63	51	37	31
75	20,150	33,150	70,500	142,420	61	49	38	33
90	13,570	24,230	48,240	88,390	67	53	41	35
97	8040	14,690	31,250	53,880	74	61	46	38

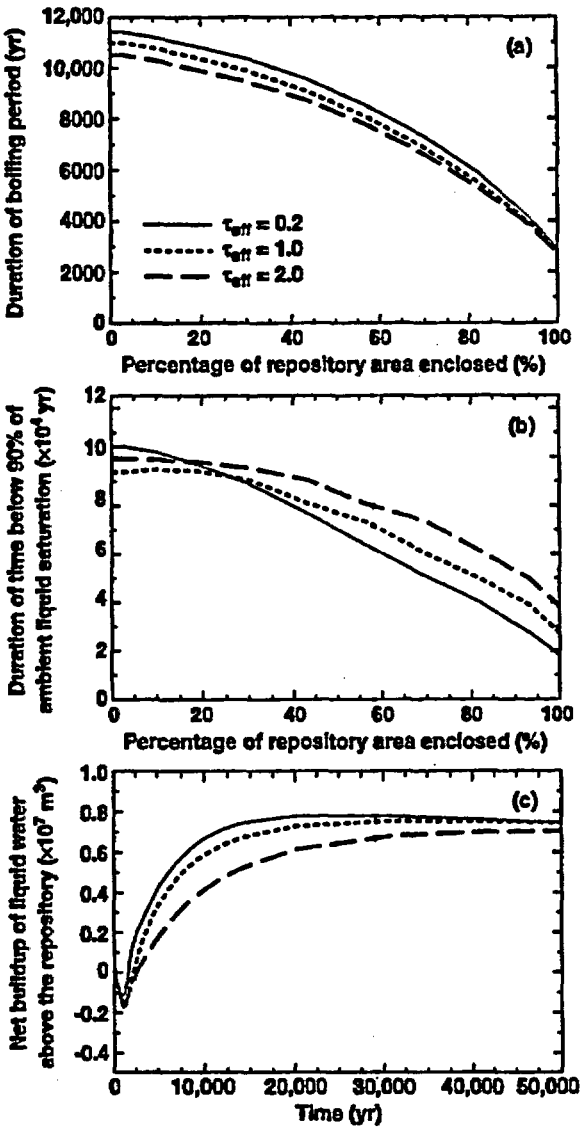

Figure 10.1.3.2.1. Duration of the boiling period (a) and duration of time below 90% of ambient liquid saturation (b) at various repository locations for an AML of 154.7 MTU/acre, k_b = 280 millidarcy, and various values of the effective diffusion factor, τ_{eff}. The repository locations are identified as the percentage of the repository area enclosed, with 0% corresponding to the repository center, and 100% corresponding to the outer perimeter. (c) The net buildup of liquid water above the repository is also plotted for these cases.

Contents

10.1.4 Influence of Overburden Thickness

10.1.4.1 Temperature and Relative Humidity in the Repository Rock. All of the mountain-scale (and drift-scale) analyses of temperature T and relative humidity RH conditions in the repository have assumed a repository depth of 343.1 m; in effect, the reference-overburden case has assumed a 343.1-m-thick overburden. Table 10.1.4.1.1 summarizes T and RH in the repository rock for the reference-overburden case and various AMLs; these cases assume k_b = 280 millidarcy, and "nominal" binary gas-phase diffusion, where the binary gas-phase diffusion tortuosity factor τ_{eff} = 0.2. Table 10.1.4.1.2a summarizes the duration of the boiling period, t_{bp}, and the value of RH at the end of the boiling period for the same suite of cases. Tables 10.1.4.1.3 and 10.1.4.1.2b summarize T and RH in the repository rock for the same suite of cases, but with a minimum-overburden of 200 m. (The 200-m-thick overburden case was chosen because it is the shallowest overburden thickness allowed by regulation.) For the reference 343.1-m-thick overburden case, the repository is 225 m above the water table, while in the 200-m-thick overburden case, it is 330 m above the water table. Because of the additional 105 m standoff from the water table, the liquid saturation at the repository horizon in the minimum-overburden case is about 10% less than in the reference-overburden case. Therefore, some of the following observations concerning RH in the repository rock may be influenced by that factor.

A comparison of Tables 10.1.4.1.2a and 10.1.4.1.2b clearly shows the influence of the overburden thickness in containing decay heat in Yucca Mountain. Effectively, the overburden acts like a thermal insulator (or blanket), determining how long it takes for decay heat to eventually be dissipated to the atmosphere. Therefore, we find that removing 143.1 m of this "thermal blanket" has the effect of reducing the duration of the boiling period, t_{bp}, especially in the center of the repository. In general, removing 143.1 m of the overburden has the following effects:

1. A substantial reduction in t_{bp} in areas associated with large t_{bp}, such as:
   a. The entire 150-MTU/acre repository.
   b. The inner 90% of the 110.5-MTU/acre repository.
   c. The inner 50% of the 83.4-MTU/acre repository.
2. A moderate reduction in t_{bp} in areas associated with intermediate t_{bp}, such as:
   a. The inner 50% of the 55.3-MTU/acre repository.
   b. The inner 75% of the 70.0-MTU/acre repository.
   c. The outer 10% of the 110.5-MTU/acre repository.
3. A negligible reduction in t_{bp} in areas associated with small t_{bp}, such as:
   a. The outer 50% of the 55.3-MTU/acre repository.
   b. The outer 10% of the 70.0-MTU/acre repository.
   c. The outer 3% of the 83.4-MTU/acre repository.

In general, the edge-cooling effect influences t_{bp} at the repository edge more than the impact of overburden thickness. We also generally observe for the minimum-overburden cases, a reduction in RH associated with the end of the boiling period relative to the reference-overburden cases.

In past work [Buscheck and Nitao, 1992] we have observed for cases where boiling effects (both convective and diffusive) dominate net moisture movement away from the dryout zone, roughly 95% of the cumulative dryout occurs during the first 1000 yr. Because the reduction in the insulating effect of the overburden does not begin to reduce repository temperatures until after 1000 yr, it does not significantly reduce the cumulative dryout effects. Consequently, we find in comparing Tables 10.1.4.1.1 and 10.1.4.1.3 that the duration of drier-than-ambient RH in the repository rock is generally similar for the reference-overburden and minimum-overburden case. Perhaps had we adjusted the standoff to the water table to be the same (thereby, yielding nearly identical initial liquid saturation profiles), the shallow-overburden

cases may have resulted in slightly shorter periods of drier-than-ambient *RH* in the repository rock than in the reference-overburden cases.

It is important to note that all of our modeling work has assumed a very humid value of *RH* in the atmosphere (99% for the cases that are in gravity-capillary-pressure equilibrium with the water table). Under ambient conditions, the partial pressure vapor of water vapor P_v in the atmosphere is assumed to be in equilibrium with P_v in the upper TCw unit. This prevents any diffusive loss of moisture to the atmosphere under ambient conditions. The decay-heat-driven temperature gradient near the ground surface is substantially greater than the temperature gradient under ambient conditions. For the reference-overburden, 150.0-MTU/acre case the temperature gradient at the ground surface exceeds the ambient temperature gradient by factors of 34, 25, 8, 5, 2.2, and 1.1 at t = 500, 1000, 10,000, 20,000, 50,000, and 100,000 yr, respectively. For the minimum-overburden, 150.0-MTU/acre case, the temperature gradient at the ground surface exceeds the ambient temperature gradient by factors of 62, 44, 11, 6, 3, and 1.6 at t = 200, 1000, 10,000, 20,000, 50,000, and 100,000 yr, respectively. The effect of a shallower overburden is to significantly steepen the temperature gradient at the ground surface relative to the reference-overburden case. In Section 10.1.3.2, we noted that binary gas-phase diffusion is primarily driven by temperature gradients. It is possible that binary gas-phase diffusion drives a substantial vapor flux to the atmosphere even under the ambient geothermal temperature gradient. As noted, because we assume *RH* = 99% in the atmosphere, our models do not yield any diffusive vapor flux to the atmosphere under ambient conditions. Had our models represented the actual atmospheric *RH* conditions, it is likely that we would have observed:

1. Moisture loss to the atmosphere under the ambient geothermal temperature gradient.
2. A substantially greater decay-heat-driven moisture loss to the atmosphere for both the reference- and shallow-overburden cases.
3. The greatest atmospheric moisture loss would occur for the shallow-overburden cases, resulting in lower *RH* in the repository rock than in the reference-overburden cases.

This last observation implies that had we modeled the actual *RH* conditions in the atmosphere, repository *RH* conditions may be substantially drier for the shallow-overburden cases than for the reference-overburden cases.

Enhanced binary gas-phase diffusion would result in even larger evaporative losses to the atmosphere under both ambient and decay-heat-disturbed conditions. It is possible that a substantial evaporative loss could significantly reduce the liquid-phase saturation all the way down to the PTn unit (and perhaps even below the PTn), thereby significantly reducing much of the condensate buildup that may occur above a high-AML repository. Shallow *in situ* heater tests would provide valuable information concerning the influence of decay heat on the moisture balance near the ground surface at Yucca Mountain and to help validate T-H models that are required to assess the influence of decay heat on the overall moisture balance at Yucca Mountain.

Because the stored decay heat in Yucca Mountain is dissipated to the atmosphere significantly earlier in the minimum-overburden cases, T associated with a given value of *RH* is significantly lower than in the reference-overburden cases (compare Tables 10.1.4.1.1 and 10.1.4.1.3). For the 150-MTU/acre case, T associated with *RH* = 70% is reduced by 20°C for the inner 50% of the repository and by 11 to 12°C for the outer 25% of the repository. This reduction in T associated with a given *RH* reduces the likelihood of generating significant aqueous reactions and aqueous-transport processes that could give rise to altered flow and tranport properties in the repository rock.

Table 10.1.4.1.1: Reference-Overburden Cases

Time required to attain the indicated relative humidity *RH* at various repository locations and the temperature at which that value of *RH* is attained for 22.5-yr-old SNF, gas-phase diffusion tortousity factor τ_{eff} = 0.2, k_b = 280 millidarcy, and a repository depth of 343.1 m. The locations are identified as the percentage of the repository area enclosed, with 0% corresponding to the repository center, and 100% corresponding to the edge.

Table 10.1.4.1.1a: AML = 55.3 MTU/acre

Percentage of repository area enclosed (%)	Time required to attain the indicated *RH* (yr)				Temperature at which the indicated *RH* is attained (°C)			
	70%	80%	90%	95%	70%	80%	90%	95%
50	670	1660	3330	4630	107	97	80	72
75	410	940	1610	2280	107	99	89	81
90	NA	200	380	490	NA	103	97	95
97	NA	NA	NA	NA	NA	NA	NA	NA

Table 10.1.4.1.1b: AML = 70 MTU/acre

Percentage of repository area enclosed (%)	Time required to attain the indicated *RH* (yr)				Temperature at which the indicated *RH* is attained (°C)			
	70%	80%	90%	95%	70%	80%	90%	95%
50	3350	8700	16,150	23,560	91	69	56	49
75	1940	4080	7630	10,450	97	77	66	61
90	630	1030	1760	2460	105	97	85	78
97	80	170	290	390	107	103	99	96

Table 10.1.4.1.1c: AML = 83.4 MTU/acre

Percentage of repository area enclosed (%)	Time required to attain the indicated *RH* (yr)				Temperature at which the indicated *RH* is attained (°C)			
	70%	80%	90%	95%	70%	80%	90%	95%
50	8110	17,710	29,290	38,360	76	58	48	43
75	3910	8250	13,820	19,040	86	70	59	53
90	1240	2030	3530	4800	104	91	78	73
97	370	590	890	1140	107	103	98	94

Table 10.1.4.1.1c: AML = 110.5 MTU/acre

Percentage of repository area enclosed (%)	Time required to attain the indicated *RH* (yr)				Temperature at which the indicated *RH* is attained (°C)			
	70%	80%	90%	95%	70%	80%	90%	95%
50	15,960	27,910	40,990	49,980	68	54	45	42
75	9540	15,520	24,950	32,590	76	64	53	48
90	3190	4890	7460	9890	93	82	73	68
97	1410	1810	2360	2890	106	101	93	88

Table 10.1.4.1.1e: AML = 150 MTU/acre

Percentage of repository area enclosed (%)	Time required to attain the indicated *RH* (yr)				Temperature at which the indicated *RH* is attained (°C)			
	70%	80%	90%	95%	70%	80%	90%	95%
50	20,630	34,850	50,920	64,150	68	52	45	41
75	16,400	24,520	32,700	43,360	70	59	51	46
90	8660	12,090	16,520	19,780	81	72	64	59
97	4330	6020	8180	10,060	93	84	77	72

Table 10.1.4.1.2a: Reference-Overburden Cases

Duration of boiling period at various repository locations and relative humidity *RH* attained at the end of the boiling period for 22.5-yr-old SNF, and various AMLs, gas-phase diffusion tortousity factor τ_{eff} = 0.2, k_b = 280 millidarcy, and a repository depth of 343.1 m. The repository locations are identified as the percentage of the repository area enclosed, with 0% corresponding to the repository center,and 100% corresponding to the edge.

Table 10.1.4.1.2a: Reference-Overburden Cases
repository depth = 343.1 m

Percentage of repository area enclosed (%)	Duration of boiling period (yr) and *RH* (%) at end of boiling period for indicated AMLs				
	55.3 MTU/acre	70.0 MTU/acre	83.4 MTU/acre	110.5 MTU/acre	150.0 MTU/acre
50	1760 yr 80.8%	2830 yr 68.1%	3870 yr 57.2%	6130 yr 44.3%	9590 yr 46.8%
75	1100 yr 83.7%	2000 yr 70.5%	2740 yr 65.2%	4290 yr 51.4%	7210 yr 45.1%
90	440 yr 92.7%	1090 yr 81.0%	1700 yr 76.6%	2870 yr 67.6%	5010 yr 54.1%
97	80 yr 98.5%	410 yr 95.5%	990 yr 92.5%	2150 yr 86.6%	3960 yr 66.8%

Table 10.1.4.1.2b: Minimum-Overburden Cases
repository depth = 200 m

Percentage of repository area enclosed (%)	Duration of boiling period (yr) and *RH* (%) at end of boiling period for indicated AMLs				
	55.3 MTU/acre	70.0 MTU/acre	83.4 MTU/acre	110.5 MTU/acre	150.0 MTU/acre
50	1390 yr 76.7%	1960 yr 61.8%	2450 yr 54.7%	3600 yr 43.1%	5720 yr 27.6%
75	1070 yr 77.4%	1550 yr 61.3%	1930 yr 54.8%	2700 yr 47.6%	4170 yr 36.3%
90	460 yr 86.3%	980 yr 76.7%	1360 yr 67.5%	1960 yr 56.9%	2970 yr 49.0%
97	80 yr 96.9%	450 yr 92.0%	900 yr 86.2%	1590 yr 73.7%	2440 yr 60.7%

Table 10.1.4.1.3: Minimum-Overburden Cases

Time required to attain the indicated relative humidity *RH* at various repository locations and the temperature at which that value of *RH* is attained for 22.5-yr-old SNF, gas-phase diffusion tortousity factor τ_{eff} = 0.2, k_b = 280 millidarcy, and a repository depth of 200 m. The locations are identified as the percentage of the repository area enclosed, with 0% corresponding to the repository center, and 100% corresponding to the edge.

Table 10.1.4.1.3a: AML = 55.3 MTU/acre

Percentage of repository area enclosed (%)	Time required to attain the indicated *RH* (yr)				Temperature at which the indicated *RH* is attained (°C)			
	70%	80%	90%	95%	70%	80%	90%	95%
50	960	1820	4270	6320	105	87	61	55
75	680	1260	2640	4120	105	91	68	57
90	130	280	620	810	106	100	93	86
97	NA	NA	NA	NA	NA	NA	NA	NA

Table 10.1.4.1.3b: AML = 70 MTU/acre

Percentage of repository area enclosed (%)	Time required to attain the indicated *RH* (yr)				Temperature at which the indicated *RH* is attained (°C)			
	70%	80%	90%	95%	70%	80%	90%	95%
50	4680	10,270	16,370	24,020	67	54	47	41
75	3340	7350	12,070	18,150	69	55	48	43
90	680	1210	2410	3930	104	90	68	58
97	120	200	380	560	106	102	97	93

Table 10.1.4.1.3c: AML = 83.4 MTU/acre

Percentage of repository area enclosed (%)	Time required to attain the indicated *RH* (yr)				Temperature at which the indicated *RH* is attained (°C)			
	70%	80%	90%	95%	70%	80%	90%	95%
50	8300	15,510	24,760	31,050	62	50	43	389
75	6300	10,905	16,210	21,800	62	53	47	43
90	1550	3110	5660	8000	91	67	57	53
97	420	680	1090	1500	106	101	91	82

Table 10.1.4.1.3c: AML = 110.5 MTU/acre

Percentage of repository area enclosed (%)	Time required to attain the indicated *RH* (yr)				Temperature at which the indicated *RH* is attained (°C)			
	70%	80%	90%	95%	70%	80%	90%	95%
50	15,710	24,480	34,490	48,000	57	48	41	36
75	10,230	14,850	19,410	28,820	61	54	49	42
90	4120	6480	8830	11,040	71	63	58	54
97	1360	1920	2910	4220	101	87	73	65

Table 10.1.4.1.3e: AML = 150 MTU/acre

Percentage of repository area enclosed (%)	Time required to attain the indicated *RH* (yr)				Temperature at which the indicated *RH* is attained (°C)			
	70%	80%	90%	95%	70%	80%	90%	95%
50	30,780	45,790	68,730	100,200	48	41	35	32
75	16,930	23,230	30,370	44,000	58	51	45	40
90	8000	10,650	13,380	17,070	69	63	58	53
97	3600	5190	6870	8680	82	72	66	62

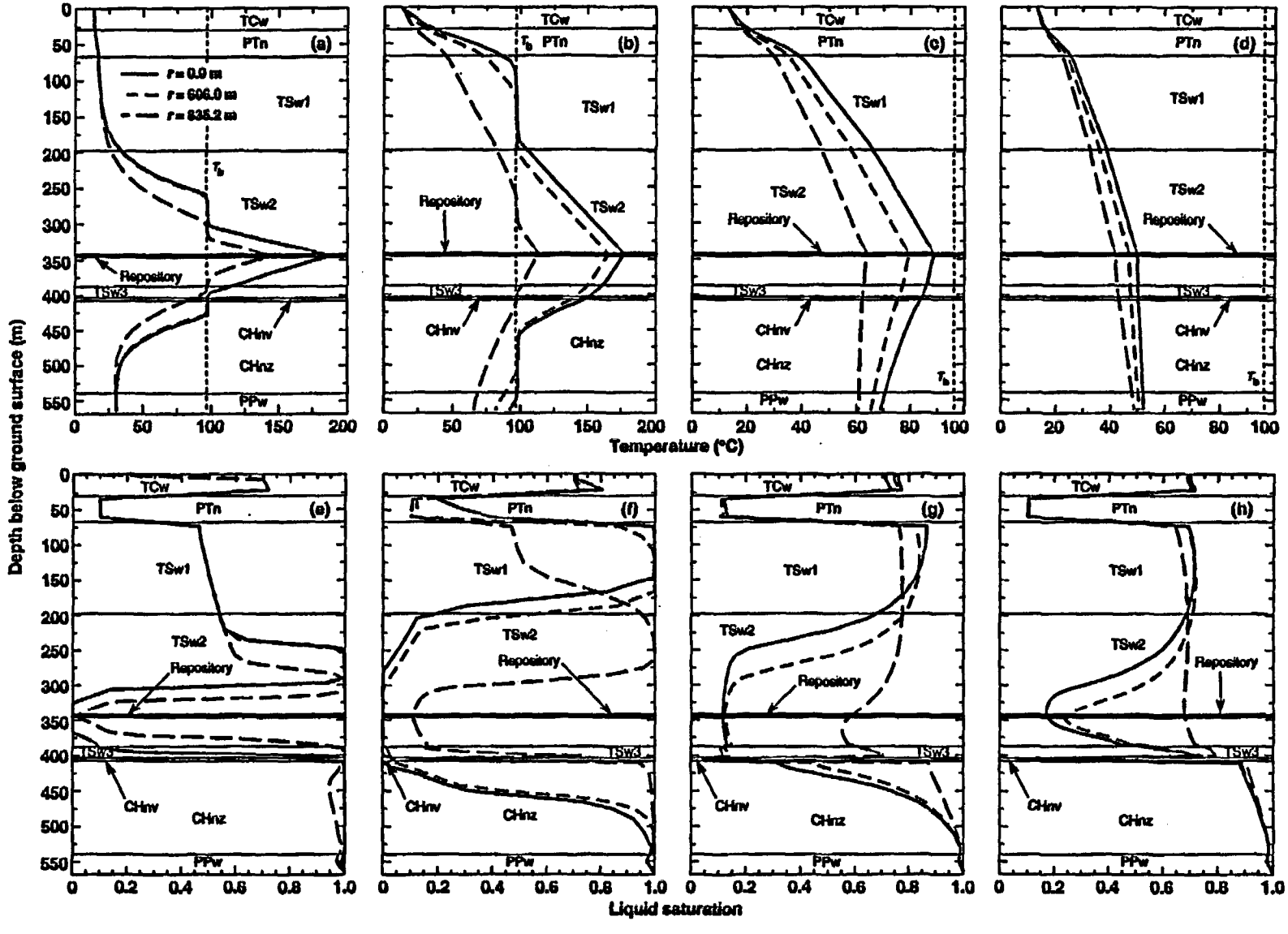

Figure 10.1.4.2.1. Vertical temperature profiles at various radial distances, r, for AML = 110.5 MTU/acre at (a) t = 100 yr, (b) t = 1000 yr, (c) t = 10,000 yr, and (d) t = 36,000 yr. Note different temperature scales. Vertical liquid saturation profiles are also plotted at (e) t = 100 yr, (f) t = 1000 yr, (g) t = 10,000 yr, and (h) t = 36,000 yr. Matrix properties for the TSw1 and TSw2 are based on Klavetter and Peters (1986). Binary gas-phase tortuosity factor $\tau_{eff} = 0.2$ for all units.

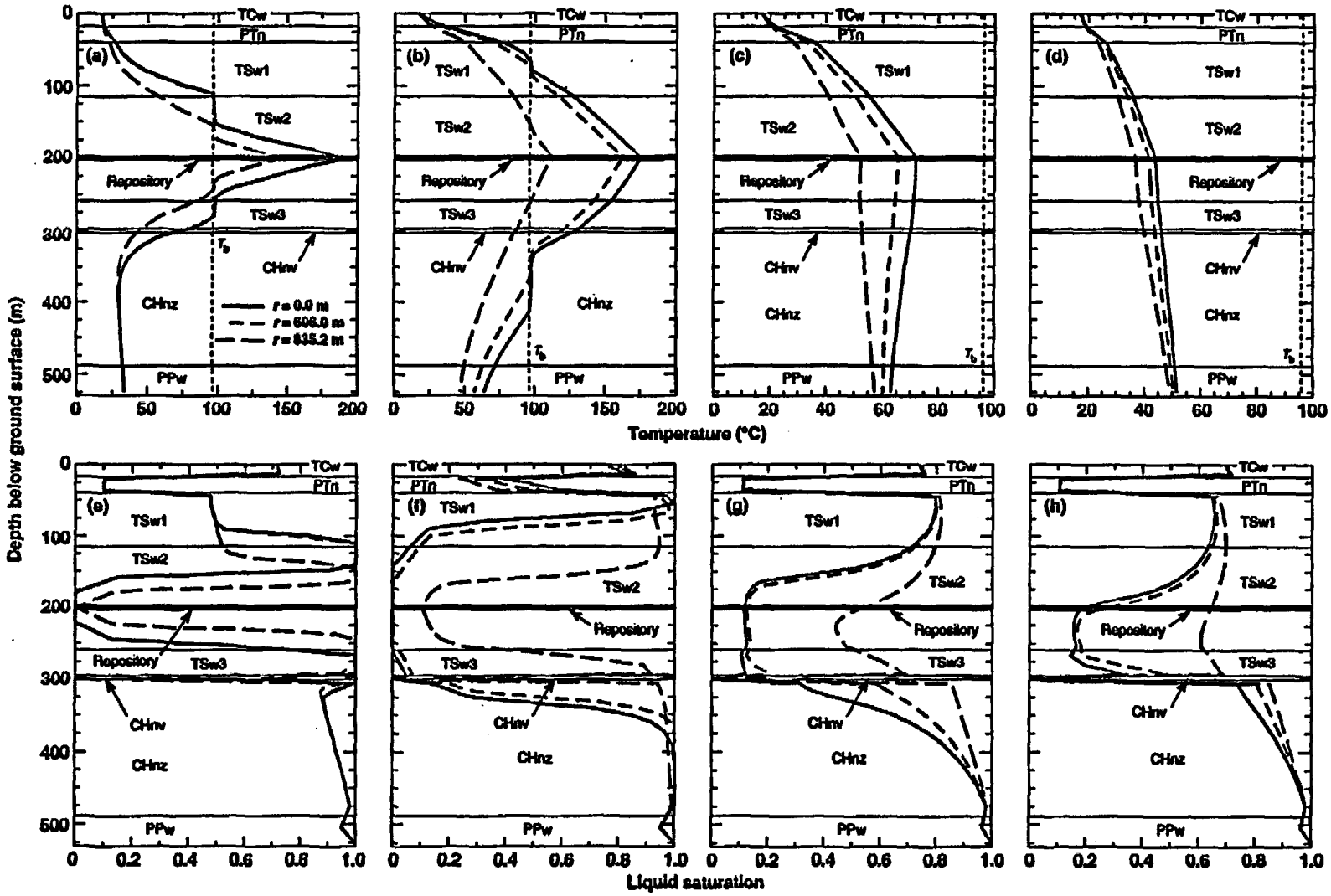

Figure 10.1.4.2.2. Vertical temperature profiles at various radial distances, r, for AML = 110.5 MTU/acre and the minimum-overburden-thickness (200 m) case at (a) t = 100 yr, (b) t = 1000 yr, (c) t = 10,000 yr, and (d) t = 32,730 yr. Note the different temperature scales. Vertical liquid saturation profiles are also plotted at (e) t = 100 yr, (f) t = 1000 yr, (g) t = 10,000 yr, and (h) t = 32,730 yr. The water table is at a depth of 530 m. Matrix poperties for all units (including the TSw1 and TSw2) are based on Klavetter and Peters [1986]. Binary gas-phase tortuosity factor τ_{eff} = 0.2 for all units.

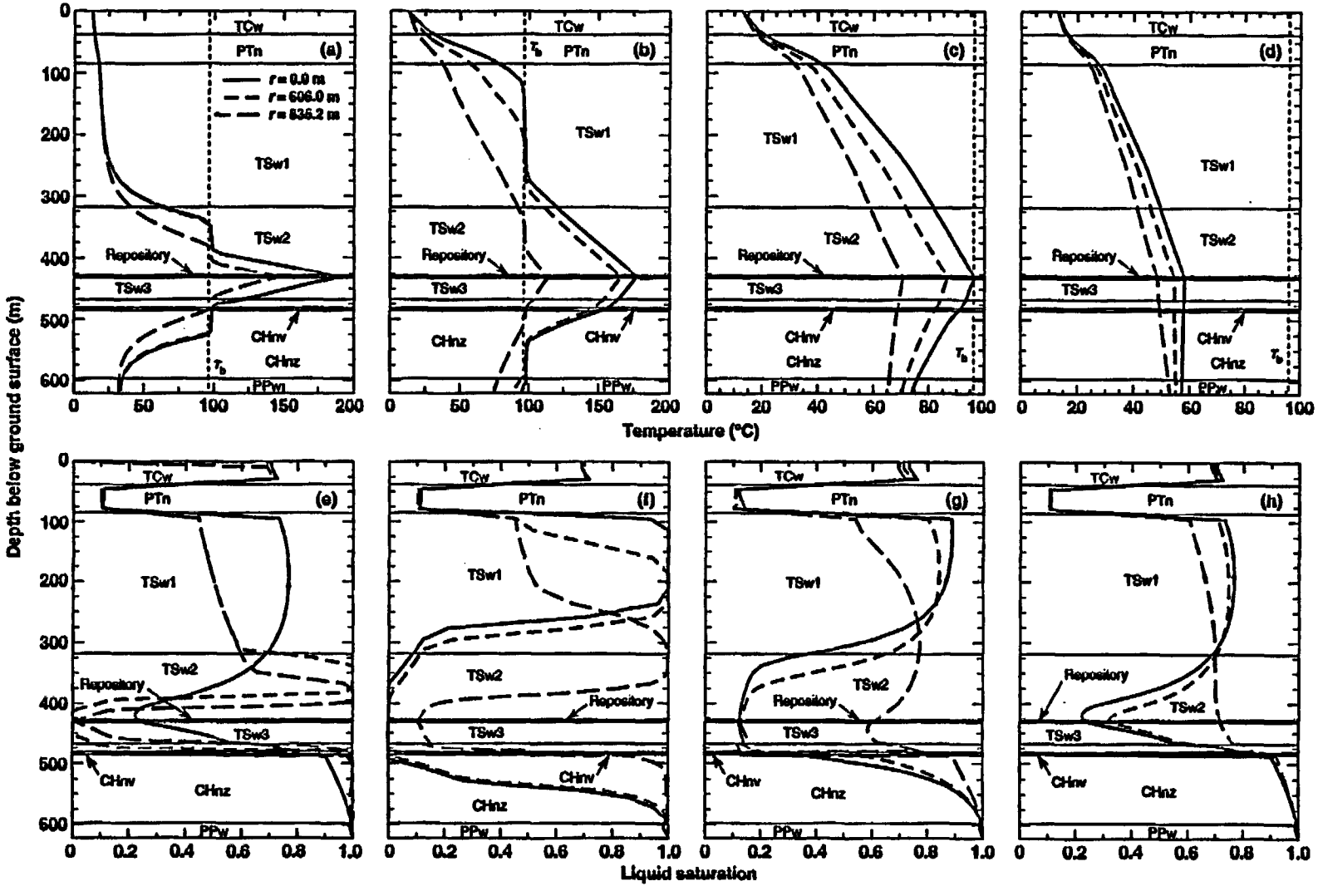

Figure 10.1.4.2.3. Vertical temperature profiles at various radial distances, r, for AML = 110.5 MTU/acre and the maximum-overburden-thickness (430 m) case at (a) t = 100 yr, (b) t = 1000 yr, (c) t = 10,000 yr, and (d) t = 31,680 yr. Note the different temperature scales. Vertical liquid saturation profiles are also plotted at (e) t = 100 yr, (f) t = 1000 yr, (g) t = 10,000 yr, and (h) t = 31,680 yr. The water table is at a depth of 622 m. Matrix poperties for all units (including the TSw1 and TSw2) are based on Klavetter and Peters [1986]. Binary gas-phase tortuosity factor τ_{eff} = 0.2 for all units.

10.1.4.2 Heat-Pipe Behavior. Figures 10.1.4.2.1-10.1.4.2.3 give the vertical liquid saturation profiles for AML = 110.5 MTU/acre and three repository depths, including: (1) the reference-overburden case with a repository depth of 343.1 m, (2) the minimum-overburden case with a repository depth of 200 m, and (3) the maximum-overburden case with a repository depth of 430 m. To show the influence of edge-cooling/rewetting/shedding effects on T-H behavior (see Section 1.10.6 of Chapter 1), vertical profiles are given at three repository locations, including: (1) r = 0.0 m, which is at the center of the repository, (2) r = 606.0 m, which is the "median" repository location that encloses 50% of the repository (i.e., 50% of the repository lies between that location and the repository edge), and (3) r = 835.2 m, which encloses 95% of the repository (i.e., only 5% of the repository area lies outside that location).

For the range 200-430 m, overburden thickness has a very pronounced affect on mountain-scale thermal-hydrological behavior. At very early time (t < 100 yr), thermal interference with the constant-temperature boundary at the ground surface has not yet developed; consequently, the vertical temperature profiles and liquid saturation profiles are similar for these three cases (compare Figs. 10.1.4.2.1a,b; 10.1.4.2.2a,b; and 10.1.4.2.3a,b). At 1000 yr (approximately corresponding to the maximum extent of dryout effects), the minimum-overburden case results in an almost negligible heat-pipe zone of near-96°C temperatures (Fig 10.1.4.2.2b), while the maximum-overburden case results in a 180-m-thick heat-pipe zone (Fig. 10.1.4.3b). In the reference-overburden case, the heat-pipe zone at 1000 yr is about 100-m thick (Fig. 10.1.4.1b). The maximum-overburden case has a 100-m-thick zone where liquid saturation is nearly 100% (Fig. 10.1.4.2.3f), while in the minimum-overburden case, the zone of near-100% liquid saturation is only 25-m thick (Fig. 10.1.4.2.2f).

The extra 230 m of insulating rock above the maximum-overburden case (compared with the minimum-overburden case) results in four major effects:

- It conserves the decay heat better than the shallower-overburden cases, thereby providing thermal energy with which to vaporize (i.e., mobilize) *in situ* water from the rock matrix.
- It contains much more *in situ* water (than the shallower-overburden cases) that can be vaporized and mobilized by decay heat.
- It imposes a longer pathway for vapor to escape out of the top of the mountain; therefore, it loses a smaller fraction of the mobilized water than the shallower-overburden cases.
- It takes longer to develop a steady-state temperature profile with the constant-temperature boundary at the ground surface.

The last point is significant because the heat-pipe will continue to increase in length until there is full interference between the heat source at the repository and the ground surface. During this initial heat-pipe-development period, the cooling effect of heat pipes is greatest. In theory, if the repository were infinitely deep and heat generation from the repository did not decay with time the heat pipes could continue to increase in length indefinitely. Taken together, the deeper repository has (1) more heat, (2) more water, and (3) more time to develop heat pipes; moreover, the deeper repository provides a greater distance over which near-boiling temperatures can exist.

The differences between the minimum- and maximum-overburden cases in condensate buildup above the repository would be even larger if the atmosphere was not assumed to have a relative humidity RH = 99%. The much steeper temperature gradient close to the ground surface (compare Figs. 10.1.4.2.2a-d with Figs. 10.1.4.3a-d), and the fact that the condensate buildup zone is driven closer to the ground surface (compare Figs. 10.1.4.2.2e-h with Figs. 10.1.4.3e-h) would result in a greater moisture loss to the atmosphere, driven by the diffusive and advective transport of water vapor. The assumption of near-100% RH in the atmosphere virtually precludes any diffusive flux of water vapor to the ground surface.

Because the actual overburden thickness varies at Yucca Mountain as a result of its topography, these calculations indicate that T-H behavior above the repository can vary significantly with areal location.

Contents

10.2 Mountain-Scale Saturated Zone (SZ) Thermal-Hydrology

10.2.1 Influence of SZ Heatflow on UZ Heatflow

We investigated the effect of hydrothermal flow in the saturated zone (SZ) on repository temperatures by comparing results from the UZ model (which assumes a fixed-depth, constant-temperature water table) with those obtained with the UZ-SZ model (which includes hydrothermal flow in the SZ down to an effectively infinite depth). For all of the cases considered (AMLs of 27.1 to 154.7 MTU/acre; 30- and 60-yr-old SNF), the treatment of the water table and the SZ has little effect on repository temperatures during the first 1000 yr (Fig. 10.2.1.1). Because temperatures peak within 1000 yr, T_{peak} is not affected by the treatment of the water table and SZ. For 30-yr-old SNF and an AML = 49.2 MTU/acre (Fig. 10.2.1.1a), T_{peak} = 114.9 and 115.3°C for the UZ and UZ-SZ models, respectively. For 30-yr-old SNF and an AML = 154.7 MTU/acre (Fig. 10.2.1.1b), T_{peak} = 201.6 and 202.9°C for the UZ and UZ-SZ models, respectively.

For t > 1000 yr (after repository temperatures have peaked), the SZ begins to heat up significantly (Fig. 10.2.1.2), thereby reducing the rate at which heat can flow from the UZ to the SZ. Consequently, the duration of boiling t_{bp} substantially increases, particularly for higher AMLs (t_{bp} » 1000 yr). For lower AMLs (t_{bp} < 1000 yr), the increase in t_{bp} is less substantial. For the reference SCP-CDR thermal load (AML = 49.2 MTU/acre; 10-yr-old SNF), t_{bp} increases from 550 to 670 yr (Fig. 10.2.1.1c). For 30-yr-old SNF and an AML = 77.4 MTU/acre, t_{bp} increases from 2080 to 3510 yr (Fig. 10.2.1.1a). For 30-yr-old SNF and an AML = 154.7 MTU/acre (Fig. 10.2.1.1b), t_{bp} increases from 6500 to 11,450 yr. For 60-yr-old SNF and an AML = 248.5 MTU/acre (not shown), t_{bp} increases from 12,630 to 18,120 yr.

Low AMLs (with $t_{peak} < t_{bp}$) are also affected by the treatment of the water table and SZ. For 30-yr-old SNF and an AML = 27.1 MTU/acre, hydrothermal flow in the SZ extends the duration of time the repository is above 50°C from 2200 to 3600 yr and extends the duration of time the repository is above 40°C from 5060 to 14,150 yr.

10.2.2 Buoyancy-Driven SZ Flow and Transport

In the previous section, we investigated the impact of hydrothermal flow in the SZ on thermal-hydrological (T-H) behavior in the UZ. Here we examine T-H behavior of the SZ itself. We examine the sensitivity of SZ T-H behavior to thermal loading design parameters as well as to the T-H properties. We also address the question of whether decay-heat-driven T-H behavior in the SZ will dominate hydrological flow and transport in the SZ, and begin to investigate the magnitude of convective effects on heat flow between the UZ and SZ. Note that our model assumes no lateral flow in the SZ at $t = 0$ yr.

We compare the magnitude of decay-heat-driven buoyancy flow in the SZ for three cases of 30-yr-old SNF having the same total mass of SNF: (a) 27.1 MTU/acre over a repository area of 3162 acres, (b) 77.4 MTU/acre over 1118 acres, and (c) 154.7 MTU/acre over 559 acres. We have observed that temperatures in the SZ build up considerably, even for low thermal loads (Fig. 10.2.1.2). Although convection does not dominate heat flow in the SZ, after ~1000 yr, heat flow in the SZ appears to dominate fluid flow in the SZ. This dominant influence of decay-heat-driven flow was found to occur for all AMLs investigated, 27.1 to 154.7 MTU/acre. As the SZ temperatures (below the repository footprint) rise, the accompanying decrease in mass density results in significant upward component of flow from considerable depth, generating buoyant convection cells.

Decay-heat-driven convection cells in the SZ require tens of thousands of years to fully develop. As the thermal pulse from the repository propagates both vertically and radially into the SZ, the region over which decay-heat-driven convection occurs continues to expand during (at least) the first 20 000 yr (Figs. 10.2.2.1 and 10.2.2.2). As this region expands, additional parallel convection cells are added to the convective system. After 1000 yr, two convection cells (one on each side of the symmetry axis) have developed (in cross section), extending radially ~2 to 3 km from the repository center (Fig. 10.2.2.1a); after 5000 yr, the radial extent of repository-heat-driven convection is ~5 km (Fig. 10.2.2.1b); after 10 000 yr, the radial extent of the convection cells is ~8 to 10 km (Fig. 10.2.2.2a); after 20 000 yr, the radial extent of the convection cells exceeds 10 km from the repository center (Fig. 10.2.2.2b). Because the matrix permeability of the SZ is presumably quite small, these large-scale, buoyant convection cells require large-scale connectivity within the fracture system.

The connectivity and bulk permeability k_b of the fracture system in the SZ will be determined through the analysis of multiple-well, multiple-level, packer tests. However, the use of *in situ* heater tests in the SZ would give us much more direct evidence that the fracture properties are sufficient to result in significant buoyant convection. Because the driving force for buoyant convection is primarily propagated by heat conduction (rather than by direct hydraulic communication through connected fracture networks), the use of heater tests would provide valuable information about the bulk fracture network properties that cannot be obtained through conventional packer tests. The temperature field acts as a signature for convective effects. Diagnostic thermal probes, which are extremely sensitive to differences between conductive and convective heat flow, would also assist in the interpretation of convective effects [Danko and Buscheck, 1993]. The heater tests would provide a valuable tool in understanding the ambient system as well as how the SZ system responds to heat.

Although the geometric details of the convection cells differed, we found that the overall magnitude of decay-heat-driven buoyancy flow is relatively insensitive to AML. For example, at $t = 5000$ yr, the maximum horizontal fracture velocity $(v_h)_{max}$ is 1180 m/yr for 27.1 MTU/acre (Fig. 10.2.2.3a), and 1580 m/yr for 154.7 MTU/acre (Fig. 10.2.2.3b). Although the AML varies by a factor of 5.7, the difference in $(v_h)_{max}$ is only 33% between these two cases. For 77.4 MTU/acre, $(v_h)_{max}$ is 1510 m/yr at $t = 5000$ yr (Fig. 10.2.2.1b). The fracture velocity is obtained by multiplying Q_{ECM} (which is the bulk-porosity-averaged liquid-phase velocity) by the ratio of the bulk porosity divided by the fracture porosity. Using the same k_b applied in these calculations (k_b = 280 millidarcy) and applying a relatively steep hydraulic gradient of 10^{-3} m/m results in an ambient v_h of only 63 m/yr. Therefore, it appears that decay-heat-driven flow may dominate SZ flow and transport for tens of thousands of years. The large difference between the

decay-heat-driven v_h and that driven by even a very steep hydraulic gradient indicates that the effect of assuming an initially stagnant SZ in our model should be negligible.

Decay-heat-driven buoyancy flow in the SZ is a result of changes in fluid volume ΔV that occur as the region below the repository is heated. Because ΔV increases with ΔT, the magnitude of buoyancy flow generally increases with ΔT. Although ΔV per unit volume of heated SZ is less for lower AML, the larger footprint associated with the low-AML repository results in a larger overall region where this heat-driven change in volume takes place (compare Figs. 10.2.2.3a and 10.2.2.3b). Consequently, for a given amount of time-integrated heat, the cumulative effect of repository heating on driving convection cells in the SZ is similar over a wide range of AML. In general, the magnitude of decay-heat-driven buoyancy flow in the SZ is insensitive to the actual design of the repository and is primarily sensitive to the time-integrated heat (i.e., total mass of SNF emplaced in the repository). Consequently, the T-H and potential geochemical consequences of heat in the SZ should not be considered a design issue but rather the inherent response of the SZ to the emplacement of a given quantity of SNF.

For $t \geq 5000$ yr, the isotherms of the temperature buildup (Figs. 10.2.2.1b, 10.2.2.2a, 10.2.2.2b, 10.2.2.3a, and 10.2.2.3b) show significant deviations relative to what would be expected for conduction-dominated heat flow. These deviations do not arise from the convection of repository heat; instead, they are caused by the convection of hotter water from below (hotter because of the geothermal gradient). Because a constant-temperature boundary is maintained 1 km below the water table, and liquid flow is both entering and leaving this boundary, the convection cells are not within a closed loop. Consequently, the model-boundary effect prevents cooler water that enters the boundary from cooling the warmer water leaving the boundary. Therefore, it is possible that this boundary effect may introduce additional heat that would not have occurred had the finite extent of the convection cell been fully represented in our model. On the other hand, the close proximity of a constant-temperature boundary to significant temperature changes would tend to lower temperatures. To evaluate which of these effects might dominate or whether their combined effect is negligible (with respect to SZ heat flow), we analyzed several cases with no fracture flow (effectively causing heat flow to be entirely dominated by conduction) and found negligible differences in heat flux crossing the water table. Therefore, the model-boundary effect that occurs 1 km below the water table does not influence heatflow at the water table; moreover, it does not affect temperature rise in the UZ and the upper SZ. It should be noted that few data exist concerning the vertical extent of connected fracture networks in the SZ and that the thermal property data below the PPw unit is lacking in the RIB [DOE, 1990]. We plan to continue our study of decay-heat-driven T-H behavior in the SZ, utilizing other available sources of thermal property data [Sass et al., 1988].

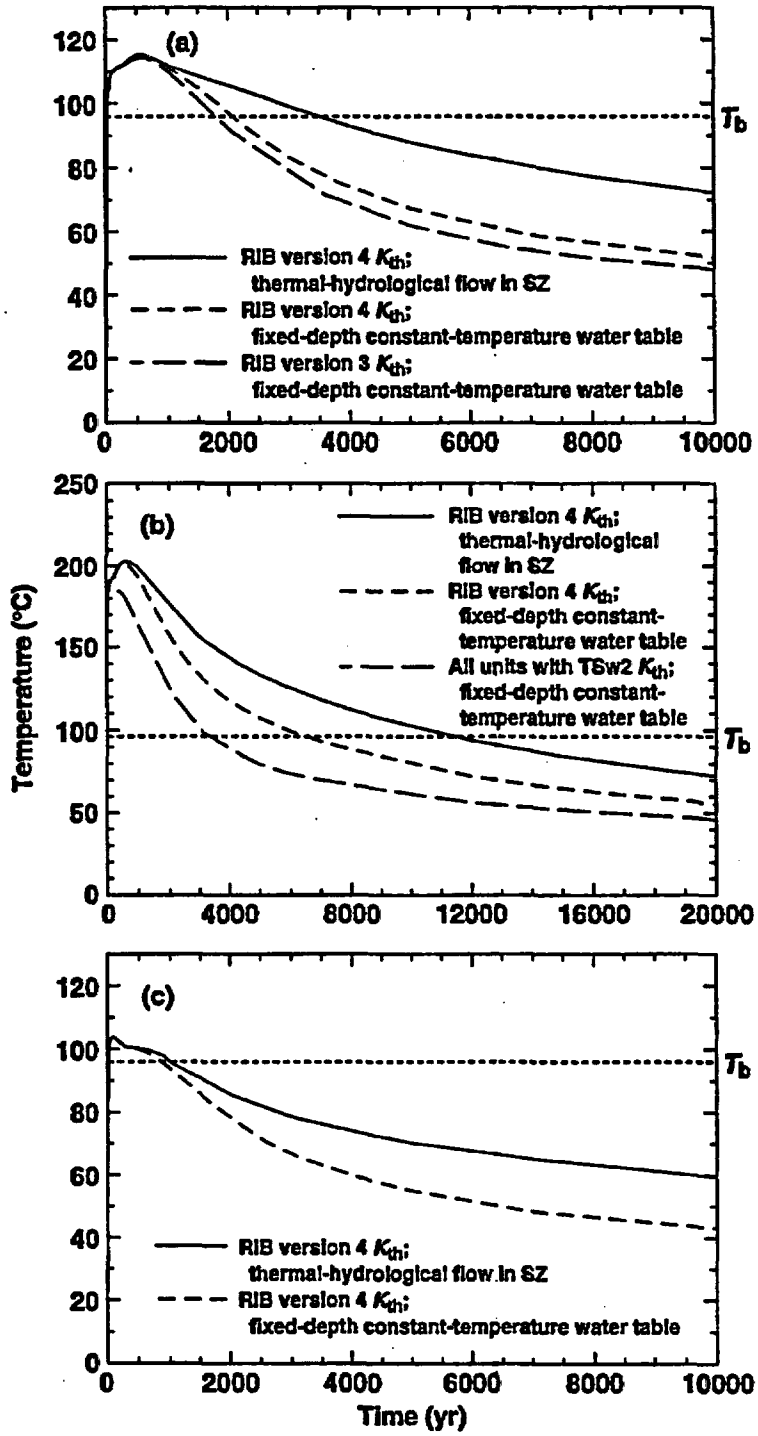

Figure 10.2.1.1. Temperature history at the center of the repository for ambient percolation flux = 0.0 mm/yr. Curves are plotted for (a) AML = 77.4 MTU/acre and 30-yr-old SNF, (b) AML = 154.7 MTU/acre and 30-yr-old SNF, (c) AML = 49.2 MTU/acre and 10-yr-old SNF.

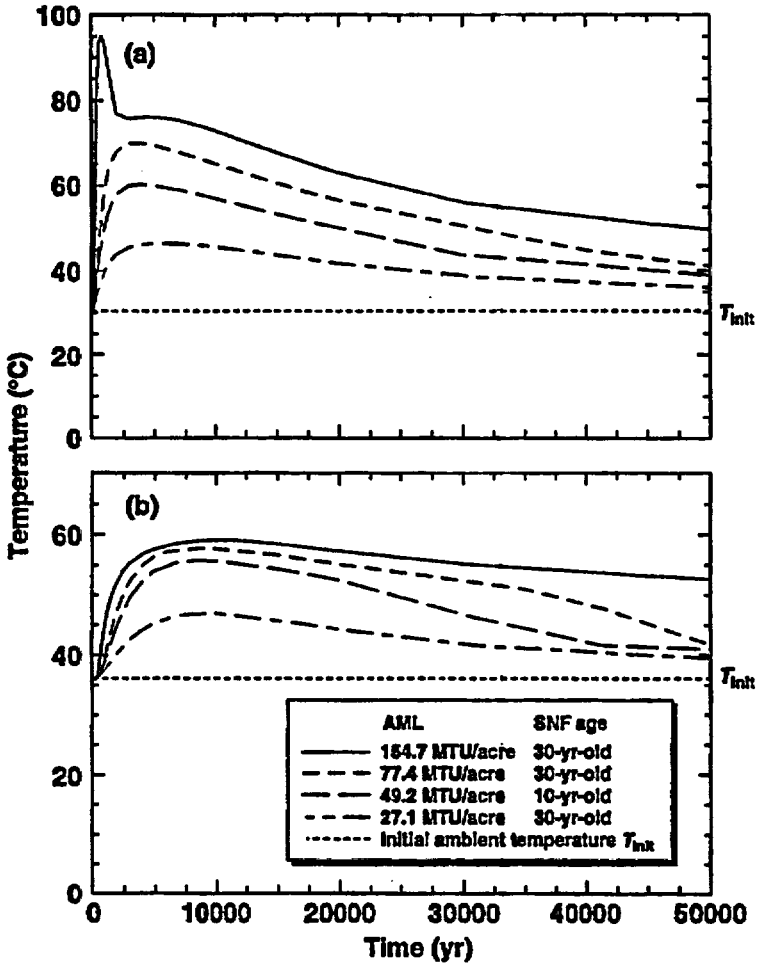

Figure 10.2.1.2. Temperature history at locations below the center of the repository for various AMLs and SNF ages, including (a) the water table and (b) 250 m below the water table.

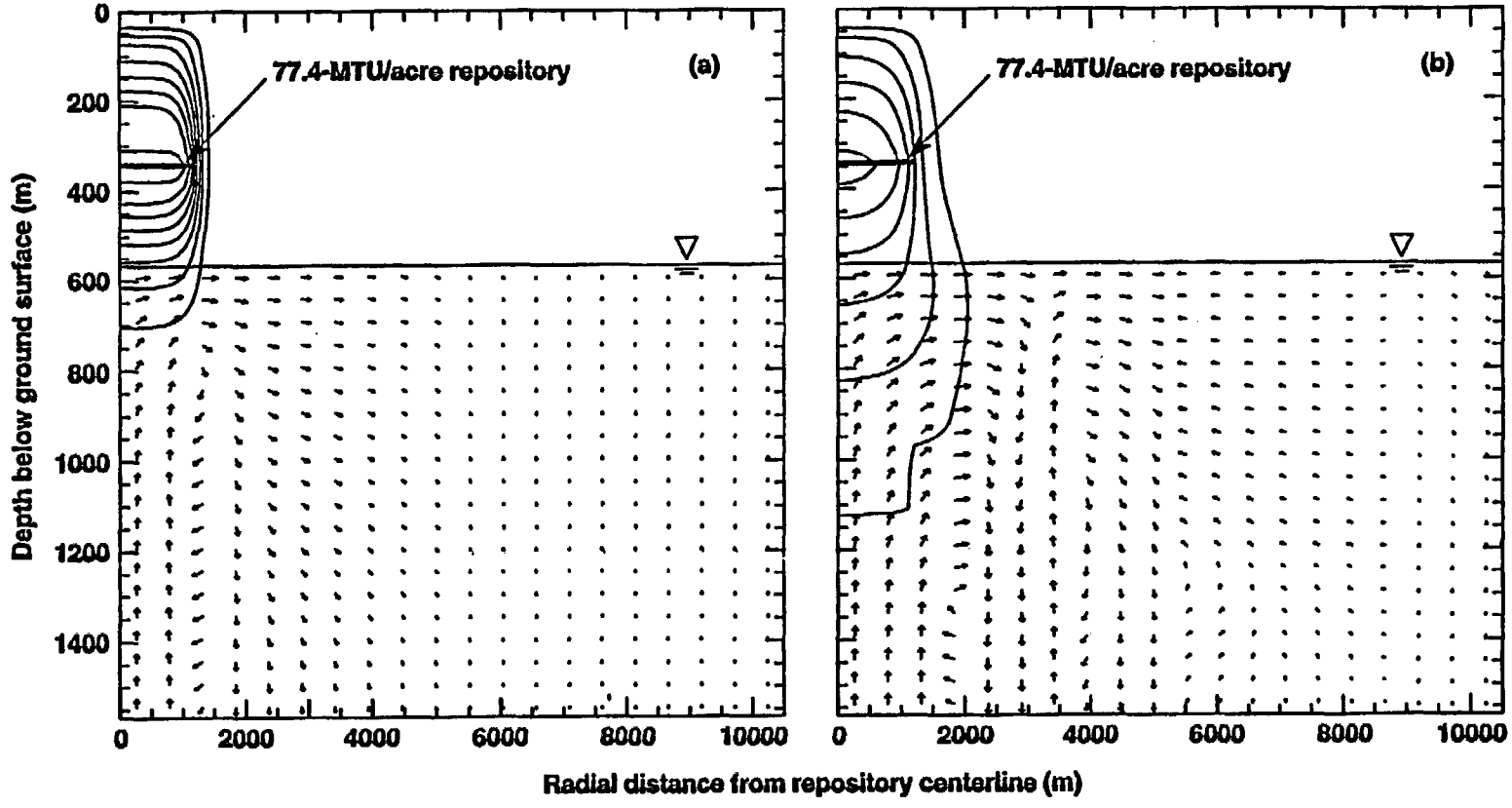

Figure 10.2.2.1. Temperature buildup contours (temperature rise above ambient temperature) and velocity vectors for liquid-phase flow in fractures in the SZ for AML = 77.4 MTU/acre, 30-yr-old SNF, 1118-acre repository area, and ambient percolation flux = 0.0 mm/yr at (a) t = 1000 yr and (b) t = 5000 yr. Temperature contour interval is 5°C. Liquid-phase velocity vectors are scaled logarithmically from 0.03 m/yr to 1600 m/yr/.

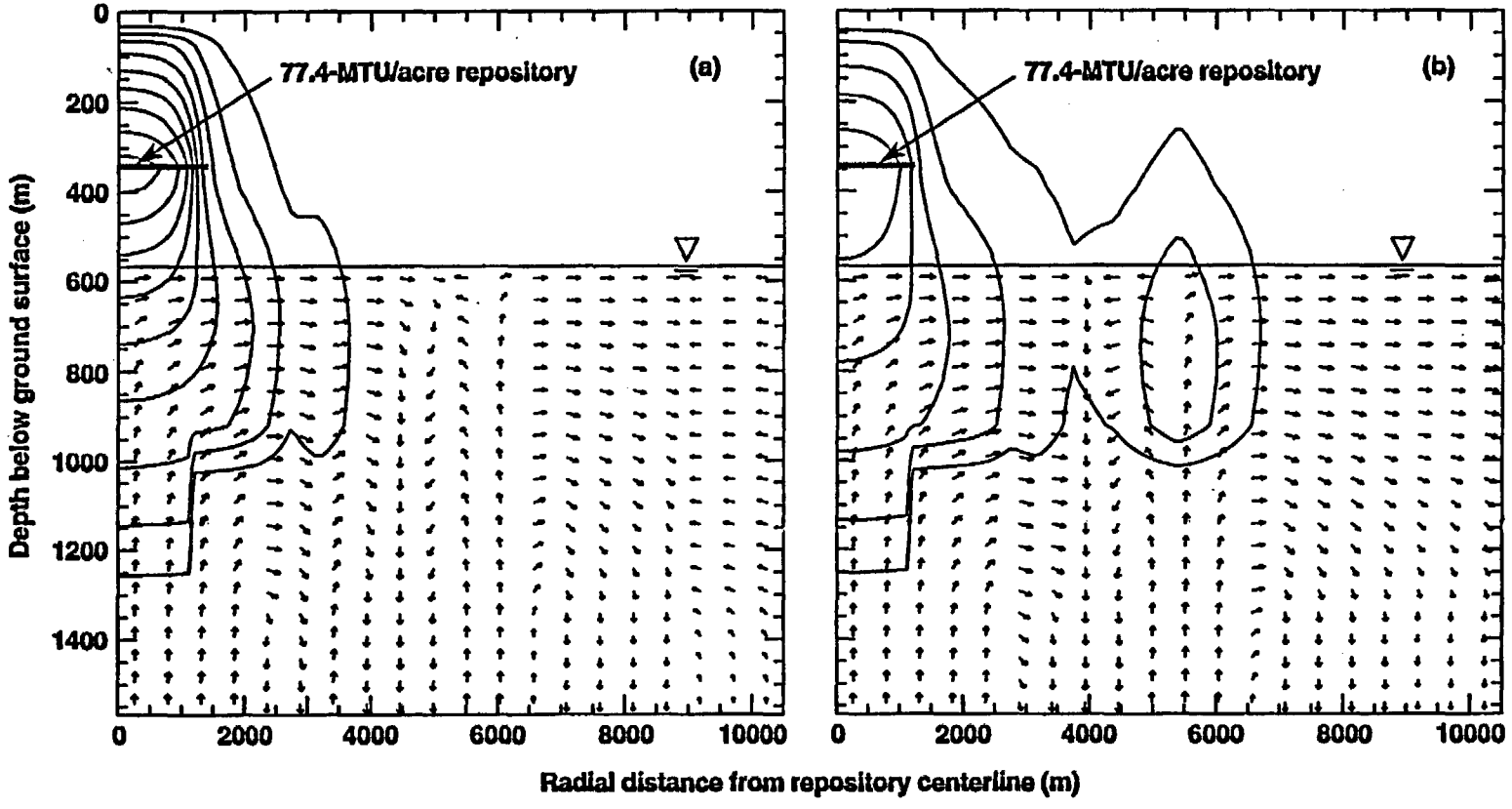

Figure 10.2.2.2. Temperature buildup contours (temperature rise above ambient temperature) and velocity vectors for liquid-phase flow in fractures in the SZ for AML = 77.4 MTU/acre, 30-yr-old SNF, 1118-acre repository area, and ambient percolation flux = 0.0 mm/yr at (a) t = 10,000 yr and (b) t = 20,000 yr. Temperature contour interval is 5°C. Liquid-phase velocity vectors are scaled logarithmically from 0.03 m/yr to 1600 m/yr/.

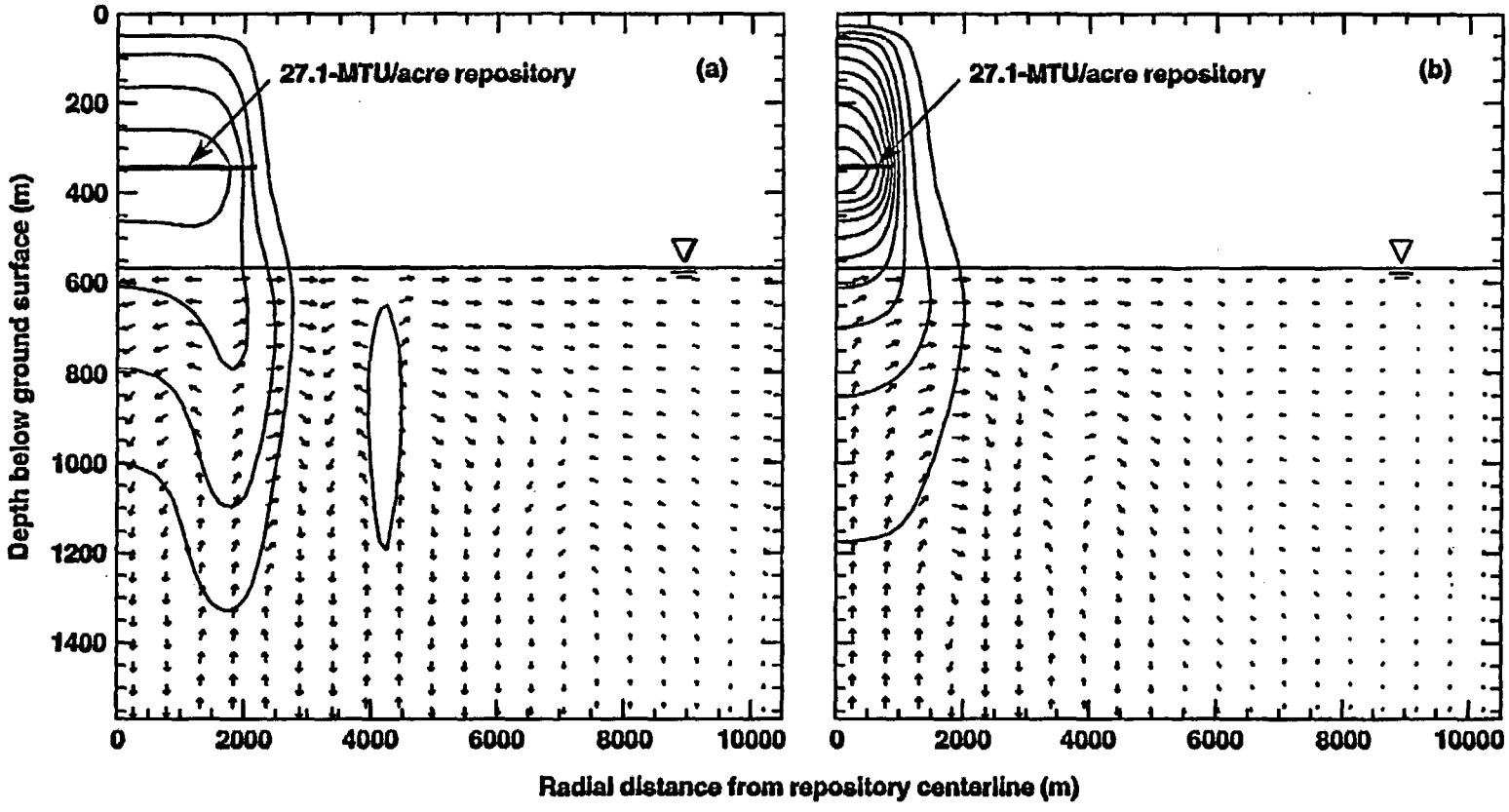

Figure 10.2.2.3. Temperature buildup contours (temperature rise above ambient temperature) and velocity vectors for liquid-phase flow in fractures in the SZ for AML = 27.1 MTU/acre, 30-yr-old SNF, 3162-acre repository area, and ambient percolation flux = 0.0 mm/yr at (a) t = 1000 yr and (b) t = 5000 yr. Temperature contour interval is 5°C. Liquid-phase velocity vectors are scaled logarithmically from 0.03 m/yr to 1600 m/yr/.

References

Buscheck, T.A. and J.J. Nitao, "Estimates of the Width of the Wetting Zone Along a Fracture Subjected to an Episodic Infiltration Event in Variably Saturated, Densely Welded Tuff," *UCID-21579*, Lawrence Livermore National Laboratory, Livermore, CA (1988).

Buscheck, T.A. and J.J. Nitao, "Modeling Hydrothermal Flow in Variably Saturated, Fracture, Welded Tuff During the Prototype Engineered Barrier System Field Test of the Y ucca Mountain Project," *UCRL-JC-1106521*, Lawrence Livermore National Laboratory, Livermore, CA (1991).

Buscheck, T.A., J.J. Nitao, and D.A. Chesnut, "The Impact of Episodic Nonequilibrium Fracture-Matrix Flow on Geological Repository Performance," *Proceedings American Nuclear Society Topical Meeting on Nuclear Waste Packaging (Focus 91)*, Las Vegas, NV, Sept. 30-Oct. 2, 1991. Also, *UCRL-JC-106759*, Lawrence Livermore National Laboratory, Livermore, CA (1991).

Buscheck, T.A., and J.J. Nitao, "The Impact of Thermal Loading on Repository Performance at Yucca Mountain," American Nuclear Society, *Proceedings Third International High-Level Radioactive Waste Management Conference*, Las Vegas, NV, April 12-16, 1992. Also, *UCRL-JC-109232*, Lawrence Livermore National Laboratory, Livermore, CA (1992).

Buscheck, T.A., and J.J. Nitao, "The Impact of Repository Heat on Thermo-Hydrological Performance at Yucca Mountain," *Proceedings American Nuclear Society Topical Meeting on Site Characterization and Model Validation (Focus 93)*, Las Vegas, NV, Sept. 26-30, (1993a).

Buscheck, T.A., and J.J. Nitao, "Repository-Heat-Driven Hydrothermal Flow at Yucca Mountain, Part I: Modeling and Analysis," *Nuclear Technology*, Vol. 104, No. 3, pp. 418-448, (1993b).

Buscheck, T.A., D.G. Wilder, and J.J. Nitao, "Large-Scale In Situ Heater Tests for the Characterization of Hydrothermal Flow at Yucca Mountain," American Nuclear Society, *Proceedings Fourth International High-Level Radioactive Waste Management Conference*, Las Vegas, NV, April 1993. Also, *UCRL-JC-112445*, Lawrence Livermore National Laboratory, Livermore, CA (1993a).

Buscheck, T.A., D.G. Wilder, and J.J. Nitao, "Repository-Heat-Driven Hydrothermal Flow at Yucca Mountain, Part II: Large-Scale In Situ Heater Tests," *Nuclear Technology*, Vol. 104, No. 3, pp. 449-471 (1993b).

Buscheck, T.A., and J.J. Nitao, "The Impact of Buoyant Gas-Phase Flow and Heterogeneity on Thermo-Hydrological Behavior at Yucca Mountain," American Nuclear Society, La Grange Park, IL, *Proceedings Fifth International High-Level Radioactive Waste Management Conference*, Las Vegas, NV, May 1994a. Also *UCRL-JC-115351*, Lawrence Livermore National Laboratory, Livermore, CA, (1994a).

Buscheck, T.A. and J.J. Nitao, "The Importance of Thermal Loading Conditions to Waste Package Performance at Yucca Mountain," Materials Research Society, Pittsburgh, PA, *Proceedings Materials Research Society XVIII International Symposium on the Scientific Basis for Nuclear Waste Management*, Oct. 23-27, 1994. Also UCRL-JC-116429, Lawrence Livermore National Laboratory, Livermore, CA, (1994b).

Buscheck, T.A., J.J. Nitao, and L.D. Ramspott, "Localized Dry-Out: An Approach for Managing the Thermal-Hydrological Effects of Decay Heat at Yucca Mountain," Materials Research Society, Pittsburgh, PA, *Proceedings Materials Research Society XIX International Symposium on the Scientific Basis for Nuclear Waste Management*, Nov. 27-Dec. 1, (1995).

Buscheck, T.A., J.J. Nitao, and S.F. Saterlie, "Evaluation of Thermo-Hydrological Performance in Support of the Thermal Loading Systems Study," American Nuclear Society, *Proceedings Fifth International High-Level Radioactive Waste Management Conference*, Las Vegas, NV, May 1994; Also *UCRL-JC-115352*, Lawrence Livermore National Laboratory, Livermore, CA, (1994).

Buscheck, T.A. and J.J. Nitao, "Thermal-Hydrological Analysis of Large-Scale Thermal Tests in the Exploratory Studies Facility at Yucca Mountain," *UCRL-ID-121791*, Lawrence Livermore National Laboratory, Livermore, CA (1995).

DOE (U.S. Dept. of Energy), "Site Characterization Plan: Yucca Mountain Site, Nevada Research and Development Area," *DOE/RW-0199* (1988).

DOE (U.S. Dept. of Energy), "Yucca Mountain Project Reference Information Base," *YMP/CC-0002 (Version 04.002)*, Nevada Operations Office, Las Vegas, NV (1990).

Forsythe, P.A., "Radioactive Waste Disposal Heating Effects in Unsaturated Fractured Rock," *Numerical Heat Transfer Part A—Applications* 17 (1), 29-51 (1990).

Jones, D.A., *Principles and Prevention of Corrosion*, Macmillan Publishing Company, New York (1992).

Klavetter, E.A., and R.R. Peters, "Estimation of Hydrologic Properties of an Unsaturated Fractured Rock Mass," *SAND84-2642*, Sandia National Laboratories, Albuquerque, NM (1986).

Konikow, L.F., and J.D. Bredehoeft, "Ground-water Models Cannot Be Validated," *Advances in Water Resources*, Vol. 15, pp. 75-83 (1992).

Lin, W., D.G. Wilder, J.A. Blink, S.C. Blair, T.A. Buscheck, R.S. Glass, W.E. Glassley, K. Lee, R.D. McCright, M.W. Owen, and J.J. Roberts, "A Large Block Heater Test for High Level Nuclear Waste Management," Materials Research Society, Pittsburgh, PA, *Proceedings Materials Research Society XVIII International Symposium on the Scientific Basis for Nuclear Waste Management*, Oct. 23-27, 1994. Also UCRL-JC-116431, Lawrence Livermore National Laboratory, Livermore, CA (1994).

Montazer, P., and W.E. Wilson, "Conceptual Hydrologic Model of Flow in the Unsaturated Zone, Yucca Mountain, Nevada," Water Resources Investigation Report 84-4345, U.S. Geological Survey (1984).

Nuclear Regulatory Commission, "Generic Technical Position on *In Situ* Testing During Site Characterization for High-Level Nuclear Waste Repositories," Engineering Branch, Division of Waste Management (December 1985).

U.S. Code of Federal Regulations Part 60, "Disposal of High-Level Radioactive Waste in a Geologic Repository," March (1990).

Nitao, J.J., "Numerical Modeling of the Thermal and Hydrological Environment Around a Nuclear Waste Package Using the Equivalent Continuum Approximation: Horizontal Emplacement," *UCID-21444*, Lawrence Livermore National Laboratory, Livermore, CA (1988).

Nitao, J.J., "V-TOUGH - An Enhanced Version of the TOUGH Code for the Thermal and Hydrologic Simulation of Large-Scale Problems in Nuclear Waste Isolation," *UCID-21954*, Lawrence Livermore National Laboratory, Livermore, CA (1989).

Nitao, J.J., "The NUFT Code for Modeling Nonisothermal, Multiphase, Multicomponent Flow and Transport in Porous Media," EOS, American Geophysical Union, Vol. 74, no. 3, pr. 3 (1993).

Nitao, J.J., T.A. Buscheck, and D.A. Chesnut, "Implications of Episodic Nonequilibrium Fracture-Matrix Flow on Repository Performance," *Nuclear Technology*, Vol. 104, No. 3, pp. 385-402, (1993).

Nitao, J.J., "The NUFT Code for Modeling Nonisothermal, Multiphase, Multicomponent Flow and Transport in Porous Media," EOS Supplement 74 (3), 313 (1993).

Nitao, JJ, and T.A. Buscheck, "Discrete-Fracture Modeling of Thermal-Hydrological Processes at Yucca Mountain and the LLNL G-Tunnel Field Test," Materials Research Society, Pittsburgh, PA, *Proceedings Materials Research Society XIX International Symposium on the Scientific Basis for Nuclear Waste Management*, Nov. 27-Dec. 1, (1995).

Peters, R.R., E.A. Klavetter, I.J. Hall, S.C. Blair, P.R. Hellers, and G.W. Gee, "Fracture and Matrix Hydrologic Characteristics of Tuffaceous Materials from Yucca Mountain, Nye County, Nevada," *SAND84-1471*, Sandia National Laboratories, Albuquerque, NM (1984).

Popper, K., *The Logic of Scientific Discovery*, Harper and Row, New York (1959).

Pruess, K., "TOUGH User's Guide," *NUREG/CR-4645*, Nuclear Regulatory Commission (1987).

Pruess, K., J.S.Y. Wang, and Y.W. Tsang, "Numerical Modeling Studies of Fluid and Heat Flow near High-Level Nuclear Waste Packages in Partially Saturated Fractured Tuff," *LBL-18522*, Lawrence Berkeley Laboratory, Berkeley, CA (1984).

Ramirez, A.L., T.A. Buscheck, R. Carlson, W. Daily, K. Lee, W. Lin, N. Mao, T.S. Ueng, H. Wang, and D. Watwood, "Prototype Engineered Barrier System Field Test (PEBSFT) Final Report," *UCRL-ID-106159*, Lawrence Livermore National Laboratory, Livermore, CA (1991).

Stahl, D., J.K. McCoy, and R.D. McCright, "Impact of Thermal Loading on Waste Package Material Performance," Material Research Society, Pittsburgh, PA, *Proceedings Material Research Society XVIII Symposium on the Scientific Basis for Nuclear Waste Management*, Oct. 23-27 (1994).

Contents

10.3 Geochemistry and Mineralogy of the Altered Zone (*William E. Glassley*)

Introduction

Geochemical processes that will occur as a result of emplacement of high-level radioactive waste will be driven by heat transferred into the rock surrounding the emplacement drifts. The consequences of these geochemical effects will depend upon the rate of temperature change, and the maximum temperature reached, as well as the flux of water and vapor through the rock. In some waste emplacement scenarios, temperature changes of more than 10°C extend hundreds to thousands of meters away from the emplacement drifts. In other scenarios, temperature changes of this magnitude are restricted to regions less than 100 meters from emplacement drifts. For any given emplacement scenario, the rate at which temperature changes occur depend, in general, on the distance from the heat source: the further the distance, the slower the heating rate. Regardless of emplacement scenarios, within the immediate vicinity (several tens of meters) of emplacement drifts, temperatures will increase relatively rapidly to more than 100°C.

This temperature behavior has led to a conceptual model in which "near-field" effects (the Near-Field Environment) are distinguished from "altered zone" effects (the Altered Zone). In the near-field region, hydrological processes will be dominated by water vaporization, water movement by means of gas phase transport, and condensation in those outer regions of the near-field environment where temperatures are below the boiling point. Geochemical processes will be dominated by evaporation and boiling, mineral dehydration, and solid-vapor interactions. In the altered zone, hydrological processes will be dominated by an increase in water availability and increased saturation, associated with vapor condensation. The geochemical processes will be dominated by fluid-rock interactions, and reactive transport. Within the altered zone, these interactions will result in significant coupling between hydrological and geochemical processes, such that fluid flow pathways and geochemical conditions will evolve in a synergistic way.

Although the geochemical processes (e.g., recrystallizations, hydration or dehydration of mineral phases, or both; dissolution and precipitation; rock-water interaction involving water in pores and fractures; cation exchange, sorption, etc.) in both regions are the same, their impact on rock properties will be different, due to contrasts in heating and cooling rates, and in the abundance and temperature of liquid water. These differences will be expressed as differences in the magnitude and nature of chemical and mineralogical changes, and the duration of specific processes. As a result, the repository performance will be affected differently in the two regions as a result of water-mineral interactions. For purposes of this report, the Near-Field Environment (NFE) will be considered to be those regions that acheive temperatures well above the boiling point, and the Altered Zone (AZ) will be considered to be those regions that maintain temperatures low enough to allow liquid water to exist in pores and fractures. This distinction has the advantage of focusing attention on the dominant processes that may effect performance in different regions of the repository (e.g., evaporation of water and mineral dehydration in the NFE, and rock-water interaction and the kinetics of dissolution and precipitation in the AZ). Refer to Chapter 3 for results to date of activities investigating processes in the NFE.

10.4 Summary of Recent Studies Concerning Geochemical and Mineralogical Evolution of the Altered Zone (*William E. Glassley*)

The results of four studies are reported here. These studies consider the geochemical and mineralogical evolution of the AZ.

One study (Section 10.4.2.1 Hydrothermal Alteration of Vitric Tuff from Yucca Mountain) considers the effects of liquid water interacting with vitric material typical of the Tsw3 unit and the vitric Calico Hills lithology. The results indicate that extent of alteration, as a function of time, is sensitive to temperature (as expected from well established models of reaction kinetics), and to the extent of prior alteration. The latter interpretation is based on the observation that reaction progress, for any given time or temperature was less for vitric material in which clay occured as a ubiquitous, but trace, component covering the surfaces of vitric material. As with previous experiments using glassy material from the region, secondary minerals that form are primarily zeolites and clays.

A second study (Section 10.4.2.2. Amorphous Silica Precipitation (60 to 120°C): Comparison of Laboratory and Field Rates) was concerned with evaluating apparent discrepancies between laboratory-based and field-based measurements of reaction rates. In this case, the precipitation rates for amorphous silica were measured. Rate measurements were carried out in the laboratory using collapsible-bag autoclaves, and were compared with measurements made in the field using a fluidized-bed reactor. The field measurements were made at the Wairakei geothermal field in New Zealand, which has been selected as a key site in which processes relevant for repository evolution can be examined and monitored (Bruton et al., 1995). The results show that the field-based rates are 10 to 300 times faster than those measured in the laboratory. Observations suggest that these differences are sensitive to temperature, and may be influenced by the presence of other chemical species in solution (e.g., Al). The precipitation mechanism in the field may be controlled by surface defects.

A third study (Section 10.4.2.3 Preliminary Bounds on the Water Composition and Secondary Mineral Development That May Influence the Near-Field Environment) places preliminary bounds on the chemical composition of water that may enter the NFE, and on the secondary mineralogy that may develop within the AZ. This study considered the effect of temperature and uncertainty in reaction kinetics to place limits on fluid composition for devitrified and vitric tuffs intereacting with a J-13 - like water over a range of temperatures. The simulations were carried out assuming that fluid was in equilibrium with atmospheric gases. The results indicate that water compositions remain mildly oxidizing, and slightly to mildly alkaline (pH between 7.5 and 8.8), for most conditions. The exception noted was that in which very large water volumes interacted with small volumes of vitric material. In that case, the buffering effect of atmospheric gases was overwhelmed and the solution became acidic (pH ca. 4). Secondary minerals that formed were sensitive to extent of reaction and temperature. In most cases, zeolites and clays were present, with minor to trace amounts of other minerals present.

The effect of uncertainty in reaction kinetics was also evaluated. It is established that uncertainty in the time at which secondary minerals form can be as great as hundreds to thousands of years, for the uncertainties described in Section 10.4.2.2. These results are consistent with the conclusion in Section 3.4.2, in which it is argued that a mineral facies concept needs to be employed when considering secondary mineral development within the repository.

The fourth study describes the results of reactive transport simulations in which porosity modification is monitored during dissolution and precipitation of a wide range of silicates along a flow path that is similar to that expected for water condensed from steam generated in the near-field environment. The results show that porosity may more than double in devitrified and welded tuff, due to the dissolution of cristobalite in the regions immediately adjacent to the condensation front. As these waters migrate along and across isotherms, the dissolved constituents eventually precipitate as complex silicates, reducing porosity, and forming altered regions composed of zeolites, clays, and hydrated alumino-silicates. This complex coupling of fluid flow and reactive chemical transport demonstrates

that large changes in bulk rock hydrological properties may occur within a few hundred years of repository operation.

These results are expected to be the foundation upon which refined estimates of mineral facies would be developed for specific repository scenarios of waste emplacement strategies, infiltration fluxes, and rock properties. These scenarios have yet to be developed. It is expected that future work will focus on developing these mineralogical and chemical scenarios, and reducing the uncertainties in key thermodynamic and kinetic data in order to better bound the behavior of the repository.

10.4.1 Hydrothermal Alteration of Vitric Tuff from Yucca Mountain, by Kevin G. Knauss and Sally A. Copenhaver, Lawrence Livermore National Laboratory

10.4.1.1 Introduction and Methods. Alteration of the basal vitrophyre of the Topopah Spring tuff (Tsw3 unit) represents a potentially profound modification of the lithologic units currently composing the potential repository block at Yucca Mountain (see Sections 3.4.3 and 10.4.3). A suite of experiments was designed to evaluate the effects of this potential alteration. An initial set of three experiments was conducted to investigate the hydrothermal alteration of the vitric tuff, the results of which were summarized earlier (Knauss and Peifer, 1986; Knauss, 1987). Additional experiments, to more fully characterize the alteration effects, were also conducted, and are reported below. The experimental methods and analytical techniques described in the earlier papers were used in the runs described here. The only exception is that the initial fluid composition in the runs with Calico Hills tuff was 3 mmolal $NaHCO_3$, rather than well J-13 water. The following table identifies the pertinent information for all of the vitric experiments, including the three already reported, and the two runs made with zeolitized Topopah Spring tuff.

The rock samples taken from G4-1362 (the moderately welded, essentially unaltered vitric airfall/ashflow below the basal vitrophyre) have been characterized in detail (Knauss and Peifer, 1986). The rock samples taken from GU3-1226, Ue25a1-1297 and outcrop Tchnv have been characterized in a similar fashion, and will be reported later. Briefly, the material from GU3-1226 samples the densely welded vitrophyre and is essentially unaltered glass. Both of these samples of Tpt glass (G4-1362 and GU3-1226) have low (~2%) phenocryst content. The material from Ue25a1-1297 also samples the Tpt vitrophyre, but at this location the glass has been extensively altered to zeolite (heulandite) and clay (smectite). It also has a low phenocryst content. The outcrop material (outcrop Tchnv), taken from the north end of Busted Butte, samples the Tuff of Calico Hills and is mostly glass (~80%) and phenocrysts (~16%), although some alteration to clay has occurred (~4%). This amount of clay alteration is similar to that observed in the vitric intervals of Tchnv in drillcore. The sample locality is equivalent to DEB 3/90-48 (Broxton et al., 1993).

Run	Rock	Fluid	T(°C)	P(bar)	Duration(d)	Source
DB27	G4-1362	J-13	90	100	64	(1)
DB20	G4-1362	J-13	150	100	64	(2)
DB22	G4-1362	J-13	250	100	64	(2)
DB29	G4-1362	J-13	150	100	178	(3)
DB30	G4-1362	J-13	350	100	16(57)	(3)
DB25	GU3-1226	J-13	90	100	64	(3)
DB21	GU3-1226	J-13	150	100	64	(3)
DB23	GU3-1226	J-13	250	100	64	(3)
DB28	Ue25a1-1297*	J-13	90	100	64	(3)
DB24	Ue25a1-1297*	J-13	150	100	64	(3)
CH3	outcrop Tchnv	$NaHCO_3$	90	100	210	(4)
CH2	outcrop Tchnv	$NaHCO_3$	150	100	93	(4)
CH1	outcrop Tchnv	$NaHCO_3$	250	100	94	(4)

* = zeolitized Tpt
(1) Knauss and Peifer, 1986
(2) Knauss, 1987
(3) Knauss and Copenhaver (1995)
(4) in progress

All of the hydrothermal experiments with Tpt core wafers used water collected from well J-13 as the fluid. The three runs with Tch core wafers used a 3 mmolal $NaHCO_3$ solution as the fluid phase, since sufficient J-13 water was not available at the time the experiments were conducted. This solution has approximately the same carbonate alkalinity as J-13 water, but contains about 50% more Na+ (the dominant cation in J-13 water) and, of course, lacks the other cations (and anions).

In all runs the fluids were analyzed for a suite of cations and anions, the quench pH, and dissolved carbonate. The geochemical modeling code EQ3/6 (Wolery et al., 1990) was used to calculate the *in situ* pH. The fluid chemistry data have been reported as noted. Note that the pH in the tables is the 25°C pH of the quenched fluid sample. The unreacted solid wafers of tuff and the reacted wafers recovered at the end of each run were characterized using XRD and SEM/EMP analyses.

10.4.1.2 Results and Discussion. The results of earlier hydrothermal alteration experiments, in which the devitrified (repository-equivalent) Tpt was reacted with well J-13 water at 150° and 250°C, showed that the primary alteration products were the Ca-rich, mordenite-type zeolite, dachiardite, and mordenite itself (Knauss et al., 1987). The aqueous SiO_2 activity was controlled by cristobalite saturation. The fluid chemistry was in accord with the production of these zeolites.

In contrast, results of earlier hydrothermal alteration experiments, in which the vitric airfall/ashflow at the base of the Tpt was reacted with well J-13 water at 250°C, showed production of the zeolite clinoptilolite, exclusively (Knauss, 1987). In these runs with vitric tuff the aqueous SiO_2 activity was controlled by amorphous silica saturation. Runs at lower temperature (150° and 90°C) were extended for times insufficient to quite reach amorphous silica saturation and no zeolites formed, although significant changes in water chemistry occured during the course of the water-rock interaction. In all of the vitric airfall runs at temperatures of 250° or below, at least some glass remained unconsumed at the end of the run.

Continuing the series of runs using vitric airfall/ashflow from the base of the Tpt, we have found that even after 6 months at 150°C (DB29) the SiO_2 activity remained below amorphous silica saturation and no zeolites precipitated. However, at 350°C (DB30) amorphous silica saturation was quickly reached and the glass was completely consumed by the end of the run. The dominant run product was a non-stoichiometric feldspar (possibly orthoclase based on XRD), which had completely replaced the glass, and lesser amounts of the zeolite mordenite.

We ran three 2-month-long experiments to study the hydrothermal alteration of Tpt vitrophyre in well J-13 water at 90°C (DB25), 150°C (DB21) and 250°C (DB23). Although compositionally identical to the vitric basal airfall/ashflow material, the vitrophyre has a much smaller specific surface area, because it is densely welded. This changes the rate at which the glass dissolves and, hence, the fluid chemistry and run products differ for the same reaction time from those of the airfall. For example, in all three of these runs with Tpt vitrophyre the degree of undersaturation with respect to amorphous silica solubility was significantly greater than in the corresponding airfall/ashflow runs. We found only evidence of glass

dissolution at the two lowest temperatures. At 250°C, it is clear from SEM/EMP analyses that early in the run the dominant product was a clay, but as the run progressed the zeolite clinoptilolite became the major product. Given sufficient time/reaction progress, one would expect the vitrophyre to result in mostly zeolite alteration.

We ran two 2-month-long experiments to study the hydrothermal alteration of naturally zeolitized Tpt in well J-13 water at 90° (DB28) and 150° (DB24). In these samples, the starting material is predominately the zeolite heulandite, although a significant amount of smectite is also present. No new run products were identified in either run. The heulandite appeared to remain a stable phase. In fact, there was no obvious evidence of dissolution. Interestingly, the EMP analyses of the reacted wafer from the 150°C experiment suggested that the exchangeable cation composition of the heulandite had become more potassic and less sodic as a consequence of the hydrothermal reaction.

Preliminary results from the three experiments to study the hydrothermal alteration of vitric Calico Hills tuff (Tchnv) at 90° (CH3), 150° (CH2) and 250°C (CH1) contrast with those from the other experiments. Although the glass in the vitric Tch is compositionally fairly similar to the vitric Tpt, the phenocryst content is significantly higher in Tch and the phenocryst composition is distinct from that in the Tpt. More importantly, while the basal airfall/ashflow and vitrophyric Tpt samples were largely fresh (unaltered) glass, the vitric Tch material contains a significant amount of smectite. The smectite is observed to coat the matrix shards and pumice lapilli. This is true of both drillcore and outcrop specimens. Preliminary results suggest that this has a profound effect on the glass alteration. Even in samples with comparable specific surface area and glass composition, the Tch samples did not produce zeolite alteration. Only smectite was detected in XRD.

10.4.1.3 References

Broxton, D. E., S. J. Chipera, F. M. Byers, and C. A. Rautman(1993) Geologic evaluation of six nonwelded tuff sites in the vicinity of Yucca Mountain, Nevada for a surface-based test facility for the Yucca Mountain Project. Los Alamos National Laboratory Report LA-12542.

Knauss, K. G., and D. W. Peifer (1986) Reaction of vitric Topopah Spring tuff and J-13 ground water under hydrothermal conditions using Dickson-type, gold-bag rocking autoclaves: Lawrence Livermore National Laboratory Report, UCRL-53795.

Knauss, K. G. (1987) Zeolitization of glassy Topopah Spring tuff under hydrothermal conditions: *Mat. Res. Soc. Symp.* 84, 737–745.

Knauss, K. G., W. J. Beiriger, and D. W. Peifer (1987) Hydrothermal interaction of solid wafers of Topopah Spring tuff with J-13 water at 90 and 150∞C using Dickson-type, gold-bag rocking autoclaves: Long-term experiments: Lawrence Livermore National Laboratory Report, UCRL-53722.

Knauss, K. G., and S. A. Copenhaver (1995) Progress report on hydrothermal alteration of vitric tuff from Yucca Mountain. Lawrence Livermore National Laboratory Yucca Mountain Site Characterization Project Milestone MOL124, Data Tracking Number LL950613804241.009.

Wolery, T. J., K. J. Jackson, W. L. Bourcier, C. J. Bruton, B. E. Viani, K. G. Knauss, and J. M.Delany (1990) The EQ3/6 software package for geochemical modeling: Current Status: Amer. Chem. Soc. Symposium Series 416, *Chemical Modeling in Aqueous Systems II*, ed. D.C. Melchior and R.L. Bassett, p. 104–116.

10.4.2 Kinetics of Rock-Water Interaction: Amorphous Silica Precipitation (60 to 120°C); Comparison of Laboratory and Field Rates, by Susan Carroll[1], Edward Mroczek[2], Maureen Alai[1], and Margeret Ebert[1.1]-Earth Sciences Division, Lawrence Livermore National Laboratory, Livermore CA, USA, [2]-Institute of Geological & Nuclear Sciences, Wairakei Research Center, Wairakei, New Zealand

10.4.2.1 Introduction. Dissolution of silica in response to water movement at the elevated temperatures expected in a nuclear waste repository, and subsequent precipitation of silica on cooling may have an effect on local porosity and permeability. Changes in porosity and permeability will effect flow pathways, imbibition characteristics, and heat transfer, all of which may significantly influence repsotiory performance. In order to evaluate the effect of these processes, it is important that the behavior of amorphous silica precipitation be understood and predictable over relevant conditions. To obtain these needed data, a study was conducted to measure rates of precipitation in natural and laboratory settings. This work was to form the first stage in an effort to place bounds on kinetics effects, over a range of humidities, by resolving differences between rates measured in the laboratory and in the field.

Dissolution kinetics of amorphous silica and quartz are fairly well understood at conditions far from equilibrium as a function of solution composition and temperature (Brady and Walther, 1989; Carroll et al. 1994; Dove and Crerar, 1990; Dove and Elston, 1992; El-Shamy et al., 1972; House, 1994; Knauss and Wolery; 1988; Knauss et al., 1990; Tester et al., 1994). However, silica polymorph precipitation data are limited. Rimstidt and Barnes (1980), Bird et al., (1986) and Renders et al. (1995) model quartz, cristobalite, and amorphous silica precipitation rates assuming that the mechanisms controlling dissolution and precipitation are microscopically reversible and are related to the equilibrium constants by the principal of detailed balancing (Lasaga, 1981). Although these studies cover temperatures ranging from 18 to 300°C at conditions near saturation, they have only been performed at near

neutral pH. Bohlmann et al. (1980), Fleming (1986), Hosaka and Taki (1981a,b), Laudise (1958), Weres et al., (1981), and Yokoyama et al. (1989, 1991) have investigated the effect of activities of OH^-, Na^+ and Al^{3+} on silica precipitation.

It is necessary to study silica precipitation from complex field environments as well as from well controlled laboratory experiments because some aspects of natural systems may not be adequately accounted for in laboratory studies. Laboratory rate equations would therefore be rendered useless for prediction of amorphous silica precipitation in the earth's crust. Aspects of natural systems which may be important to silica precipitation include unknown effects of dissolved major and trace elements in natural waters.

Mroczek (1994) summarized previous field silica precipitation rates from geothermal waters, and compared them with rates calculated from theoretical and empirical models based on well controlled laboratory experiments (Bohlmann et al., 1980; Rimstidt and Barnes, 1980; Weres et al., 1981). These data were selected from a larger set of field data based on the anticipated conditions at a potential radioactive waste repository at Yucca Mountain, spanning temperatures less than 150°C and moderate to low degrees of silica supersaturation. At these conditions, heterogeneous reactions at the solid-solution interface are expected to be the dominant precipitation mechanism. Field silica precipitation rates were determined from the buildup of silica scale over time, where reactive surface area is the most uncertain parameter. Despite this, the rates calculated from empirical equations of Weres et al. (1981) and Bohlmann et al. (1980) were within an order of magnitude of the field rates. In contrast, the rates calculated from the Rimstidt and Barnes (1980) model are slower by approximately three orders of magnitude than the observed field rates. Their laboratory experiments were conducted under much smaller degrees of silica supersaturation than the field experiments and in pure water. The rates measured by Rimstidt and Barnes (1980) are very similar in magnitude to those measured by (Bird et al., 1986) in a similar experimental study.

In this work, we discuss the impact of temperature (60 to 120°C) and solution composition (pH 3-10, and aqueous silica, alkali, and aluminum concentrations) on amorphous silica precipitation by comparing field rates determined from Wairakei,

New Zealand, geothermal waters and laboratory rates using simple buffer solutions and Wairakei geothermal waters. For details of the study, see Carroll et al. (1996).

10.4.2.2 Experimental Methods

10.4.2.2.1 Starting Materials. A fine grained, well rounded 99% pure quartz sand from Glorit, New Zealand was used in the field experiments. X-ray diffraction analysis showed no indication of other crystalline material. The initial and final surface area were calculated to be 0.8 and 0.4 m^2g^{-1} from BET Kr gas adsorption isotherms, respectively. These BET determinations of surface area are approximately 1.7 orders of magnitude higher than the geometric determination of surface area (1.13×10^{-2} m^2g^{-1}) assuming spherical non-porous particles with a density of 2.65 $g\ cm^{-3}$ (Gregg and Sing, 1982). This discrepancy is consistent with other reported differences between BET and geometric surface area determinations of quartz sand (White and Peterson, 1990) and is probably due to significant surface roughness and the non-spherical nature of the sand.

Amorphous silica used in the laboratory experiments was Mallickrodt Silicar Silica Gel, which was repeatedly cleaned ultrasonically with Milli-Q filtered water to remove fines, dried at 40°C for 24 hours, and then stored in a plastic container at room temperature. Initial total surface area determined from BET N_2 gas adsorption isotherm is 270 m^2g^{-1}; final total surface areas range from 50 to 280 m^2g^{-1}.

Simple solutions used to control solution pH in the laboratory experiments are HCl/KHphthalate buffer at pH 3, Na-acetate buffer at pH 5, NaOH/Na-borate buffer at pH 8 and 9. With the exception of one experiment, the total alkali concentration of all the experiments is 0.13 *M*. The composition of the Wairakei geothermal waters used in the laboratory and field experiments is listed in Table 10.4-1.

10.4.2.2.2 Geochemical Calculations. Solution speciation, pH, and extent of saturation with respect to silica phases at the experimental temperatures were calculated from the measured solution compositions at room temperature using *React* (Bethke, 1994) and EQ3/EQ6 (Wolery, 1992) geochemical codes and the SUPCRT92 thermodynamic data base (Johnson et al., 1992), augmented with o-

phthalic acid stability constants at 25°C (Martell and Smith, 1989). Differences in program algorithms result in very small differences in calculated Gibb's free energy of reaction (200 $Jmol^{-1}$) with respect to amorphous silica solubility between 60 and 120°C.

10.4.2.2.3 Laboratory Experiments. The precipitation experiments were run in Dickson-type, gold bag autoclaves (250 *ml*) capped with a commercially pure titanium head fitted with titanium or gold capillary-lined stainless steel sampling tube that allowed the experiment to be sampled *in situ* (Seyfried et al., 1987). A copper coil around the sampling tube allowed fluids to be quenched prior to sampling.

At the beginning of each experiment, the gold bag was filled with the reactants (approximately 5 grams of amorphous silica, and buffer solution or Wairakei geothermal waters), sealed with the titanium head, pressure tested with an inert gas, and placed in a pressure vessel filled with de-ionized water, which served as the pressure medium. Throughout the experiment, the furnace temperature was controlled by digital proportioning controllers, and the internal vessel temperature was monitored with chromel-alumel thermocouples and digital thermometers accurate to ±1°C.

Reaction was allowed to proceed at temperature until amorphous silica saturation was achieved, and then the temperature was lowered to yield a solution supersaturated with respect to amorphous silica by a factor of approximately 1.3. One experiment contained geothermal waters alone to determine whether silica precipitation occurs via homogeneous nucleation in the bulk solution. During sampling, a nominal pressure (*35 -70 bar*) was maintained by externally pumping water into the pressure vessel as the sample was taken. The sampling port was maintained in an up-right position, keeping the amorphous silica at the bottom of the gold bag, which allowed only the aqueous phase to be sampled. At the completion of the experiment, the amorphous silica was removed, rinsed in MilliQ filtered water five times, and dried.

10.4.2.2.4 Field Experiments. Silica precipitation was measured in the field with a fluidized bed reactor, FBR, constructed at the Wairakei geothermal energy plant in

New Zealand (Fig. 10.4-1). Geothermal waters were passed through steam grade iron pipe, at approximately 130°C and 2 bars, to a heat exchanger. A 100 mesh stainless steel filter upstream of the heat exchanger removed fines from the fluid. Temperature and flow of the fluid through the FBR were controlled by valves on the bypass line and prior to the FBR inlet, respectively. Flow rate was measured at the effluent stream. Inlet and outlet sampling points were located at the bypass line and at the top of the reactor column. The FBR unit was insulated with 50 *mm* thick fiberglass covered with aluminum foil to minimize conductive heat loss.

The reactor was loaded with 4.5 to 6 *kg* of sand, desired temperature and flow regime were adjusted, and the FBR was then left for at least 48 hours to coat sand particles with amorphous silica. After each adjustment of temperature or flow rate, at least 2 to 4 hours elapsed prior to sampling, which was more than ample time to reach steady-state conditions for the 3 to 5 minute fluid residence times within the FBR. Inlet and outlet samples were collected, preserved with HCl to avoid polymerization, and analyzed for monomeric silica within 30 minutes. Filtered samples (0.2 *um* pore size) were analyzed for total silica at a later time.

On shutdown, the bed was dismantled, the sand was washed, dried and weighed. The inside of the reactor wall was evenly coated with a very thin, hard, translucent layer of silica almost to the top. Precipitation was also observed in the mesh filters at the base of the reactor and was much softer than along the FBR walls.

10.4.2.3 Analytical Techniques

10.4.2.3.1 Solution Analysis. All aqueous samples were analyzed by inductively coupled plasma-atomic emission spectrometry (ICP-AES) or atomic absorption spectrometry (AA) for total dissolved silica. In addition, ICP-AES was used to analyze for Al, B, Ca, Fe, K, Li, Mg, Na, Rb, and S concentrations, inductively coupled plasma-mass spectrometry (ICP-MS) was used to analyze for total As, Cs, and Rb and ion chromatography (IC) was used to analyze for Cl^-, F^-, and SO_4^{2-} concentrations in the initial geothermal waters. Samples were pretreated to remove Cl^- to quantitatively analyze F^- and SO_4^{2-} by IC. Reproducibility of each of these analytical techniques is better than 2% and analyte concentrations are at least one

order of magnitude greater than the detection limits of the analytical technique. The relative standard deviation for the analyses was typically less than 3%. Monomeric silica was measured using a UV photospectrometer and the yellow-β silicomolybdate method (Iler, 1979). This method has a detection limit of approximately 1 *ppm* and an error typically less than 6%.

10.4.2.3.2 Solid Phase Analysis. Starting materials and run products were analyzed by powder x-ray diffraction (XRD), scanning electron microscopy (SEM), energy dispersive spectroscopy (EDS), and BET gas adsorption, to check for changes in crystalinity, morphology, chemical composition, and surface area, respectively. Krypton and nitrogen were the gas adsorbents used to determine the surface area of the solids in the field and laboratory experiments, respectively.

10.4.2.4 A General Rate Equation. For amorphous silica precipitation, the reaction of interest is:

$$\underset{\Leftarrow\Leftarrow\ precipitation}{SiO_{2(Am.\ Si.)} + 2H_2O \Leftrightarrow H_4SiO_4.} \qquad (1)$$

$$dissolution\ \Rightarrow\Rightarrow$$

where the Gibb's free energy of reaction, ΔG_r:

$$\Delta G_r = RT \ln Q / K_{eq}, \qquad (2)$$

and solution saturation is equal to the ratio of the aqueous ion activity quotient and amorphous silica solubility constant, Q/k_{eq}, assuming ideal unit activity of the solid phase.

A generalized equation which relates net precipitation rate, $Rate_{ppt}$ to reaction affinity may be written as:

$$Rate_{ppt} = -d[Si]/dt = -k_{ppt}^{*} [1-n \exp(\Delta G_r/RT)]^m \qquad (3)$$

where k_{ppt} is a rate constant that may be dependent on temperature, pressure, total reactive surface area, surface defect density, and on any unidentified effect of the

solution composition (such as the activities of OH^-, Na^+, or Al^{3+}), and n and m are empirical constants. The form of the Gibb's free energy function, $f(\Delta G_r)$, in equation (3):

$$f(\Delta G_r) = [1-n \exp (\Delta G_r/RT)] \quad (4)$$

and the overall order of reaction affinity, m, provide insight to the rate controlling mechanism, which may include elementary reactions at the solid-solution interface or growth at the surface defect sites.

Although mineral kinetics are likely to be controlled by complex reactions at the solid-solution interface, transition state theory (Lasaga, 1981; Aagaard and Helgeson, 1982) and surface complexation theory (Stumm and Wieland, 1990) have played critical roles in the development and application of generalized rate expressions for dissolution and precipitation reactions. Irreversible thermodynamics may be applied to complex solid-solution reactions, if a single elementary reaction or several elementary reactions at steady-state control the precipitation reaction (Nagy et al., 1991; Nagy and Lasaga, 1992). For both of these cases $Rate_{ppt}$ is linearly dependent on $f(\Delta G_r)$. If precipitation involves a series of elementary reactions, where the rate is controlled by the slowest elementary reaction, then equation (3) simplifies to:

$$Rate_{ppt} = -k_{ppt} * [1 - exp(\Delta G_r/RT)] \quad (5)$$

where n and m equal 1. If the reaction rate is controlled by more than one elementary reaction at steady-state, then the equation (3) may be expressed by:

$$Rate_{ppt} = -k_{ppt} * [1- n \exp (\Delta G_r/RT)] \quad (6)$$

where n is a constant not equal to 1 and m equals 1.

Mineral precipitation rates controlled by surface defects, such as dislocations and impurities, have a non-linear dependence on $f(\Delta G_r)$:

$$Rate_{ppt} = -k_{ppt}^{*} \; [1-exp\ (\Delta G_r/RT)]^m \qquad (7)$$

where n equals 1 and m does not equal 1. For example, the BCF model (Burton et al., 1951, Ohara and Reid, 1973) describes continuous spiral growth along energetically favorable sites, and has a second order dependence on $f(\Delta G_r)$. Heterogeneous nucleation is not required with this model, allowing precipitation to occur from slightly supersaturated solutions ($Q/K_{eq} = 1.05$). Nielson (1986) has successfully predicted experimental precipitation rates for a variety of chloride, sulfate, carbonate, and oxalate salts using the BCF model. Several amorphous silica precipitation experiments mathematically describe the rates with a second order dependence on $f(\Delta G_r)$ (Bohlmann et al., 1980; Weres et al., 1981).

10.4.2.5 Results and Discussion

10.4.2.5.1 Laboratory Experiments. For our calculations, we assume that the reactive surface area available for precipitation is proportional to the BET surface area of amorphous silica at the end of each experiment. The final BET surface areas deviate from the initial value of 270 m^2g^{-1} and range from 50 to 280 m^2g^{-1} (Table 10.4-2). We assume that most of the surface area reduction occurs during reaction at elevated temperature prior to the decrease to precipitation run temperature. This is reasonable, because the solutions have reached amorphous silica saturation at elevated temperature, and because there is a systematic decrease in BET surface area with increasing pH. This trend is in agreement with decreasing surface area of silica gels synthesized at increasing pH (Iler, 1979). No observable changes in surface morphology are observed in SEM images of initial and final solids to account for a two to five factor change in surface area. Therefore, the reduction in surface area must be due to a reduction in internal porosity. No crystalline phases were detected in the solid phases with XRD.

To calculate amorphous silica precipitation rates from the laboratory experiments, curves are fit to the exponential decrease in aqueous silica concentrations normalized with respect to surface area as a function of time. Only data from the first 10 days of precipitation are used in the exponential curve fit to

minimize potential artifacts of increasing relative surface area as aqueous samples are extracted from the reaction vessel over time.

Amorphous silica precipitation rates (Fig. 10.4-2) are best modeled with the following form of the general rate equation (3):

$$Rate_{ppt} = -d[Si]m^{-2}/dt = -k_{ppt}(pH, T) * (1 - exp\Delta G_r/RT) \quad (8)$$

where $n = m = 1$ and $k_{ppt}([Si]m^{-2}d^{-1})$ is dependent on pH and temperature. For each experiment, there is a linear relationship between $Rate_{ppt}$ and $f(\Delta G_r)$ with a slope proportional to k_{ppt}. At all pH, precipitation rates approach zero in solutions slightly undersaturated with respect to amorphous silica, corresponding to ΔG_r between 0 to $-670\ Jmo^{-1}$.

The pH-dependence of amorphous silica precipitation is shown in Fig. 10.4-3 as $log\ k_{ppt}$ versus pH. At 100°C, k_{ppt} is proportional to $(H^+)^{-0.2}$ from pH 3 to 8.7. At 80°C, k_{ppt} is proportional to $(H^+)^{-0.3}$ from pH 3 to 7; no experiments were conducted at greater pH. At 120°C, there is not enough data to establish a pH-dependence of k_{ppt}. These results are in agreement with lower temperature results; amorphous silica precipitation rates increase from pH 4 to 8 at 25°C (Fleming 1986). Additionally, these results qualitatively agree with aqueous silica polymerization, which occurs within a couple hours at acid pH and within a couple of minutes at pH > 7 (Iler, 1979).

Dissolved components other than silica and pH do not significantly impact amorphous silica precipitation rates (Fig. 10.4-3). At 80 and 100°C, k_{ppt} determined from experiments containing chemically complex Wairakei geothermal waters are consistent with the pH-dependence of the rate constant observed from batch experiments containing simple buffer solutions. At 120°C and approximately pH 7, k_{ppt} determined from the experiments containing geothermal waters is about 0.5 orders of magnitude higher than k_{ppt} determined from the experiment containing NaCl solution.

Temperature dependence of amorphous silica precipitation rates is evaluated in an Arrhenius plot of log k_{ppt} versus 1/T (K) (Fig. 10.4-4), where activation energy, E_a, is equal to:

$$E_a = -2.303\ R\ (d\log k_{(ppt)}/d(1/T)) \qquad (9)$$

Activation energies range from 51.6 to 82.6 (kJ mol^{-1}) at pH 7 and 3, respectively. These values are consistent for rates controlled by reactions at the solid-solution interface, and in the same range as activation energies (30 to 150 kJ mol^{-1}) determined for a variety of silica polymorphs over a temperature range of 20 to 500°C (Table 10.4-3).

Amorphous silica precipitation is controlled by reactions at the solid-solution interface, and not by homogeneous nucleation. This conclusion is supported by the lack of silica precipitation in the absence of amorphous silica seed material (Fig. 10.4-5A). Wairakei geothermal waters are slightly supersaturated with respect to amorphous silica at 120°C. In the presence of amorphous silica, aqueous silica decreases to amorphous silica saturation value at 100°C within 24 hours after the drop in temperature. In the absence of amorphous silica, there is no measurable decrease in silica concentrations up to 3 days after the temperature is decreased from 120 to 100°C. Additionally, for experiments in which both total and monomeric silica were measured, all silica is present as monomeric silica with the exception of one experiment at pH 8.7 and 100°C (Fig. 10.4-5B). At pH > 7 polymerization kinetics are rapid (Iler 1979), therefore it is possible that monomeric silica polymerized in the 30 minute period between sample extraction at 100°C and sample analysis at room temperature for this experiment.

The results of this study do not support the principle of detailed balancing as applied to silica dissolution and precipitation kinetics. According to the principle of detailed balancing, precipitation, k_{ppt}, and dissolution rate constants, k_{diss}, are related to each other through the equilibrium constant, thus requiring k_{ppt} and k_{diss} to have the same dependence on solution composition (i.e. $f(\Delta G_r)$ and pH).

Amorphous silica precipitation (this study) and dissolution (Rimstidt and Barnes, 1980) rates have the same form of $f(\Delta G_r)$:

$$f(\Delta G_r) = (1\text{-}exp\Delta G_r\ /RT), \tag{10}$$

but the pH-dependencies of k_{ppt} and k_{diss} are distinct. Amorphous silica precipitation increases with increasing pH from pH 3 to 8.7. In contrast, quartz and amorphous silica dissolution rates at conditions far from equilibrium are independent of solution pH in the acid to near neutral region, and increase with increasing pH at more alkaline pH (Brady and Walther, 1989; Carroll et al., 1994, Knauss and Wolery, 1988). Silica precipitation rate equations based on the experimental data of Rimstidt and Barnes (1980) and Renders et al. (1996) should not be extrapolated to acid and alkaline pH solutions. All of their experiments were conducted in deionized water.

Other studies find that the principle of detailed balancing does not adequately model mineral dissolution and precipitation reactions over a wide range of solution compositions. Nagy and Lasaga (1992) observe that the principle of detailed balancing describes gibbsite dissolution and precipitation kinetics at 80°C and pH 3 in solutions close to equilibrium, $-0.8 < \Delta G_r < 0.8$ (kJ/mol), but not at greater degrees of understaturation. For more complicated mineral phases, it is not clear that this model applies even very close to equilibrium (Burch et al, 1993; Nagy and Lasaga, 1993).

10.4.2.5.2 Field Experiments. The steady-state precipitation rate, $Rate_{ppt}$ $([Si]\ m^{-2}d^{-1})$ from FBR experiments may be calculated from the following equation:

$$Rate_{ppt} = \frac{v \times \Delta[Si]}{SA} \tag{11}$$

where v $(L\ d^{-1})$ is the flux of fluids flowing through the reactor, $\Delta[Si]$ (mol/L) is change between inlet and outlet Si concentrations, and SA (m^2) is the total surface area of the particles in the FBR. Equation (10) applies if the FBR behaves as a

continuously stirred reactor, such that fluid velocity approximates the settling velocity of the particles, resulting in a dynamic suspension (Posey-Dowty et al., 1986). The use of equation (10) to calculate amorphous silica precipitation rates is supported by the linear decrease in Δ[Si] as a function of increasing fluid flow rate over limited temperature intervals (± 2°) and constant surface area (Fig. 10.4-6).

Amorphous silica precipitation was measured from Wairakei geothermal solutions supersaturated with respect to amorphous silica by as much as a factor of two ranging in temperature from 60 to 117°C. The results are summarized in Table 10.4-4 and Fig. 10.4-7. Overall, precipitation rates increase with decreasing temperature and increasing supersaturation; (1 - exp (ΔG_r/RT)) becomes more negative with increasing supersaturation. The effects of supersaturation and temperature are interrelated, because an approximately constant inlet silica concentration from the geothermal waters yields an increase in supersaturation with decreasing temperature. The error in the precipitation rate shown in Fig. 10.4-7 is due to the uncertainty in the silica analysis. The difference in the silica concentration between the inlet and outlet solutions was only a small fraction of the total, between 1 and 8 mol.%, which translates to a 3 to 23% error in the calculated rates. Another source of error in the calculated precipitation rates is the BET surface area measurements; surface areas for the reacted and unreacted sand are 0.4 and 0.8 m^2g^{-1}, respectively. A limitation of the FBR is that surface area cannot be evaluated at each run temperature.

However, measured rates are reproducible over the duration of the experiments, indicating no major changes in the solid surface area. We have chosen to normalize the field precipitation rates to initial BET surface area.

In these experiments, we assume that amorphous silica rapidly coats the quartz grains, and therefore steady-state values of Δ[*Si*] are controlled by heterogenous precipitation at the amorphous silica-solution interface. This reasoning is consistent with the results of Axtmann and Grant-Taylor (1986) and Bohlmann et al. (1980), who have shown that rutile and quartz grains are quickly coated with amorphous silica. Homogeneous nucleation of amorphous silica from the bulk solution is

minimized by the short residence time of the solutions in the FBR (3–5 *min.*). Induction times observed before the onset of polymerization are typically 0.5 and 2 hours at 70 and 100°C, respectively (Rothbaum and Rhode, 1979). With the exception of two sample sets at 69 and 61°C, inlet and outlet polymeric silica concentrations calculated from the difference between total silica and monomeric measurements are constant and typically within analytical error, between 2 and 4% of the total silica (Fig. 10.4-8).

Evidence of silica precipitation is seen in SEM images comparing morphology of the unreacted and reacted sand. The reacted sand is covered with hemispherical silica precipitates with 1 to 2 wt.% aluminum. No aluminum was detected in the unreacted sand. The presence of significant surface roughness in both the reacted and unreacted sand supports the use of BET determined surface areas in the precipitation rate calculations.

It is not possible to unequivocally determine the exact nature of the surface reaction mechanism controlling amorphous silica precipitation. If $Rate_{ppt}$ is modeled within the framework of transition state theory, where n = m = 1, there is an almost linear trend between $Rate_{ppt}$ and $(1 - \exp(\Delta G_r/RT)$ with $k_{ppt} = -1.99\ e\text{-}4$ $([Si]\ m^{-2}\ d^{-1})$ (Fig. 10.4-7). Although this expression mathematically describes the relationship between measured rate and solution silica concentrations, it is doubtful that the form of $f(\Delta G_r)$ is indicative of a rate-limiting elementary reaction, because k_{ppt}, and consequently $Rate_{ppt}$, would be independent of temperature. Recall that temperature and the extent of solution saturation mask one another in the field study. Surface controlled reactions are strongly temperature dependent (White and Brantley, 1995 and references therein). Table 10.4-3 lists a range of activation energies reported for a variety of silica polymorphs. Only Bohlmann et al. (1980) observed zero temperature dependence for amorphous silica precipitation rates.

10.4.2.5.3 Comparison Of Laboratory and Field Precipitation Rates. Figure 10.4-9 is a comparison of laboratory and field rates using field chemistry and the laboratory rate equation describing the amorphous silica precipitation as a function of temperature from those experiments containing Wairakei geothermal waters:

$$Rate_{ppt} = -10^{(1.77-(Ea/2.303R)*(1/T))} (1 - exp (\Delta G_r/RT) \quad (12)$$

At field conditions most similar to the laboratory experiments, $f(\Delta G_r) > -0.4$ and temperatures between 90 and 115°C, rates are 10 to 20 times faster than laboratory rates. At lower temperature and more supersaturated solutions, the field rates may be as much as 250 times greater than predicted with the laboratory rate equation.

Rate equations derived from static laboratory experiments cannot be used to model amorphous silica precipitation in complex natural environments, because amorphous silica precipitation appears to be controlled by different mechanisms in laboratory and field studies. The first order dependence of the laboratory rates on reaction affinity indicates amorphous silica precipitation kinetics are controlled by a rate-limiting elementary reaction at the solid-solution interface. By comparison, the second order dependence of the field rates on reaction affinity and the hemispherical surface morphology of the reacted sand in the field study indicates that reactions at surface defects control amorphous silica precipitation rates.

Other factors that may contribute to the observed discrepancy between the field and laboratory experiments are effective surface area, precipitation of quartz, and effect of dissolved aluminum. It is doubtful that the reactive surface area in the field experiments increases by two orders of magnitude at lower temperature in the more supersaturated solutions. The final surface area of the reacted sand, which reflects precipitation from a highly supersaturated solution at ambient temperatures as the FBR was dismantled, is only a factor of two higher than initial surface area.

Another possibility is that quartz, and not amorphous silica, precipitates at the sand-solution interface. If this is the case, then the calculated field precipitation rate would increase by approximately one order of magnitude, because the solution would be more saturated with respect to quartz. It is not likely that quartz precipitates, given the high aluminum content of reacted sand surfaces. Additionally, quartz precipitation does not explain the increasing precipitation rates at lower temperature in more supersaturated experiments.

A third possible explanation is the impact of dissolved aluminum on amorphous silica precipitation. The aluminum concentration in the reacted sand

surfaces (1–2 wt.%) is enriched by four orders of magnitude over the low concentrations in the geothermal waters (>1 ppm). The fact that no significant effects of the geothermal waters on amorphous silica precipitation occur in the laboratory experiments may be an artifact of the two different types of experiments. The total dissolved aluminum available for precipitation in the laboratory experiments is limited by the volume of the reaction vessel. In the field experiments, the FBR design allows for continual preferential removal of the aluminum and silica as high volumes of fluid flow through the reactor.

10.4.2.6 Conclusions. The results of this study confirm the need for complementary laboratory and field studies to determine the factors that control mineral-water interactions in tuff. Amorphous silica precipitation rates appear to be controlled by distinct mechanisms in the laboratory and field studies. Amorphous silica precipitation rates determined from the field study at Wairakei, New Zealand, are 10 to 300 times higher than rates predicted from the laboratory experiments. The deviation between the rates increases as temperatures decrease and the solution composition increases.

Amorphous silica precipitation rates determined from the batch experiments are controlled by reactions at the solid-solution interface and are dependent on temperature, solution pH, and aqueous silica concentration. The presence of trace elements in the Wairakei geothermal waters does not significantly enhance or inhibit amorphous silica precipitation in these experiments. The precipitation rate constant has a fractional dependence on solution pH; k_{ppt} is proportional to $\{H^+\}^{-0.3}$ and $\{H^+\}^{-0.2}$ at 80 and 100°C, respectively. E_a measured at pH 7 is 51.6 *kJ mol*$^{-1}$. The first order dependence of precipitation rate on reaction affinity $(1 - \exp \Delta G_r/RT)$ is consistent with an elementary rate-limiting surface reaction. However, the pH-dependencies of amorphous silica precipitation and dissolution rates show that the principle of detailed balancing cannot be applied to amorphous silica kinetics.

Amorphous silica precipitation behavior in the field experiments is distinct from the laboratory experiments. Amorphous silica precipitation may be controlled by surface defects, such as dislocation or impurities, but it does not appear to be

controlled by elementary rate-limiting reactions at the solid-solution interface. Aluminum is enriched in the precipitating phase by four orders of magnitude. However, the enrichment mechanism or the impact of dissolved aluminum on amorphous silica precipitation rates is not known.

10.4.2.7 References

Aagaard, P., and H. C. Helgeson(1982) Thermodynamic and kinetic constraints on reaction rates among minerals and aqueous solutions. I. Theoretical consideration. *Amer. J. Sci.* 282, 237–285.

Axtmann , R. C., and D. Grant -Taylor (1986) Desilication of geothermal waste waters in fluidized beds. *Geothermics* 15, 185–191.

Bethke, C. M. (1994) *The Geochemist's Workbench. A Users Guide to Rxn, Act2, Tact, React, and Gtplot.* Board of Trustees of the University of Illinois.

Bird, G., J. Boon, and T. Stone (1986) Silica transport during steam injection into oil sands. 1. Dissolution and precipitation kinetics of quartz: new results and review of existing data. *Chem. Geol.* 54, 69–80.

Bohlmann, E. G., R. E. Mesmer, and P. Berlinski (1980) Kinetics of silica deposition from simulated geothermal brines. *Soc. Petroleum Engineers J.*, 239–248.

Brady P. V. and Walther J. V. (1989) Controls on silicate dissolution rates in neutral and basic pH solutions at 25°C. *Geochim. Cosmochim. Acta* 53, 2823–2830.

Burch, T. E., K. L. Nagy, and A. C. Lasaga (1993) Free energy dependence of albite dissolution kinetics at 80°C and pH 8.8. *Chemical Geology* 105, 137–172.

Burton, W. K., N. Cabrera, and F. C. Frank (1951) The growth of crystals and the equilibrium structure of their surfaces. *Phil. Trans. Roy. Soc. London* A243, 299–358.

Carroll, S. A., W. L. Bourcier, and B. L. Phillips (1994) Surface chemistry and durability of borosilicate glass. *Mat. Res. Soc. Sym.* 333, 533–540.

Carroll, S. A., E. Mroczek, B. Bourcier, M. Alai, and M. Ebert (1995) Comparison of field and laboratory precipitation of amorphous from geothermal waters at 100°C. Lawrence Livermore National Laboratory Yucca Mountain Site Characterization Project Milestone MOL207.

Dove, P. M., and D. A. Crerar (1990) Kinetics of quartz dissolution in electrolyte solutions using a hydrothermal mixed flow reactor. *Geochim. Cosmochim. Acta* 54, 955–969.

Dove, P. M., and S. F. Elston (1992) Dissolution kinetics of quartz in sodium chloride solution: Analysis of existing data and a rate model for 25°C. *Geochim. Cosmochim. Acta* 56, 4147–4156.

El-Shamy, T. M., J. Lewins, and R. W. Douglas (1972) The dependence on the pH of the decomposition of glasses by aqueous solutions. *Glass Technology* 13, 81–87.

Fleming, B. A. (1986) Kinetics of reaction between silicic acid and amorphous silica surfaces in NaCl solutions. *J. Colloid Interface Sci.* 110, 40-64.

Gregg, S. J., and K. S. W. Sing (1982) *Adsorption, Surface Area and Porosity.* Academic Press, London.

Hosaka, M., and S. Taki (1981a) Hydrothermal growth of quartz crystals in NaCl solution. *J. Crystal Growth* 52, 837–842.

Hosaka, M., and S. Taki (1981b) Hydrothermal growth of quartz crystals in KCl solution. *J. Crystal Growth* 53, 542–546.

House, W. A. (1994) The role of surface complexation in the dissolution kinetics of silica: Effects of monovalent and divalent ions at 25°C. *J. Colloid Interface Sci.* 163, 379–390.

Iler, R. K. (1979) *The Chemistry of Silica. Solubility, Polymerization, Colloid and Surface Properties, and Biochemistry.* John Wiley and Sons, 866p.

Johnson, J. W., E. H. Oelkers, and H. C. Helgeson (1992) SUPCRT92: A software package for calculating the standard molal thermodynamic properties of minerals, gases, aqueous species and reactions from 1 to 5000 bar and 0 to 1000°C. *Computers and Geosciences* 8, 899–947.

Knauss, K., and T. J. Wolery (1988) The dissolution kinetics of quartz as a function of pH and time at 70°C. *Geochim. Cosmochim. Acta* 52, 43–53.

Lasaga, A. C. (1981) Transition State Theory. In Kinetics of Geochemical Processes (eds. A.C. Lasaga and R.J. Kirkpatrick); *Reviews in Mineralogy* 8, 135–169.

Laudise, R. A. (1959) Kinetics of hydrothermal quartz crystallization. *J. Amer. Chem. Soc.* 81, 562–566.

Martell, A. E. and R. M. Smith (1989) *Critical Stability Constants: Other Organic Ligands.* Plenum Press, New York. V. 3. 495p.

Mroczek, E. K. (1994). Review of silica deposition rates at Ohaaki, Rotokawa, and Wairakei geothermal fields and comparison of observed rates with predicted deposition rates calculated using three different kinetic deposition models. Report No. 722305.15. Institute of Geological and Nuclear Sciences.

Nagy, K. L., A. E. Blum, and A. C. Lasaga (1991) Dissolution and precipitation kinetics of kaolinite at 80°C and pH 3: The dependence on solution saturation state. *Am. J. Sci.* 291, 649–686.

Nagy, K. L., and A. C. Lasaga (1992) Dissolution and precipitation kinetics of gibbsite at 80°C and pH 3: The dependence on solution saturation state. *Geochim. Cosmochim. Acta* 56, 3093–3111.

Nagy, K. L., and A. C. Lasaga (1993) Simultaneous precipitation kinetics of kaolinite and gibbsite at 80°C and pH 3. *Geochim. Cosmochim. Acta* 57, 4329–4336.

Nielsen, A. E. (1986) Mechanisms and rate laws in electrolyte crystal growth from aqueous solution. In *Geochemical Processes at Mineral Surfaces* (ed. J. A. Davis and D. F. Hayes); ACS Symp. Ser. 323, 600–614.

Ohara, M., and R. C. Reid (1973) *Modeling Crystal Growth Rates from Solution.* Prentice-Hall.

Posey-Dowty, J., D. Crerar, R. Hellmann, and C. D. Chang (1986) Kinetics of mineral-water reactions: theory, design and application of circulating hydrothermal equipment. *American Mineralogist* 71, 85–94.

Renders, P. J. N., C. H. Gammons, and H. L. Barnes (1995) Precipitation and dissolution rate constants for cristobalite from 150 to 300°C. *Geochim. Cosmochim. Acta* 59, 77–85.

Rimstidt, J. D., and H. L. Barnes (1980) The kinetics of silica-water reactions. *Geochim. Cosmochim. Acta* 44, 1683–1699.

Rothbaum, H. P., and A. G. Rhode (1979) Kinetics of silica polymerization and deposition from dilute solutions between 5 and 180°C. *J. Colloid Interface Sci.*, **71**, 533–559.

Seyfried, W. E., D. R. Janecky, and M. E. Berndt (1987) Rocking autoclaves for hydrothermal experiments. II. The flexible reaction-cell system. In *Hydrothermal Experimental Techniques* (eds. G. C. Ulmer and H. L. Barnes). 216–239.

Stumm, W., and E. Wieland (1990) Dissolution of oxide and silicate minerals: Rates depend on surface speciation. In *Aquatic Chemical Kinetics* (ed. W. Stumm), pp. 367-400. J. Wiley & Sons.

Tester, J. W., W. G. Worely, B. A. Robinson, C. O. Grigsby, and J. L. Feerer (1994) Correlating quartz dissolution kinetics in pure water from 25 to 625°C. *Geochim. Cosmochim. Acta* **58**, 2407–2420.

Walther, J. V., and H. C. Helgeson (1977) Calculation of the thermodynamic properties of aqueous silica and the solubility of quartz and its polymorphs at high pressures and temperatures. *Amer. J. Sci.* **277**, 1315–1351.

Weres, O., A. Yee, and L. Tsao (1981). Kinetics of silica polymerization. *J. Colloid Interface Sci.*, **84**, 379–402.

White, A. F., and S. L. Brantley (1995) Chemical Weathering Rates of Silicate Minerals. (ed. A. F. White and S. L. Brantley). *Reviews in Mineralogy* **31**, 583p.

White, A. F., and M. L. Peterson (1990) Role of reactive-surface-area characterization in geochemical kinetic models. In *Chemical Modeling of Aqueous Systems II* (ed. D. C. Melchior and R. L. Bassett, ACS Symp. Ser. **416**, 461–475.

Wolery, T. J. (1992) EQ3NR, A computer program for geochemical aqueous speciation-solubility calculations: Theoretical manual, user's guide, and related documentation. Lawrence Livermore National Laboratory, UCRL-MA-110662 PTIII.

Yokoyama, T., Y. Takahshi, C. Yamanaka, and T. Tarutani (1989). Effect of aluminum on the polymerization of silicic acid in aqueous solution and the deposition of silica. *Geothermics*, **18**(1/2),321–325.

Yokoyama, T., Y. Takahshi, C. Yamanaka, and T. Tarutani (1991). Retarding and accelerating effects of aluminum on the growth of polysilicic acid particles. *J. Colloid Interface Sci.* **141**(2), 559–569.

10.4.3 Thermal Effects in the Altered Zone: Preliminary Bounds on the Water Composition and Secondary Mineral Development in the Altered Zone That May Influence the Near-Field Environment, by Michael Whitbeck and William E. Glassley, Lawrence Livermore National Laboratory

10.4.3.1 Introduction. The proposed repository site is within the unsaturated zone, where ambient saturation of matrix pore volumes is as high as 75%. Heat-driven evaporation, boiling, and condensation processes will lead to movement of water vapor away from the repository, resulting in increased saturation of some rocks within some parts of the repository block (Nitao, 1988; Buscheck and Nitao, 1992, 1993). In some cases, the saturation may approach 100% under some operation scenarios after waste is emplaced. During cool down, or as a result of fracture flow or dehydration of hydrous minerals, it is possible that liquid water may return to or enter the near-field environment (NFE), or may affect rock units bounding the repository horizon. Most of the minerals currently present in the rock making up the potential repository horizon are not in thermodynamic equilibrium with water at elevated temperatures, nor is the glassy material preserved within the PTn or the TSw3 units. As a result, water will interact with existing minerals and glass, causing new minerals to form, existing minerals to change their compositions or dissolve, and modifying the water chemistry in the process. In order to bound these effects, an effort to model reaction processes was undertaken. The focus of this effort was on identifying the likely minerals that would form, the effect on water chemistry, and determine the rates at which these changes would occur. It was also the intent to determine the uncertainty in these calculations, considering the known uncertainty in the kinetics of dissolution and precipitation reactions.

10.4.3.2 Approach. Rock units considered in the simulations were the TSw2 and TSw3 units of the Topopah Spring tuff. The mineral abundances for the TSw2 unit were taken from Delany (1985). The dissolution rates of the mineral phases, and their respective surface areas, were also taken from Delany (1985). The glass composition was taken to be that of Sample 2A from Table II of Broxton et al (1989).

The EQ3/6 code, version 7.2a, (Wolery, 1992 a,b; Wolery et al., 1990; Wolery and Daveler, 1992) was used for the simulations. The database used was COM, version 22a. All calculations were done using the "B-dot" activity coefficient model (see Wolery, 1992b for a description of this model).

The initial water composition reacting with the rock materials was assumed to be that of J-13 water. The composition used was the average composition reported in Harrar et al (1990).

Since the purpose of these simulations was to consider the effect of reaction progress on water chemistry and mineral assemblages, it was necessary to develop a conceptual model in which there was sufficient water available to allow reactions to procede until steady state was achieved. However, the extent to which reactions will progress in the near-field and altered zone systems may be limited by water availability. In such cases, the natural systems will only progress part way along the reaction paths suggested by the modleing described here.

It was also assumed that reaction would take place in a system open to the atmosphere. Hence, the coexisting gas phase had a constant H_2O and CO_2 partial pressure equivalent to that of present day atmosphere (0.2 and 0.003 bars, respectively). Reaction progress was constrained to be sufficiently large to allow steady state to be achieved for the tuffs. In the case of the water-glass simulations, the extent of reaction progress was determined by the amount of glass present and the dissolution rate.

Simulations were conducted for both rock types at 40, 50, 60, 75 and 90°C. This temperature interval was selected because it covers the range between ambient conditions and boiling. Reaction of rock and water at higher temperatures will be conducted at a later time when the EQ3/6 code has been modified to simulate reactions off the liquid-vapor saturation curve of water. Detailed simulations involving flow pathways with restricted flux will also be conducted at a later time. Preliminary results are presented in Section 10.4.4.

Quartz, talc, and tridymite were suppressed from precipitation in all of the runs. This was done because these phases, although less soluble than other silica polymorphs or hydrous Mg-silicates, do not readily precipitate due to kinetic

barriers. It may be, however, that after sufficient time has passed in natural systems, these phases would appear, as the kinetic barriers are overcome. In that case, inclusion of these phases would be appropriate at some point in the reaction progress. When sufficient information is available to reasonably simulate this process, the type of simulations reported here will be redone.

To evaluate the effect of uncertainty in the dissolution rate, two methods were used. One method evaluated the propagation of error in a generalized reaction sequence:

$$A \Leftrightarrow B \Leftrightarrow C$$

This simple system has an exact analytical solution yet is sufficiently general to represent many of the subsets of more complex geochemical systems that are not strongly coupled with other parts of the system. The results of this evaluation will not be treated in detail here, but are described in Whitbeck and Glassley (1995). The second method used is simulation of the reactions of water with the volcanic rocks, using different rate constants. This method allows representation of the specific effects on the simulations described in this study. To illustrate these effects, we consider dissolution of sanidine, which has a measured dissolution rate constant of 5×10^{-15} moles/cm^2-sec (Holdren and Speyer, 1985). The effect of different rates of glass dissolution was examined by using a slow relative rate constant (8.66 E-14) and a very fast relative rate constant (4.0 E-4) in different suites of runs. This wide range of rates was selected because the effective surface area that the fluid will interact with is unknown. Overall reaction rate is a function of surface area, and can vary over many orders of magnitude depending, for example, whether water flows only along a preferred flow pathway in a fracture, or permeates a rock with small glass shards and a large effective surface area. In order to evaluate these effects, the runs with a slow reaction rate constant had a total mass of .1735 grams (.08029 moles) of glass per kg of water and the runs with the fast reaction rate constants had 17.29 grams (8.0 moles) of glass (where the glass molecular weight was arbitrarily chosen to be 2.21454 grams per mole).

10.4.3.3 Results. The water compositions and secondary mineralogies obtained at steady state conditions, at a given temperature, for the tuffs are constrained by the fixed composition of the starting material, and the solubilities of the starting phases. For the vitric material, however, dissolution is treated as though it is congruent, hence, the amount of material dissolved (or, in other words, the extent of reaction progress) will determine the mineralogical products and water chemistry. In this case, therefore, a steady state composition will not be achieved, except under extreme conditions in which very high absolute amounts of glass are dissolved. The simulations conducted here were not taken to steady state for the glasses, because this would require dissolution of unrealistically large volumes of glass. Described below are the mineralogical and chemical results obtained for the different rock types.

As noted by Bruton (1995 and Section 3.4.2, this volume) the accuracy of predictions of mineral occurences at any given time in a numerical simulation is limited by a variety of constraints, including inaccuracies in, or a complete absence of thermodynamic data or kinetic data for specific minerals. Hence, the mineral suites described below must be considered representative "facies" of the assemblage of minerals that may form, and not absolute descriptions of the specific identities of minerals that will be present. In particular, the occurrence of zeolites such as mesolite, clinoptilolite, and stilbite, or the occurrence of muscovite in simulations must be taken to indicate that a zeolite(s) and a sheet silicate are expected to form, but the specific composition of those phases will depend on local effects that cannot be accounted for *a priori*.

10.4.3.3.1 Secondary Mineralogy of the Tuffs (Fig. 10.4-10 (a–e)). Throughout reaction progress saponite (a clay), carbonate, and fluorapatite are present at low abundances at all temperatures. These phases are joined by clays (celadonite and smectite), authigenic feldspar (microcline), and zeolites (clinoptilolite at low temperature, stilbite at 50 and 75°C, with mesolite present throughout the temperature range), relatively early in the reaction progress period, and they persist to steady state conditions. The actual time of appearance of specific phases depends upon temperature. At 40°C, important secondary alumino-silicate phases do not

appear until after approximately 100 days of reaction progress. At temperatures greater than 50°C, important alumino-silicates appear within a few days. However, in all cases, steady state conditions with relatively high abundances of secondary minerals are not approached until thousands of days have elapsed. In all cases, one of the last phases to appear is a silica polymorph (in this case, chalcedony), but it quickly becomes the most abundant secondary phase. At high temperatures (90°C), garnet and tremolite appear in the secondary mineral assemblage. As discussed below, these phases probably would not be the stable phases that would form under these conditions, given evidence from metamorphic petrology in low temperature systems. Their presence in the simulations attests to the limitations of the thermodynamic data currently available, and emphasizes the importance of the facies concept to describe future mineral alteration, as described by Bruton in Section 3.4.2.

10.4.3.3.2 Water Chemistry of the Tuffs (Fig. 10.4-11 (a–g). The initial water composition reflects equilibration of J-13 water at the temperature of the simulation. At all temperatures, this initial composition is moderately alkaline (pH of ca. 8.5), oxidizing (Eh between 580 and 680 millivolts), and has a low ionic strength (ca. 0.0028 molal). Concentrations of the dissolved elements are low. In decreasing order of abundance, they are:

- Na [ca. 40 mg/kg]
- Si [ca. 30 mg/kg]
- Cl [ca. 10 mg/kg]
- S [ca. 6.0 mg/kg]
- Ca [ca. 5 mg/kg]
- F [ca. 2.0 mg/kg]
- Mg [ca. 0.1 mg/kg]
- Li [ca. 0.05 mg/kg]
- Al [<1.0E-4 mg/kg]
- P [2.0E-5 mg/kg]).

Water composition remains relative constant, at a given temperature, until reaction progress reaches approximately 100 days, at which point the composition changes significantly due to formation of secondary mineral phases, and dissolution of significant quantities of the rock components. Calcium and magnesium are both largely removed from solution due to precipitation of carbonates and, to a lesser extent, a variety of silicates.

The elements Na, Si, and Al increase significantly, even though they are incorporated in the secondary minerals, due to the fact that the amount added to solution by dissolution of the solids, is much greater than the amount removed by precipitation. Nevertheless, the final concentration reached for these elements is controlled by the solubilities of the major secondary phases. Silicon, for example, is buffered at chalcedony saturation, at steady state conditions. Other elements are controlled by a combination of secondary phases, since many of these phases are complex, multi-component solid solutions.

The redox state is effectively determined by the assumption that the solution is in equilibrium with atmospheric gases. Hence, total oxygen is assumed to be maintained at approximately 20% of the coexisting gas phase. This assumption ignores the temperature effect on fugacity, since the calculations are actually carried out on the liquid vapor saturation curve for H_2O. This assumption, however, has negligible effect on the results presented here, which are generated for the purpose of providing gross bounds to the water composition.

The variation in pH is strongly controlled by the fact that CO_2 fugacity is fixed in the simulations. This parameter, in turn influences carbonic acid equilibria in such a way that pH remains slightly alkaline throughout reaction progress. However, the final steady state achieved differs by approximately one log unit between the 40°C and 90°C simulations. These results differ somewhat from those described in Section 3.4.1, where water evaporation is modeled. In the latter study, the effect of including rock interaction with the water was not considered. In addition, changes in elemental concentrations, due to loss of H_2O during evaporation, lead to the different results. Nevertheless, the overall character of the systems are similar, in that pH remains relatively alkaline when CO_2 is controlled by atmospheric gases.

The conservative elements Cl, F, Li and P show no significant variation during reaction progress because they are not incorporated into any secondary phases that form in significant quantities, other than apatite which maintains a constant abundance throughout the reaction progress.

10.4.3.3.3 Secondary Mineralogy of the Vitric Material (Fig. 10.4-10(a-e). For dissolution of relatively small volumes of glass, the secondary phases that form during reaction progress are similar to those formed in the tuffs (pyrolusite, clays, and zeolites). The principal differences that occur are in the respective amounts of secondary phases, and the specific zeolites that form. These results are qualitatively consistent with the description of glass alteration (Levy, 1984a,b) in the vicinity of Yucca Mountain. At the end of the reaction progress, very similar end points are achieved. The main exception to this is calcite, which persists to the end point of the calculations for all temperatures except 40°C.

For dissolution of large volumes of glass, the reaction progress is similar to that for small volumes of glass dissolution, for small values of reaction progress, but rather quickly achieves a state in which the only secondary phases that are present are pyrolusite, chalcedony and hematite.

Finally, in none of the simulations with vitric material was muscovite or microcline present as reaction products at any temperature, in contrast to the tuff runs where these two phases are present throughout.

10.4.3.3.4 Water Chemistry of the Vitric Material (Fig. 10.4-12, (a-g). Water composition in simulations involving small degrees of glass dissolution reaches end points that are nearly identical to those for the tuff-water system, and tend to follow very similar trends during reaction progress. The simulations involving large volumes of glass dissolution followed the same trends early in the simulations, but ultimately achieved much higher total concentrations of all elements except Si, which drops to very low values controlled by large volumes of precipitated chalcedony. The latter buffers aqueous SiO_2. In addition, at high degrees of glass dissolution, pH drops, reaching acidic values (ca. 3.8) in the low temperature simulations and slightly alkaline (ca. 7.8) at the 90°C simulation. This pH behavior primarily reflects the effects of temperature, the glass chemistry components, and

the solubility of C-bearing aqueous species (e.g., HCO_3^-) and solids on pH. In these simulations, total dissolved elemental carbon decreased by three orders of magnitude during reaction progress, which will profoundly influence alkalinity, as vitric material dissolves and other elements are added to the solution. The magnitude of this effect is also implied by the fact that the concentration of solutes increases from ca. 0.02% (on a weight basis) at the beginning of the reaction progress, to ca. 0.6% at the end of reaction progress.

The conservative elements Cl, F, Li and P were not included in the simulations of the glasses because no analyses were available for them.

10.4.3.3.5 Propagation of Time Errors. To examine the effects of differences in rates on specific simulations, variation in the sanidine dissolution rate was examined. To determine the propagated uncertainty in the amount of sanidine formed at a given time, we used the results shown in Fig. 10.4-13. Approximate error bars, indicated in Fig. 10.4-14, were generated by differencing the runs shown in Figure 10.4-13. The results (Fig. 10.4-14) demonstrate that the propagated error increases with time, until sanidine vanishes. The 'error', or uncertainty, represents uncertainty regarding the amount of the mineral present at any given time, or uncertainty regarding the time at which a specific abundance of the mineral is achieved. The error in predicting when a phase appears or disappears from the model can be substantially greater than the prediction of the amount made. For example, the maximum uncertainty in the amount of sanidine produced is ca 50%, but the uncertainty of when it is consumed is ca –60% to +2100%.

10.4.3.4 Discussion. The simulations that were conducted were designed to be the preliminary simulations for bounding water compositions that could evolve within the Altered Zone and migrate into the Near-Field Environment, and for bounding the mineralogy that could evolve in the Altered Zone. Emphasis, therefore, is placed on establishing a baseline upon which refinements would be made at a future date. The key constraints upon which the simulations were based were: 1) constant gas fugacity, equivalent to atmospheric values; 2) suppression of precipitation of certain phases; 3) selection of rate constants and surface areas; 4) water volume to surface area ratios for the tuff simulations typical of experiments

conducted in Dickson rocking autoclaves, thus representing scenarios in which very large volumes of water are available, relative to the accessible effective surface area. The simulations involving the vitric material, on the other hand, cover a very wide range of possible accessible surface areas, and thus represent a range of conditions from water flow in fractures, to water wetting non-welded, highly porous vitric materials.

10.4.3.4.1 Baseline Secondary Mineralogy. Under all conditions, clays and zeolites occur within the secondary mineral assemblages. The specific time in the reaction progress when these phases may appear, and the compositions and structures that will occur may vary, depending on the evolving chemical conditions and temperatures. The respective volumes that develop, at steady state conditions, are generally less than other coexisting alumino-silicates. These phases, nevertheless, form an important part of the secondary assemblages, due to their potentially important role as materials in which radionuclides may be sequestered.

Silica polymorphs develop early on in reaction progress. This is an important observation, since silica polymorphs are the most abundant secondary phases to form, in all conditions. This suggests that silica may play an important role in coupling hydrology and geochemistry/mineralogy via precipitation/dissolution-induced changes in porosity and permeability, and transport (see Section 10.4.4).

In all of the simulations, carbonates play an important role in the secondary mineral assemblage, but they are not always present when steady state is reached. Because carbonates may be important in both influencing water composition and sequestering ^{14}C through isotope exchange, the ubiquitous presence of this phase in various stages during reaction progress may be significant.

10.4.3.4.2 Baseline Water Composition. The composition of water that may enter the NFE is restricted to a relatively narrow range, except for the condition in which large volumes of glass are dissolved. For those conditions not involving large volumes of glass, the bounds suggest that the solution will be approximately neutral to slightly basic, relatively oxidizing, saturated in a silica polymorph, and with low to moderate concentrations of dissolved species. Total ionic strength

remains below 0.1 molal. For the case where large volumes of glass are dissolved, pH may become strongly acidic, and total dissolved species can be quite high.

Despite these characteristics, solution composition changes significantly during the course of reaction progress. For the non-conservative elements, changes in concentration of many times are evident, and correlated with the dissolution or precipitation of a specific phase or phases.

10.4.3.4.3 Uncertainty. The uncertainty in final amounts of a mineral is shown to be problem specific and potentially significant with respect to long-term predictions of geochemical properties in slowly reacting systems, such as systems involving mineral dissolution or precipitation. The results in which sanidine was considered demonstrate that there is an increase in the uncertainty of the amount of mineral that may be present, or when that mineral may appear or disappear from an assemblage, for a relatively small initial uncertainty in the rate parameter. The results show that, in this case, an order of magnitude uncertainty in the rate results in the disappearance of sanidine sometime between a few hundred days to nearly a hundred years.

10.4.3.5 Conclusions. The results presented here provide initial bounds on secondary mineralogy and water chemistry, for a very specific set of conditions and simulation constraints. These constraints, along with similar efforts to bound pore water chemistry during evaporation (Glassley, 1995, and Section 3.4.1), provide baseline information from which to further refine simulation strategies and thus refine bounds on water chemistry and secondary mineralogy.

These results also document the very great uncertainties that exist in establishing the nature of secondary minerals that may form, the resulting water chemistry, and the absolute times at which specific changes might be expected to develop during reaction progress. This is consistent with the results described in Section 3.4.2 (Bruton, 1995) in which it was demonstrated that mineral facies may be identified, as a function of time, but that specific and detailed projections of mineral assemblages cannot be provided, due to uncertainty in thermodynamic and kinetic data. Much work is still needed before quantitative bounds can be confidently placed on the

evolution of water chemistry entering the NFE, and the resulting secondary mineral assemblages that may influence radionuclide migration.

These results clearly document that both the times at which mineral phases may be present or absent during reaction progress, and their respective amounts, may be uncertain by orders of magnitude. Because these parameters are also important for describing water chemistry as a function of time, it is clear that only very gross bounds can be placed on either the mineralogical or water chemistry evolution, unless more measurements of dissolution and precipitation rates are obtained.

This point is also important for radionuclide retardation in the EBS or Altered Zone. The magnitude of retardation depends upon the mineral phases that are present, and their respective amounts. However, these results demonstrate that there is substantial uncertainty about when any specific phase may form or be consumed in reactions. This uncertainty will remain until further work is completed to establish more precise values for dissolution and precipitation kinetics rate constants.

It should also be borne in mind that these water chemistries are not the chemistries that a waste package is likely to see. Materials introduced into the repository during construction and waste emplacement will probably be the primary controls on water chemistry in the NFE.

10.4.3.6 References

L. Brisqueu & H de la Boisse (1990), "U-Pb geochronology; Systematic development of mixing equations and application of Monte Carlo numerical simulation to the error propagation in the Concordia diagram," *Chemical Geology*, 88, 69–83.

Broxton, D. E., W. G. Warren, R. C. Hagen, and G. Luedemann (1989), *Chemistry of Diagenetically Altered Tuffs At A Potential Nuclear Waste Repository at Yucca mountain, Nevada.* Los Alamos National Laboratory, Los Alamos, New Mexico, LANL-10802-MS.

Buscheck, T. A., and J. J. Nitao (1992), *The Impact of Thermal Loading on Repository Performance at Yucca Mountain,* in Third International Conference on High Level Radioactive Waste Management, Las Vegas, American Nuclear Society, LaGrange Park, Ill., pp. 1003–1017.

Buscheck, T. A., and J. J. Nitao (1993), *The Impact of Repository-Heat-Driven Hydrothermal Flow on Hydrological Performance at Yucca Mountain,* Lawrence Livermore National Laboratory, Livermore, Calif., UCRL-JC-112444.

Delany, J. M. (1985), *Reaction of Topopah Spring Tuff with J-13 Water: A Geochemical Modeling Approach Using the EQ3/6 Reaction Path modeling Code*, Lawrence Livermore National Laboratory, Livermore, Calif., UCRL-53631, 48p.

Glassley, W. E. (1995), Report on Near-Field Geochemistry: Water Composition Changes Due to Evaporation. Yucca Mountain Milestone M0L 206.

Harrar, J. E, J. F. Carley, W. F. Isherwood, and E. Raber (1990), *Report of the Committee to Review the Use of J-13 Well Water in the Nevada Nuclear Waste Storage Investigation*, Lawrence Livermore National Laboratory, Livermore, Calif., UCID-21867.

Holdren, G. R. Jr., and P. M. Speyer (1985), "Reaction rate-surface area relationships during the early stages of weathering: II. Data on eight additional feldspars," *Geochim. Cosmochim. Acta* 51, 2311–2318.

Levy, S. S. (1984a), "Studies of altered vitrophyre for the prediction of nuclear-waste-repository induced thermal alteration at Yucca Mountain, Nevada," in *Scientific Basis for Nuclear Waste Management VII*, G. L. McVay, ed., Materials Research Society, pp. 959–966.

Levy S. S. (1984b), *Petrology of samples from drill holes USW H-3, H-4, and H-5, Yucca Mountain, Nevada*. Los Alamos National laboratory Report LA-9706-MS, 77 pp.

Nitao, J. (1988), *Numerical Modeling of the Thermal and Hydrological Environment Around a Nuclear Waste Package Using the Equivalent Continuum Approximation: Horizontal Emplacement*, Lawrence Livermore National Laboratory, Livermore, CA, UCID-21444.

Thompson, A.M., and R.W. Stewart, (1991), "Effect of Chemical Kinetics Uncertainties on Calculated Constituents in a Tropospheric Photochemical Model," *J. Geophysical Research* 96, 13089–13108.

Whitbeck, M., and W. E., Glassley (1995), *Preliminary Bounds on the Water Composition and Secondary Mineral Development That May Influence The Near-Field Environment*. Lawrence Livermore National Laboratory, Yucca Mountain Site Characterization project milestone MOL205.

Wolery, T. (1992a), *EQ3/6, A Software Package for Geochemical Modeling of Aqueous Systems: Package Overview and Installation Guide (Version 7.0)*, Lawrence Livermore National Laboratory, Livermore, CA, UCRL-MA-110662 PT I.

Wolery, T. (1992b), *EQ3NR, A Computer Program for Geochemical Aqueous Speciation-Solubility Calculations: Theoretical Manual, User's Guide and Related Documentation (Version 7.0)*, Lawrence Livermore National Laboratory, Livermore, CA, UCRL-MA-110662 PT. III.

Wolery, T., and S. A. Daveler (1992), *EQ6, A Computer Program for Reaction Pat h Modeling of Aqueous Geochemical Systems: Theoretical Manual, User's Guide and Related Documentation (Version 7.0)*, Lawrence Livermore National Laboratory, Livermore, CA, UCRL-MA-110662 PT. IV.

Wolery, T., K. J. Jackson, W. L. Bourcier, C. J. Bruton, B. E. Viani, K. G. Knauss, and J. M. Delany (1990), "Current Status of the EQ3/6 Software Package for Geochemical Modeling," in *Chemical Modeling in Aqueous Systems II.*

10.4.4 Formation of Flow and Transport Barriers Within The Altered Zone (*James W. Johnson and William E. Glassley*)

10.4.4.1 Introduction. Radioactive decay within the waste package will establish and maintain lateral thermal gradients and resultant advective mass transport within the altered zone. This hydrothermal activity will invariably lead to porosity evolution as a consequence of reaction-controlled mineral dissolution and precipitation both along fractures and within bounding matrix blocks. Preliminary reactive transport modeling conducted in FY 1995 suggested that these processes might result in significant modification of flow porosity both above and below the repository (Glassley, 1995). However, owing to limitations of the software available at that time, these preliminary studies considered only the equilibrium dissolution/precipitation of silica polymorphs and advective transport of silica as SiO_2(aq); as a result, they provided only a first-order approximation of the effect. Subsequently, new reactive transport simulators have been developed that facilitate analogous modeling of systems that involve complex fluid-rock compositions and explicitly account for temperature-dependent reaction kinetics as well as advective, diffusive, and dispersive transport. A hands-on review of several such simulators (Glassley et al., 1995) concluded that the modeling capabilities of GIMRT (Steefel and Yabusaki, 1995; Steefel and Lasaga, 1994) most closely matched those required for detailed simulation of porosity evolution in the post-emplacement altered zone. Specifically, GIMRT permits direct monitoring of kinetically controlled, reaction-dependent porosity evolution in compositionally complex porous media where the full range of transport phenomena are considered. Hence, GIMRT was selected for use in the series of one-dimensional simulations described in this section, which provide a significantly more rigorous predictive representation of porosity evolution in the altered zone than was previously possible.

Reactive transport simulations can be viewed as an iterative five-stage process: (1) precise specification of the initial chemical and hydrologic state of the fluid-rock system, (2) translation (which often includes approximation) of these specifications into the analogous model parameters of the software, (3) specification of certain

system-independent numerical parameters, (4) successful execution of the software, and (5) interpretation of calculated results. The process is iterative in that several cycles through (1-3) are often required for initial achievement of (4); subsequently, additional cycles through (1-3) can be used to further refine the simulation to provide the closest possible representation of the natural system. Using this five-stage process, the approach taken in this study was to first establish validity of the software-encoded numerical model by successfully predicting the outcome of two well-characterized, experimentally verifiable "benchmark" problems. Next, increasingly complex, yet still experimentally verifiable problems having some relevance to porosity evolution in the backfill zone were addressed. Finally, a critical simulation that cannot be addressed directly by physical experiment was carried out: modeling of long-term porosity evolution in the altered-zone.

10.4.4.2 Benchmark Simulations. Accurate simulation of a well-constrained physical experiment is the critical first step in any numerical modeling study; this is particularly true in the case of reactive transport modeling, where the use of approximate numerical methods to mathematically represent coupled processes and the uncertainties in many different data (thermodynamic, kinetic, diffusion-coefficient, dispersivity, etc.) make it exceedingly difficult to assess the accuracy of simulations that involve even relatively simple chemistry and hydrology. Hence, in order to ensure the possibility that meaningful conclusions can be drawn from complex simulations, one must first provide clear evidence that the model accurately predicts the outcome of simple reactive transport problems. Toward this end, two plug-flow reactor (PFR) experiments were designed, carried out[i], and simulated using GIMRT.

In the first experiment, Suprasil material[ii] was pulverized to 125-75 μm size fraction, placed within a Ti-cylinder of 3.1-cm length and 0.66-cm effective diameter, and infiltrated by distilled water at an outflow rate of 26 ml/day for two weeks at 238°C and 84.1 bar. As silica-charged fluid exited the PFR during progressive

[i] These PFR experiments were carried out by Kevin Knauss in support of WBS 1.2.3.10.2.
[ii] Supracil material is essentially silica glass, which from a structural and thermodynamic standpoint can be approximated as amorphous silica.

dissolution of the Suprasil plug, aqueous silica concentrations were systematically monitored; these attained approximately steady-state values of 300-320 ppm Si (log $a[SiO_2(aq)]$ = -1.97 to -1.94), well below the limit of amorphous silica saturation (log $a[SiO_2(aq)]$ = -1.709) in 3-4 days. In this experiment involving the simple system SiO_2-H_2O, the temperature, pressure[8], fluid flux (277.4 $m^3/m^2/yr$), initial porosity (40%), size fraction, thermodynamic and kinetic data (Johnson et al., 1992; Rimstidt and Barnes, 1980), and outlet aqueous silica concentrations are all tightly constrained. As a result, GIMRT can be used iteratively to independently calculate specific surface area of the crushed amorphous silica, which was measured prior to the experiment. Optimal fits to the experimental data were obtained for a predicted value of 1050 cm^2/g (Fig. 10.4-15), which is in close agreement with BET measurements for this mineral of ca. 900 cm^2/gm.

The second experiment was conducted under the same conditions as the first except that crushed quartz was used in place of the Suprasil material. This quartz substitution removes the potential ambiguity associated with thermodynamic approximation of the Suprasil material as amorphous silica in the first experiment. Again, GIMRT was used iteratively to determine specific surface of the pulverized quartz. The experimental data were most closely fit by a predicted value (920 cm^2/g; Fig. 10.4-16) that falls within the range determined by BET measurement (460-940 cm^2/gm, Knauss and Wolery, 1988).

Close agreement between GIMRT-predicted and BET-measured specific surface areas for amorphous silica and quartz has significance beyond accuracy validation of the various PFR measurements (fluid flux, aqueous silica concentrations, etc.) and thermodynamic and kinetic data (standard molal properties, equation-of-state parameters, dissolution rate constants, activation energies, etc.). Specifically, it also demonstrates the reasonableness of values employed in the GIMRT simulations for several geochemical and hydrologic parameters (bulk diffusion coefficient, longitudinal and transverse dispersivity, etc.) and numerical variables

[8] Although the PFR experiment was carried out at 238°C and 84.1 bar, the thermodynamic data base used in the GIMRT-simulation analog is constructed for Psat(T), which at 238°C is 32.3 bar. However, this pressure discrepancy is insignificant (e.g., amorphous silica saturation at 238°C, 84.1 bar and 238°C, 32.3 bar corresponds to log $a[SiO_2(aq)]$ values of -1.709 and -1.720, respectively).

(initial/maximum timestep, cementation exponent, etc.) which in many cases are imprecisely known. Sensitivity of the reactive transport calculations to variations in these variables was examined as an aid to obtaining optimal values.

Having demonstrated GIMRT's ability to accurately simulate amorphous-silica and quartz dissolution in the PFR experiments, the same experimental-verification approach can be extended to address problems that involve the more complex fluid-rock compositions characteristic of the pre-emplacement altered zone.

10.4.4.3 Compositional Specifications and Parameterization of the Altered Zone. The composition and relative abundance of mineral phases in the potential repository host rock, the Topopah Spring Member of the Paintbrush Tuff (TSw2), have been determined experimentally by Warren et al. (1984), and translated into model compositions/abundances by Delany (1985) for use in EQ3/6 calculations. Because GIMRT, unlike EQ3/6, is not yet configured to account for solid solutions, for the present work it is necessary to further approximate Delany's (1985) model TSw2 mineralogy by resolving its alkali feldspar and plagioclase compositions into the corresponding end-member K-feldspar, albite, and anorthite components. Although the Mg-beidellite and biotite compositions could be similarly resolved, these phases together compose only 1.1 vol.% of the TSw2 (Delany, 1985); in addition, they represent the only Mg- and Fe-bearing phases in the system, and inclusion of these elements in the simulation would necessitate tremendous expansion of the set of mineral and aqueous species considered. Hence, in these preliminary simulations, Mg-beidellite and biotite have been eliminated from the model TSw2 composition. Although these phases will be incorporated into future simulations, such inclusion is anticipated to represent a second-order effect. The model TSw2 mineralogy given by Delany (1985) and its approximated form used in this study are summarized in Table 10.4-5.

The fluid phase anticipated to form within, and react with, the TSw2 in the altered zone is derived from condensation of a vapor phase moving radially outward from the repository (Buscheck et al., 1993). This condensate is likely to be a highly dilute, neutral-pH fluid. In the simulations, this fluid is modeled to initially contain very low concentrations of aqueous ions and complexes within the

chemical system defined by TSw2 mineralogy (Na_2O-K_2O-CaO-SiO_2-Al_2O_3-H_2O) augmented by the additional component CO_2, which is necessary owing to the presence of atmospheric gases (Bruton et al., 1993). The initial fluid composition, specified as the log molal concentration of basis species, is given in Table 10.4-6. Note that this solution is much more dilute than J-13 and other relevant fluid compositions in the vicinity of Yucca Mountain, reflecting its condensation from a vapor phase.

Following specification of the model TSw2 and vapor condensate compositions, it is necessary to select a thermodynamic data base that includes all of the relevant species as well as kinetic and surface-area data for the minerals. For this work, we have employed the thermodynamic data base typically used with both the original and our modified version of GIMRT, mastertemp.data, which is a reformatted version of the "composite" data base distributed with the EQ3/6 software package (Wolery, 1992). Although this data base contains reference-state and elevated P-T data taken from numerous sources and extrapolated using a variety of equations, the particular subset relevant to the present altered-zone modeling is for the most part taken from the SUPCRT92 database and software package (Johnson et al., 1992). Reference-state dissolution-rate constants, activation energies, and specific surface areas needed for the primary and potential alteration minerals were taken from a variety of experimental and theoretical studies (Renders et al., 1995; Oelkers and Schott, 1995; Gautier et al., 1994; Rose, 1991; Knauss and Wolery, 1989, 1988, 1986; Helgeson et al., 1984; Rimstidt and Barnes, 1980).

Using the model TSw2 fluid-rock compositions and specified thermodynamic/kinetic database, there are two distinct altered-zone environments whose porosity evolution can be addressed with GIMRT. The first of these is the localized, interior backfill environment, for which crushed, unaltered TSw2 has been discussed as a possible backfill material; the second is the much larger-scale, relatively outlying condensation zone (Buscheck et al., 1993), where gravity-driven flow of vapor-exsolved fluid represents the most likely catalyst for significant, long-term porosity evolution in the altered zone.

10.4.4.4 Backfill Simulations. Because the backfill environment bridges the EBS/WP and pristine TSw2, post-emplacement porosity evolution within this spatially restricted zone is a potentially critical variable affecting overall repository performance. Reactive transport simulations of this evolution are analogous to those described above for the silica dissolution experiments in that experimental PFR analogs can be constructed, carried out, and used to refine and verify the calculations. Two such simulations were completed; in both cases, an inlet fluid was streamed through a 31-cm length of crushed Tpt material having an initial porosity of 40%, where constant outlet flux of 266.7 $m^3/m^2/yr$ is maintained over six months. This flow length, porosity, outlet flux, and duration were selected for consistency with the existing PFR geometry, measured value for crushed Tsw2 material (125-75 μm size fraction), attainable experimental outflow rate (25 ml/day for a plug having an effective diameter of 0.66 cm), and the anticipated maximum duration of the experiment, respectively. Because the porosity of actual backfill material and especially the *in situ* fluid flux are likely to be lower than these adopted values, the simulations provide an upper bound to the potential magnitude of porosity evolution. In both simulations, boundary conditions are set such that the entire one-dimensional reaction domain is initialized (but not fixed) to contain the model TSw2 fluid-rock system summarized in Tables 10.4-5 and 10.4-6, while only the inlet fluid composition is initialized *and fixed* per Table 10.4-6.

In the first TSw2-backfill simulation, the fluid-rock system is maintained in isothermal equilibrium at 90°C, a conservative yet representative value for this environment. As the inlet fluid flows through and reacts with the crushed TSw2, spatial and temporal variations in porosity, mineral volume fractions and saturation indices, and fluid composition are continuously monitored. At the inlet node (1 cm into the 31-cm reaction domain), steady-state saturation indices for all primary and potential secondary minerals are achieved within one hour (Fig. 10.4-17). As can be seen in Fig. 10.4-17, the fluid remains undersaturated with respect to all primary and potential secondary minerals at this inlet node (all log

(Q/K) < 0) throughout the simulation; hence, at this location all primary phases will dissolve to varying degrees controlled by the encoded kinetic rate law, and no secondary minerals will precipitate. At the outlet node, mineral saturation indices reach steady-state values in about 9 hours; here again the fluid remains undersaturated with respect to all primary minerals, but in contrast to the initial node, several secondary phases (kaolinite, gibbsite, diaspore, boehmite, and muscovite) do achieve steady-state supersaturation with the fluid (Fig. 10.4-18). Because steady-state saturation indices are attained throughout the reaction domain within just a few hours of this six-month run, time-integrated saturation-indices across this domain together with calculated reaction rates can be used to assess the spatial zoning of secondary phases and the magnitude of mineral dissolution/precipitation and porosity evolution (Fig. 10.4-19).

At 90°C, kinetic dissolution rates for the undersaturated primary phases are on the order of -10^{-1} vol.%/yr for cristobalite and albite, -10^{-2} vol.%/yr for quartz, and $<-10^{-3}$ vol.%/yr for K-feldspar and anorthite. As a result, over six months the aggregate dissolution of primary minerals will be <0.25 vol.%. Some of this minute volume loss will be filled by precipitation of secondary phases following their sequential supersaturation along the flowpath. Specifically, gibbsite will precipitate first (at node 2; nodes were located at each cm along the flowpath), subsequently joined by diaspore (node 4), kaolinite (node 9), boehmite (node 14), and finally muscovite (node 29). However, because maximum precipitation rates for these phases are so slow at 90°C (ranging from 10^{-11} vol.%/yr for kaolinite to 10^{-14} vol.%/yr for muscovite and boehmite), the aggregate precipitation of secondary minerals is < $2.5(10^{-3})$ vol.%/yr throughout the domain, i.e., negligible. As a consequence, six months of reactive flow through crushed Tpt at 90°C results in a relatively uniform but minute increase in porosity (from 40 to approx. 40.25%) as a function of minor dissolution of primary phases and trace precipitation of alteration minerals (Figs. 10.4-[20-21]).

Hence, at 90°C, despite likely overestimation of initial porosity and fluid flux in the simulation, post-emplacement porosity evolution of TSw2 backfill will be insignificant. Because the predicted porosity variations and alteration-phase

concentrations are well below what one could reasonably expect to discern from post-mortem analysis of the analogous PRF experiment, such an experiment was not conducted. Rather, a second GIMRT simulation was performed, identical to the first except for the temperature, which was increased to 250°C. Although this temperature exceeds the maximum likely to be attained in the backfill zone, thermodynamic and kinetic considerations suggest that it will lead to readily observable porosity evolution and alteration-phase precipitation; hence, the corresponding PFR experiment can be run and analyzed to provide validation for both this and, by implication, the experimentally unverifiable 90°C run.

Although the time-scale for attainment of steady-state saturation indices is similar for the 90° and 250°C simulations (*cf.* Figs. 10.4-17 and 10.4-22, 10.4-18 and 10.4-24), the enhanced solubilities and faster reaction rates of primary Tsw2 minerals at the higher temperature and their effect on dissolution (and secondary phase precipitation) are readily apparent. At the 250°C inlet node (Fig. 10.4-22), all primary minerals are far less undersaturated than at 90°C, and six secondary phases are supersaturated—versus none at 90°C. Because initial dissolution rates for albite (-130 vol.%/yr), cristobalite (-118 vol.%/yr), and quartz (-23 vol.%/yr) are orders of magnitude higher here than at 90°C, the continuous stream of dilute fluid through this node dissolves these phases rapidly: albite has disappeared after 90 days, and after 150 days, cristobalite and quartz have been reduced to less than 1.0 and 2.5 vol.%, respectively. Despite concomitant precipitation of kaolinite, whose reaction rate and volume fraction ultimately attain 50 vol.%/yr and 14 vol.%, respectively, this near-complete consumption of cristobalite, albite, and quartz causes porosity to increase from 40 to 70% at the initial node (Fig. 10.4-23), and, of course, results in the late marked decline in saturation indices for these and all other silica-bearing phases (Fig. 10.4-22).

At the outlet node, the fluid is supersaturated with not only the same six secondary minerals that characterize the inlet node, but also with albite and quartz (Fig 10.4-24) as a consequence of the continuous introduction of relatively concentrated solutions generated by the large-scale dissolution upstream. Hence, although the *initial* dissolution rates for primary phases are identical to their large

inlet-node values, here they diminish quickly owing to rapid increase in log Q; in fact, primary albite ceases to dissolve and secondary albite begins to precipitate within 20 minutes, quartz follows suit about 40 minutes later, and within nine hours the cristobalite dissolution rate has dropped to and essentially leveled off at about 20% of its original magnitude. As a result, after six months, total quartz and albite volume fractions have actually increased (Fig. 10.4-25), and the net volume fraction of cristobalite, albite, and quartz has only declined from 45.9% to 37.2% (versus the inlet node where the six-month aggregate value is only 1.4%). Hence, despite slightly reduced precipitation of secondary kaolinite relative to the inlet (10.2% versus 15.2%), the six-month outlet porosity has actually decreased from 40 to 38.8% (Fig. 10.4-25).

In the 250°C simulation, the inlet node can essentially be viewed as a pure "dissolution" node, since infiltrating fluid is never concentrated by upstream reactions, while the outlet node continuously encounters the most concentrated fluid from such reactions. Within the intervening domain, one would expect the gradient in dissolution/precipitation behavior to be sharpest across the first few nodes, where the fluid concentration gradient is steep, and relatively flat across the last few, where this fluid gradient is relatively flat. This is exactly the case, as illustrated by the time-integrated spatial distribution of saturation indices and porosity/volume fractions (Figs. 10.4-[26-27]). Here, the functional form of spatial variation in log (Q/K), which for this isothermal-isobaric simulation is just the spatial variation in log Q, closely mirrors that of the corresponding mineral volume fractions. Differences in the relative position of minerals in the log (Q/K) and volume fraction plots are accounted for almost entirely by differences in their reference-state (25°C) reaction rate constants and activation energies. Note that the region of enhanced porosity is restricted to the first few nodes and characterized by very steep gradients, while that of reduced porosity accounts for roughly 90% of the reaction domain and is characterized by much subtler variations.

The spatial variations in porosity and in the volume fractions of primary and secondary minerals illustrated in Fig. 10.4-27 are sufficient to be detected by post-mortem analysis of the proposed PFR analog. As a result, this experiment was set-

up and initiated. Unfortunately, owing to a malfunction in one of the pressure regulators, the run was unavoidably terminated after five weeks, well short of the planned six-month duration. As can be seen in, and implied from, Figs. 10.4-23 and 10.4-25, at five weeks the predicted spatial variations in porosity and mineral volume fractions are far smaller than would have been realized in six months, and therefore much more difficult to discern and accurately characterize in the PFR post-mortem analysis. Nevertheless, such an analysis is currently under way, with results expected by early FY 1997. The availability of these PFR results are anxiously anticipated, as they will be of critical importance in refining and validating the predictions described above.

However, even prior to such experimental validation these two short-term TSw2-backfill simulations provide insight into the time-scale of potential porosity evolution in this highly localized environment. Comparison of the 90° and 250°C dissolution rates for silica polymorphs and feldspars and examination of the dependent six-month spatial variations in porosity and mineral volume fractions at these two temperatures leaves little doubt that significant porosity evolution in the 90°C backfill zone will not be realized for at least 100 yr. Moreover, recalling the likely overestimation of initial porosity and almost certain overestimation of fluid flux, this time frame must be considered extremely conservative. Because accurate values for the initial porosities and flow rates relevant to the potential crushed-TSw2 backfill environment are currently unavailable, a more detailed, longer time-scale simulation addressing porosity evolution here cannot be pursued at this time. Instead, we now address such long-term porosity variation in a critical environment where initial porosity and likely fluid fluxes *are* relatively well constrained: the pre-emplacement altered zone.

10.4.4.5 Altered-Zone Simulations. The potential repository horizon lies well above the present-day water table within the welded, devitrified section, which is characterized by low porosity (11%) and extremely low, fracture-controlled permeability (10^{-18} m^2) (Klavetter and Peters, 1988). As described by Buscheck et al. (1993), hydrology of the post-emplacement NFE may be characterized by a boiling zone, where vapor moves radially outward from the EBS/WP and an outer but

partially overlapping condensation zone, where temperature-dependent condensation of the vapor leads to primarily gravity-driven flow of a fluid phase. In the vicinity of emplacement drifts, average calculated trajectories (Buscheck, pers. comm.) indicate that the condensate may flow along pathlines characterized by an initial isothermal segment (at 90-100°C) of several meters and subsequent cooling segment (-1° to-3°C/m), also of several meters. Although these average flow trajectories and thermal gradients represent a relatively wide range of potential trajectories and gradients, they do provide a representative model framework for the reactive transport simulation of potential long-term porosity evolution in the altered zone.

In the model system, a fixed-composition inlet fluid (Table 10.4-6) flows through and reacts with a 10-m length of 11%-porosity TSw2 material (Table 10.4-5); over the first 5 m, the temperature is maintained at 95°C, while a gradient of -1°C/m is imposed on the last 5 m. Fluid flux is maintained at 2.67 $m^3/m^2/yr$, which is appropriate for this setting, but reduced two orders of magnitude relative to the earlier models. This "double" thermal gradient flow regime is maintained for 10,000 yr, which facilitates an analysis of long-term porosity evolution.

The temporal evolution of mineral saturation indices at the inlet (0.25 m), center (5 m), and outlet (10 m) nodes are illustrated in Figs. 10.4-[28-30]. As can be seen in these plots, initial steady-state mineral saturation indices are attained after about 1 month, during which time the fluid obtains supersaturation with quartz and the secondary phases kaolinite and pyrophyllite, but remains undersaturated with respect to cristobalite (and the primary feldspars) throughout the reaction domain. As a result, over the entire reactive flowpath, cristobalite (and the feldspars) will dissolve, while quartz, kaolinite, and pyrophyllite will precipitate. Given the relatively sluggish dissolution rates of the feldspars at 90-95°C, dissolution of these primary aluminous phases and dependent precipitation of kaolinite and pyrophyllite will be very minor; hence, the fundamental mechanism of porosity evolution in this environment is expected to be metasomatic replacement of cristobalite by quartz.

That this hypothesis is valid can be seen in Figs. 10.4-[32-33], where the temporal evolution of porosity and mineral volume fractions at the central and outlet nodes is effectively controlled by cristobalite (and relatively minor, late-stage [> 1,000 yr] albite) dissolution and quartz precipitation. At the inlet (pure dissolution) node (Fig. 10.4-31), behavior analogous to the center and outlet of the domain is observed until cristobalite has been completely dissolved at about 650 yr; subsequently, the dilute inlet fluid begins to dissolve quartz, which disappears completely after 3,100 yr, and then albite.

The time-integrated spatial variations in porosity and mineral volume fractions are illustrated in Figs. 10.4-[34-37]. Because the reference-state standard molal volume of cristobalite exceeds that of quartz by approximately 13.5%, the complete replacement of cristobalite (initial volume fraction: 39.6%) by quartz throughout the reaction domain leads directly to a background increase in porosity from 11% to about 16% after roughly 3,100 yr (Figs. 10.4-[36-37]). Superimposed on this is a secondary porosity enhancement, resulting from quartz dissolution (initiated following complete cristobalite consumption) at the first few inlet nodes, beginning with the inlet node at 650 yr. Because the 90-95°C dissolution rate of quartz is only about 40% that of cristobalite, it takes dilute inlet fluid roughly 2,500 years to completely dissolve the inlet-node quartz from its maximum concentration (29 vol.%), which coincided with cristobalite disappearance at 650 yr. Hence, this secondary quartz dissolution front advances quite slowly, and the advection of quartz-derived SiO_2(aq) maintains nearly uniform levels of slight quartz supersaturation and resultant minor quartz precipitation over the entire downstream reaction domain. As a result, this secondary porosity enhancement is characterized by steep gradients that advance downstream quite slowly (*cf.* Figs. 10.4-[36-37]).

Important implications for the post-emplacement evolution of porosity in the altered zone can be drawn from this simulation. First, thermodynamic, kinetic, and volumetric constraints strongly suggest that long-term (> 3,000 yr), gravity-driven flow of vapor-derived dilute condensate at 90-95°C will result in nearly 50% background porosity enhancement (from 11% to 16%) as a consequence of

mole-for-mole, quartz-for-cristobalite replacement. Should this local "condensation" zone (Buscheck et al., 1993) persist for longer time periods, the *in situ* porosity may further increase dramatically, albeit slowly, to more than 65% as quartz dissolution occurs. Hence, it is conceivable, if not in fact likely, that the post-emplacement altered zone will evolve toward extreme porosity heterogeneity, characterized by relatively large porosities in the condensation-zone "cap" above the repository and relatively low porosities (which nevertheless exceed pre-emplacement porosity) in the outlying margins of this cap; in addition, these extremes may be joined by a narrow, steep-gradient interface. All of this dissolved silica will, of course, eventually precipitate farther downstream, presuming this gravity-driven flow continues down thermal gradients. Hence, it is anticipated that a zone of very low (less than ambient) porosity may develop at depth, perhaps below and radially outward from the repository.

10.4.4.6 Concluding Remarks. In this study, the reactive transport simulator GIMRT (Steefel and Yabusaki, 1995) has been used to accurately predict experimentally verifiable specific surface areas of amorphous silica and quartz, to predict potentially verifiable porosity and mineralogic evolution during reaction between idealized TSw2 and infiltrating fluid compositions, and to model unverifiable, long-term porosity evolution in the post-emplacement altered zone. The successful simulation of dissolution experiments involving silica polymorphs provided valuable benchmarking for the code; and the short-term, high-porosity simulations involving fluid-TSw2 interaction facilitated its necessary extension to potentially verifiable systems of considerably greater compositional complexity. But most clearly, the use of GIMRT to simulate long-term porosity and mineralogic variation in the post-emplacement altered zone demonstrates its value as a powerful investigative tool. Recognizing the abundance of compositional and hydrologic approximations, assumptions, and simplifications that are necessarily embodied in these still preliminary models, they nevertheless serve to elucidate the fundamental time scales (thousands of years) and geochemical processes (e.g., cristobalite for quartz replacement) likely to govern active evolution of the altered zone, and can be used to imply the distant-future porosity distributions that are so

critically important. As described above, our initial modeling efforts suggest that post-emplacement reactive transport will lead to porosity enhancement in the altered zone, most dramatically in the condensation "cap" overlying the repository. Further modeling of fluid transport to regions below the emplacement drifts will evaluate the extent to which flow barriers may form due to porosity reduction.

The simulation results presented herein are extremely preliminary in nature, and the quantitative accuracy of our models will steadily improve as a function of advances in reactive transport theory, numerical methods, computer science, reaction kinetics, and thermodynamic/kinetic data on the modeling side, and in our understanding of the pre-emplacement TSw2 chemistry, hydrology, and heterogeneity on the field-data side. Nevertheless, our results to date strongly suggest that significant porosity changes will occur in the post-emplacement, repository-block environment. Long-term performance assessment of this environment must explicitly account for such porosity evolution and its effect on dependent geochemical and hydrologic processes.

10.4.4.7 References

Bruton, C.J., W.E. Glassley, and B.E. Viani, (1993), Geochemistry, in *Preliminary Near-Field Environment report Volume II. Scientific overview of near-field environment and phenomena*: Lawrence Livermore National Laboratory, Livermore, CA, UCRL-LR-107476 Vol 2, p. 37-60.

Buscheck, T.A., J.J. Nitao, and D.A. Chesnut, (1993), Hydrologic modeling, in *Preliminary Near-Field Environment report Volume II. Scientific overview of near-field environment and phenomena*: Lawrence Livermore National Laboratory, Livermore, CA, UCRL-LR-107476 Vol 2, p. 5-27.

Delany, J.M., 1985, *Reaction of Topopah Spring Tuff with J-13 water: A geochemical modeling approach using the EQ3/6 reaction path code*: Lawrence Livermore National Laboratory, UCRL-53631, 46 p.

Gautier, J.-M., E.H. Oelkers, and J. Schott, (1994), Experimental study of K-feldspar dissolution rates as a function of chemical affinity at 150°C and pH 9: Geochim. Cosmochim. Acta, v. 58, n. 21, p. 4549-4560.

Glassley, W.E., 1995, *Preliminary, scoping estimates of rates and magnitudes of changes of coupled hydrological-geochemical properties*: LLNL-YMP MOL79, 18 p.

Glassley, W.E., W.L. Bourcier, and J.W. Johnson, (1995), Review of existing reactive transport software: LLNL-YMP MOL25, 24 p.

Helgeson, H.C., W.M. Murphy, and P. Aagaard, (1984), "Thermodynamic and kinetic constraints on reaction rates among minerals and aqueous solutions: II. Rate

constants, effective surface area, and the hydrolysis of feldspar:" *Geochim. Cosmochim. Acta*, V. 48, p. 2405-2432.

Johnson, J.W., E.H. Oelkers, and H.C. Helgeson, (1992), "SUPCRT92: A software package for calculating the standard molal thermodynamic properties of minerals, gases, and aqueous species from 0° to 1000°C and 1 to 5000 bar:" *Comp. Geosci.*, V. 18, (7) p. 799-847.

Klavetter, E.A., and R.R. Peters., (1988), "A continuum model for water movement in an unsaturated fracture rock mass:" *Water Resour. Res.*, V. 24, p. 416-430.

Knauss, K.G., and T.J. Wolery, (1989), "Muscovite dissolution kinetics as a function of pH and time at 70°C:" *Geochim. Cosmochim. Acta*, V. 53, p. 1493-1501.

Knauss, K.G., and T.J. Wolery, (1988), "The dissolution kinetics of quartz as a function of pH and time at 70°C:" *Geochim. Cosmochim. Acta*, V. 52, p. 43-53.

Knauss, K.G., and T.J. Wolery, (1986), "Dependence of albite dissolution kinetics on pH and time at 25°C and 70°C:" *Geochim. Cosmochim. Acta*, V. 50, p. 2481-2497.

Oelkers, E.H., and J. Schott, (1995), "Experimental study of anorthite dissolution and the relative mechanism of feldspar hydrolysis:" *Geochim. Cosmochim. Acta*, V. 59, (24), p. 5039-5053.

Renders, P.J.N., C.H. Gammons, and H.L. Barnes, (1995), "Precipitation and dissolution rate constants for cristobalite from 150 to 300°C:" *Geochim. Cosmochim. Acta*, V. 59, (1), p. 77-85.

Rimstidt, J.D., and H.L. Barnes, (1980), "The kinetics of silica-water reactions:" *Geochim. Cosmochim. Acta*, V. 44, p. 1683-1699.

Rose, N.M., (1991), "Dissolution rates of prehnite, epidote, and albite:" *Geochim. Cosmochim. Acta*, V. 55, p. 3273-3286.

Steefel, C.I., and A.C. Lasaga, 1994, "A coupled model for transport of multiple chemical species and kinetic precipitation/dissolution reactions with application to reactive flow in single phase hydrothermal systems:" *Amer. J. Sci.*, V. 294, p. 529-592.

Steefel, C.I., and S.B. Yabusaki, (1995), "OS3D/GIMRT: Software for modeling multicomponent-multidimensional reactive transport:" *User's manual and programmer's guide*, Version 1.0, 58 p.

Warren, R.G., F.M. Byers, and F.A. Caporuscio, (1984), *Petrography and mineral chemistry of units of the Topopah Spring, Calico Hills and Crater Flat Tuffs, and older volcanic units, with emphasis on samples from drill hole USW G-1, Yucca Mountain, Nevada Test Site*: Los Alamos National Laboratory, Los Alamos, NM, LA-10003-MS.

Wolery, T.W., (1992), "EQ3/6, a software package for geochemical modeling of aqueous systems:" *Package overview and installation guide (Version 7.0)*: Lawrence Livermore National Laboratory, Livermore, CA, UCRL-MA-110662 PT I, 66 p.

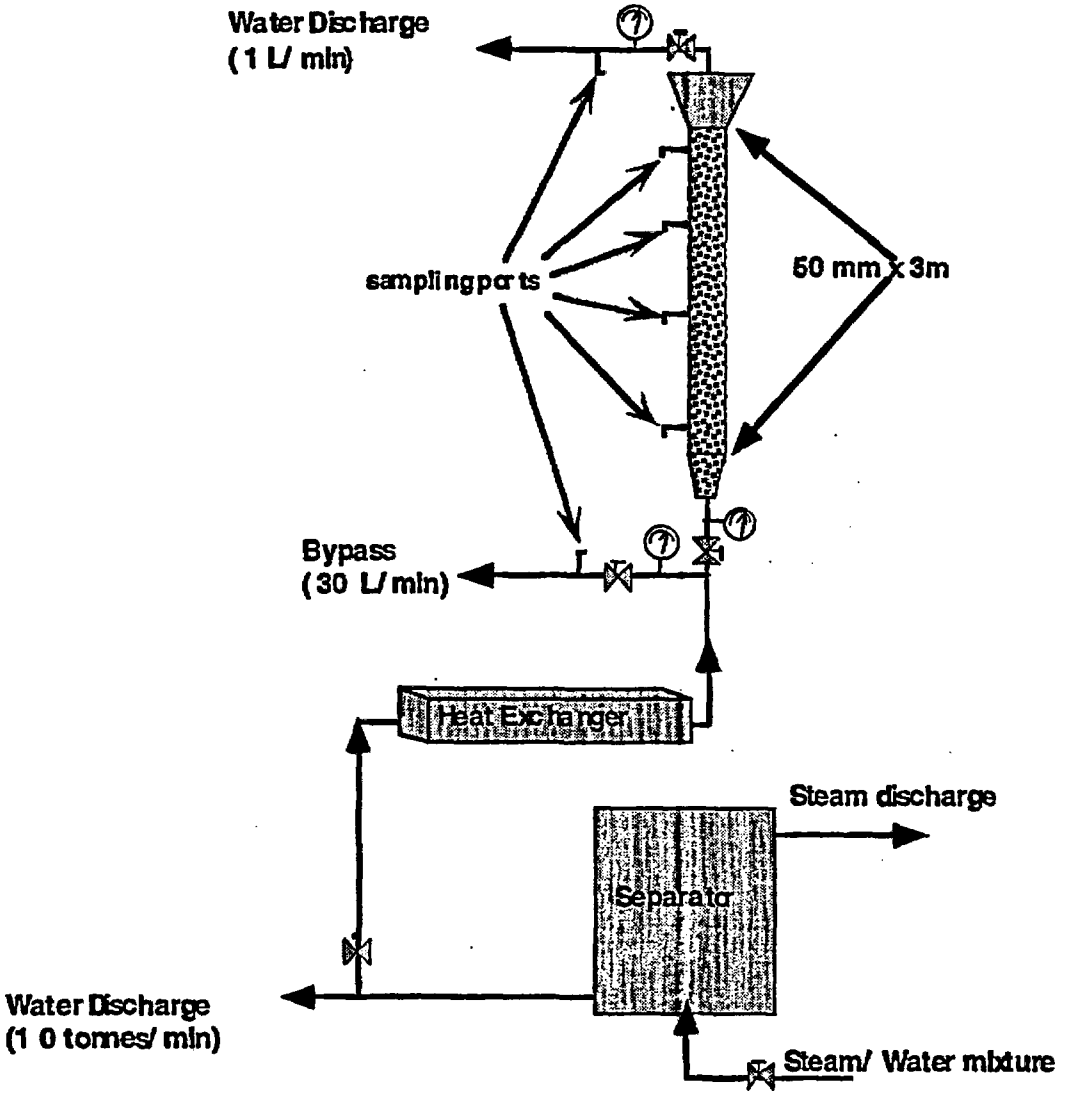

Figure 10.4-1. Schematic of the fluidized bed reactor used in the amorphous silica precipitation field experiments.

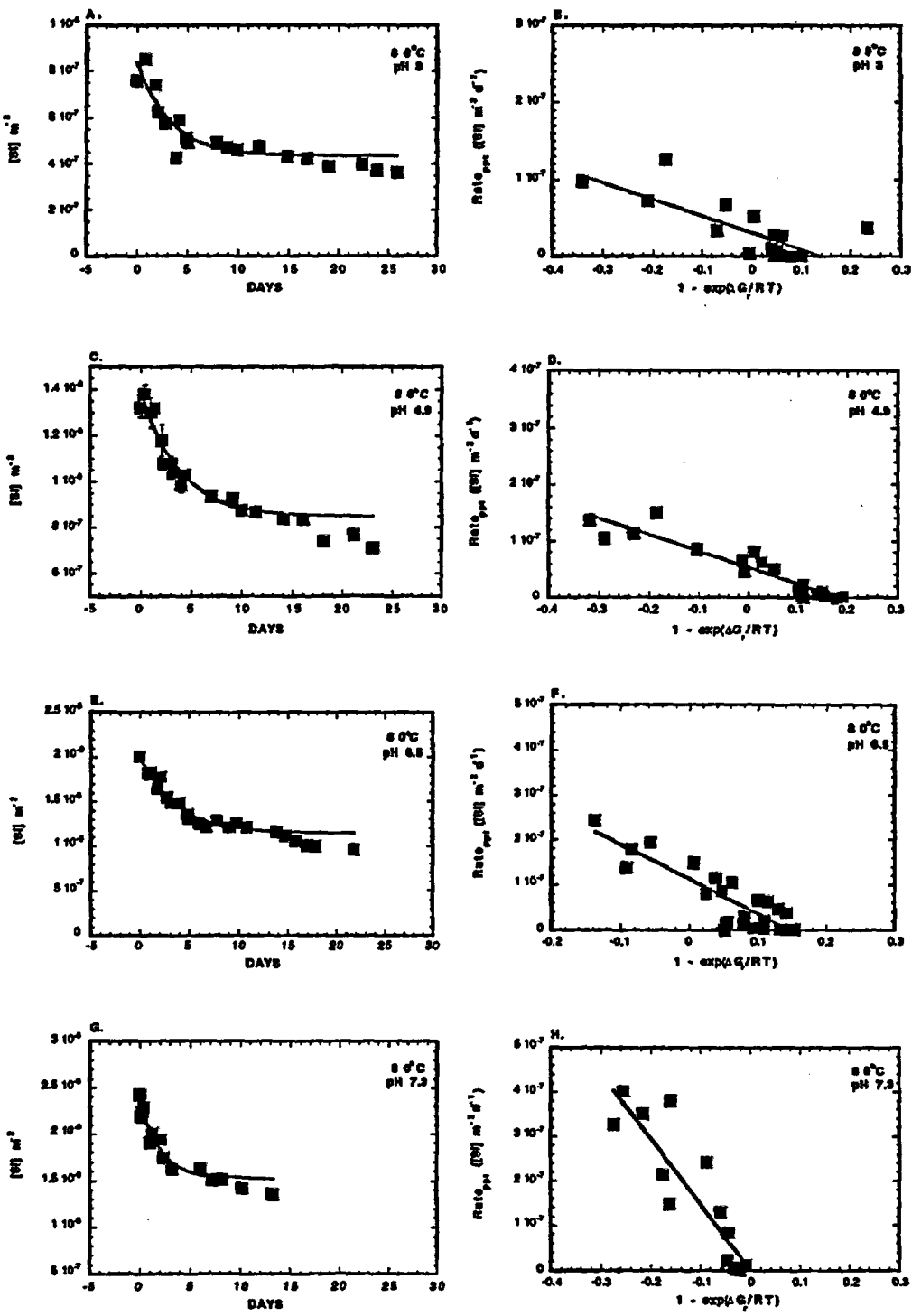

Figure 10.4-2. Amorphous silica precipitation rates plotted as [Si] m^{-2} vs. Days and as $Rate_{ppt}$ ([Si] $m^{-2}d^{-1}$) vs. [1 – exp(ΔGr/RT)] at 80 (A-H), 100 (I-T) and 120°C (U-X).

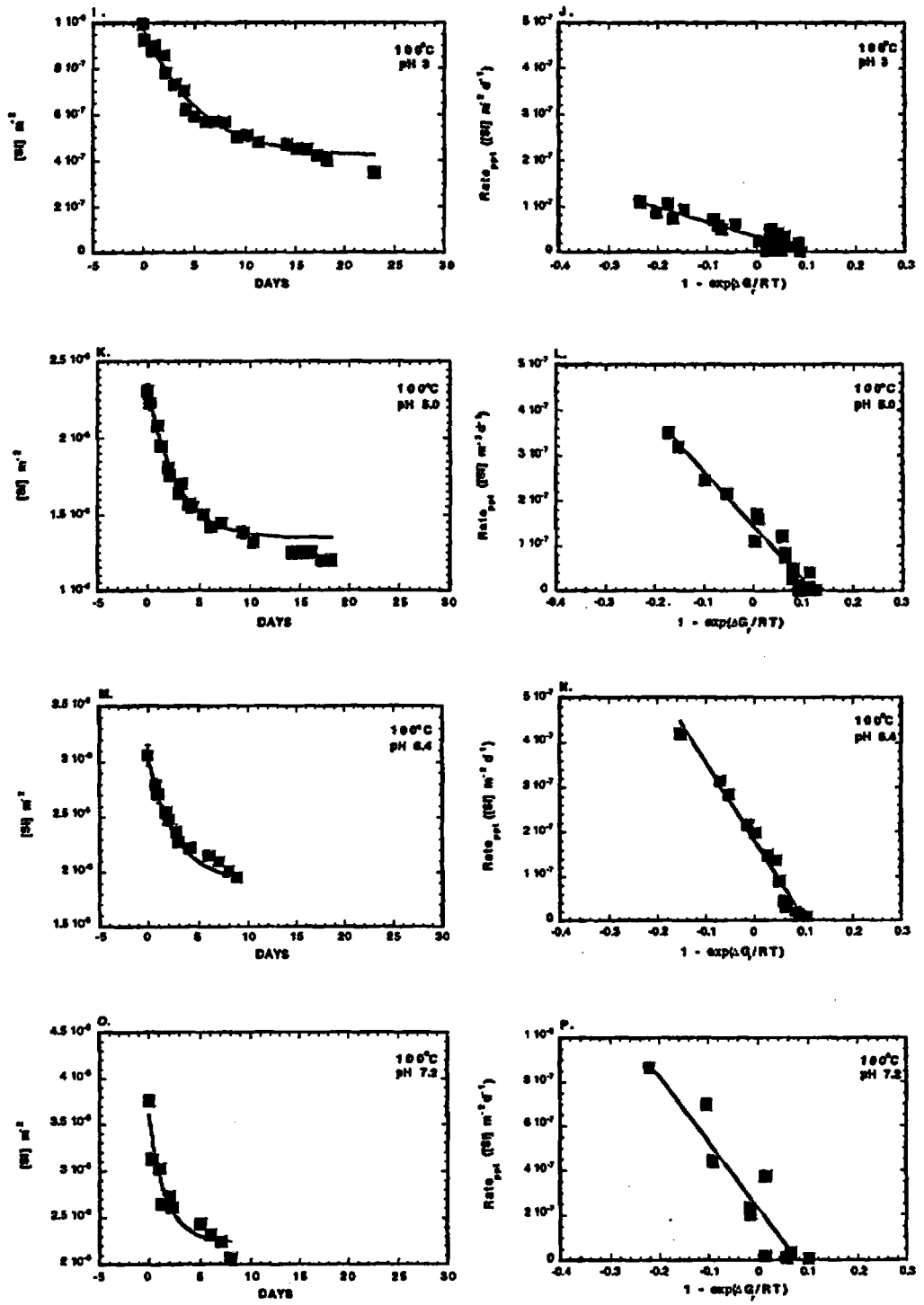

Figure 10.4-2. Continued.

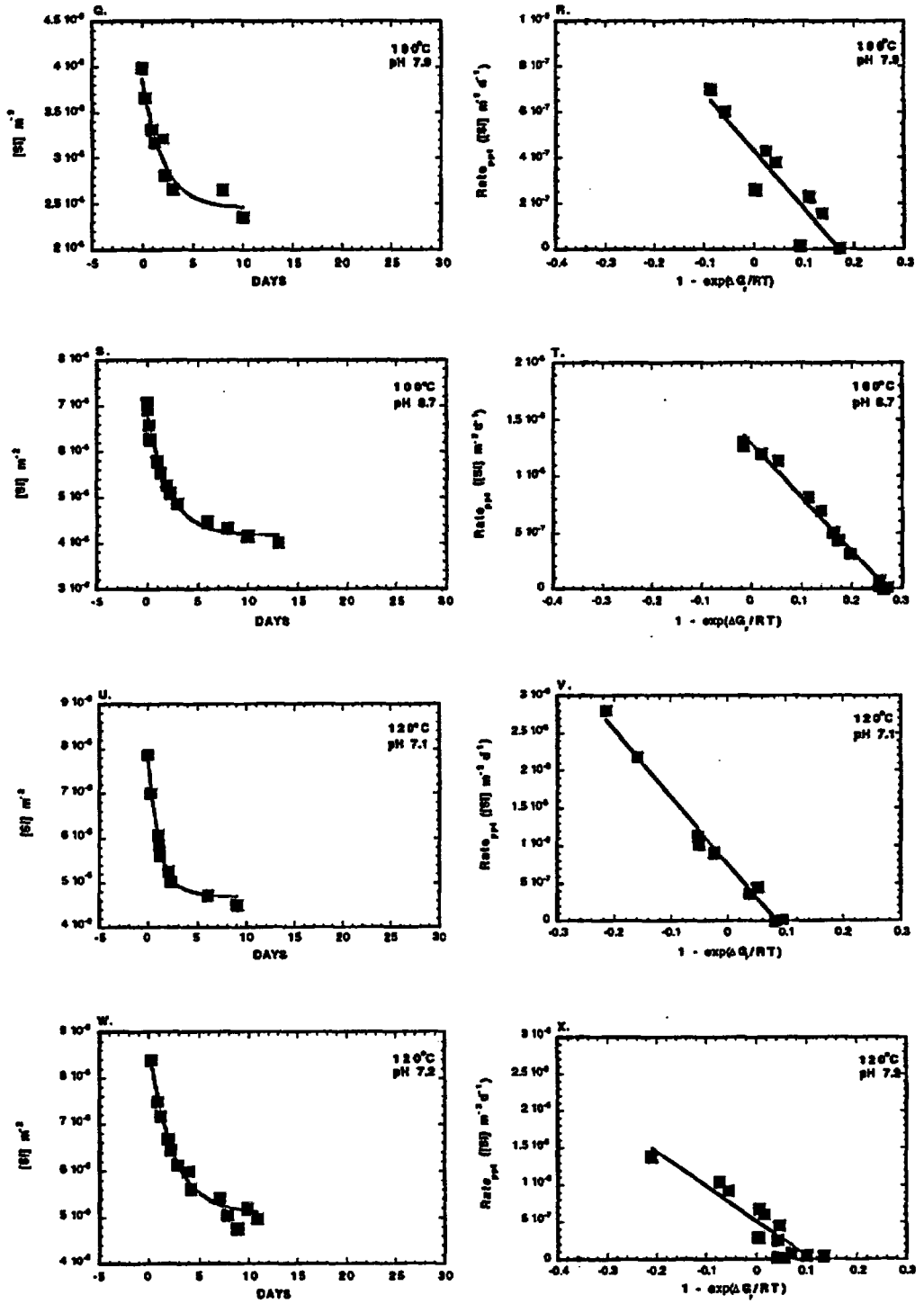

Figure 10.4-2. Continued.

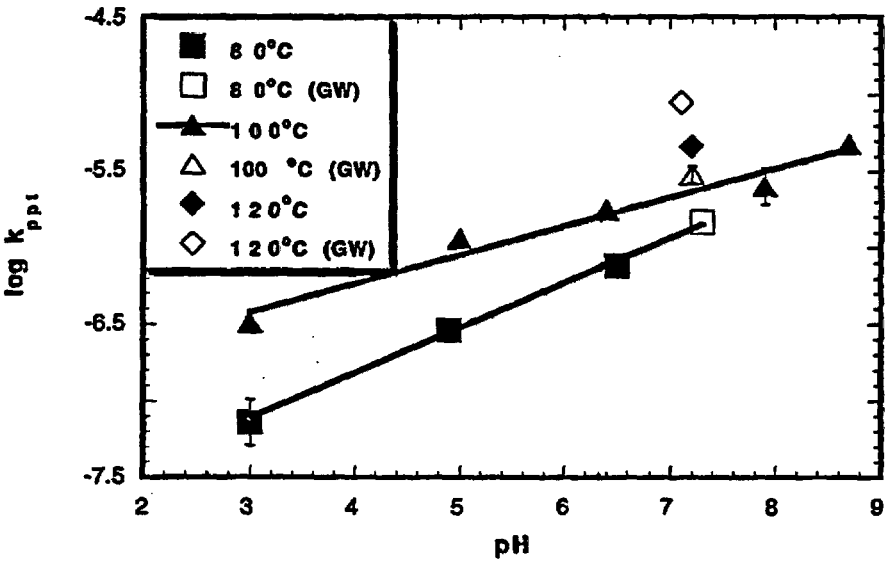

Figure 10.4-3. pH-dependence of amorphous silica precipitation rates plotted as log k_{ppt} ([Si] $m^{-2}d^{-1}$) vs. pH at 80, 100, and 120°C. GW refers to amorphous silica precipitation from Wairakei geothermal waters.

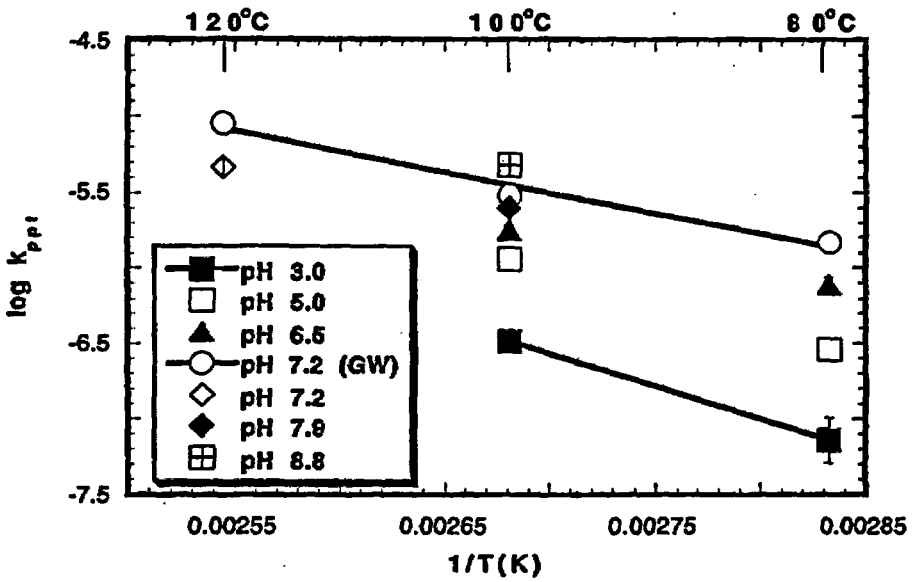

Figure 10.4-4. Temperature dependence of amorphous silica precipitation rates plotted as log k_{ppt} ([Si] $m^{-2}d^{-1}$) vs. 1/T(K). GW refers to amorphous silica precipitation from Wairakei geothermal waters.

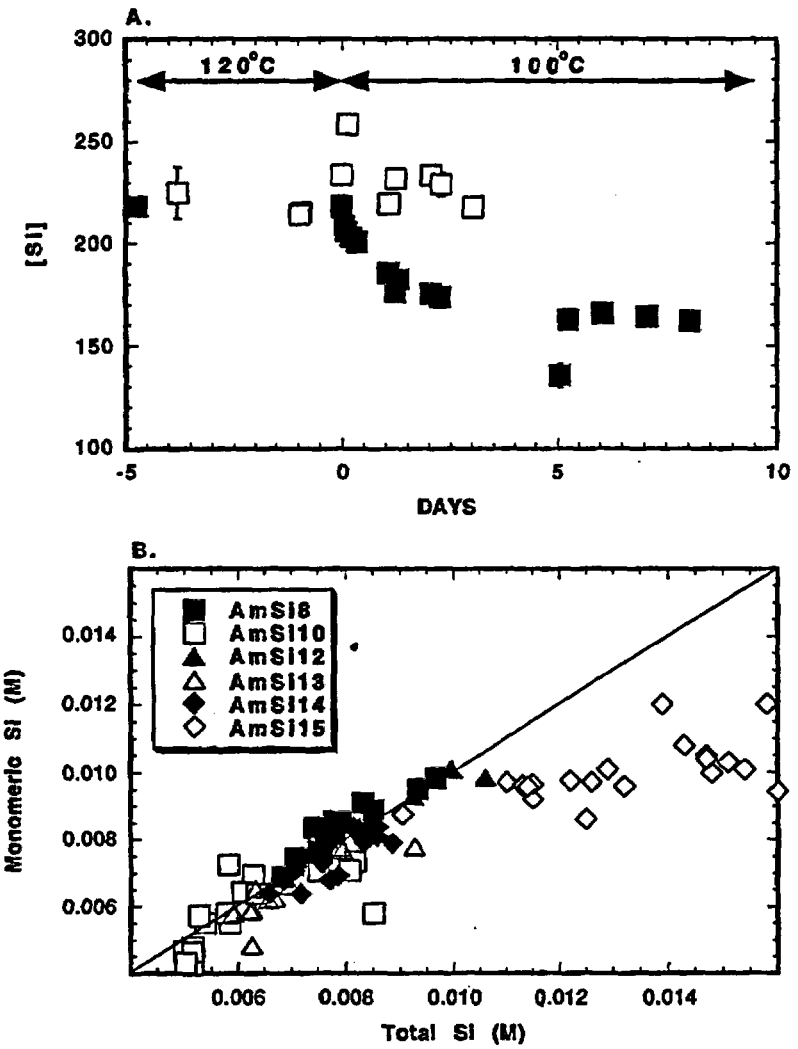

Figure 10.4-5. A. Monomeric silica concentrations vs. time in Wairakei geothermal waters in the absence (open squares) and presence (solid squares) of amorphous silica seed material. Negative days refer to time before temperature change. B. Ratio of monomeric to total silica.

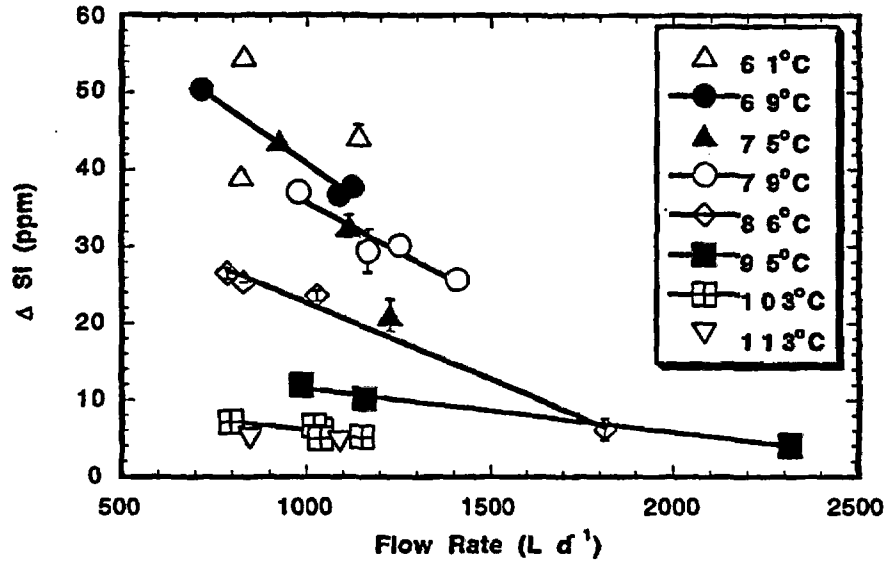

Figure 10.4-6. Amorphous silica precipitation from Wairakei Flash Plant 10 FBR experiments. Shown as the net silica removed from solution as a function of flow rate over discreet temperature intervals (61, 69±1, 75±1, 79±1, 86±2, 95±2, 103±2, and 113±2°C).

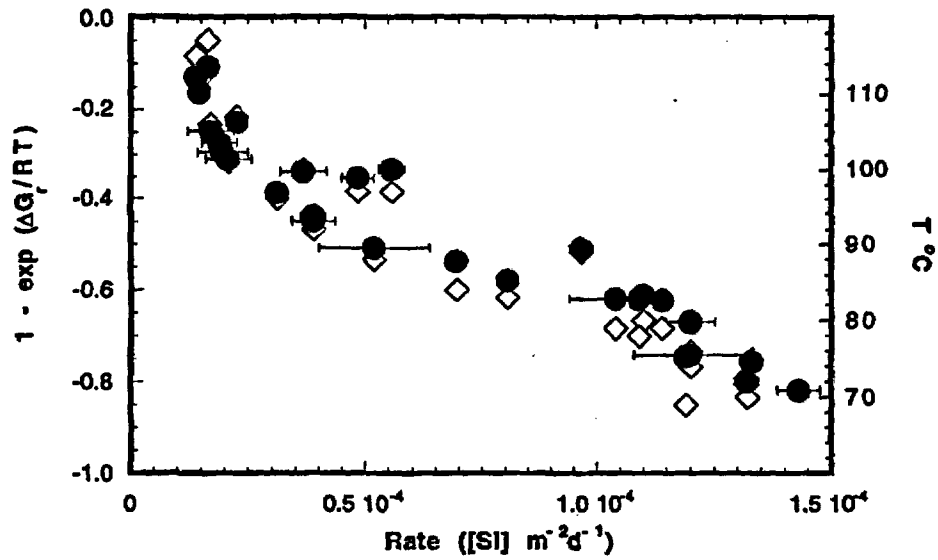

Figure 10.4-7. Precipitation rates determined in the fluidized bed reactor at Wairakei plotted as a function of T°C (open diamonds) and (1 – exp (ΔG_r/RT)) (solid circles).

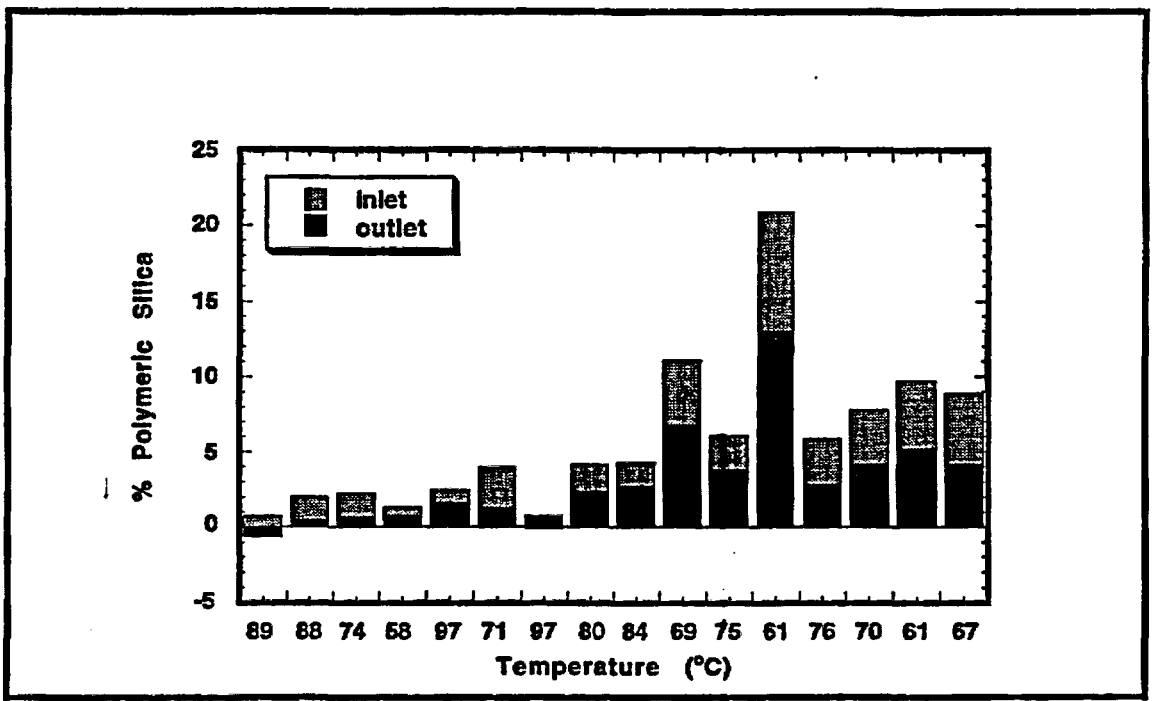

Figure 10.4-8. Stacked percentage of polymeric silica in inlet and outlet samples taken at a given time and temperature calculated from measurements of total Si and monomeric silica.

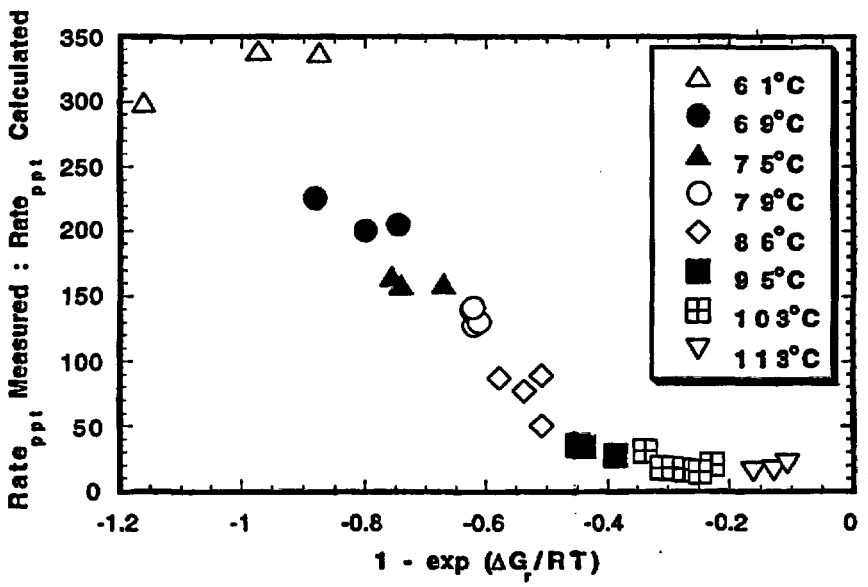

Figure 10.4-9. Comparison of field and laboratory amorphous silica precipitation rates by plotting the ratio of the measured and calculated rates from the Wairakei, New Zealand, field study. The rates were calculated based on the laboratory results (see text).

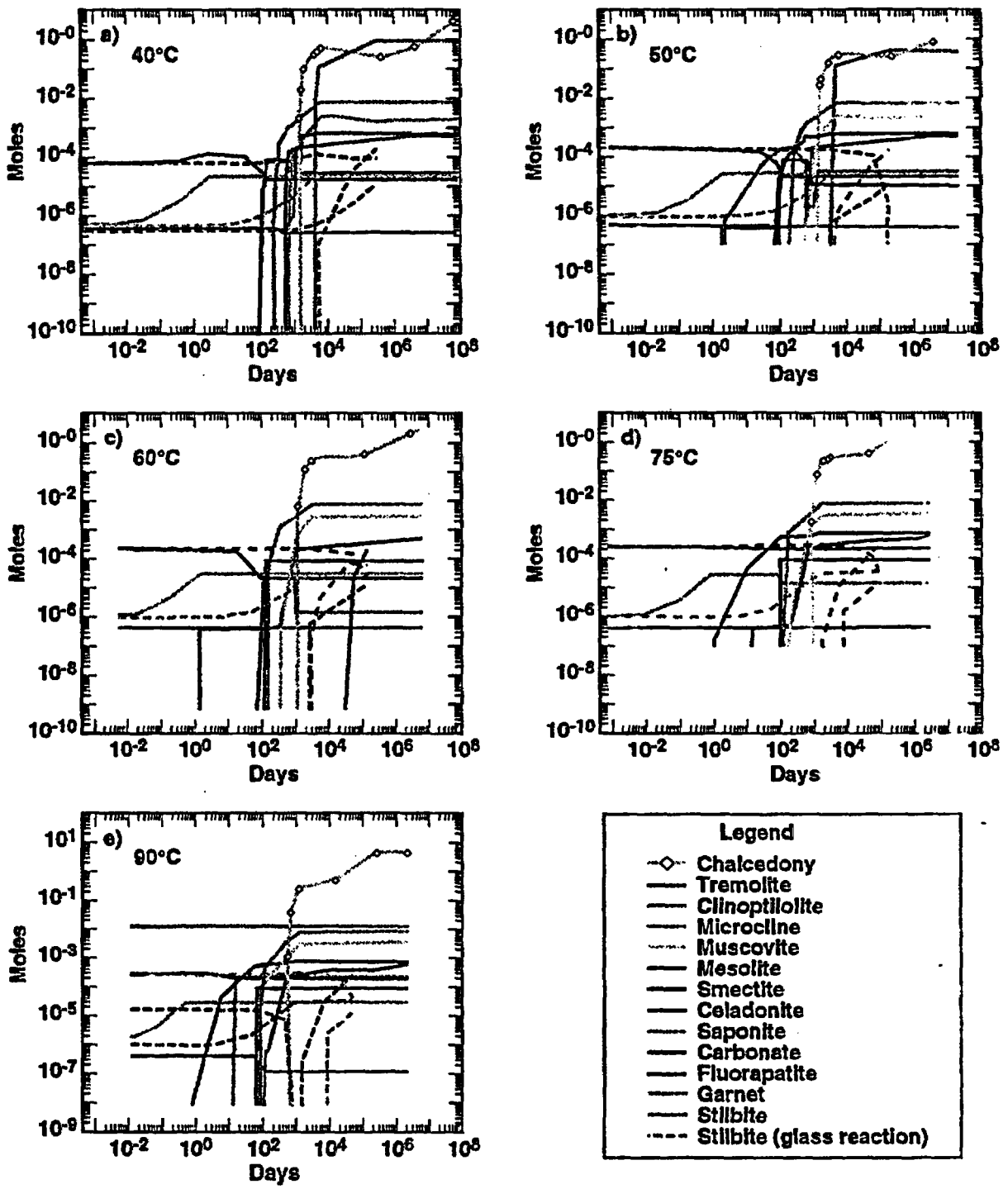

Figure 10.4-10. Secondary mineralogy as a function of time. a) 40° C; b) 50° C; c) 60° C; d) 75° C; e) 90° C. Mineralogy of the tuffs is shown as solid lines, mineralogy of the vitrophyre is shown as broken lines. These relationships for the vitrophyre are for the case in which the water:glass mass ratio is 5763. Rate constants and surface areas for the vitrophyre case were adjusted so that the time at which most of the secondary minerals developed was similar to that for the tuff. For the case in which the water:rock mass ratio was much lower (57.8), the same mineral phases developed for the vitrophyre during the early stages of reaction progress, but were eventually superseded by chalcedony and hematite.

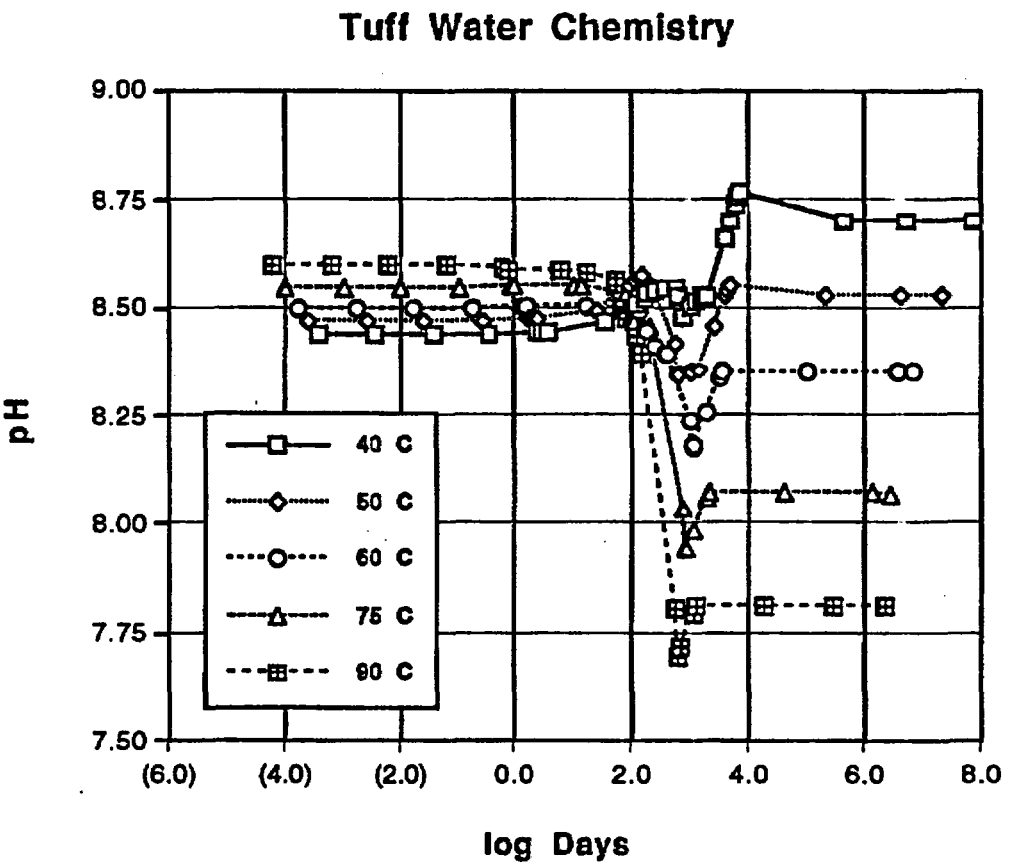

Figure 10.4-11(a) pH

Figure 10.4-11. Tuff-water system aqueous compositions, as a function of time and temperature. a) pH; b) Eh; c) Si; d) Na; e) Ca; f) Mg; g) Al. All elemental values are for total element concentrations.

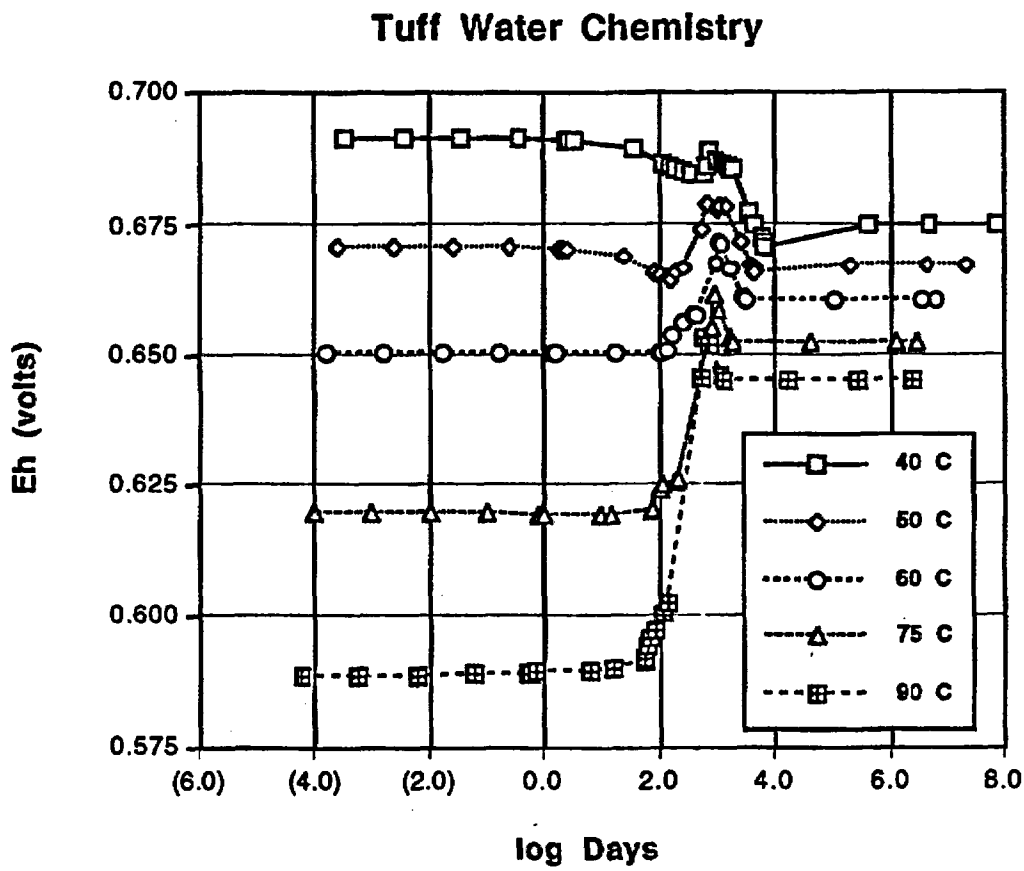

Figure 10.4-11(b) Eh

Figure 10.4-11. Tuff-water system aqueous compositions, as a function of time and temperature. a) pH; b) Eh; c) Si; d) Na; e) Ca; f) Mg; g) Al. All elemental values are for total element concentrations.

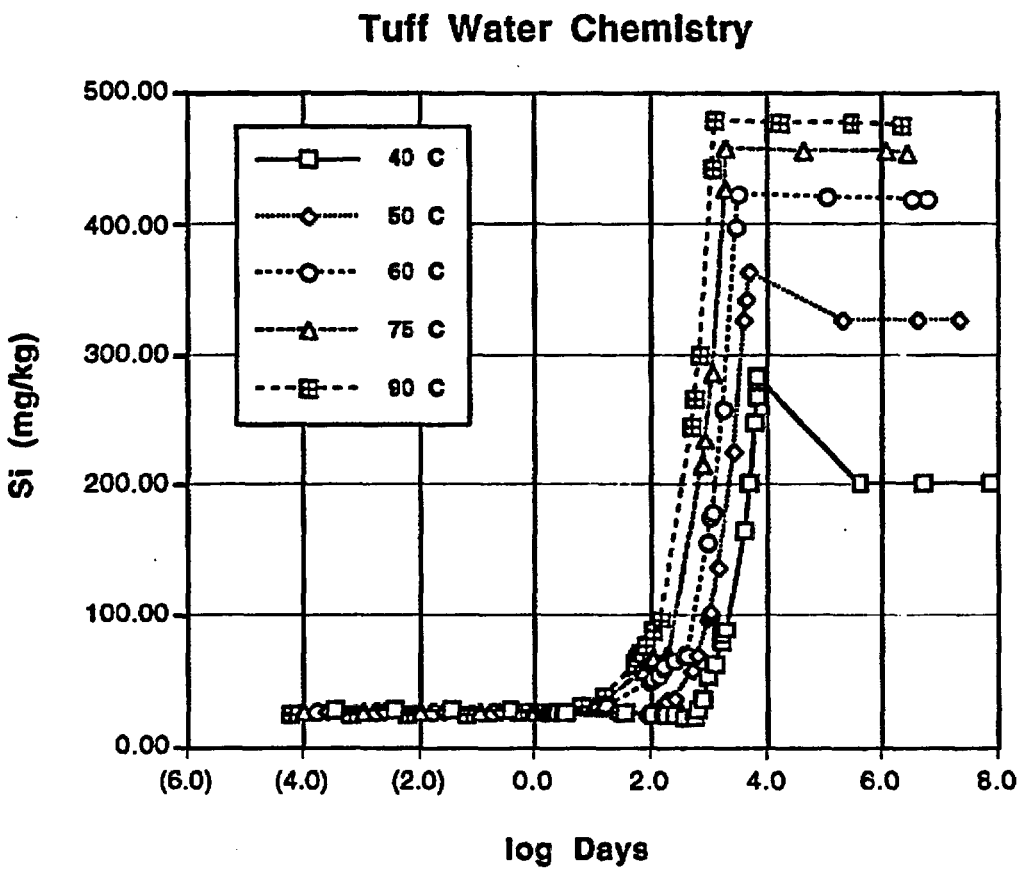

Figure 10.4-11(c) Si

Figure 10.4-11. Tuff-water system aqueous compositions, as a function of time and temperature. a) pH; b) Eh; c) Si; d) Na; e) Ca; f) Mg; g) Al. All elemental values are for total element concentrations.

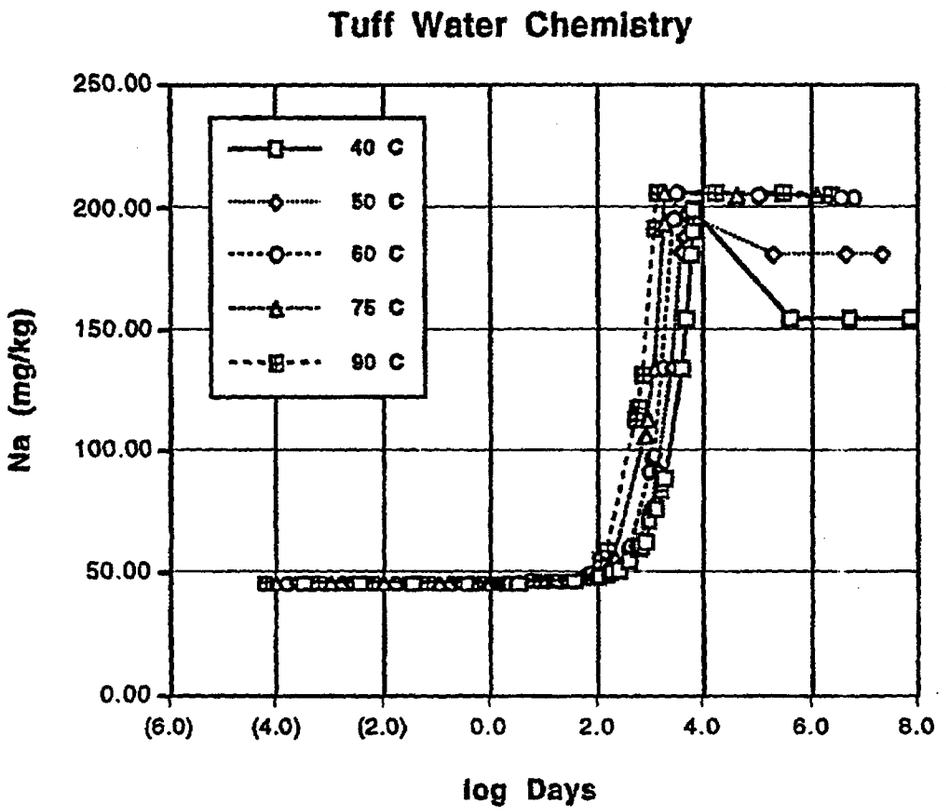

Figure 10.4-11(d) Na

Figure 10.4-11. Tuff-water system aqueous compositions, as a function of time and temperature. a) pH; b) Eh; c) Si; d) Na; e) Ca; f) Mg; g) Al. All elemental values are for total element concentrations.

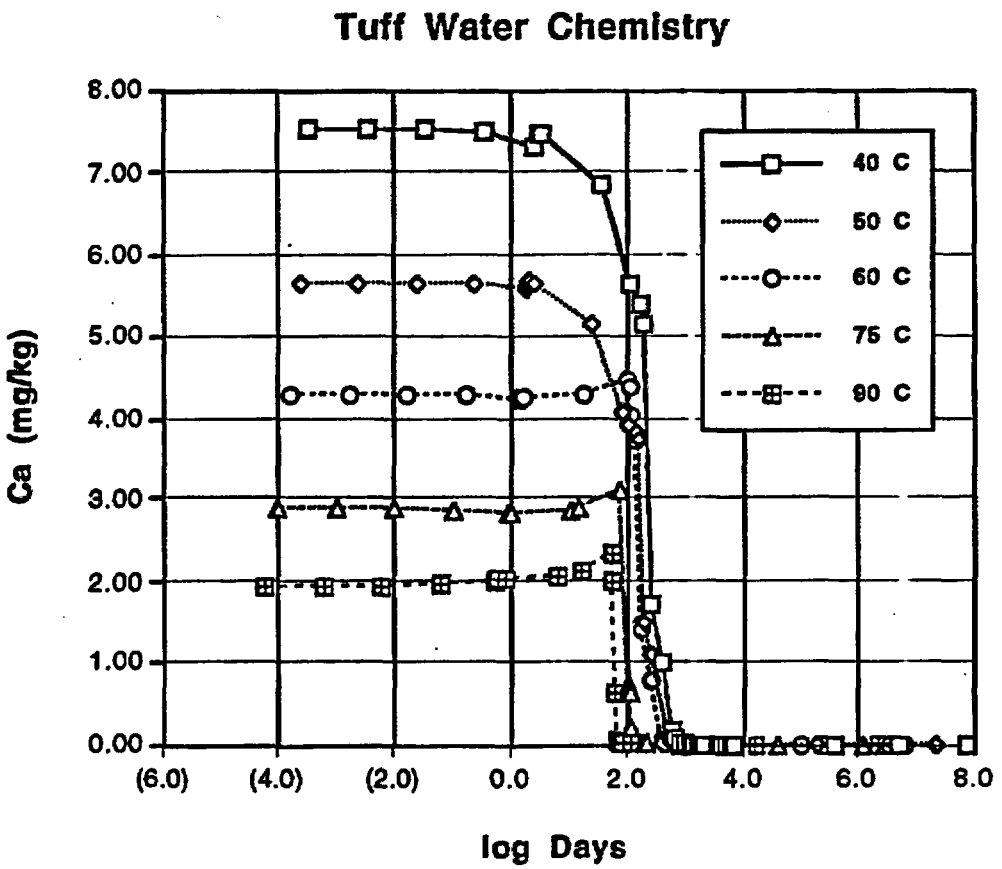

Figure 10.4-11(e) Ca

Figure 10.4-11. Tuff-water system aqueous compositions, as a function of time and temperature. a) pH; b) Eh; c) Si; d) Na; e) Ca; f) Mg; g) Al. All elemental values are for total element concentrations.

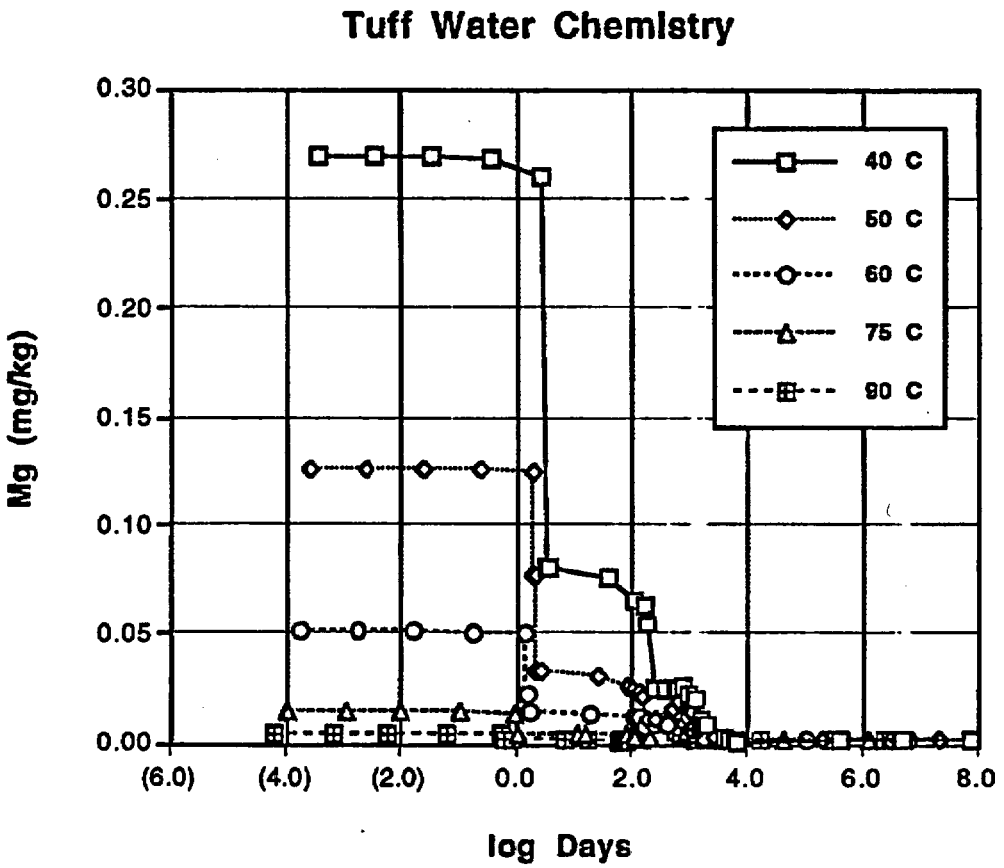

Figure 10.4-11(f) Mg

Figure 10.4-11. Tuff-water system aqueous compositions, as a function of time and temperature. a) pH; b) Eh; c) Si; d) Na; e) Ca; f) Mg; g) Al. All elemental values are for total element concentrations.

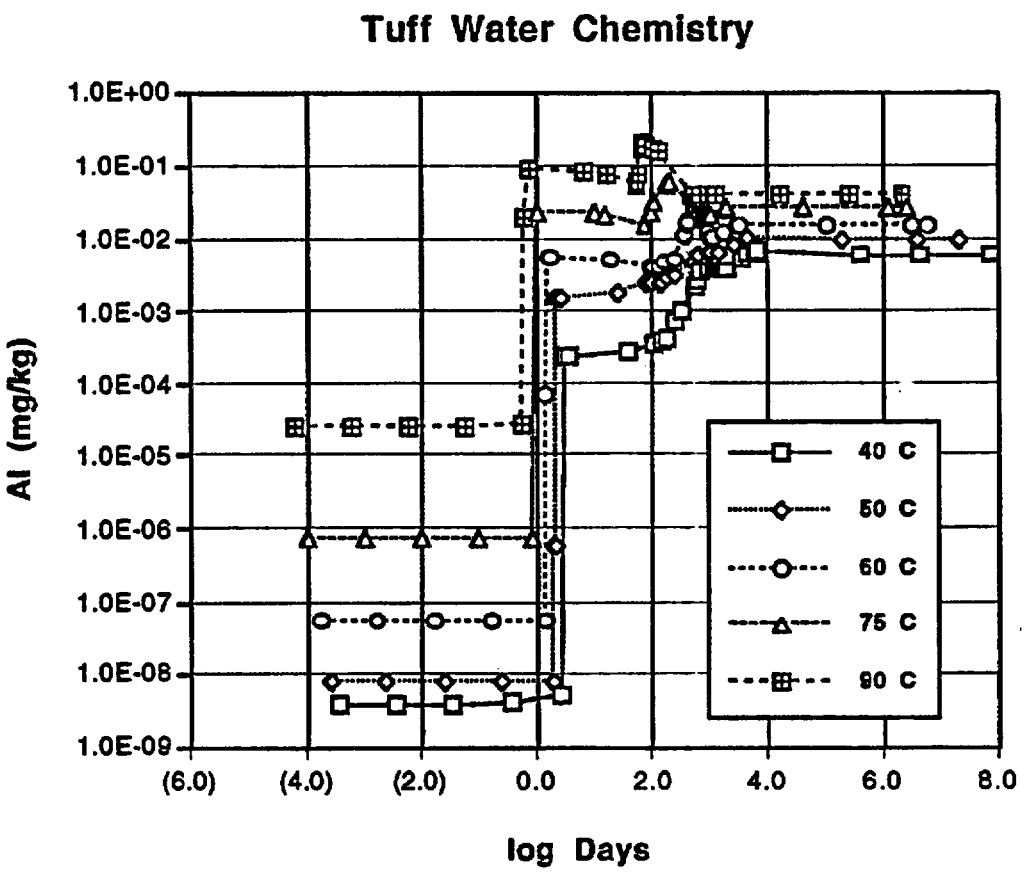

Figure 10.4-11(g) Al

Figure 10.4-11. Tuff-water system aqueous compositions, as a function of time and temperature. a) pH; b) Eh; c) Si; d) Na; e) Ca; f) Mg; g) Al. All elemental values are for total element concentrations.

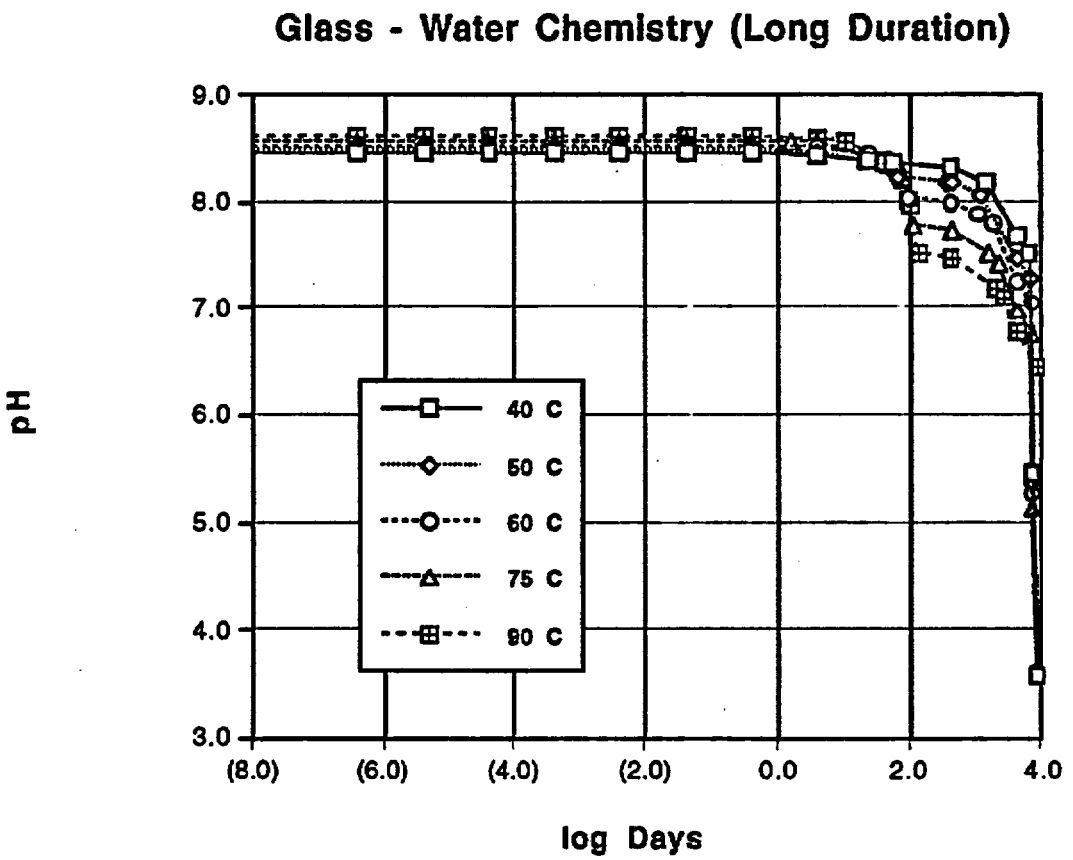

Figure 10.4-12(a) pH

Figure 10.4-12. Vitrophyre-water system aqueous compositions for water:rock mass ratio of 57.8, as a function of time and temperature. a) pH; b) Eh; c) Si; d) Na; e) Ca; f) Mg; g) Al. All elemental values are for total element concentrations. For the case in which the water:rock mass ratio was 5763, the water compositions reached the values shown in these figures at ca. 10^2 days, although in those simulations reaction rates were such that these values were not acheived until ca. 4×10^5 days.

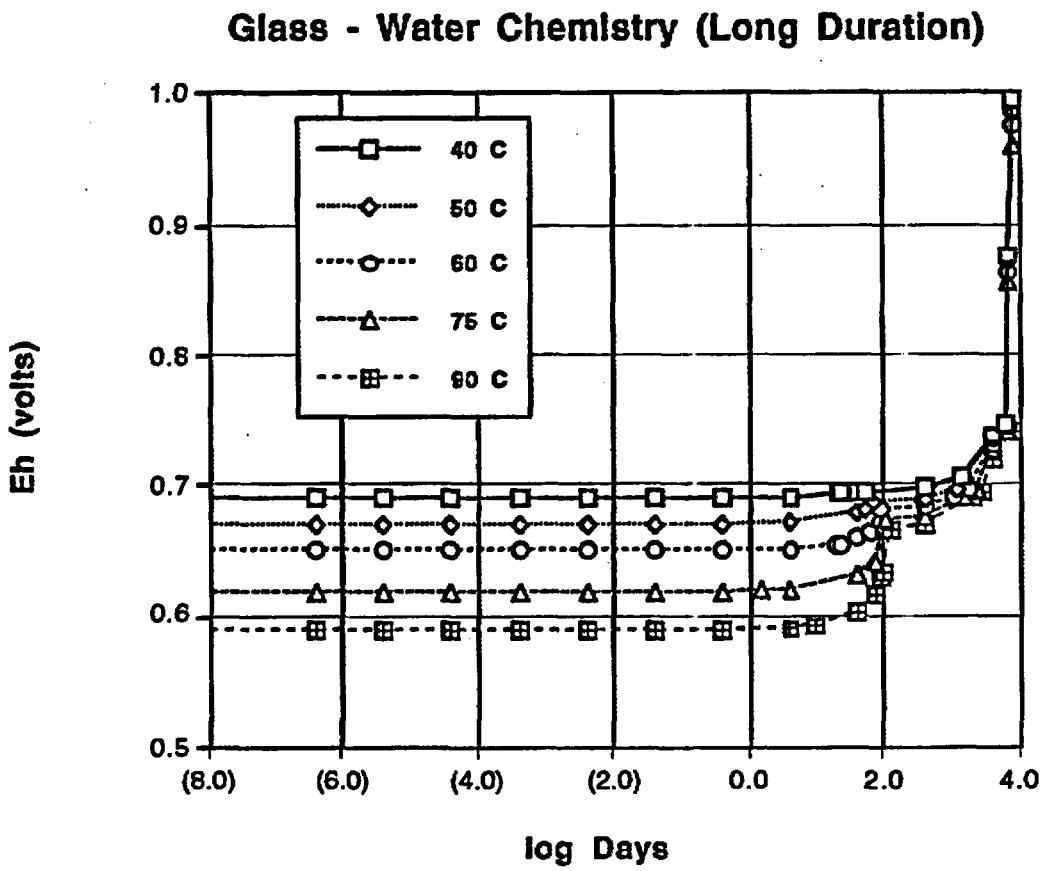

Figure 10.4-12(b) Eh

Figure 10.4-12. Vitrophyre-water system aqueous compositions for water:rock mass ratio of 57.8, as a function of time and temperature. a) pH; b) Eh; c) Si; d) Na; e) Ca; f) Mg; g) Al. All elemental values are for total element concentrations. For the case in which the water:rock mass ratio was 5763, the water compositions reached the values shown in these figures at ca. 10^2 days, although in those simulations reaction rates were such that these values were not acheived until ca. 4×10^5 days.

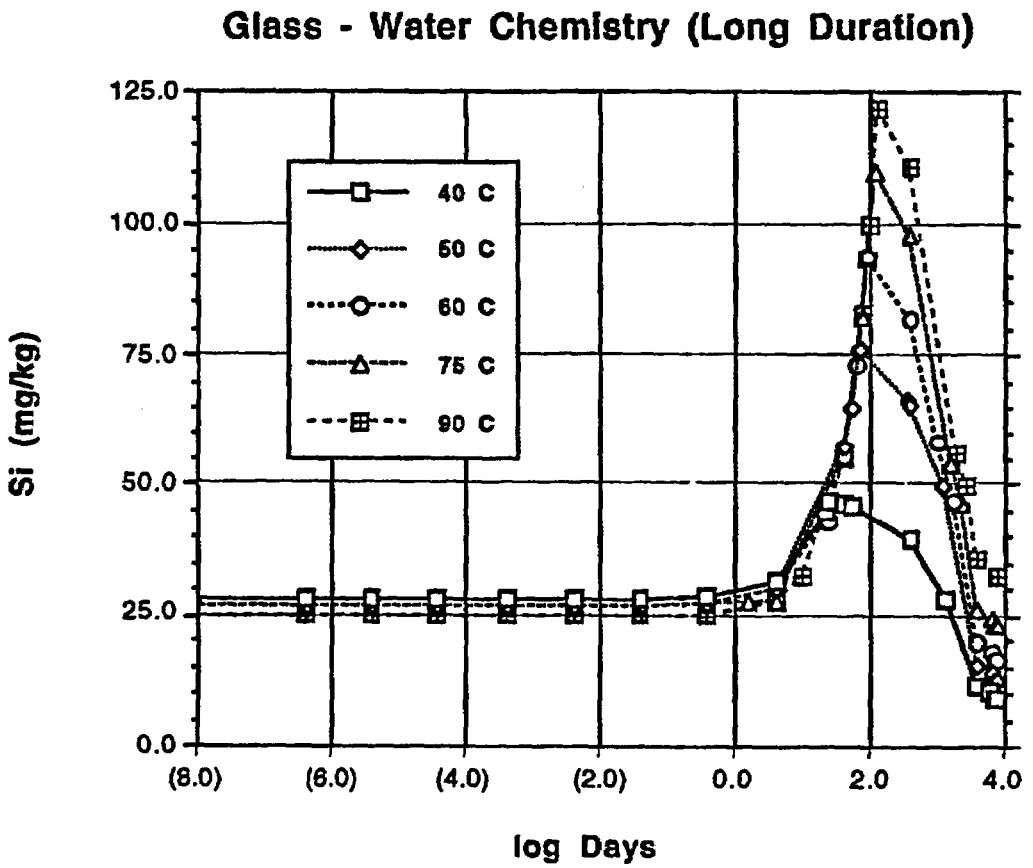

Figure 10.4-12(c) Si

Figure 10.4-12. Vitrophyre-water system aqueous compositions for water:rock mass ratio of 57.8, as a function of time and temperature. a) pH; b) Eh; c) Si; d) Na; e) Ca; f) Mg; g) Al. All elemental values are for total element concentrations. For the case in which the water:rock mass ratio was 5763, the water compositions reached the values shown in these figures at ca. 10^2 days, although in those simulations reaction rates were such that these values were not acheived until ca. 4×10^5 days.

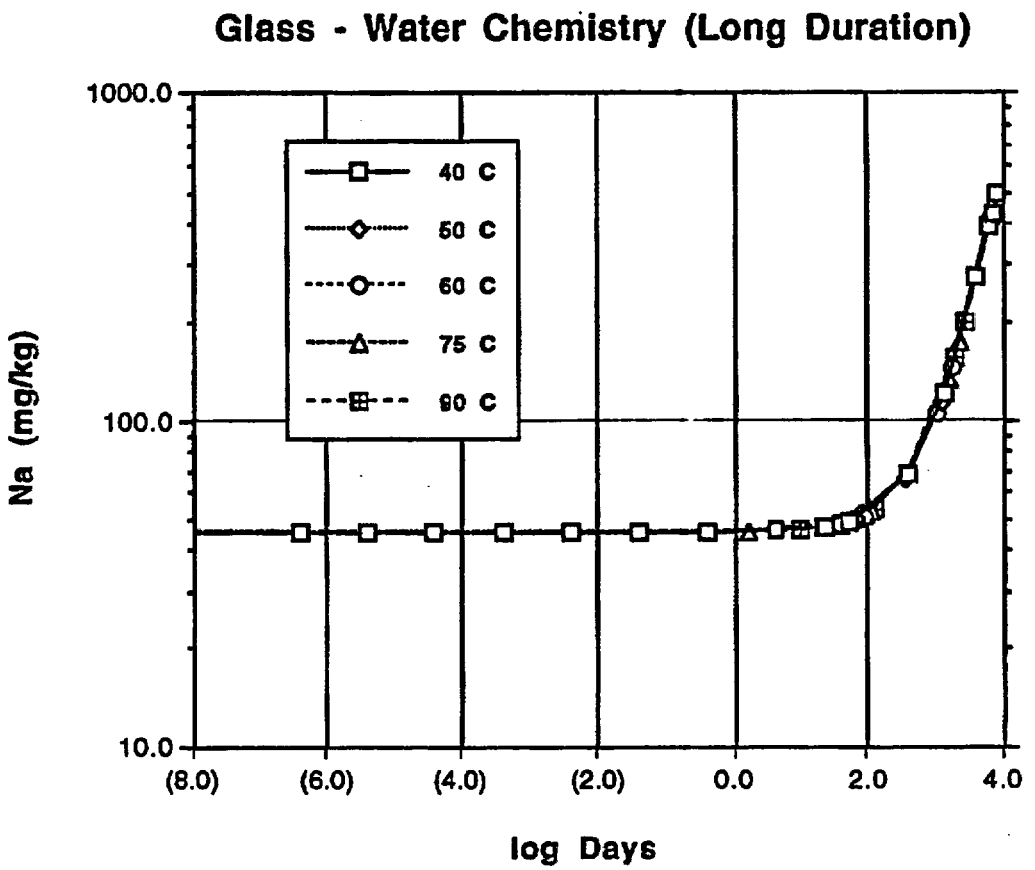

Figure 10.4-12(d) Na

Figure 10.4-12. Vitrophyre-water system aqueous compositions for water:rock mass ratio of 57.8, as a function of time and temperature. a) pH; b) Eh; c) Si; d) Na; e) Ca; f) Mg; g) Al. All elemental values are for total element concentrations. For the case in which the water:rock mass ratio was 5763, the water compositions reached the values shown in these figures at ca. 10^2 days, although in those simulations reaction rates were such that these values were not acheived until ca. 4×10^5 days.

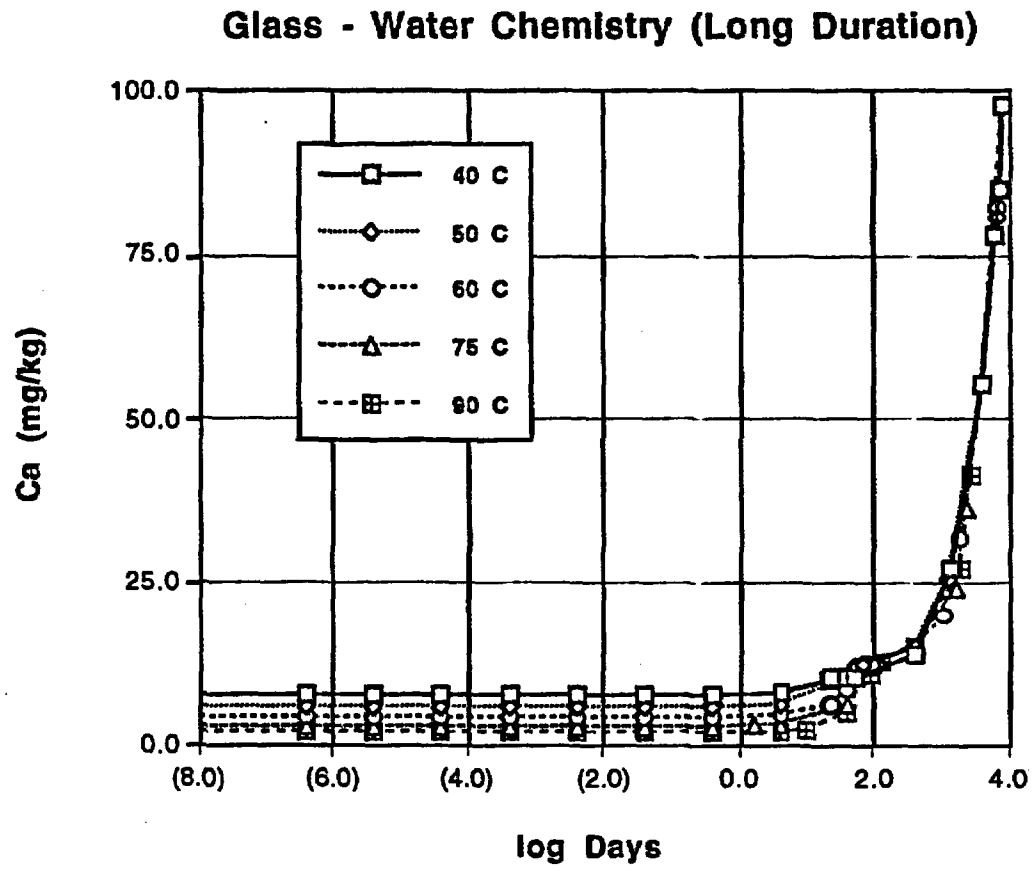

Figure 10.4-12(e) Ca

Figure 10.4-12. Vitrophyre-water system aqueous compositions for water:rock mass ratio of 57.8, as a function of time and temperature. a) pH; b) Eh; c) Si; d) Na; e) Ca; f) Mg; g) Al. All elemental values are for total element concentrations. For the case in which the water:rock mass ratio was 5763, the water compositions reached the values shown in these figures at ca. 10^2 days, although in those simulations reaction rates were such that these values were not acheived until ca. 4×10^5 days.

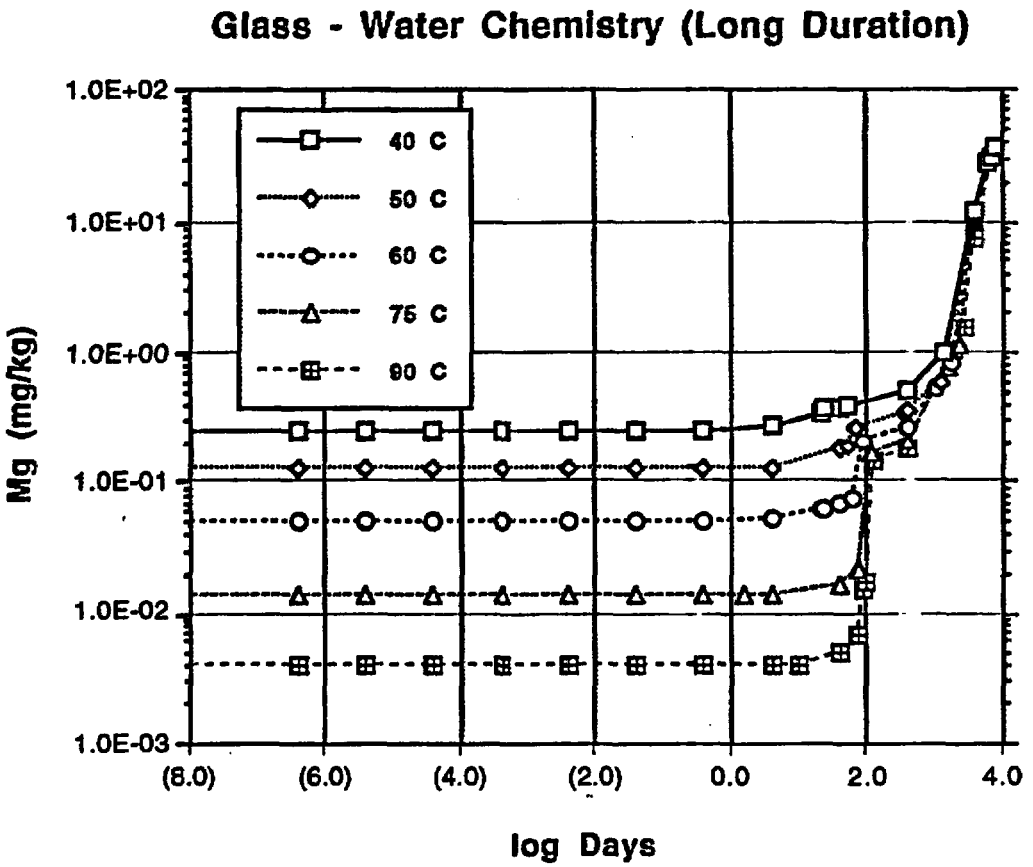

Figure 10.4-12(f) Mg

Figure 10.4-12. Vitrophyre-water system aqueous compositions for water:rock mass ratio of 57.8, as a function of time and temperature. a) pH; b) Eh; c) Si; d) Na; e) Ca; f) Mg; g) Al. All elemental values are for total element concentrations. For the case in which the water:rock mass ratio was 5763, the water compositions reached the values shown in these figures at ca. 10^2 days, although in those simulations reaction rates were such that these values were not acheived until ca. 4×10^5 days.

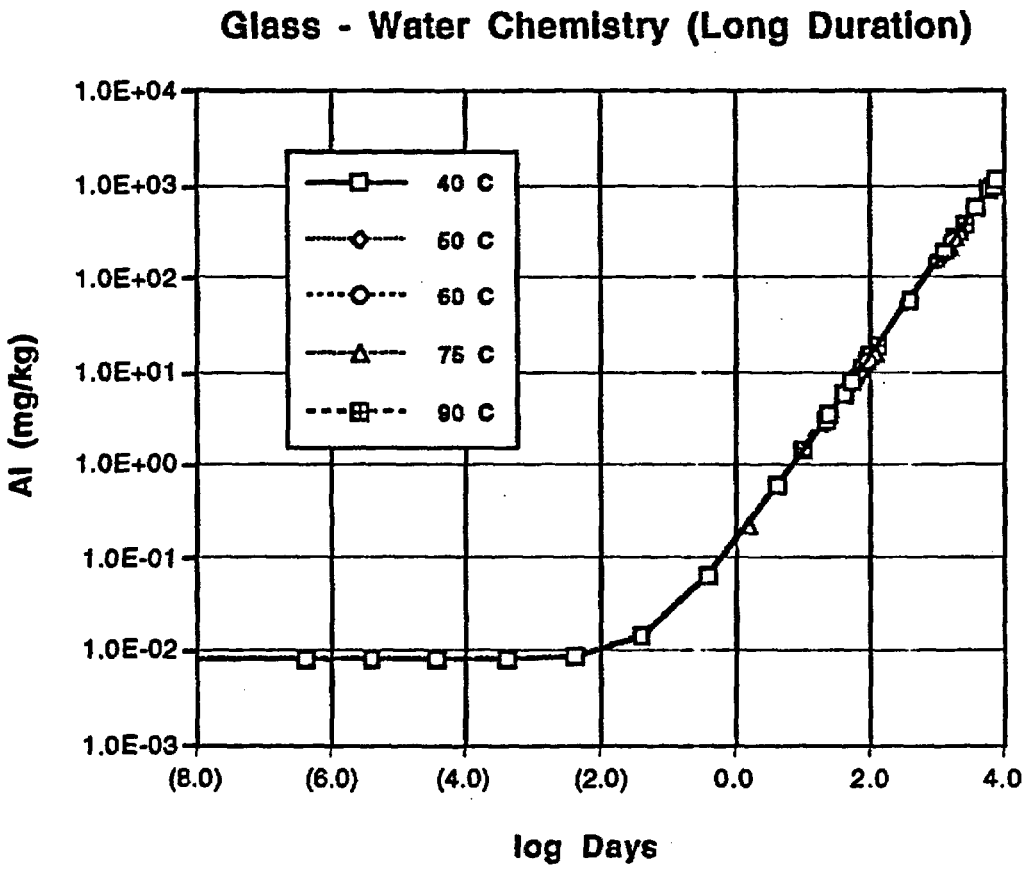

Figure 10.4-12(g) Al

Figure 10.4-12. Vitrophyre-water system aqueous compositions for water:rock mass ratio of 57.8, as a function of time and temperature. a) pH; b) Eh; c) Si; d) Na; e) Ca; f) Mg; g) Al. All elemental values are for total element concentrations. For the case in which the water:rock mass ratio was 5763, the water compositions reached the values shown in these figures at ca. 10^2 days, although in those simulations reaction rates were such that these values were not acheived until ca. 4×10^5 days.

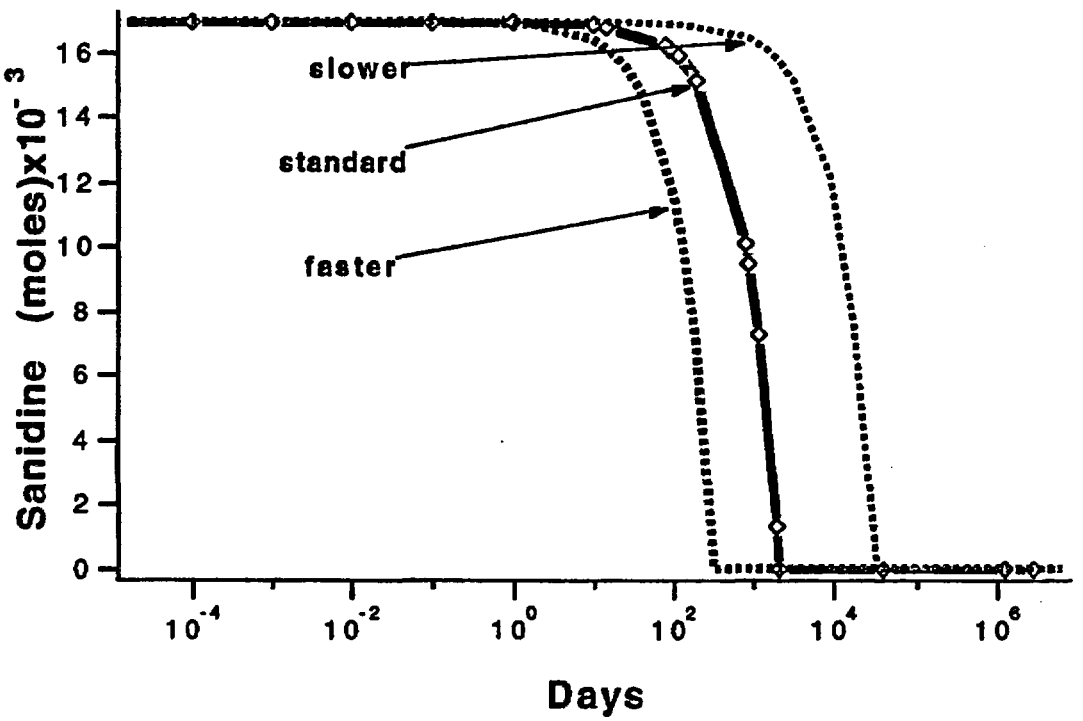

Figure 10.4-13. Changes in sanidine abundance resulting from plus or minus one order of magnitude change in its dissolution rate.

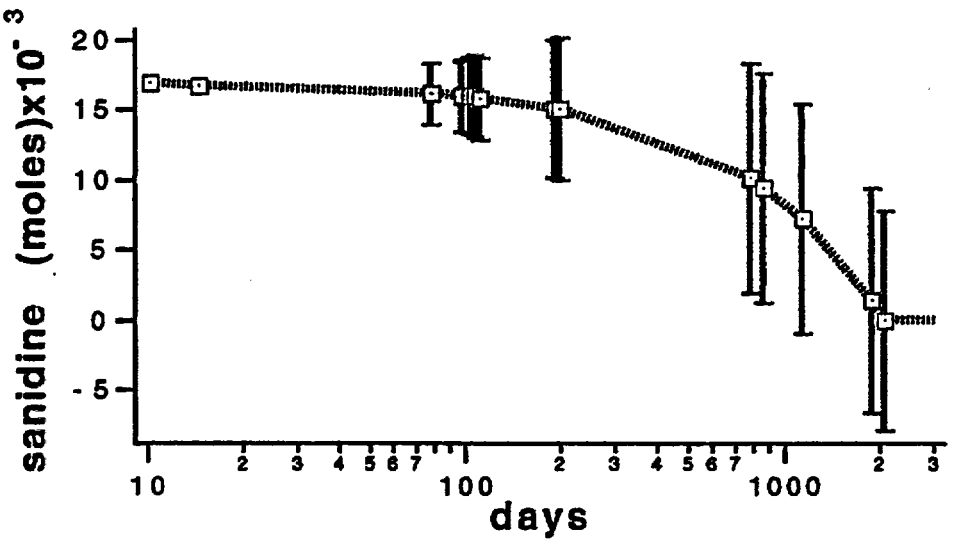

Figure 10.4-14. Estimates of sanidine abundance, assuming the dissolution rates used to construct Fig. 10.4-13. The error bars represent the abundances computed from the curves in Fig. 10.4-13.

Figure 10.4-15. GIMRT simulation of SiO2(am) dissolution

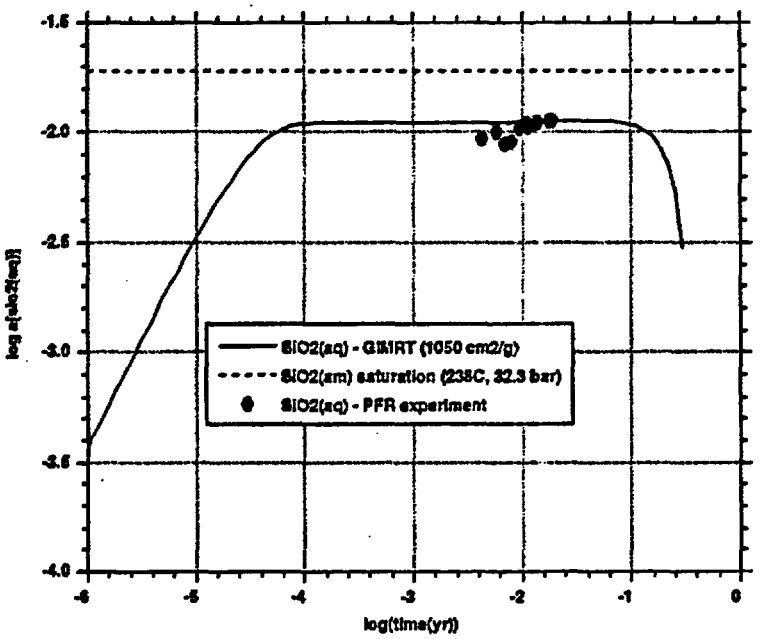

Figure. 10.4-15. Aqueous silica concentration (log activity [SiO_2(aq)]) as a function of time (log yr) in outlet fluid of the plug-flow reactor (PFR) containing crushed amorphous silica. The solid circles represent expermental measurements, the solid curve traces GIMRT predictions for an amorphous-silica specific surface area of 1050 cm^2/g, and the dashed line denotes amorphous silica saturation. In this PFR experiment and GIMRT simulation, T = 238°C, P = 84.1 bar (PFR) and 32.3 bar (GIMRT)—see text, fluid flux = 26ml/day (277.4 $m^3/m^2/yr$), and porosity = 40%.

Figure 10.4-16. GIMRT simulation of quartz dissolution

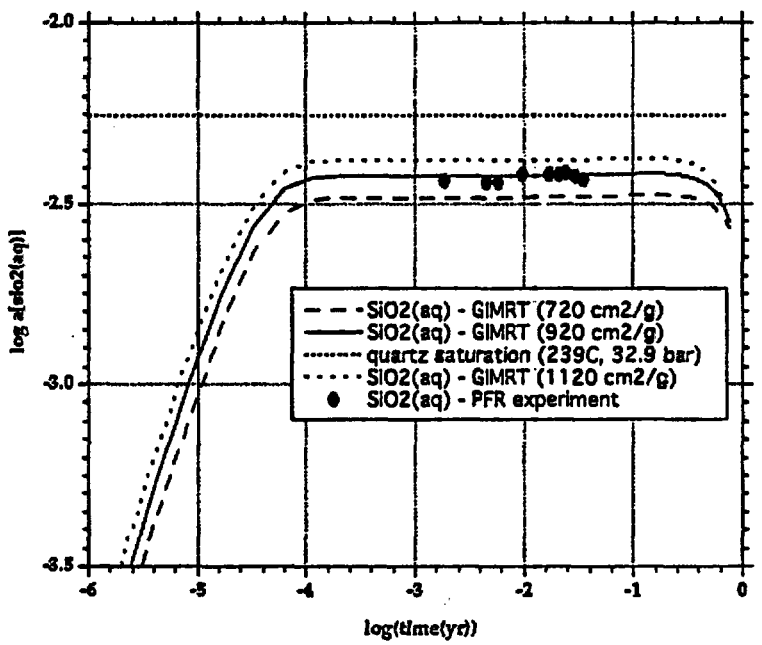

Figure. 10.4-16. Aqueous silica concentration (log activity [SiO_2(aq)]) as a function of time (log yr) in outlet fluid of the the plug-flow reactor (PFR) containing crushed quartz. The solid circles represent expermental measurements, the solid curve traces GIMRT predictions for a quartz specific surface area of 920 cm^2/g, the heavy and light dashed curves represent GIMRT predictions for 720 and 1120 cm^2/s, and the light dotted line denotes quartz saturation. In this PFR experiment and GIMRT simulation, T = 239°C, P = 84.1 bar (PFR) and 32.9 bar (GIMRT)—see text, fluid flux = 26 ml/day (277.4 $m^3/m^2/yr$), and porosity = 40%.

Figure 10.4-17. GIMRT sim2c: log(Q/K)(t) at 1 cm (inlet)

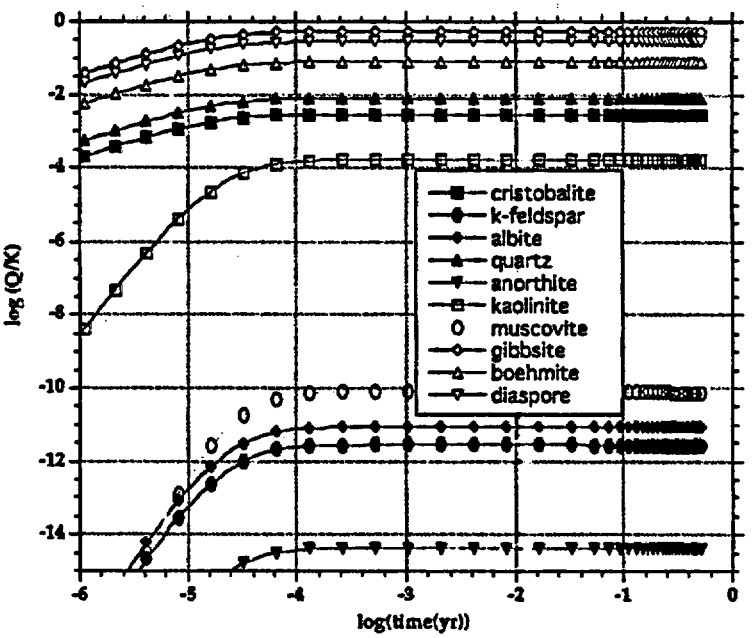

Figure. 10.4-17. Mineral saturation indices (log Q/K) as a function of time (log yr) at the inlet node (1 cm) of GIMRT simulation 2c, where initial composition of the 31-cm one-dinensional fluid-rock system is given in Tables 10.4-5 and 10.4-6, T = 90°C, P = vapor saturation, fluid flux = 25 ml/day (266.7 $m^3/m^2/yr$), and porosity = 40%. Primary and secondary minerals are represented by solid and open symbols, respectively.

Figure 10.4-18. GIMRT sim2c: log (Q/K)(t) at 31 cm (outlet)

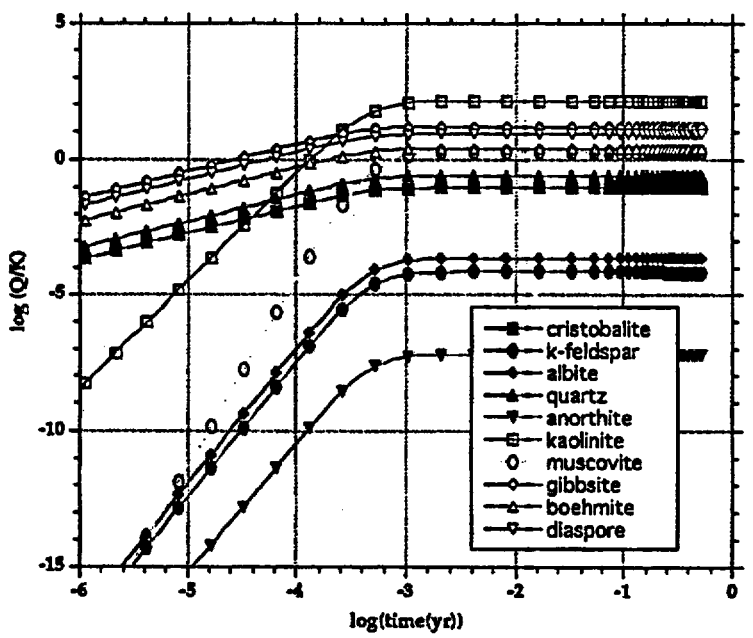

Figure. 10.4-18. Mineral saturation indices (log Q/K) as a function of time (log yr) at the outlet node (31 cm) of GIMRT simulation 2c.

Figure 10.4-19. GIMRT sim2c: log (Q/K)(x) at 6 mo.

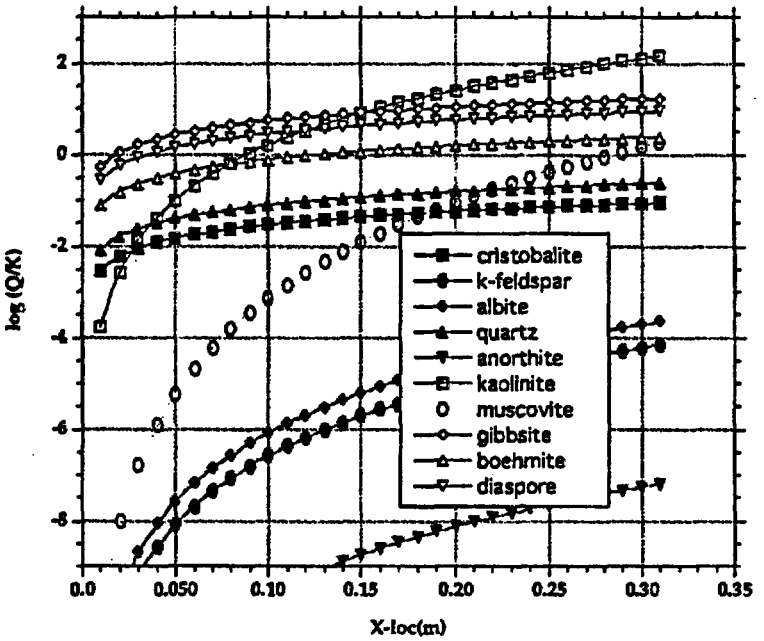

Figure. 10.4-19. Mineral saturation indices (log Q/K) as a function of distance (m) after six months for GIMRT simulation 2c.

Figure 10.4-20. GIMRT sim2c: vol%(x) at 6 mo.

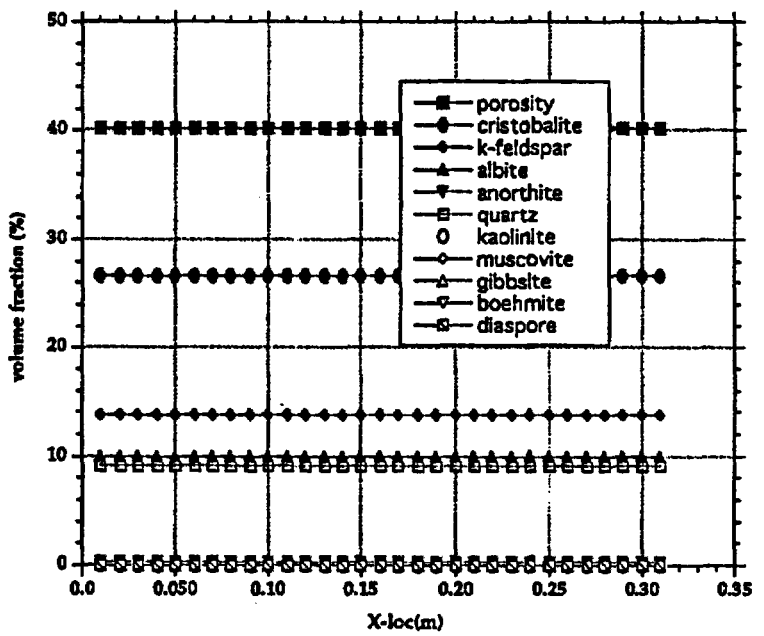

Figure. 10.4-20. Porosity and volume fractions of primary and secondary minerals as a function of distance at six months for GIMRT simulation 2c, where initial composition of the 31-cm one-dinensional fluid-rock system is given in Tables 10.4-5 and 10.4-6, T = 90°C, P = vapor saturation, fluid flux = 25 ml/day (266.7 $m^3/m^2/yr$), and porosity = 40%. Primary and secondary minerals are represented by solid and open symbols, respectively.

Figure 10.4-21. GIMRT sim2c: vol%(sec.min.)(x) at 6 mo.

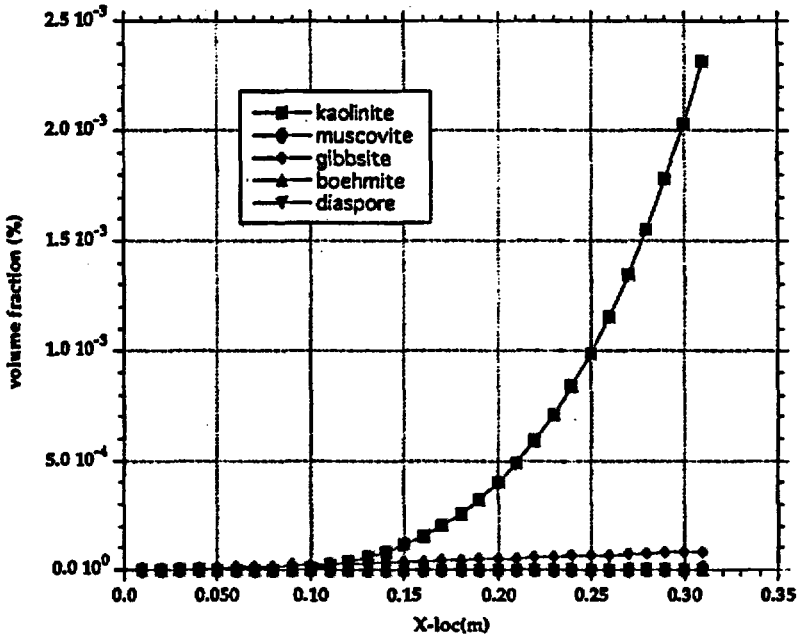

Figure. 10.4-21. Porosity and volume fractions of trace secondary minerals as a function of distance after six months for GIMRT simulation 2c.

Figure 10.4-22. GIMRT sim3a: log(Q/K)(t) at 1 cm (inlet)

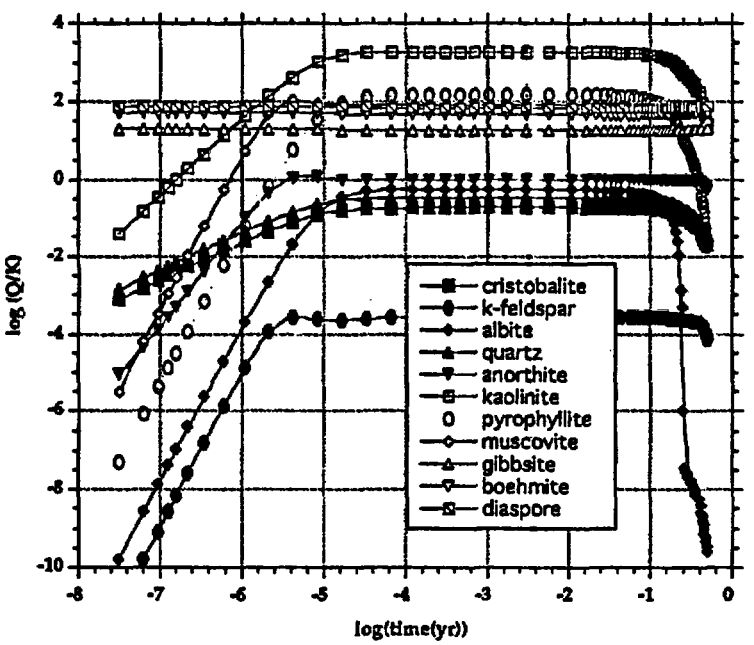

Figure. 10.4-22. Mineral saturation indices (log Q/K) as a function of time (log yr) at the inlet node (1 cm) of GIMRT simulation 3a, where initial composition of the 31-cm one-dinensional fluid-rock system is given in Tables 10.4-5 and 10.4-6, T = 250°C, P = vapor saturation, fluid flux = 25 ml/day (266.7 $m^3/m^2/yr$), and porosity = 40%. Primary and secondary minerals are represented by solid and open symbols, respectively.

Figure 10.4-23. GIMRT sim3a: vol%(t) at 1cm (inlet)

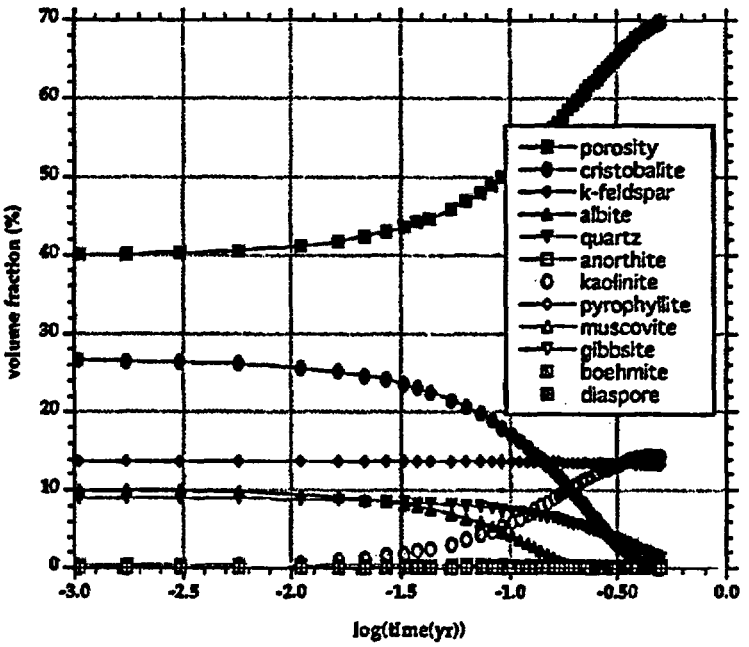

Figure 10.4-23. Porosity and volume fractions of primary and secondary minerals as a function of time (log yr) at the inlet node (1 cm) of GIMRT simulation 3a.

Figure 10.4-24. GIMRT sim3a: log(Q/K)(t) at 31 cm (outlet)

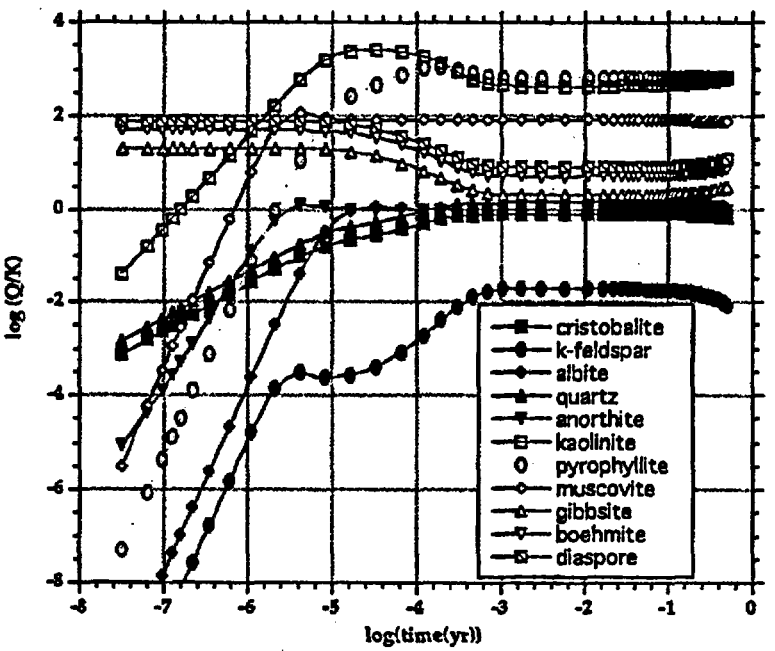

Figure 10.4-24. Mineral saturation indices (log Q/K) as a function of time (log yr) at the oulet node (31 cm) of GIMRT simulation 3a.

Figure 10.4-25. GIMRT sim3a: vol%(t) at 31cm (outlet)

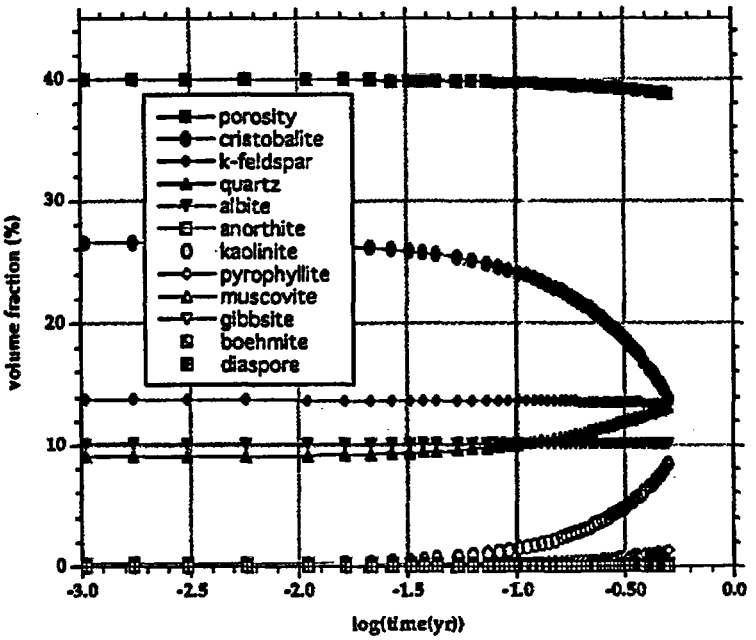

Figure 10.4-25. Porosity and volume fractions of primary and secondary minerals as a function of time (log yr) at the outlet node (31 cm) of GIMRT simulation 3a.

Figure 10.4-26. GIMRT sim3a: log(Q/K)(x) at 6 mo.

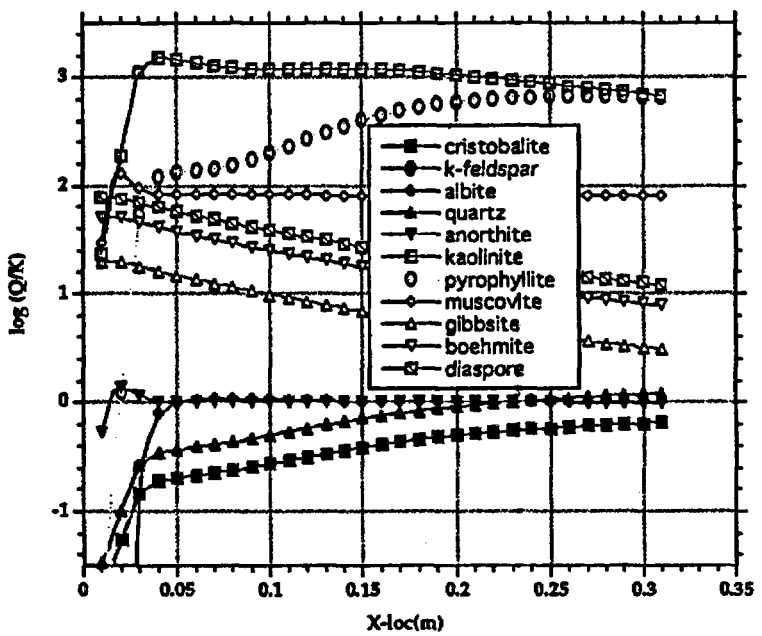

Figure 10.4-26. Mineral saturation indices (log Q/K) as a function of distance after six months for GIMRT simulation 3a.

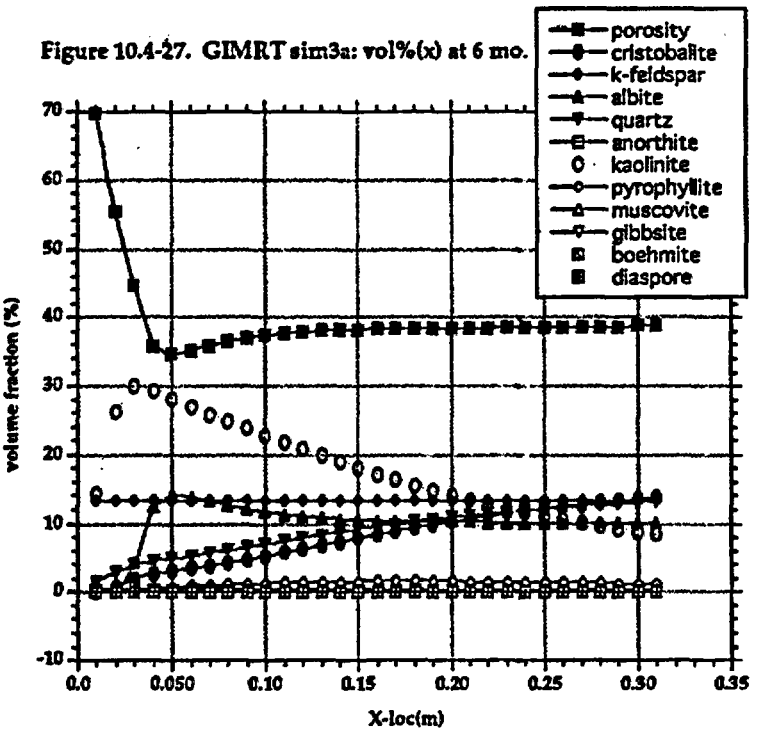

Figure 10.4-27. Porosity and volume fractions of primary and secondary minerals as a function of distance after six months for GIMRT simulation 3a.

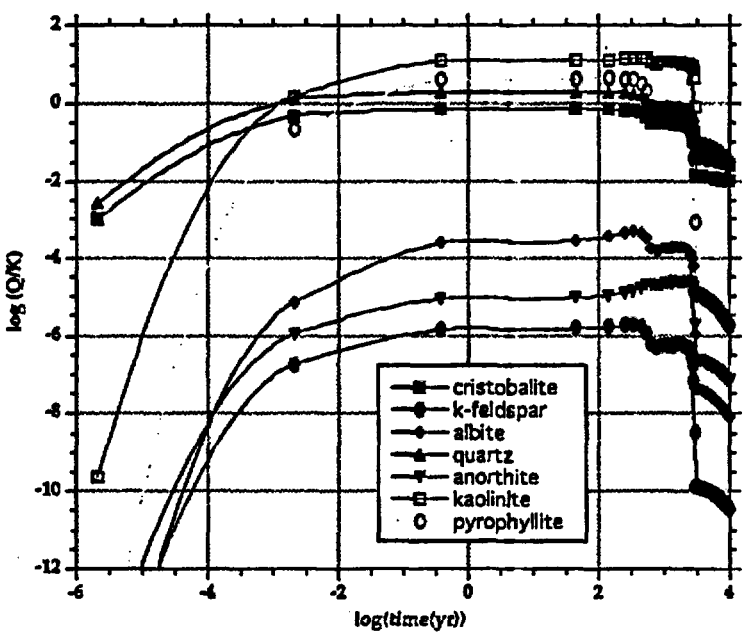

Figure 10.4-28. Mineral saturation indices (log Q/K) as a function of time (log yr) at the inlet node (0.25 m) of GIMRT simulation 6dg2, where initial composition of the 10-m one-dimensional fluid-rock system is given in Tables 10.4-5 and 10.4-6, T = 95oC over the first 5 m with a gradient of -1 °C/m over the last 5 m, P = 1 bar, fluid flux = 2.67 $m^3/m^2/yr$), and porosity = 11%. Primary and secondary minerals are represented by solid and open symbols, respectively.

Figure 10.4-29. GIMRT sim6dg2: log (Q/K)(t) at 5 m (center)

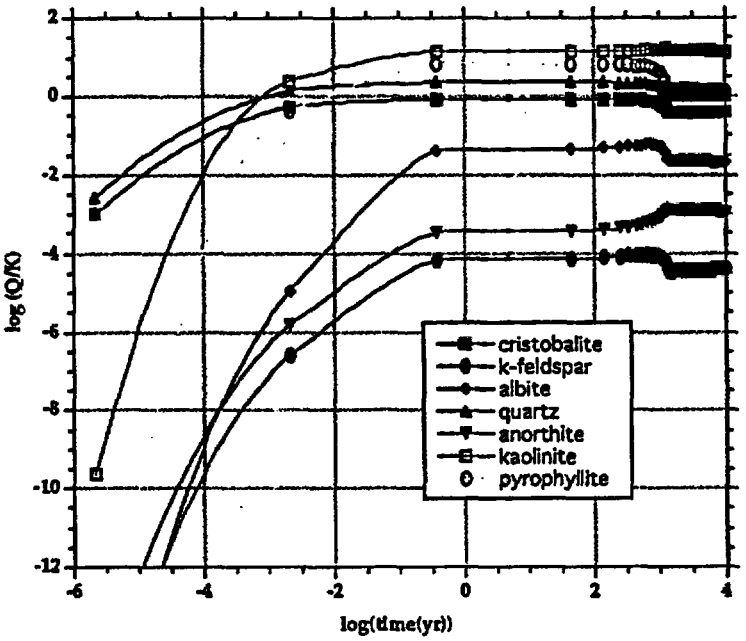

Figure 10.4-29. Mineral saturation indices (log Q/K) as a function of time (log yr) at the center node (5 m) of GIMRT simulation 6dg2.

Figure 10.4-30. GIMRT sim6dg2: log (Q/K) at 10 m (outlet)

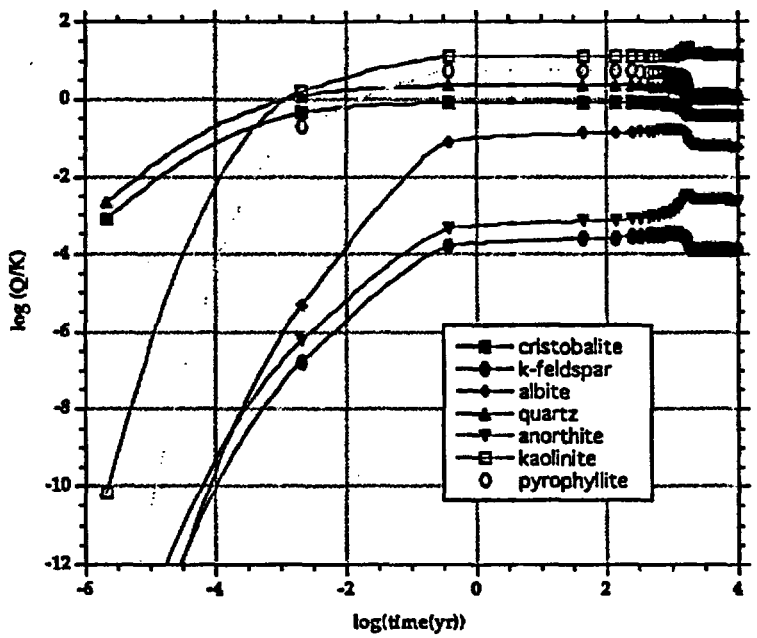

Figure 10.4-30. Mineral saturation indices (log Q/K) as a function of time (log yr) at the outlet node (10 m) of GIMRT simulation 6dg2.

Figure 10.4-31: GIMRT sim6dg2: vol%(t) at 0.25 m (inlet)

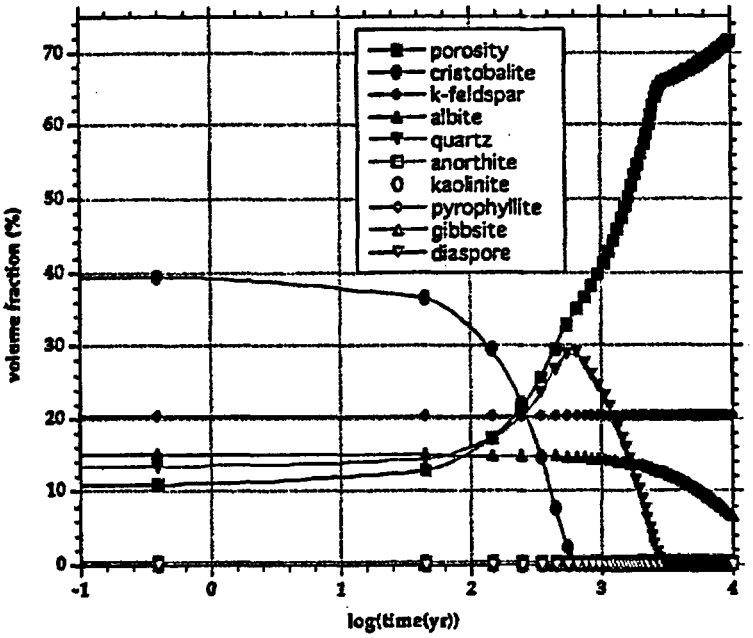

Figure. 10.4-31. Porosity and volume fractions of primary and secondary minerals as a function of time (log yr) at the inlet node (0.25 m) of GIMRT simulation 6dg2.

Figure 10.4-32. GIMRT sim6dg2: vol%(t) at 5 m (center)

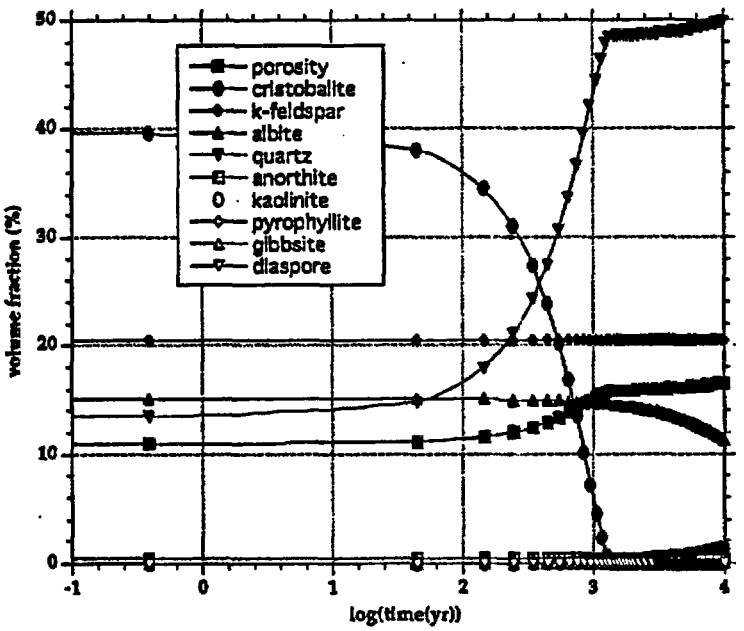

Figure. 10.4-32. Porosity and volume fractions of primary and secondary minerals as a function of time (log yr) at the center node (5 m) of GIMRT simulation 6dg2.

Figure 10.4-33. GIMRT sim6dg2: vol%(t) at 10 m (outlet)

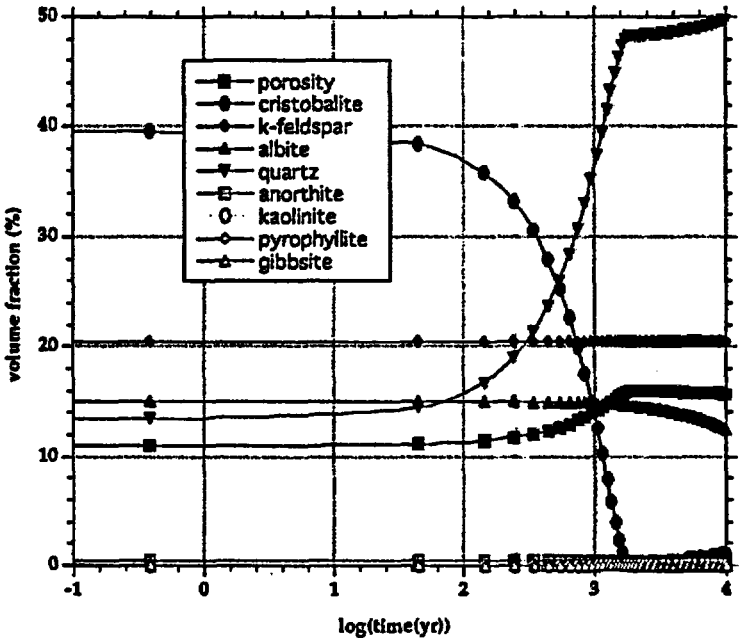

Figure. 10.4-33. Porosity and volume fractions of primary and secondary minerals as a function of time (log yr) at the outlet node (10 m) of GIMRT simulation 6dg2.

Figure 10.4-34. GIMRT sim6dg2: vol%(x) at 100 yr

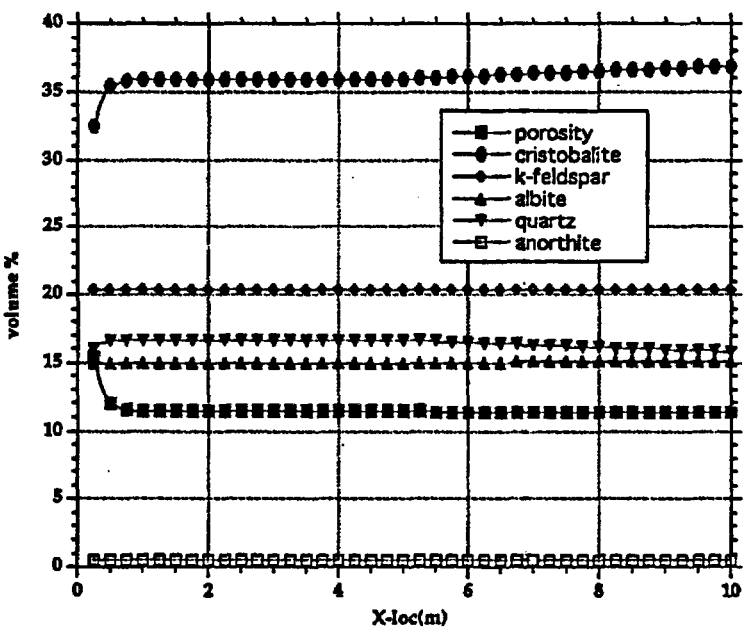

Figure. 10.4-34. Porosity and volume fractions of primary and secondary minerals as a function of distance after 100 yr for GIMRT simulation 6dg2.

Figure 10.4-35: GIMRT sim6dg2: vol%(x) at 1,000 yr

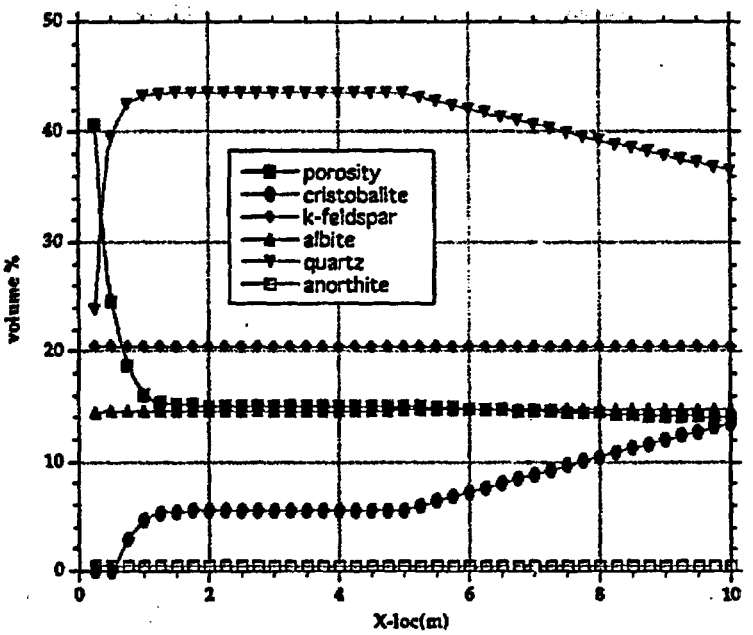

Figure. 10.4-35. Porosity and volume fractions of primary and secondary minerals as a function of distance after 1,000 yr for GIMRT simulation 6dg2.

Figure 10.4-36. GIMRT sim6dg2: vol%(x) at 5,000 yr

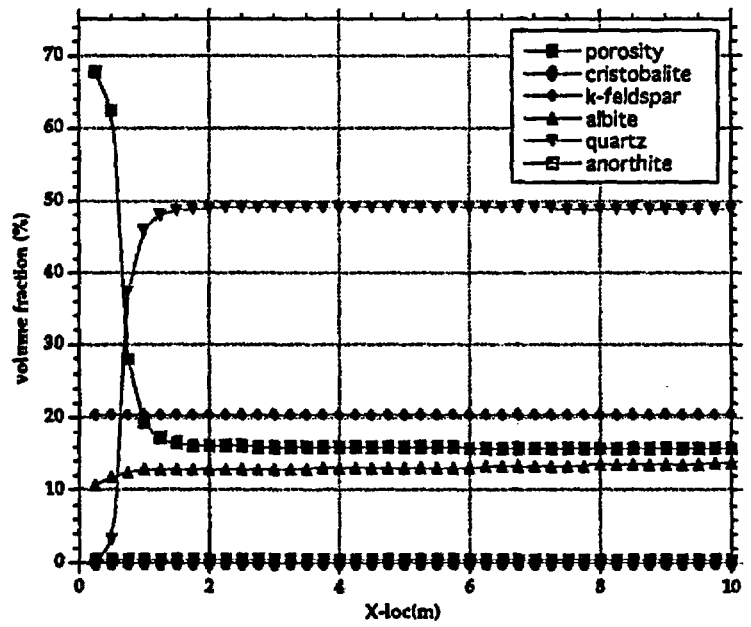

Figure. 10.4-36. Porosity and volume fractions of primary and secondary minerals as a function of distance after 5,000 yr for GIMRT simulation 6dg2.

Figure 10.4-37. GIMRT sim6dg2: vol%(x) at 10,000 yr

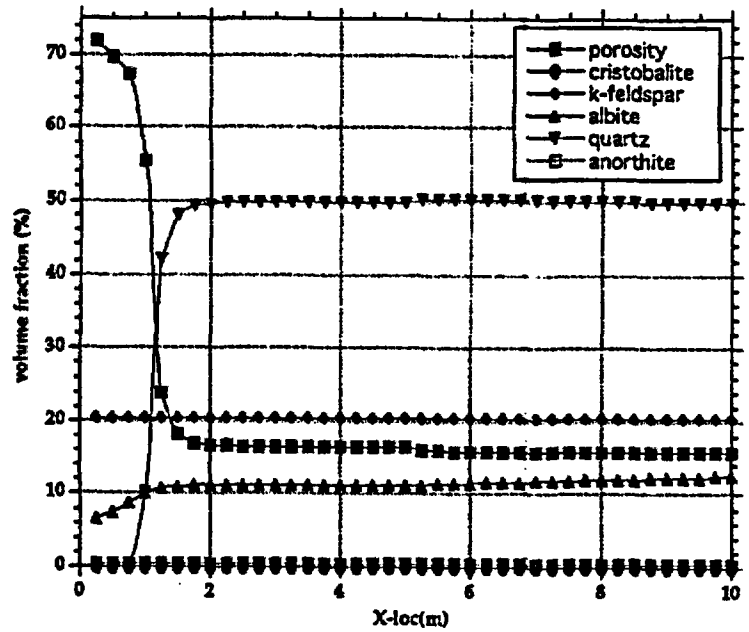

Figure. 10.4-37. Porosity and volume fractions of primary and secondary minerals as a function of distance after 10,000 yr for GIMRT simulation 6dg2.

Table 10.4-1. Chemical composition of geothermal waters from Flash Plant 10, Wairakei, New Zealand.

	Total Concentration
pH(25∞C)	7.8
	ppm
Na	1314
Li	12.8
K	211
Ca	18.3
Mg	0.08
Rb	2.77
Cs	2.59
S	11
B	26.9
Si	234.0
F	7.0
As	4.86
Al	0.6
Fe	0.13
Cl	2043

Table 10.4-2. Laboratory Amorphous Silica Precipitation Results. T_i is the temperature at which the starting materials were saturated with respect to amorphous silica, T_{ppt} is the precipitation run temperature, k_{ppt} is the precipitation rate constant, and SA is BET surface area of the amorphous silica at the end of the experiment.

EXPT	Solution Composition	T_i°C	T_{ppt} °C	pH(T)	k_{ppt}	SA (m^2g^{-1})
AmSi1	0.1 M NaCl (unbuffered)	120	100	6.4	1.77e-6 ± 9e-8	118
AmSi2	0.1 M NaCl + 0.013 M HCl + 0.03 M KHphthalate	120	100	5.0	1.15e-6 ± 7e-8	168
AmSi3	0.1 M NaCl + 0.03 M Na Acetate + 0.02 M Acetic Acid	120	100	3.0	3.23e-7 ± 3e-8	260
AmSi5	0.13 M NaCl (unbuffered)	100	80	6.5	7.68e-7 ± 9e-8	135
AmSi6	0.1 M NaCl + 0.013 M HCl + 0.03 M KHphthalate	100	80	3.0	7.27e-8 ± 3e-8	280
AmSi7	0.1 M NaCl + 0.03 M Na Acetate + 0.02 M Acetic Acid	100	80	4.9	2.89e-7 ± 3e-8	209
AmSi8	0.13 M NaCl (unbuffered)	150	120	7.2	4.61e-6 ± 6e-7	53
AmSi10	Geothermal Water (Table 10.4-1)	100	80	7.3	1.48e-6 ± 2e-7	135
AmSi11	Geothermal Water (Table 10.4-1)	120	100	7.2		
AmSi12	Geothermal Water (Table 10.4-1)	150	120	7.1	8.92e-6 ± 5e-7	66
AmSi13	Geothermal Water (Table 10.4-1)	120	100	7.2	2.99e-6 ± 4e-7	108
AmSi14	0.121 M NaCl + 0.009 M NaOH + 0.05 M Boric Acid	120	100	7.9	2.53e-6 ± 8e-7	107
AmSi15	0.094 M NaCl + 0.036 M NaOH + 0.05 M Boric Acid	120	100	8.7	4.76e-6 ± 1e-8	99

Table 10.4-3. Summary of silica polymorph precipitation experiments.

Phase	T°C	E_a (kJ/mol)	Q/K_{eq}	Solution Composition	Reference
Quartz	18–300	49.8	1.7	distilled water	Rimstidt and Barnes, 1980
a-cristobalite	18–30	49.8	1.7	distilled water	Rimstidt and Barnes, 1980
b-cristobalite	18–30	49.8	1.7	distilled water	Rimstidt and Barnes, 1980
Amorphous Silica	18–30	49.8	1.7	distilled water	Rimstidt and Barnes, 1980
Amorphous Silica	60–120	0	4	pH 5-8 1 N NaCl	Bohlmann et al., 1980
a-cristobalite	150–300	52.9	2		Renders et al., 1995
Amorphous Silica	25–50	54.8	10	pH 4-8 0.1 - 1 m NaCl	Fleming, 1985
Quartz	120–255	34	2		Bird and Boon, 1986
Quartz	300–420	57–164	—	0.5 m NaCl	Laudise, 1958
Quartz	300–500	88–159	—	0.1–1 m NaCl	Hosaka and Taki, 1981a
Quartz	300–500	29.3–33.5	—	0.1–1 m KCl	Hosaka and Taki, 1981b

Table 10.4-4. Amorphous silica precipitation rates determined in the field using a fluidized bed reactor with waters from Wairakei geothermal Flash Plant 10, New Zealand.

Date	T (°C)	v ($L\ d^{-1}$)	Δ *ppm*	pH (T°C)	log (Q/K_{eq})	$Rate_{(ppt)}$ ($mol\ m^{-2} d^{-1}$)
3 July 95	89	786.2	26.6±0.7	7.66	.1787	9.67e-5
4 July 95	88	1814.4	6.2±1.4	7.63	.1784	5.20e-5
5 July 95	74	1226.9	21.1±2.1	7.73	.2408	1.20e-4
10 July 95	58	820.8	39.2±0.7	7.86	.3348	1.49e-4
11 July 95	97	1071.4	9.8±0.7	7.58	.1310	4.85e-5
12 July 95	71	1417.0	21.8±0.7	7.75	.2596	1.43e-4
13 July 95	97	838.1	14.4±0.7	7.58	.1248	5.58e-5
28 Sept 95	79	1166.4	29.5±2.8	7.70	.2093	1.04e-4
28 Sept 95	79	1252.8	30.2±0.0	7.70	.2102	1.14e-4
28 Sept 95	80	1408.3	25.8±0.0	7.69	.2070	1.10e-4
28 Sept 95	78	976.3	37.1±1.4	7.71	.2097	1.09e-4
29 Sept 95	96	2315.5	4.1±0.0	7.58	.1418	3.14e-5
29 Sept 95	84	829.4	25.4±0.0	7.66	.1866	6.96e-5
29 Sept 95	69	717.1	50.4±0.0	7.79	.2417	1.19e-4
2 Oct 95	92	985.0	12.0±1.4	7.61	.1611	3.90e-5
2 Oct 95	75	924.5	43.7±0.7	7.73	.2446	1.33e-4
2 Oct 95	61	829.4	54.7±0.0	7.86	.2731	1.50e-4
3 Oct 95	93	1158.0	10.2±0.7	7.60	.1579	3.90e-4
3 Oct 95	100	1062.7	10.5±1.4	7.61	.1264	3.68e-5
3 Oct 95	83	1028.2	23.7±0.7	7.67	.1981	8.05e-5
4 Oct 95	76	1114.6	32.7±1.4	7.72	.2226	1.20e-4
4 Oct 95	70	1088.6	36.7±0.7	7.77	.2549	1.32e-4
5 Oct 95	61	1140.5	44.4±1.4	7.85	.2951	1.67e-4
5 Oct 95	67	1123.2	37.7±0.7	7.79	.2743	1.40e-4
6 Oct 95	112	846.7	5.3±0.7	7.51	.0654	1.48e-4
6 Oct 95	115	846.7	5.0±0.7	7.50	.0530	1.40e-5
6 Oct 95	104	794.9	7.2±1.4	7.54	.1050	1.89e-5
9 Oct 95	102	1149.1	5.2±1.4	7.55	.1123	1.97e-5
9 Oct 95	117	1088.6	4.6±0.0	7.49	.0445	1.65e-5
9 Oct 95	107	1019.5	6.7±0.7	7.53	.0893	2.26e-5
10 Oct 95	101	1036.8	6.1±1.4	7.6	.1173	2.09e-5
10 Oct 95	106	1036.8	5.0±1.4	7.53	.0962	1.71e-5

Table 10.4-5. Summary of Tpt mineralogy as modeled by Delany (1985) and in this study.

Mineral	Mineral Composition	Vol.% (Delany, 1985: no por.)	Vol.% (this study: no por.)	Vol.% (this study: 11% por.)	Vol.% (this study: 40% por.)
Cristobalite	SiO_2	44.0	44.49	39.60	26.69
Alkali feldspar	$Or_{0.53}Ab_{0.41}An_{0.01}$	39.0	---	---	---
Quartz	SiO_2	14.9	15.07	13.41	9.04
Plagioclase	$Or_{0.07}Ab_{0.76}An_{0.17}$	1.0	---	----	---
Mg-beidellite	$Mg_{0.165}Al_{2.33}Si_{3.67}O_{10}(OH)_2$	1.0	---	---	---
Biotite	$Phl_{0.43}Ann_{0.57}$	0.1	---	---	---
K-feldspar (Or)	$KAlSi_3O_8$	---	22.94	20.42	13.77
Albite (Ab)	$NaAlSi_3O_8$	---	16.94	15.07	10.16
Anorthite (An)	$CaAl_2Si_2O_8$	---	0.57	0.50	0.34
TOTAL		100.0	100.0	89.0	60.0

Table 10.4-6. Summary of infiltrating fluid composition used in this study. Note that in the simulations, Ca^{+2} and HCO_3^- represent the mass and charge balancing species, respectively.

Basis species	Log Activity
H^+	-7
K^+	-10
Na^+	-10
Ca^{+2}	-5
Al^{+3}	-20
$SiO_2(aq)$	-10
HCO_3^-	-5

Contents

Chapter 11.0 Introduction to the Thermodynamic Data Determination

Cynthia Palmer

In the Thermodynamic Data Determination area, actinide and fission product solubility limits are determined, evaluated, and delivered to the database. The solubility limits can be an important control on potential release rates from the waste package under aqueous conditions as they represent the upper limit to non-colloidal solution concentrations measured in leach rate experiments. Chemical thermodynamic data are needed to model the solubility limits and speciation for changes in the groundwater parameters, e.g., temperature, pH, Eh, and chemical composition. Chemical equilibria are affected by changes in temperature, and reaction constants are in general a function of temperature. To predict solubility limits for actinides under a wide variety of temperature and complex groundwater compositions, two types of information are needed:

1. Actual actinide solubility and speciation measurements, both individually and in mixtures, in appropriate groundwaters actual or synthetic, as a function of temperature;
2. Measurements of thermodynamic constants from the formation of solid phases and solution species as a function of temperature (i.e., solubility product and complexation constants). Both are required for reliable modeling of solubility limits. As the model is being assembled its reliability must be assured by comparing results predicted from the database with experimental results. This is an interactive process and requires a close working relationship between the database development task and the data determination task.

11.1 The Database

"The thermodynamic data base is a summary of the available thermodynamic data for aqueous species, solids, and gases in tabular form that are necessary to serve as input to the geochemical modeling codes EQ3NR and EQ6. The data base will be evaluated by testing predictions of

host-rock phases, secondary phases, solution species, and total solution concentrations against the results of laboratory measurements made over a range of identified parameters that include: temperature, ionic strength, redox conditions, and solution composition" (ref. UCID-20864 *Geochemical Modeling (EQ3/6) Plan*, Office of Civilian Radioactive Waste Management Program (8/86)—Section 4.0 "Thermodynamic Data Base").

Recent revisions of the thermodynamic data for several of the aqueous and solid species of U, Am, Np, and Pu have demonstrated the need for an experimental data base activity that would be able to provide data that is currently lacking for solubility limiting solid phases and/or solution species. Measurements will be made as a function of temperature, ionic strength, and oxidation state, as required. The activity, which commenced in mid-FY 1986, has been divided into three sections: sensitivity analysis, development of thermodynamic data, and validation.

Two members of the EQ3/6 data base staff are participants on critical review teams for the International Thermodynamic Data Base, sponsored by the Nuclear Energy Agency (NEA). As a result of this work, the following principles have been accepted for the EQ3/6 data base.

1. Incorporate results of peer reviewed data. This will provide compatibility with CODATA (Committee on Data for Science and Technology) task group recommended key values and with NEA as their data values are released.
2. Implement EQ3/6 data base methodology for new and existing data.
3. Create and maintain a data base library on the computer for all documented sources of thermodynamic data.

A significant review and revising of thermodynamic data for the actinides was performed. A Nuclear Energy Agency (NEA) document, *Chemical Thermodynamics of Americium* (NEA, 1995) was reviewed and data is ready to be entered into the GEMBOCHS data base.

11.2 U.S. Contribution to the NEA Organization for Economic Co-operation and Development (OECD) Critical Reviews of the Chemical Thermodynamics of the Actinides and Fission Products

In 1984, the NEA/OECD initiated the writing and publication of a series of critical reviews of the chemical thermodynamics of those elements that are of

particular importance in the safety assessment of radioactive waste disposal systems. The U.S., through the Yucca Mountain Site Characterization Project, has participated in this international project.

11.2.1 Lawrence Livermore National Laboratory's Role

Lawrence Livermore National Laboratory (LLNL), through the Yucca Mountain Site Characterization Project (YMP), has been responsible for coordinating the United States' role in the NEA's Critical Reviews of the Chemical Thermodynamics of the Actinides and Fission Products. FY 1995 was the last year the U.S. participated in the Reviews through the Yucca Mountain Project.

The YMP Activity under which these reviews were completed is graded "Quality Affecting." All Procurements reflected this grading and included appropriate Quality Assurance training to comply with the grading. The coordinator represented the U.S. participants during Quality Assurance Audits.

11.2.2 Procedure

The process of reviewing experimentally obtained data that has been published in the open literature is described in a series of publications that address:

- Guidelines for the Review Procedure and Data Selection
- Guidelines for the Extrapolation to Zero Ionic Strength
- Guidelines for the Assignment of Uncertainties
- Guideline for Temperature Corrections (Draft)
- Standards and Conventions for TDB Publications
- Guidelines for the Independent Peer Review of TDB Reports

To serve as the reviewers, the NEA assembled teams of internationally recognized chemists with backgrounds in actinide and physical chemistry. These panel members evaluated the reported experiments, considered the results, and decided whether each data set warranted inclusion in the final volume. As needed, reports were rejected from further consideration and reported data reinterpreted using different sets of species. Written comments describing the analysis of each literature report are included in the review. A second panel of reviewers was convened to verify that the initial panel's decisions were sound and consistent and to confirm that the published

procedures were followed. This second review process was added at the United States' request to address the NUREG 1297, 1298 which describes the NRC process for qualification of existing data.

11.2.3 Auxiliary Data

The interpretation of chemical thermodynamic data for the actinides and fission products require the use of auxiliary data, for example, acid dissociation constants. These data, themselves, must be internally consistent. It is, therefore, necessary to always use the identified auxiliary data in conjunction with the selected NEA values. The NEA project selected the database available from the Committee on Data for Science and Technology (CODATA) as their principle source of auxiliary data. The qualification of the actinide and fission product data from the NEA requires (and implies) the qualification of the CODATA database. Data not available from CODATA were evaluated as part of the uranium review and made available to the other review teams.

11.3 Qualification of Data for Using in Quality Affecting Calculations

Publications describing the process for qualifying existing data are listed below:

- OCRWM *QAP* 2.5, "Peer Review"
- Letter addressed to Susan Jones, Assistant Manager for Scientific Programs, YMSCO, NV (ID: LLYMP9503063), describing the process that the Solubility Working Group will use to qualify radionuclide thermochemical data.
- *YAP* 2.1Q, "Technical Assessment"
- *YAP* SIII.1Q, "Qualification of Existing Data"
- *YMP* AP-5.9Q, "Qualification of Data"

11.4 Review of Thermodynamic Data

11.4.1 Chemical Thermodynamics of Uranium

In 1992, the NEA published the volume, *Chemical Thermodynamics of Uranium* (NEA, 1992), which includes the U.S. contributions. Individual contributions are not separable.

- As the only U.S. scientist to participate in the technical review of the Uranium data, Anthony Muller initiated the *Uranium* volume work during his assignment at the NEA. Muller left the NEA in 1986 and is currently affiliated with SAIC in McLean, VA. There are no records that any of his efforts were supported by the YMP.
- Donald Langmuir participated in an early meeting of the Uranium team and was unable to continue his participation due to lack of funding.
- U.S. scientists, R.E. Mesmer, D.A. Palmer, and C.F. Baes, Jr., all from Oak Ridge National Laboratory, were acknowledged by the technical reviewers in the *Uranium* volume.

The U.S., through the YMP, supplied three independent experts to the second review panel. They were as follows:

- Dr. C.F. Baes, Jr., Oak Ridge National Laboratory, Oak Ridge, TN
- Dr. D.L. Hildenbrand, SRI International, Menlo Park, CA
- Dr. F. J. Pearson, Jr., Ground-Water Geochemistry, Irving, TX

Other U.S. scientists were thanked for their technical comments and suggestions: M.W. Chase, National Institute of Standards and Technology, Gaithersburg, MD; K. Czyscinski, Roy Weston Inc., Washington, D.C.; D. Garvin, National Institute of Standards and Technology, Gaithersburg, MD; L. Maya, Oak Ridge National Laboratory, Oak Ridge, TN; L.R. Morss, Argonne National Laboratory, Argonne, IL; T.W. Newton, Los Alamos National Laboratory, Los Alamos, NM; D.K. Nordstrom, U.S. Geological Survey, Menlo Park, CA; V.B. Parker, National Institute of Standards and Technology, Gaithersburg, MD; S.L. Phillips, Lawrence Berkeley Laboratory, Berkeley, CA; J.A. Rard, Lawrence Livermore National Laboratory, Livermore, CA; W.J. Ullman, University of Delaware, Lewes, DE; and E.F. Westrum, Jr., University of Michigan, Ann Arbor, MI.

11.4.1.1 Corrections to the Uranium NEA–TDB review. In Appendix D of the *Americium* volume (NEA, 1995), there are corrections and additions to the *Uranium* volume. These data have not be submitted for independent peer review and, therefore, are not considered qualified by YMP.

11.4.2 Chemical Thermodynamics of Americium

In 1995, the NEA published the volume, *Chemical Thermodynamics of Americium*, which includes the U.S. contributions. Individual contributions are not separable.

Following discussions in 1986 with Dr. Robert Silva (USA), Hans Wanner initiated the *Americium* volume work during his assignment at the NEA. The review committee was selected and met at the NEA Data Bank, Saclay, France in the fall of 1987.

The U.S., through the YMP, supplied all three independent experts to the second review panel, listed as follows:

- Dr. C.F. Baes, Jr., Oak Ridge National Laboratory, Oak Ridge, TN
- Dr. Lester Morss, Argonne National Laboratory, Argonne, IL
- Dr. Arthur Martell, Texas A&M University, College Station, TX

Dr. Edward Patera (currently of Los Alamos National Laboratory, Los Alamos, NM) was on assignment to the NEA Division for Radiation Protection and Waste Management during the compilation of the *Americium* volume.

11.4.3 Chemical Thermodynamics of Technetium

A volume covering the Thermodynamics of Technetium was part of the initial NEA Review project design in 1984. When complete, this volume will contain a comprehensive review of material related to the inorganic compounds of technetium and their aqueous solutions. While there is extensive literature covering the organometallic chemistry of technetium, only a small portion of these complexes are of interest to the radioactive waste management community. Consequently, the review committee will limit their coverage of the organometallic chemistry to those systems containing thermodynamic or kinetic data. Technetium containing compounds of radiopharmaceutical interest will be covered in the review volume.

YMP funding for this volume has not been continuous during the project. There is no FY 1996 funding supporting the completion of the final draft. As a result, YMP can neither gain access to the information that will be contained therein, nor influence the priorities of the work of the review committee members. Since this work is not completed, it can not be discussed in this revision of the NFER but will be included in the future.

A working draft of the volume, *Chemistry and Thermodynamics of Technetium*, was published in 1992, and a final draft is expected this calendar year. Internal LLNL contributions provide some idea of the material to be included, summarized as follows:

1. Chemical Thermodynamics of Technetium I—Contributions to the NEA volume on Technetium Thermodynamics: hydrides, polynuclear halides, oxohalides, hydroxohalide salts, oxohalide salts, chalcogenides and calcogen complexes, oxosulphur complexes, nitrogen compounds, nitrogen complexes, phosphorus compounds, other pnictide compounds and complexes (As, Sb, and Bi), pseudo-halide and oxopseudo-halide complexes, nitrosyl complexes, and tin complexes (Rard, 1989).
2. Chemical Thermodynamics of Technetium II—Contributions to the NEA volume on Technetium Thermodynamics: mononuclear halides (binary and ternary), phosphorus complexes, silicon complexes, and update of Chemical Thermodynamics of Technetium I (Rard, 1989).
3. Chemical Thermodynamics of Technetium III—Contributions to the NEA volume on Technetium Thermodynamics: hydroxide compounds and complexes containing other ligands, inorganic carbon complexes, and update of Chemical Thermodynamics of Technetium II (Rard, 1990).
4. Chemical Thermodynamics of Technetium IV - Contributions to the NEA Book on Technetium Thermodynamics: anhydrous binary oxides, hydrated oxides and hydrous oxides, $Tc_2O_7 \cdot H_2O$, pertechnetate and oxypertechnetate salts, aqueous halide complexes, aqueous TcO4-, and aqueous ions of Tc(VI) through Tc(III) (Rard, 1991).
5. Chemical Thermodynamics of Technetium V - Contributions to the NEA Book on Technetium Thermodynamics: anhydrous binary oxides, hydrous oxides, $Tc_2O_7 \cdot H_2O$, pertechnetate salts, undissociated $HTcO_4$, and comments on Tc(III) and Tc(II) (Rard, 1992).

6. Chemical Thermodynamics of Technetium VI - Contributions to the NEA Book on Technetium Thermodynamics: TcO_2(cr), ternary technetium sulphides and selenides, new oxyhalides, additional calculations for TcF_6(g), and updating of previous contributions (Rard, 1995, unpublished).

11.4.4 Chemical Thermodynamics of Plutonium and Neptunium

Volumes covering the thermodynamics of Plutonium and Neptunium were part of the initial NEA Review project design in 1984. When this volume is complete it will contain a comprehensive review of material related to the inorganic compounds of neptunium and plutonium and their aqueous solutions.

YMP funding for this volume has not been continuous during the project. There is no FY 1996 funding supporting the completion of the final draft. As a result, YMP can neither gain access to the information that will be contained therein, nor influence the priorities of the work of the review committee members. Since this work is not completed, it can not be discussed in this revision of the NFER but will be included in the future.

11.5 References

Geochemical Modeling (EQ3/6) *Plan*, Office of Civilian Radioactive Waste Management Program (8/86)—Section 4.0 "Thermodynamic Data Base," Lawrence Livermore National Laboratory, Livermore, CA, UCID-20864,

Nuclear Energy Agency (NEA, 1995), *Chemical Thermodynamics 2: Chemical Thermodynamics of Americium*, Nuclear Energy Agency, Organization for Economic Co-Operation and Development, Elsevier, 1995.

Nuclear Energy Agency (NEA, 1992), *Chemical Thermodynamics 1: Chemical Thermodynamics of Uranium*, Nuclear Energy Agency, Organization for Economic Co-Operation and Development, North-Holland, 1992.

Rard, J. A. (1989), *Chemical Thermodynamics of Technetium I*, Lawrence Livermore National Laboratory, Livermore, CA, UCRL-JC-100554.

Rard, J. A. (1989), *Chemical Thermodynamics of Technetium II*, Lawrence Livermore National Laboratory, Livermore, CA, UCRL-JC-102708.

Rard, J. A. (1990), *Chemical Thermodynamics of Technetium III*, Lawrence Livermore National Laboratory, Livermore, CA, UCRL-JC-103728.

Rard, J. A. (1991), *Chemical Thermodynamics of Technetium IV*, Lawrence Livermore National Laboratory, Livermore, CA, UCRL-JC-108178.

Rard, J. A. (1992), *Chemical Thermodynamics of Technetium V*, Lawrence Livermore National Laboratory, Livermore, CA, UCRL-JC-109638.

Rard, J. A. (1995), *Chemical Thermodynamics of Technetium VI*, Lawrence Livermore National Laboratory, Livermore, CA, (to be published at a later date).

Appendix A

References (copied from the PNFER document)

Aagaard, P., and H. C. Helgeson (1983), "Activity/Composition Relations among Silicates and Aqueous Solutions: II. Chemical and Thermodynamic Consequences of Ideal Mixing of Atoms on Homological Sites in Montmorillonites, Illites, and Mixed-Layer Clays," *Clays and Clay Miner.* 31, 207–217.

Ames, L. L., Jr. (1964a), "Some Zeolite Equilibria with Alkali Metal Cations," *Am. Miner.* 49, 127–145.

Ames, L. L., Jr. (1964b), "Some Zeolite Equilibria with Alkaline Earth Metal Cations," *Am. Miner.* 49, 1099–1110.

Anderson, L. A. (1984), *Rock Property Measurements on Large-Volume Core Samples From Yucca Mountain USW GU-3/G-3 and USW G-4 Boreholes, Nevada Test Site, Nevada*, U.S. Geological Survey, Denver, CO, OFR-84-552.

Anderson, L. A., and G. R. Johnson (1976), "Application of the Self-Potential Method to Geothermal Exploration in Long Valley, California," *Journal of Geophysical Research* 81, 1527–1532.

Andersson, K., B. Allard, M. Bengtsson, and B. Magnusson (1989), "Chemical Composition of Cement Pore Solutions," *Cem. Concr. Res.* 19, 327–332.

Arulmoli, K., and C. M. St. John (1987), *Analysis of Horizontal Waste Emplacement Boreholes of a Nuclear Waste Repository in Tuff*, Sandia National Laboratories, Albuquerque, NM, SAND86-7133.

Atkinson, B. K., and P. G. Meredith (1987), "The Theory of Subcritical Crack Growth with Applications to Minerals and Rocks," *Fracture Mechanics of Rocks*, B. K. Atkinson, Ed. (Academic Press, London).

Babushkin, V. I., G. M. Matveyev, and O. P. Mchedlov-Petrossyan (1985), *Thermodynamics of Silicates* (Springer-Verlag).

Barnes, I., T. S. Presser, M. Saines, P. Dickson, and A. F. K. van Groos (1982), "Geochemistry of Highly Basic Calcium Hydroxide Groundwater in Jordan," *Chem. Geol.* 35, 147–154.

Barnes, M. W., and D. M. Roy (1983), "The Buffering Mechanisms in Leaching of Composites of Cement with Radioactive Waste," *Mat. Res. Soc. Symp. Proc.* 15, 159–166.

Barrenblatt, G. I., Y. P. Zheltov, and I. N. Kochina (1960), "Basic Concepts in the Theory of Seepage of Homogeneous Liquids in Fissured Rocks," *PMM* 24(5), 852–864.

Barrer, R. M., R. Papadopoulos, and L. V. C. Rees (1967), "Exchange of Sodium in Clinoptilolite by Organic Cations," *J. Inorg. Nucl. Chem.* 29, 2047–2063.

Barrer, R. M. (1978a), "Cation-Exchange Equilibria in Zeolites and Feldspathoids," *Natural Zeolites*, L. B. Sand and F. A. Mumpton, Eds. (Pergamon Press), pp. 385–396.

Barrer, R. M. (1978b), *Zeolites and Clay Minerals as Sorbents and Molecular Sieves* (Academic Press, New York).

Barret, P., and D. Bertrandie (1986), "Fundamental Hydration Kinetic Features of the Major Cement Constituents: Ca_3SiO_5 and β-Ca_2SiO_4," *J. Chemie Phys.* 83, 765–775.

Bates, J. K., W. L. Ebert, D. F. Fischer, and T. J. Gerding (1988), "The Reaction of Reference Commercial Nuclear Waste Glasses During Gamma Irradiation in a Saturated Tuff Environment," *J. Mater. Res.* 3(3), 576–597.

Bauer, S. J., and J. F. Holland (1987), "Analysis of In Situ Stress at Yucca Mountain," *Proc. of the 28th U.S. Symp. on Rock Mechanics*, I. Farmer, Ed. (A. A. Balkema, Rotterdam, The Netherlands), pp. 707–713.

Bauer, S. J., and L. S. Costin (1990), *Thermal and Mechanical Codes First Benchmark Exercise Part II: Elastic Analysis*, Sandia National Laboratories, Albuquerque, NM, SAND89-0757.

Bauer, S. J., J. F. Holland, and D. K. Parrish (1985), "Implications About In Situ Stress at Yucca Mountain," *Proc. of the 26th U.S. Symp. on Rock Mechanics*, E. Ashworth, Ed. (A. A. Balkema, Rotterdam, The Netherlands), pp. 1113–1120.

Baulch, D. L., R. A. Cox, R. F. Hampson, Jr., J. A. Kerr, J. Troe, and R. T. Watson (1980), "Evaluated Kinetic and Photochemical Data for Atmospheric Chemistry," *J. Phys. Chem. Ref. Data* 9, 295.

Baulch, D. L., R. A. Cox, R. F. Hampson, Jr., J. A. Kerr, J. Troe, and R. T. Watson (1982), "Evaluated Kinetic and Photochemical Data for Atmospheric Chemistry," *J. Phys. Chem. Ref. Data* 11, 327.

Benson, L. V. and P. W. McKinley (1985), *Chemical Composition of Ground Water in the Yucca Mountain Area, Nevada, 1971–84*, U.S. Geological Survey, Denver, CO, OFR-85-484.

Benson, L. V., J. H. Robison, R. K. Blankennagel, and A. E. Ogard (1983), *Chemical Composition of Ground Water and the Locations of Permeable Zones in the Yucca Mountain Area, Nevada*, U.S. Geological Survey, Denver, CO, OFR-83-854.

Bensted, J. (1983a), "Early Hydration of Portland Cement—Effects of Water/Cement Ratio," *Cem. Concr. Res.* 13, 493–498.

Bensted, J. (1983b), "Hydration of Portland Cement," S. N. Ghosh, Ed., pp. 307–347.

Bensted, J. (1989), "Oil Well Cements—A General Review," *Chem. Ind.*, 20 February 1989, pp. 100–105.

Berner, U. R. (1987), "Modelling Porewater Chemistry in Hydrated Portland Cement," *Mat. Res. Soc. Symp. Proc.* 84, 319–330.

Bish, D. L. (1988), "Effects of Composition on the Dehydration Behavior of Clinoptilolite and Heulandite," *Occurrence, Properties and Utilization of Natural Zeolites*, D. Kallo and H. S. Sherry, Eds. (Akademiai Kiado Pub., Budapest).

Bish, D. L. (1989), *Evaluation of Past and Future Alterations in Tuff at Yucca Mountain, Nevada, Based on the Clay Mineralogy of Drill Cores USW G-1, G-2, and G-3*, Los Alamos National Laboratory, Los Alamos, NM, LA-10667-MS.

Bish, D. L., A. E. Ogard, D. T. Vaniman, and L. Benson (1984), "Mineralogy, Petrology and Groundwater Chemistry at Yucca Mountain Tuffs," *Mat. Res. Soc. Symp. Proc.* (Elsevier, New York), vol. 26, pp. 283–291.

Bish, D. L., and S. J. Chipera (1986), *Mineralogy of Drill Holes J-13, UE-25A#1, and USW G-1 at Yucca Mountain, Nevada*, Los Alamos National Laboratory, Los Alamos, NM, LA-10764-MS.

Bish, D. L., and S. J. Chipera (1989), *Revised Mineralogic Summary of Yucca Mountain, Nevada,* Los Alamos National Laboratory, Los Alamos, NM, Report LA-11497.

Bish, D. L., D. T. Vaniman, F. M. Byers, Jr., and D. E. Broxton (1982), *Summary of the Mineralogy-Petrology of Tuffs of Yucca Mountain and the Secondary Phase Thermal Stability in Tuffs,* Los Alamos National Laboratory, Los Alamos, NM, LA-9321-MS.

Bish, D. L., F. A. Caporuscio, J. F. Copp, B. M. Crowe, J. D. Purson, J. R. Smyth, and R. G. Warren (1981), Los Alamos National Laboratory, Los Alamos, NM, LA-8840-MS.

Blum, A. E., R. A. Yund, and A. C. Lasaga (1990), "The Effect of Dislocation Density on the Dissolution Rate of Quartz," *Geochim. Cosmochim. Acta* 54, 283–297.

Blum, A. E., R. A. Yund, and A. C. Lasaga (1988), "The Effect of Dislocation Density on the Aqueous Dissolution Rate of Quartz," *Geol. Soc. Amer. Abstracts with Programs,* A41.

Bourcier, W. L., D. W. Peifer, K. G. Knauss, K. D. McKeegan, and D. K. Smith (1990), "A Kinetic Model for Borosilicate Glass Dissolution Based on the Dissolution Affinity of a Surface Alteration Layer," *Mat. Res. Soc. Symp. Proc.,* vol. 176, pp. 209–216.

Braester, C. (1986), "One-phase and Multiphase Flow through Fractured Rock Formations," *Fragmentation, Form, and Flow in Fractured Media,* R. Engleman and Z. Jaeger, Eds. (Adam Hilger, Bristol, UK), pp. 325–340.

Breck, D. W. (1974), *Zeolite Molecular Sieves* (J. Wiley and Sons, New York).

Brouwer, E., B. Baeyens, A. Maes, and A. Cremers (1983), "Cesium and Rubidium Ion Equilibria in Illite Clay," *J. Phys. Chem.* 87, 1213–1219.

Brown, P. W., E. Franz, G. Frohnsdorff, and H. F. W. Taylor (1984), "Analyses of the Aqueous Phase during Early C_3S Hydration," *Cem. Concr. Res.* 14, 257–262.

Brown, P. W., J. Pommersheim, and G. Frohnsdorff (1985), "A Kinetic Model for the Hydration of Tricalcium Silicate," *Cem. Concr. Res.* 15, 35–41.

Broxton, D. E. (1987), "Clinoptilolite Compositions in Diagenetically-Altered Tuffs at a Potential Nuclear Waste Repository, Yucca Mountain, Nevada," *The Technology of High-Level Nuclear Waste Disposal,* P. L. Hofmann, Ed., vol. 3, pp. 179–194.

Broxton, D. E., D. L. Bish, and R. G. Warren (1987), "Distribution and Chemistry of Diagenetic Minerals at Yucca Mountain, Nye County, Nevada," *Clays and Clay Miner.* 35, 89–110.

Broxton, D. E., R. G. Warren, R. C. Hagan, and G. Luedemann (1986), *Chemistry of Diagenetically-Altered Tuffs at a Potential Nuclear Waste Repository, Yucca Mountain, Nye County, Nevada,* Los Alamos National Laboratory, Los Alamos, NM, LA-10802.

Broxton, D., D. Vaniman, F. Caporuscio, B. Arney, and G. Heiken (1982), *Detailed Patrographic Descriptions and Microprobe Data for Drill Holes USW-G2 and UE25b-1H, Yucca Mountain, Nevada,* Los Alamos National Laboratory, Los Alamos, NM, LA-9324-MS.

Burch, T. E., K. L. Nagy, and A. C. Lasaga (1990), "Precipitation Kinetics of Albite and Kaolinite at ph 8 to 9 and 80°C, *Geol. Soc. Amer. Abstracts with Programs* 22, A292.

Burnett, N. C., R. D. Hooton, R. B. Heimann, and M. Onofrei (1985), "The Development of Durable Cementitious Materials for Use in a Nuclear Fuel Waste Disposal Facility," *Mat. Res. Soc. Symp. Proc.* 50, 461–468.

Buscheck, T. A., and J. J. Nitao (1988), *Estimates of the Width of the Wetting Zone Along a Fracture Subjected to an Episodic Infiltration Event in Variably Saturated, Densely Welded Tuff*, Lawrence Livermore National Laboratory, Livermore, CA, UCID-21579.

Buscheck, T. A., and J. J. Nitao (1991a), *Nonequilibrium Fracture-Matrix Flow During Episodic Infiltration Events in Yucca Mountain*, Lawrence Livermore National Laboratory, Livermore, CA, UCRL-ID-108311.

Buscheck, T. A., and J. J. Nitao (1991b), *Modeling Hydrothermal Flow in Variably Saturated, Fractured, Welded Tuff During the Prototype Engineered Barrier System Field Test of the Yucca Mountain Project*, Lawrence Livermore National Laboratory, Livermore, CA, UCRL-ID-106521.

Buscheck, T. A., J. J. Nitao, and D. A. Chesnut (1991a), *The Impact of Hydrology on the Engineered Barrier System of the Potential Yucca Mountain Repository Site*, Lawrence Livermore National Laboratory, Livermore, CA, UCRL-ID-107910.

Buscheck, T. A., J. J. Nitao, and D. A. Chesnut (1991b), "The Impact of Episodic Nonequilibrium Fracture-Matrix Flow on Geological Repository Performance," *Proc. of the ANS Topical Mtg. on Nuclear Waste Packaging, Focus '91*, Las Vegas, NV, Sept. 30–Oct. 2, 1991; Lawrence Livermore National Laboratory, Livermore, CA, UCRL-JC-106759.

Carlos, B. (1985), *Minerals in Fractures of the Unsaturated Zone from Drill Core USW-G4, Yucca Mountain, Nye County, Nevada*, Los Alamos National Laboratory, Los Alamos, NM, LA-10415-MS.

Carlos, B. (1989), *Fracture-Coating Minerals in the Topopah Spring Member and Upper Tuff of Calico Hills from Drill Hole J-13*, Los Alamos National Laboratory, Los Alamos, NM, LA-11504-MS.

Chipera, S. J., and D. L. Bish (1989), *Quantitative X-ray Diffraction Analyses of Samples Used for Sorption Studies by the Isotope and Nuclear Chemistry Division*, Los Alamos National Laboratory, Los Alamos, NM, LA-11669-MS.

Christiansen, R. L., P. W. Lipman, W. J. Carr, F. M. Byers, Jr., P. P. Orkild, and K. A. Sargent (1977), "Timber Mountain–Oasis Valley Caldera Complex of Southern Nevada," *Bull. Geol. Soc. Am.* 88, 2573–2593.

Christianson, M. C., and B. Brady (1989), *Analysis of Alternative Waste Isolation Concepts*, U.S. Nuclear Regulatory Commission, Washington, DC, NRC-FIN D1016, NUREG/CR-5389.

Cohen, L. H., and W. Klement, Jr. (1975), "Differential Thermal Analysis Investigation of the High-Low Cristobalite Inversion under Hydrostatic Pressure to 7 kbar," *Jour. Am. Cerm. Soc.* 58(5-6), 206–208.

Cooper, H. W., and G. Simmons (1977), "The Effects of Cracks on Thermal Expansion of Rocks," *Earth and Planetary Science Letters* 36, 404.

Corwin, R. F., and D. B. Hoover (1979), "The Self-Potential Method in Geothermal Exploration," *Geophysics* 44, 226–245.

Daily, W., A. Ramirez, T. Ueng, and V. LaTorre (1989), "High Frequency Electromagnetic Tomography," *Proc. of the ANS Topical Mtg. on Nuclear Waste Isolation in an Unsaturated Zone, Focus '89* (Amer. Nuc. Soc., La Grange Park, IL), pp. 409–416. (NNA.910326.0098)

Daily, W., and W. Lin (1991), *Laboratory Determined Suction Potential of Topopah Spring Tuff*, Lawrence Livermore National Laboratory, Livermore, CA, UCRL-102127.

Daily, W., W. Lin, and T. Buscheck (1987), "Hydrological Properties of Topopah Spring Tuff—Laboratory Measurements," *J. Geophys. Res.* 92(B8), 7854–7864.

Delany, J. M. (1985), *Reaction of Topopah Spring Tuff with J-13 Water: A Geochemical Modeling Approach Using the EQ3/6 Reaction Path Code*, Lawrence Livermore National Laboratory, Livermore, CA, UCRL-53631.

Delany, J. M., and S. R. Lundeen (1991), *The LLNL Thermochemical Data Base: Revised Data and File Format for the EQ3/6 Package*, Lawrence Livermore National Laboratory, Livermore, CA, UCID-21658.

Dixon, R. S. (1970), "Dissociation of Water Vapor by Photolytic, Radiolytic and Electron Impact Methods," *Rad. Res. Rev.* 2, 237.

DOE (U.S. Department of Energy) (1986), *Environmental Assessment: Yucca Mountain Site, Nevada Research and Development Area, Nevada, Volume II*, DOE/RW-0073.

DOE (U.S. Department of Energy) (1988), *o, Yucca Mountain Site, Nevada Research and Development Area, Nevada*, Office of Civilian Radioactive Waste Management, Washington, DC, DOE/RW-0199.

DOE (U.S. Department of Energy) (1990), *Yucca Mountain Project Reference Information Base*, Version 4, Yucca Mountain Site Characterization Project Office, Las Vegas, NV, YMP/CC-0002. (NNA 890330.0077)

Duffy, C. J. (1984), "Hydrothermal Chemistry," *Research and Development Related to the Nevada Nuclear Waste Storage Investigations*, Los Alamos National Laboratory, Los Alamos, NM, LA-10032.

Durham, W. B., J. M. Beiriger, M. Axelrod, and S. Trettenaro (1986), "The Effect of Gamma Radiation on the Strength and Elasticity of Climax Stock and Westerly Granites," *Nuclear and Chemical Waste Management* 6, 159–168.

Ederova, J., and V. Satava (1979), "Heat Capacities of C_3AH_6, C_4ASH_{12}, and $C_6AS_3H_{32}$," *Thermochim. Acta* 31, 126–128.

Ehgartner, B. L., and R. C. Kalinski (1988), *A Synopsis of Analyses (1981–1987) Performed to Assess the Stability of Underground Excavations at Yucca Mountain*, Sandia National Laboratories, Albuquerque, NM, SAND88-2294.

Ellezer, I., N. Ellezer, R. A. Howald, and P. Viswanadham (1981), "Thermodynamic Properties of Calcium Aluminates," *J. Phys. Chem.* 85, 2835–2838.

Fletcher, P., and G. Sposito (1989), "The Chemical Modelling of Clay/Electrolyte Interactions for Montmorillonite," *Clay Miner.* 24, 375–391.

Flint, A. (1991), personal communication with Alan Flint from the U.S. Geological Survey on the topic of "Annual Precipitation Measurements at Yucca Mountain."

Frysinger, G. R. (1962), "Caesium-Sodium Ion Exchange on Clinoptilolite," *Nature* 194, 351–353.

Fuentes, H. R., W. L. Polzer, J. Gruber, B. Lauctes, and E. H. Essington (1987), *Preliminary Report on Sorption Modeling*, Los Alamos National Laboratory, Los Alamos, NM, LA-10952.

Fujii, X., and W. Kondo (1983), "Estimation of Thermochemical Data for Calcium Silicate Hydrate (C-S-H)," *Am. Ceram. Soc. J.* 66, C220–C221.

Gartner, E. M., F. J. Tang, and S. J. Weiss (1985), "Saturation Factors for Calcium Hydroxide and Calcium Sulfates in Fresh Portland Cement Pastes," *Am. Ceram. Soc. J.* 68, 667–673.

Gast, R. G. (1972), "Alkali Metal Cation Exchange on Chambers Montmorillonite," *Soil Sci. Soc. Amer. Proc.*, vol. 36, pp. 14–19.

Gauthier, J. (1990), seminar presentation by Jack Gauthier from SPECTRA Research Institute at the *Performance Assessment Calculation Exercise (PACE 90) Year-End Review*, October 3–4, 1990, Las Vegas, Nevada.

Ghosh, S. N. (1983), "Portland Cement Phases: Polymorphism, Solid Solution, Defect Structure and Hydraulicity," *Advances in Cement Technology*, S. N. Ghosh, Ed. (Pergamon Press), pp. 289–305.

Glasser, F. P., A. A. Rahman, D. Macphee, M. Atkins, N. Beckley, and E. E. Lachowski (1986), *Immobilization of Radioactive Waste in Cement-Based Matrices*, United Kingdom Department of the Environment, DOE RW 86.084.

Glasser, F. P., and Marr (1984), "The Effect of Mineral Additives on the Composition of Cement Pore Fluids," *The Chemistry and Chemically Related Properties of Cement*, F. P. Glasser, Ed., pp. 419–429.

Glasser, F. P., M. J. Angus, C. E. McCulloch, D. Macphee, and A. A. Rahman (1985), "The Chemical Environment in Cements," *Mat. Res. Soc. Symp. Proc.* 44, 849–858.

Glasser, F. P., S. Diamond, and D. M. Roy (1987), "Hydration Reactions in Cement Pastes Incorporating Fly Ash and Other Pozzolanic Materials," *Mat. Res. Soc. Symp. Proc.* 85, 167–186.

Glassley, W. E. (1986), *Reference Waste Package Environment Report*, Lawrence Livermore National Laboratory, Livermore, CA, UCRL-53726.

Grounds, T., H. G. Midgley, and D. V. Nowell (1985), "The Use of Thermal Methods to Estimate the State of Hydratic of Calcium Trisulpho Aluminate Hydrate $3CaO_9Al_2O_3{\cdot}3CaSO_4{\cdot}nH_2O$," *Thermochim. Acta* 85, 215–218.

Grutzeck, M. W., and A. R. Ramachandran (1987), "An Integration of Tricalcium Silicate Hydration Models in Light of Recent Data," *Cem. Concr. Res.* 17, 164–170.

Haas, J. L. Jr., G. R. Robinson, Jr., and B. S. Hemingway (1981), "Thermodynamic Tabulations for Selected Phases in the System CaO-Al_2O_3-H_2O at 101.325 kPa (1 atm) between 273.15 and 1800°K," *J. Phys. Chem. Ref. Data* 10, 575–669.

Harrar, J. E., (Chairman), J. F. Carley, W. F. Isherwood, E. Raber (1990), *Report of the Committee to Review the Use of J-13 Well Water in Nevada Nuclear Waste Storage Investigations*, Lawrence Livermore National Laboratory, Livermore, CA, UCID-21867.

Heimann, R. B. (1988a), "Interaction of Cement and Radioactive Waste Forms in Multicomponent Systems Tests at 200°C. Part 1: Leaching and Sorption of Cesium, Strontium and Actinides," *Cem. Concr, Res.* 18, 389–400.

Heimann, R. B. (1988b), "Interaction of Cement and Radioactive Waste Forms in Multicomponent Systems Tests at 200°C. Part 2: Mineralogical Changes of Cement," *Cem. Concr. Res.* 18, 554–560.

Heimann, R. B., and R. D. Hooton (1986), "Mineralogical Changes of Various Cement Formulations during Reaction with Groundwater in the Presence of Ca and Na-bentonite at 150°C," *Can. Min.* 24, 289–302.

Hopkins, P. L., R. R. Eaton, S. Sinnock (1986), *Effect of Drift Ventilation on Repository Hydrology and Resulting Solute Transport Implications*, Sandia National Laboratories, Albuquerque, NM, SAND86-1571.

Howell, D. A., G. K. Johnson, I. R. Tasker, P. A. G. O'Hare, and W. S. Wise (1989), "Thermodynamic Properties of the Zeolite Stilbite," *Zeolites*, vol. 10, pp. 525–531.

Howery, D. G., and H. C. Thomas (1965), "Ion Exchange on the Mineral Clinoptilolite," *J. Phys. Chem.* 69, 531–537.

Hunter, R. J. (1981), *Zeta Potential in Colloid Science, Principles and Applications* (Academic Press, London).

Iijima, A., (1988), "Diagenetic Transformations of Minerals as Exemplified by Zeolites and Silica Minerals—A Japanese View," *Diagenesis, II*, G. V. Chilingarian, and K. H. Wolf, Eds. (Elsevier, New York), pp. 147–211.

Ishido, T., H. Mizuanti, and K. Baba (1983), "Streaming Potential Observations, Using Geothermal Wells and In Situ Electrokinetic Coupling-Coefficients under High-Temperature," *Tectonophysics* 91(1-2), 89–104.

Jeffrey, J. W. (1964), "The Crystal Structures of the Anhydrous Compounds," *The Chemistry of Cements*, H. F. W. Taylor, Ed. (Academic Press), pp. 131–164.

Johnson, G. K., I. R. Tasker, H. E. Flotow, P. A. G. O'Hare, and W. S. Wise (1989a), "Thermodynamic Studies of Mordenite, Dehydrated Mordenite, and Gibbsite," to be submitted to *Amer. Miner.*

Johnson, G. K., I. R. Tasker, R. Jurgens, and P. A. G. O'Hare (1989b), "Thermodynamic Studies of Zeolites: Clinoptilolite," *J. Chem. Therm.*, in review.

Johnson, G. L., and D. N. Montan (1990), *Thermal Calculations Pertaining to a Proposed Yucca Mountain Nuclear Waste Repository*, Lawrence Livermore National Laboratory, Livermore, CA, UCRL-ID-103534.

Jones, A. R. (1959), "Radiation-Induced Reactions in the N_2-O_2-H_2O System," *Rad. Res.* 10, 655.

Kana, D. D., B. H. G. Brady, B. W. Vanzant, and P. K. Nair (1989), *Critical Assessment of Seismic and Geomechanics Literature Related to a High-Level Nuclear Waste Underground Repository*, Nuclear Regulatory Commission, Center for Nuclear Waste Regulatory Analyses, San Antonio, Texas.

Kemeny, J., and N. Cook (1990), "Rock Mechanics and Crustal Stress," *Demonstration of a Risk-Based Approach to High-Level Waste Repository Evaluation*, R. K. McGuire, Ed., Electric Power Research Institute, Palo Alto, CA, EPRI-NP-7057.

Kerrisk, J. F. (1983), *Reaction-Path Calculations of Groundwater Chemistry and Mineral Formation at Rainier Mesa, Nevada*, Los Alamos National Laboratory, Los Alamos, NM, LA-9912.

Khoury, H. N., E. Salameh, and Q. Abdul-Jaber (1985), "Characteristics of an Unusual Highly Alkaline Water from the Maqarin Area, Northern Jordan," *J. Hydrol.* 81, 79–91.

Klavetter, E. A., and R. R. Peters (1987), *An Evaluation of the Use of Mercury Porosimetry in Calculating Hydrologic Properties of Tuffs from Yucca Mountain, Nevada*, Sandia National Laboratories, Albuquerque, NM, SAND86-0286-UC-70. (NNA.890327.0056)

Klavetter, E. A., and R. R. Peters (1988), "A Continuum Model for Water Movement in an Unsaturated Fracture Rock Mass," *Water Resources Research* 24, 416–430.

Knauss, K. G. (1987), "Zeolitization of Glassy Topopah Spring Tuff under Hydrothermal Conditions," *Mat. Res. Soc. Symp. Proc.*, vol. 84, pp. 737–745.

Knauss, K. G., and D. W. Peifer (1986), *Reaction of Vitric Topopah Spring Tuff and J-13 Groundwater under Hydrothermal Conditions Using Dickson-Type, Gold-Bag Rocking Autoclaves*, Lawrence Livermore National Laboratory, Livermore, CA, UCRL-53795.

Knauss, K. G., and T. J. Wolery (1988), "The Dissolution Kinetics of Quartz as a Function of pH and Time at 70°C," *Geochim. Cosmochim. Acta* 52, 43–53.

Knauss, K. G., and T. J. Wolery (1989a), "Reply to Comment by J. Gaffner, N. A. Marley, and D. R. Janecky, 'The Dissolution Kinetics of Quartz as a Function of pH and Time at 70°C,'" *Geochim. Cosmochim. Acta* 53, 1471–1474.

Knauss, K. G., and T. J. Wolery (1989b), "Muscovite Dissolution Kinetics as a Function of pH and Time at 70°C," *Geochim. Cosmochim. Acta* 53, 1493–1501.

Knauss, K. G., J. M. Delany, W. J. Beiriger, and D. W. Peifer (1986), "Hydrothermal Interaction of Topopah Spring Tuff with J-13 Water as a Function of Temperature," *Mat. Res. Soc. Symp. Proc.*, vol. 44, pp. 539–546,

Knauss, K. G., W. L. Bourcier, K. D., McKeegan, G. C. Merzbacher, S. N. Nguyen, F. J. Ryerson,
D. K. Smith, H. C. Weed, and L. Newton (1990), "Dissolution Kinetics of a Simple Analogue Nuclear Waste Glass as a Function of pH, Time and Temperature," *Mat. Res. Soc. Symp. Proc.*, vol. 176, pp. 371–383.

Komarneni, S., and D. M. Roy (1983), "Hydrothermal Interactions of Cement or Mortar with Zeolites or Montmorillonites," *Mat. Res. Soc. Symp. Proc.* 15, 55–62.

Levy, S. S. (1984), *Petrology of Samples from Drill Holes USW H-3, H-4, and H-5, Yucca Mountain, Nevada*, Los Alamos National Laboratory, Los Alamos, NM, Report LA-9706.

Levy, S. S. (1990), personal communication with Schon Levy from Los Alamos National Laboratory on the topic of "Unsaturated Zone Zeolite Compositions."

Lin, W. (1990a), *Laboratory Investigations of Fracture Healing, SEG Summer Workshop: Permeability, Fluid Pressure, and Pressure Seals in the Crust*, Lawrence Livermore National Laboratory, Livermore, CA, UCRL-JC-103627.

Lin, W. (1990b), *Variation of Permeability with Temperature in Fractured Topopah Spring Tuff Samples*, Lawrence Livermore National Laboratory, Livermore, CA, UCRL-JC-104765.

Lin, W., A. Ramirez, and D. Watwood (1990), *Temperature Measurements from Prototype Engineered Barrier System Field Test*, Lawrence Livermore National Laboratory, Livermore, CA, UCRL-ID-104757.

Lin, W., and W. D. Daily (1989), "Laboratory Study of Fracture Healing in Topopah Spring Tuff—Implications for Near Field Hydrology," *Proc. of the ANS Topical Mtg. on Nuclear Waste Isolation in an Unsaturated Zone, Focus '89* (American Nuclear Society, La Grange Park, IL), p. 443.

Lin, W., and W. Daily (1984), *Transport Properties of Topopah Springs Tuff*, Lawrence Livermore National Laboratory, Livermore, CA, UCRL-53602.

Lin, W., and W. Daily (1990a), "Hydrological Properties of Topopah Spring Tuff under a Thermal Gradient—Laboratory Results," *Int. J. Rock Mech. Min. Sci. and Geom. Abs.* 27(5), 373–385.

Lin, W., and W. Daily (1990b), *Role of Water in Fracture Healing of Topopah Spring Tuff Samples*, Lawrence Livermore National Laboratory, Livermore, CA, UCRL-JC-103240-ABS.

Linacre, J. K., and W. R. Marsh (1981), "The Radiation Chemistry of Heterogeneous and Homogeneous Nitrogen and Water Systems," Chemistry Division, AERE Harwell, Didcot, Berkshire, England, AERE-R-10027.

Lipman, P. W., R. L. Christiansen, and J. T. O'Connor (1966), *A Compositionally Zoned Ash-Flow Sheet in Southern Nevada*, U. S. Geological Survey, Prof. Pap. 524-F.

MacDougall, H. R., L. W. Scully, and J. R. Tillerson, (Compilers) (1987), *Site Characterization Plan Conceptual Design Report*, Sandia National Laboratories, Albuquerque, NM, SAND84-2641.

Macphee, D. E., K. Luke, F. P. Glasser, and E. E. Lachowski (1989), "Solubility and Aging of Calcium Silicate Hydrates in Alkaline Solutions at 25°C," *Am. Ceram. Soc. J.* 72, 646–654.

Majling, J., V. Tomkova, and E. Istenikova (1985), "Calorimetric Study of Reactions in the System C_4A_3S-CH-CS-H," *Thermochim. Acta* 85, 219–222.

Marshall, T. J., and J. W. Holmes (1979), *Soil Physics* (Cambridge University Press, England).

Matzing, H. (1989), *Chemical Kinetics of Flue Gas Cleaning by Electron Beam*, Kenforschung Szentrum Karlsruhe Laboratorium für Aerosophysik und Filter Technik, Karlsruhe, West Germany, KFK 4494.

Maycock, J. N., J. Skalny, and R. S. Kalyoncu (1974), "Thermal Decomposition of Cementitious Hydrates," *Analytical Calorimetry*, R. S. Porter and J. F. Johnson, Eds. (Plenum), pp. 697–711.

McNeil, M. B., D. W. Mohr, and B. J. Little (1990), "Correlation of Laboratory Results with Observations on Long-Term Corrosion of Iron and Copper Alloys," *Mat. Res. Soc. Symp. Proc., 1990 Spring Meeting on Materials Science in Archeology* (in press).

Meike, A., and W. Glassley (1989), *In-Situ Observation of the Alpha/Beta Cristobalite Transition Using High Voltage Electron Microscopy*, Lawrence Livermore National Laboratory, Livermore, CA, UCRL-ID-101323

Milestone, N. B., T. Sugama, L. E. Kukacka, and N. Carciello (1987), "Carbonation of Geothermal Grouts. Part 3: CO_2 Attack on Grouts Containing Bentonite," *Cem. Concr. Res.* **17**, 295–306.

Montazer, P., and W. E. Wilson (1984), *Conceptual Hydrologic Model of Flow in the Unsaturated Zone, Yucca Mountain, Nevada*, U. S. Geological Survey, Lakewood CO, Water Resources Investigation Report 84-4345.

Montazer, P., E. P. Weeks, F. Thamir, S. N. Yard, and P. B. Hofrichter (1985), "Monitoring the Vadose Zone in Fractured Tuff, Yucca Mountain, Nevada," *Characterization and Monitoring of the Vadose Zone, National Water Well Assoc. Symp.*, Denver, CO, Nov 19–21, 1985.

Moore, D. E., C. Morrow, and J. Byerlee (1986), "High-Temperature Permeability and Groundwater Chemistry of Some Nevada Test Site Tuffs," *J. Geophys. Res.* 91(B2), 2163–2171.

Mor, E. D., and A. M. Beccaria (1975), "Behaviour of Copper in Artificial Sea Water Containing Sulphides," *Br. Corros. J.* **10**, 33–38.

Moragues, A., A. Macias, and C. Andrade (1987), "Equilibria of the Chemical Composition of the Concrete Pore Solution. Part I: Comparative Study of Synthetic and Extracted Solutions," *Cem. Concr. Res.* **17**, 173–182.

Moragues, A., A. Macias, and J. Losada (1988), "Equilibria of the Chemical Composition of the Concrete Pore Solution. Part II: Calculation of the Equilibria Constants of the Synthetic Solutions," *Cem. Concr. Res.* **18**, 342–350.

Morrow, C., D. Moore, and J. Byerlee (1985), "Permeability Changes in Crystalline Rocks due to Temperature: Effect of Mineral Assemblage," *Mat. Res. Soc. Symp. Proc.* (Boston, MA), vol. 44, pp. 467–473.

Nagy, K. L., A. C. Lassaga, and A. E. Blum (1990a), "Kinetics of Dissolution and Precipitation of the Clay Minerals Kaolinite and Gibbsite," *Symposium on Aqueous Surface Chemistry and Kinetics, V. M. Goldschmidt Conference Program and Abstracts*, 68.

Nagy, K. L., A. E. Blum, A. C. Lasaga (1989), "Kaolinite Precipitation and Dissolution Rates: Effects on Porosity and Permeability in Diagenetic Environments," *Amer. Assoc. Petrol. Geol. Annual Meeting.*

Nagy, K. L., A. E. Blum, and A. C. Lasaga (1988), "Precipitation Kinetics and Solubility of Kaolinite in Dilute Aqueous Solutions at 80°C," *Geol. Soc. Amer. Abstracts with Programs*, A42.

Nagy, K. L., A. E. Blum, and A. C. Lasaga (1991), "Dissolution and Precipitation Kinetics of Kaolinite at 80°C and pH3: The Dependence on Solution Saturation State," *Amer. Jour. Science*, in press.

Nagy, K. L., and A. C. Lasaga (1990a), "The Effect of Deviation from Equilibrium on the Kinetics of Dissolution and Precipitation of Kaolinite and Gibbsite," *Chemical Geology* 84, 283–285.

Nagy, K. L., and A. C. Lasaga (1990b), "A Full Rate Law for Dissolution and Precipitation of Gibbsite and Simultaneous Precipitation of Gibbsite and Kaolinite at 80°C and pH3," *Geol. Soc. Amer. Abstracts with Programs* 22, A151.

Nagy, K. L., C. I. Steefel, A. E. Blum, and A. C. Lasaga (1990b), "Dissolution and Precipitation Kinetics of Kaolinite: Initial Results at 80°C with Application to

Porosity Evolution in a Sandstone," *AAPG Memoir, Predicition of Reservoir Quality through Chemical Modeling*, in press.

Neal, C., and G. Stanger (1984), "Calcium and Magnesium Hydroxide Precipitation from Alkaline Groundwaters in Oman, and their Significance to the Process of Serpentinization," *Min. Mag.* 48, 237–241.

Neretneiks, I. (1985), "Transport in Fractured Rocks," *Proceedings, Memoires of the 17th International Congress of IAH, Tucson, AZ, Vol. XVII*, pp. 301–318.

Nimick, F. B. (1990), *The Thermal Conductivity of Seven Thermal Mechanical Units at Yucca Mountain, Nevada*, Sandia National Laboratories, Albuquerque, NM, SAND88-1387.

Nimick, F. B., R. G. Van Buskirk, and A. F. McFarland (1987), *Uniaxial and Triaxial Compression Test Series on Topopah Spring Member from USW G-2, Yucca Mountain, Nevada*, Sandia National Laboratories, Albuquerque, NM, SAND85-0703.

Nimick, F. G., and B. M. Schwartz (1987), *Bulk, Thermal, and Mechanical Properties of the Topopah Spring Member of the Paintbrush Tuff, Yucca Mountain, Nevada*, Sandia National Laboratories, Albuquerque, NM, SAND85-0762.

Nitao, J. J. (1988a), *Numerical Modeling of the Thermal and Hydrological Environment Around a Nuclear Waste Package Using the Equivalent Continuum Approximation: Horizontal Emplacement*, Lawrence Livermore National Laboratory, Livermore, CA, UCID-21444. (NNA.890317.0021)

Nitao, J. J. (1988b), *Simulations of the Near-Field Transport of Radionuclides by Liquid Diffusion at Yucca Mountain—Comparisons with and without Emplacement Backfill*, Lawrence Livermore National Laboratory, Livermore, CA, UCID-21466.

Nitao, J. J. (1989a), *V-TOUGH—An Enhanced Version of the TOUGH Code for the Thermal and Hydrologic Simulation of Large-Scale Problems in Nuclear Waste Isolation*, Lawrence Livermore National Laboratory, Livermore, CA, UCID-21954.

Nitao, J. J. (1989b), *On the Infiltration of a Liquid Front in an Unsaturated, Fractured Porous Media, Part II*, Lawrence Livermore National Laboratory, Livermore, CA, UCID-21743.

Nitao, J. J. (1991), *Theory of Matrix and Fracture Flow Regimes in Unsaturated, Fractured Porous Media*, Lawrence Livermore National Laboratory, Livermore, CA, UCRL-JC-104933.

Nitao, J. J., and T. A. Buscheck (1989), "On the Infiltration of a Liquid Front in an Unsaturated, Fractured Porous Medium," *Proc. of the ANS Topical Mtg on Nuclear Waste Isolation in an Unsaturated Zone, Focus '89* (Amer. Nuc. Soc., La Grange, IL).

Norris, A. E. (1989), "The Use of Chlorine Isotope Measurements to Trace Water Movements at Yucca Mountain," *Proc. of the ANS Topical Mtg on Nuclear Waste Isolation in an Unsaturated Zone, Focus '89* (Amer. Nuc. Soc., La Grange, IL).

Nourbehecht, B. (1963), *Irreversible Thermodynamic Effects in Inhomogeneous Media and their Applications in Certain Geoelectric Problems*, Ph.D. Thesis, Massachusetts Institute of Technology, Cambridge, MA.

Ogard, A. E., and J. F. Kerrisk (1984), *Groundwater Chemistry along Flow Paths between a Proposed Repository Site and the Accessible Environment*, Los Alamos National Laboratory, Los Alamos, NM, LA-10188.

Olofsson, U., B. Allard, B. Torstenfelt, and K. Andersson (1982b), "Properties and Mobilities of Actinide Colloids in Geologic Systems," *Scientific Basis For Nuclear Waste Management* 5, W. Lutze, Ed., pp. 755–764.

Olofsson, U., B. Allard, K. Andersson, and B. Torstenfelt (1981), *Formation and Properties of Radiocolloids in Aqueous Solution—A Literature Survey*, Programrådet för Radioaktivt Avfall, National Council for Radioactive Waste, Department of Nuclear Chemistry, Chalmers University of Technology, Göteborg, Sweden, Report Prav 4.25.

Olofsson, U., B. Allard, K. Andersson, and B. Torstenfelt (1982a), "Formation and Properties of Americium Colloids in Geologic Systems," *Scientific Basis For Nuclear Waste Management* 4, S. Topp, Ed.

Olsson, W. A. (1987), *Rock Joint Compliance Studies*, Sandia National Laboratories, Albuquerque, NM, SAND86-0177.

Olsson, W. A. (1988), *Compliance and Strength of Artificial Joints in Topopah Spring Tuff*, Sandia National Laboratories, Albuquerque, NM, SAND88-0660.

Olsson, W. A., and A. K. Jones (1980), *Rock Mechanics Properties of Volcanic Tuffs from the Nevada Test Site*, Sandia National Laboratories, Albuquerque, NM, SAND80-1453.

O'Neal, W. C., D. W. Gregg, J. N. Hockman, E. W. Russell, and W. Stein (1984), *Preclosure Analysis of Conceptual Waste Package Designs for a Nuclear Waste Repository in Tuff*, Lawrence Livermore National Laboratory, Livermore, CA, UCRL-53595.

Onofrei, M. (1987), "Leaching Studies of Concrete Materials for Nuclear Fuel Waste Immobilization Containers," *The Geological Disposal of High Level Radioactive Wastes*, D. G. Brookins, Ed. (Theophrastus Publications, Athens, Greece), pp. 351–396.

Ortiz, T. S., R. L. Williams, F. B. Nimick, B. C. Whittet, and D. L. South (1985), *A Three-Dimensional Model of Reference Thermal/Mechanical and Hydrologic Stratigraphy at Yucca Mountain, Southern Nevada*, Sandia National Laboratories, Albuquerque, NM, SAND84-1076.

Peters, R. R., E. A. Klavetter, I. J. Hall, S. C. Blair, P. R. Hellers, and G. W. Gee (1984), *Fracture and Matrix Hydrologic Characteristics of Tuffaceous Materials from Yucca Mountain, Nye County, Nevada*, Sandia National Laboratories, Albuquerque, NM, SAND84-1471.

Pollard, A. M., R. G. Thomas, and P.A. Williams (1989), "Synthesis and Stabilities of the Basic Copper (II) Chlorides Atacamite, Paratacamite, and Botallackite," *Min. Mag.* 53, 557–563.

Price, R. H. (1983), *Analysis of Rock Mechanics Properties of Volcanic Tuff Units from Yucca Mountain, Nevada Test Site*, Sandia National Laboratories, Albuquerque, NM, SAND82-1315.

Price, R. H. (1986), *Effects of Sample Size on the Mechanical Behavior of Topopah Spring Tuff*, Sandia National Laboratories, Albuquerque, NM, SAND85-0709

Price, R. H., and A. K. Jones (1982), *Uniaxial and Triaxial Compression Tests Series on Calico Hills Tuff*, Sandia National Laboratories, Albuquerque, NM, SAND82-1314.

Price, R. H., F. B. Nimick, J. R. Connolly, K. Keil, B. M. Schwartz, and S. J. Spense (1985), *Preliminary Characterization of the Petrologic, Bulk, and Mechanical Properties of a Lithophysal Zone Within the Topopah Spring Member of the Paintbrush Tuff*, Sandia National Laboratories, Albuquerque, NM, SAND84-0860.

Price, R. H., J. R. Connolly, and K. Keil (1987), *Petrologic and Mechanical Properties of Outcrop Samples of the Welded, Devitrified Topopah Spring Member of the Paintbrush Tuff*, Sandia National Laboratories, Albuquerque, NM, SAND86-1131.

Pruess, K. (1987), *Tough User's Guide*, Nucl. Regul. Comm. Rep., Washington, DC, NUREG/CR-4645.

Pusch, R. (1989), *Influence of Various Excavation Techniques on the Structure and Physical Properties of Near-Field Rock around Large Boreholes*, Swedish Nuclear Fuel and Waste Management Co. (SKB), Stockholm, Sweden, Technical Report 89-32.

Ragnarsdottir, K. V. (1990), "Zeolite Stability in the Diagenetic Environment," abstract submitted to *Mineralogical Society of Great Britain, December 1989 Meeting*, London.

Raloff, J. (1990), "The Colloid Threat," *Science News*, March 17, 1990, p. 169.

Ramirez, A., D. Wilder, J. Beatty, T. Buscheck, R. Carlson, W. Daily, R. LaTorre, K. Lee, W. Lin, N-H. Mao, J. Nitao, D. Towse, T-S. Ueng, and D. Watwood (1991), *Prototype Engineered Barrier System Field Tests (PEBSFT), Progress Report through November 1, 1988*, Lawrence Livermore National Laboratory, Livermore, CA, UCID-21640.

Ramirez, A., R. Carlson, and T. Buscheck (1990), *In Situ Changes in the Moisture Content of Heated Welded Tuff Based on Thermal Neutron Measurements*, Lawrence Livermore National Laboratory, Livermore, CA, UCRL-ID-104715.

Ramirez, A., T. Buscheck, R. Carlson, W. Daily, K. Lee, W. Lin, N-H. Mao, T-S. Ueng, H. Wang, and D. Watwood (1991), *Prototype Engineered Barrier System Field Tests (PEBSFT), Final Report*, Lawrence Livermore National Laboratory, Livermore, CA, UCRL-ID-106159.

Reed, D. T., and R. A. Van Konynenburg (1988), "Effect of Ionizing Radiation on Moist Air Systems," *Mat. Res. Soc. Symp. Proc.: Scientific Basis for Nucl. Waste Mgmt. XI* (Mat. Res. Soc., Pittsburg, PA).

Reed, D. T., and R. A. Van Konynenburg (1991), "Corrosion of Copper-Based Materials in Irradiated Moist Air Systems," *Mat. Res. Soc. Symp. Proc.: Scientific Basis for Nucl. Waste Mgmt. XIV*, T. Abrajano, Jr. and L. H. Johnson, Eds. (Mat. Res. Soc., Pittsburg, PA), vol. 212, pp. 317–325.

Reed, D. T., V. Swayambunathan, B. S. Tani, and R. A. Van Konynenburg (1990), "Corrosion Product Identification and Relative Rates of Corrosion of Candidate Metals in an Irradiated Air-Steam Environment," *Mat. Res. Soc. Symp. Proc.: Scientific Basis for Nucl. Waste Mgmt. XIII* (Mat. Res. Soc., Pittsburg, PA), p. 517.

Rhoderick, J. E. (1981), *Examination of Samples of Grout after 63 Years Exposure Underground*," Office of Nuclear Waste Isolation, Washington, DC, ONWI-248.

Roy, D. M., and C. A. Langton (1983), *Characterization of Cement Based Ancient Building Materials in Support of Repository Seal Materials Study*, Batelle Memorial Institute, BMI/ONWI-523.

Roy, D. M., and C. A. Langton (1989), *Studies of Ancient Concrete as Analogs of Cementitious Sealing Materials for a Repository in Tuff*, Los Alamos National Laboratory, Albuquerque, NM, LA-11527-MS

Sarker, A. K., M. W. Barnes, and D. M. Roy (1982), *Longevity of Borehole and Shaft Sealing Materials: Thermodynamic Properties of Cements and Related Phases Applied to Repository Sealing*, U.S. Department of Energy, Office of Nuclear Waste Isolation, Washington, DC, ONWI-201.

Scheetz, B. E., and D. M. Roy (1989a), *Preliminary Survey of the Stability of Silica-rich Cementitious Mortars 82-22 and 84-12 with Tuff*, Los Alamos National Laboratory, Albuquerque, NM, LA-11222-MS.

Scheetz, B. E., and D. M. Roy (1989b), *Reactivity of a Tuff-Bearing Concrete: CL-40 CON-14*, Los Alamos National Laboratory, Albuquerque, NM, LA-114532-MS.

Schuraytz, B. D., T. A. Vogel, L. W. Younker (1986), *Geochemical Gradients in the Topopah Spring Member of the Paintbrush Tuff: Evidence for Eruption Across a Magmatic Interface*, Lawrence Livermore National Laboratory, Livermore, CA, UCRL-53698.

Scott, D. A. (1985), "Periodic Corrosion Phenomena in Bronze Antiquities," *Studies in Conservation* 30, 49–57.

Scott, R. B., and M. Catellanos (1984), *Stratigraphic and Structural Relations of Volcanic Rocks in Drill Holes USW GU-3 and USW G-3, Yucca Mountain, Nye County, Nevada*, U.S. Geological Survey, Denver, CO, OFR-84-491.

Shrivastava, O. P., and F. P. Glasser (1986), "Ion-Exchange Properties of 11-Å Tobermorite," *React. Solids* 2, 261–268 .

Soo, P., and L. W. Milian (1989), "Sulfate-Attack Resistance and Gamma-Irradiation Resistance of Some Portland Cement Based Mortars," U.S. Nuclear Regulatory Commission, Washington, D.C., NUREG/CR-5279.

Spengler, R. W., M. P. Chornack, D. C. Muller, and J. E. Kibler (1984), *Stratigraphic and Structural Characteristics of Volcanic Rocks in Core Hole USW G-4, Yucca Mountain, Nye County, Nevada*, U.S. Geological Survey, Denver, CO, OFR-84-789.

Sposito, G. (1981), *Thermodynamics of Soil Solutions* (Oxford University Press, New York).

Stock, J. M., J. H. Healy, and S. H. Hickman (1984), *Report on Televiewer Log and Stress Measurements in Core Hole USW G-2, Nevada Test Site*, U.S. Geological Survey, Denver, CO, OFR-84-172.

Stock, J. M., J. H. Healy, S. H. Hickman, and M. D. Zoback (1985), "Hydraulic Fracturing Stress Measurements at Yucca Mountain, Nevada, and Relationship to Regional Stress Field," *J. Geophys. Res.* 90(B10), 8691–8706.

Subramanian, C. V., J. L. King, D. M. Perkias, R. W. Modd, A. M. Richardson, J. C. Calovini, E. VanEeckhout, and D. D. Emerson (1990), *Exploratory Shaft Seismic Design Basis Working Group Report*, Sandia National Laboratories, Albuquerque, NM, SAND88-1203.

Taylor, H. F. W. (1964), "The Calcium Silicate Hydrates," *The Chemistry of Cement*, H. F. W. Taylor, Ed., vol. 1, pp. 167–232.

Taylor, H. F. W. (1987), "Bound Water in Cement Pastes and Its Significance for Pore Solution Compositions," *Mat. Res. Soc. Symp. Proc.* 85, 47–53.

Telford, W. M., L. P. Geldart, R. E. Sheriff, and D. A. Keys (1976), *Applied Geophysics* (Cambridge University Press, London).

Thomas, K. W. (1987), *Summary of Sorption Measurements Performed with Yucca Mountain, Nevada, Tuff Samples and Water from Well J-13*, Los Alamos National Laboratory, Los Alamos, NM, LA-10960-MS.

Thordarson, W. (1983), *Geohydrologic Data and Test Results from Well J-13, Nevada Test Site, Nye County, Nevada*, U.S. Geological Survey, Denver, CO, Water Resources Investigations Report 83-4171.

Thorstenson, D. C., E. P. Weeks, H. Haas, and J. C. Woodward (1989), "Physical and Chemical Characteristics of Topographically Affected Airflow in an Open Borehole at Yucca Mountain, Nevada," *Proc. of the ANS Topical Mtg on Nuclear Waste Isolation in an Unsaturated Zone, Focus '89*,(Amer. Nuc. Soc., La Grange, IL).

Van Konynenburg, R. A. (1986a), *Radiation Chemical Effects in Experiments to Study the Reaction of Glass in Environment of Gamma-Irradiated Air, Groundwater, and Tuff*, Lawrence Livermore National Laboratory, Livermore, CA, UCRL-53719.

Van Konynenburg, R. A. (1986b), *Radiation Doses in Granite Around Emplacement Holes in the Spent Fuel Test—Climax (Final Report)*, Lawrence Livermore National Laboratory, Livermore, CA, UCRL-53580.

Vaniman, D., D. Bish, D. Broxton, F. Byers, G. Heiken, B. Carlos, E. Semarge, F. Caporuscio, and R. Gooley (1984), *Variations in Authigenic Mineralogy and Sorptive Zeolite Abundance at Yucca Mountain, Nevada, Based on Studies of Drill Cores USW GU-3 and G-3*, Los Alamos National Laboratory, Los Alamos, NM, LA-9707.

Viani, B. E., and C. J. Bruton (1991), *Modeling Fluid-Rock Interaction at Yucca Mountain, Nevada: Progress Report*, Lawrence Livermore National Laboratory, Livermore, CA, UCRL-ID-109921.

Vortman, L. J. (1980), *Prediction of Ground Motion From Underground Nuclear Weapons Tests As It Relates to Siting a Nuclear Waste Storage Facility at NTS and Compatibility With the Weapons Test Program*, Sandia National Laboratories, Albuquerque, NM, SAND80-1020/1.

Warren, J. W., and P. J. Root (1963), "The Behavior of Naturally Fractured Reservoirs," *Society of Petroleum Engineers Journal* 3(3), 245–255.

Warren, R. G., F. M. Byers, Jr., and F. A. Caporuscio (1984), *Petrography and Mineral Chemistry of Units of the Topopah Spring, Calico Hills, and Crater Flat tuffs, and Older Volcanic Units, with Emphasis on Samples from Drill Hole USW G-1, Yucca Mountain, Nevada Test Site*, Los Alamos National Laboratory, Los Alamos, NM, LA-10003-MS.

West, K. A. (1988), *Nevada Nuclear Waste Storage Investigations Exploratory Shaft Facility Fluids and Materials Evaluation*, Los Alamos National Laboratory, Albuquerque, NM, LA-11398-MS.

Wilder, D. G. (1990), "Engineered Barrier Systems and Canister Orientation Studies for the Yucca Mountain Project, Nevada," *Proc. of International Symp. on Unique Underground Structures* (Colorado School of Mines Press, Colorado).

Wilder, D. G. (1991), *Performance Implications of Waste Package Emplacment Orientation*, Lawrence Livermore National Laboratory, Livermore, CA, UCID-21607.

Wolery, T. J. (1983), *EQ3NR: A Computer Program for Geochemical Aqueous Speciation—Solubility Calculations, User's Guide and Documentation*, Lawrence Livermore National Laboratory, Livermore, CA, UCRL-53414.

Wolery, T. J., and S. A. Daveler (1991), *EQ6, A Computer Program for Reaction Path Modeling of Aqueous Geochemical Systems: User's Guide and Documentation*, Lawrence Livermore National Laboratory, Livermore, CA, in preparation.

Wood, B. J., and D. G. Fraser (1977), *Elementary Thermodynamics for Geologists*, (Oxford University Press, UK).

Wu, Z-Q., and J. F. Young (1984), "Formation of Calcium Hydroxide from Aqueous Suspensions of Tricalcium Silicate," *Am. Ceram. Soc. J.* 67, 48–51.

Xiuji, F., and L. Shizong (1986), "Investigation of the Effect of Minor Ions on the Stability of β-C_2S and the Mechanism of Stabilization," *Cem. Concr. Res.* 16, 587–601.

Yang, I. C., A. K. Turner, T. M. Sayre, and P. Montazer (1988), *Triaxial-Compression Extraction of Pore Water from Unsaturated Tuff, Yucca Mountain, Nevada*, U. S. Geological Survey, Water Resources Investigations Report 88-4189.

Yow, Jr., J. (1985a), *Concept for WP Environment Tests in the Yucca Mountain Exploratory Shaft*, Lawrence Livermore National Laboratory, Livermore, CA, UCID-20450.

Yow, Jr., J. (1985b), "Test Concept for Waste Package Environment Tests at Yucca Mountain," in the *Proc. of the 28th U.S. Symp. on Rock Mechanics*, Tucson, AZ (A. A. Balkema, Brookfield, VT), pp. 1035–1042; also in Lawrence Livermore National Laboratory, Livermore, CA, UCRL-95568.

Zimmerman, R. M., and R. E. Finley (1986), *Summary of Geomechanical Measurements Taken in and around the G-Tunnel Underground Facility, NTS*, Sandia National Laboratories, Albuquerque, NM, SAND86-1015.

Zohdy, A. A. A. R., L. A. Anderson, and L. J. P. Muffler (1973), "Resistivity, Self-Potential, and Induced-Polarization Surveys of a Vapor Dominated Geothermal System," *Geophysics* 38, 1130–1144.

Appendix B

Appendix B
Identification of Q and non-Q data

The NFER and the LLNL conducted work reported in the NFER have all been performed in accordance with QARD or predecessor QA program procedures and therefore the material in the NFER is considered "Q". This determination is in accordance with DOE guidance dated 8/19/96 states "All reports, analyses, or models must be done under the QA program and are considered "Q", if they describe, predict, or defend how the natural barriers will or are performing their function to isolate waste (their safety function). These Q reports/analyses/models can use non-Q data that is clearly identified as such-the report is still Q...."

The planning for the activities reported in the NFER has long recognized that studies to understand mechanistic processes, lab tests on non YM materials or on non-qualified samples, or scoping calculations and lab tests may not be used directly in license activities related to Site Characterization, but will provide a basis for design, planning, or judging the ranges of conditions within which the conditions of Yucca Mountain will fall. As such the strategy incorporated in planning of these activities included a series of studies that were performed under the LLNL approved QA program that implements the QARD or predecessor YMP QA programs. The strategy provided for qualification of any data that had been determined to be non-Q, but later was deemed necessary for licensing etc., through any of a number of possible approaches including: peer review; comparison of the results with studies in which the stringent controls were applied; reperforming of the specific studies that were found applicable, or review of the procedures applied to determine if they met all requirements of qualified data. In keeping with the DOE guidance discussed above, the Q status of data used or reported in the NFER are reflected in Appendix C following the TDIF number. This Q status is listed to identify which data would need to be qualified or verified for use in quality affecting work.

Model results (viewed by some as data, but not rigorously defined as data) fall into another category which needs to be considered. First, for the results to be relied on, any codes used in the analyses must be properly qualified. Qualification of the codes is only a small part of the process of qualifying results of models. Other portions relate to whether the parameters used were appropriate, whether the model itself (which includes the conceptualization and the abstraction process) is appropriate to, or valid for, Yucca Mountain. The codes used in work reported in this Rev 1 of the NFER are as follows:

Hydrologic Codes:

V-Tough	Fully QA qualified
NUFT	LLNL developed outside of YMP. Not qualified, but comparisons to qualified codes have been performed

Geochemistry Codes:

EQ3/6	Fully QA qualified
GEMBOCHS (data base)	Some data qualified, some QA status indeterminate
GEMBOCHS suite of codes	not qualified--qualification left to user by comparison with analytical solutions of the appropriate sets.
SUPCRT92 (code)	commercial/academic code-not qualified

(data base)	Published (peer reviewed) but not qualified
OS3D/GIMRT	Commercial Code--
REACT	Commercial Code

Geomechanics Codes

FLAC	commercial code-not qualified
ABAQUS	commercial code-not qualified
FRACROCK	LLNL developed outside of YMP. Not qualified.

Man-Made Materials Codes

EQ3/6	Fully QA qualified
GEMBOCHS (data base)	Some data qualified, some QA status indeterminate. Microbial will be added.
GEMBOCHS suite of codes	not qualified--qualification left to user by comparison with analytical solutions of the appropriate sets.

As was the case for data qualification, the codes that are found to be of importance in characterization of the Near-Field Environment, if not already qualified, will need to be qualified. The QA procedures for qualifying codes will be followed which will start with an Individual Software Plan to determine the appropriate way to qualify the code.

Appendix C

Appendix C
NFER Chapter Data Status
(TDIF and Q status of data)

Overall NFER--LL960807504241.012 (non-Q)

Chapter 1: Hydrothermal Modeling

This chapter does not report data, it reports results of modeling only, using data from RIB or referenced data from other sources. Because the codes used in the models varies, model information by section is listed.

Section 1.1 Introduction--no data
Section 1.2 No new data--refers to published data or data from other sources
Section 1.3 No data--model analyses only using V-TOUGH (This section is Rev 0 and therefore was based on V-TOUGH prior to its qualification)
Section 1.4 No data, refers to work of others
Section 1.5 No new data, refers to work of others
Utilizes Log-Normal Model which is unqualified but used and reported in outside literature
Section 1.6 No new data, analyses based on V-TOUGH prior to qualification
Section 1.7 No data, analyses/models only based on V-TOUGH
Section 1.8 No data, model results based on Qualified V-TOUGH
Section 1.9 No data, model results based on Qualified V-TOUGH
Section 1.10.1-1.10.3 No data, model results based on both V-TOUGH and NUFT as well as hybrid model.
Section 1.10.4 No data, model results based on V-TOUGH and hybrid.
Sections 1.10.5.1 through 1.10.5.3 used qualified V-Tough code.
Sections 1.10.5.4 through 1.10.7 are model results (no data) using NUFT

Chapter 2: Laboratory Determined Hydrologic Properties and Processes

LL950404604242.012 (non-Q)
LL950812704242.017 (non-Q)
LL960201404244.011 (non-Q)
LL960100604244.007 (non-Q)
LL960201304244.010 (non-Q)
LL960100704244.008 (non-Q)
LL950916504242.018 (non-Q)
LL950406104242.016 (non-Q)
LL940800704242.002 (non-Q)

Chapter 3: Geochemistry

None. Modeling only based on use of qualified EQ3/6 as well as unqualified GMIRT and REACT.

Chapter 4: Geomechanics

LL960101004243.005 (non-Q)
LL960401704243.008 (non-Q)
LL960201104243.006 (non-Q)
Modeling results based on use of non-qualified codes.

Chapter 5: Radiation Effects

No new data.

Chapter 6: Man-Made Materials

LL950813104245.004 (Q)
LL940803904245.001 (non-Q)
LL960807404245.008 (non-Q)

Chapter 7: Integrated Testing

LL960401051051.007 (non-Q)
LL960400951051.006 (non-Q)
LL940803851051.002 (non-Q)

Chapter 8: Electrical Potentials

No new data.

Chapter 9: Field Thermal Tests

LL950103004244.004 (non-Q)

Chapter 10: Altered Zone, Geochemistry (10.4)

Section 10.1, and 10.2 contain no data, model results only based on qualified V-TOUGH code.
Section 10.3 No data
Section 10.4 LL960201004241.011 (non-Q)

Chapter 11: Introduction to the Thermodynamic Data Determination

Data from NEA sources.

P&S Account No.	- 1.2.3.12.1 TR	BASELINE Start Date	- 10/01/95
P&S Account Title	- Chem. & Mineral. Properties of the Waste Package	BASELINE Finish Date	- 09/30/96
WBS No.	- 1.2.3.12.1		
WBS Title	- Chem. & Mineral. Properties of the Waste Package	Element ID	- TR3C1

	Fiscal Year Distribution											
	Prior	FY1996	FY1997	FY1998	FY1999	FY2000	FY2001	FY2002	FY2003	FY2004	FY2005	Future	At Complete
Annual Budget	0	432	0	0	0	0	0	0	0	0	0	0	432

Statement of Work:

The following quality affecting work shall be controlled in accordance with approved implementing procedures identified on the current OCRWM-accepted Requirements Traceability Network Matrix

Chemical and Mineralogical Properties of the Waste Package

Determine the mineralogical and chemical variability of the Topopah Spring tuff in the vicinity of waste packages, & evaluate the mineralogical and chemical response of the waste package environment to emplacement of waste. Design, execute, and interpret laboratory and field-based experiments, test, & studies to provide data for numerical analysis. Develop & evaluate computational and conceptual models to support long-term predictions of the behavior of the waste package environment

o conduct experiments and tests to determine the mineralogical and chemical consequences of rock-water interaction at elevated temperatures, and in the presence of radiation and man-made materials

o conduct experiments and tests to evaluate the single-phase dissolution and precipitation kinetics that influence reaction progress under hydrothermal conditions

o Determine the composition of water that may be present in the vicinity of waste packages

o conduct efforts to evaluate the applicability, accuracy, and precision of codes and conceptual models used to predict the long-term behavior of the waste package environment

o develop quantitative predictions for the geochemical and mineralogical evolution of the materials in the vicinity of waste packages

o conduct validation of codes used in the long-term predictions

o QARD applies to this effort, implementing procedures will be specified in NEO/LLNL-QA Grading Reports

Participant agrees to perform tasks and activities as described in subordinate FY96 Summary Accounts.

DELIVERABLES

Deliv ID	Description/Completion criteria	Due Date
MOL305	Rvsn 1 of Vol II of the Near Fld Envrnmnt Rpt Prep	30-Aug-96

P&S Account No. - 1.2.3.12.1 TR -Chem. & Mineral. Properties of the Waste Package

DELIVERABLES

Deliv ID	Description/Completion criteria	Due Date
MOL305	Criteria - This milestone will be satisfied with a synthesis report that is reviewed and approved in accordance with all required Laurence Livermore quality assurance and publication procedures. The report (UCRL-LR) will not be published until after YMSCO acceptance. The material will be summarized and interpreted in Volume I of the Near-Field Environment Report in FY 1997. For new or developed data, the Data Tracking Number(s) shall be cited in the deliverable transmittal letter. The input to the Near-Field Environment Report shall include appropriate updates of the existing Near-Field Environment Report Revision 0 Chapters as listed below, and any new or additional information that has been developed, in addition to new chapter(s) covering the Altered Zone. Revision 1 of Volume II of the Near-Field Environment Report shall contain the following chapters: Introduction 1. Hydrothermal Modeling 2. Hydrologic Properties 3. Geochemistry 4. Geomechanics 5. Radiation Effects 6. Man-Made Materials 7. Integrated Testing 8. Electrical Potentials 9. Field Tests 10. Altered Zone Revision 1 of Volume II of the Near-Field Environment Report shall include, at a minimum, input from the below referenced Fiscal Year 1996 Summary Accounts to the referenced	

Stratigraphy referenced in the report shall be consistent with the Reference Information Base Section 1.12(a), "Stratigraphy: Geologic/Lithologic Stratigraphy" and the Prototype Three-Dimensional Framework Model (yw88) of September, 1995. The use of Q and non-Q data in the deliverable shall be clearly identified. Record accession numbers and Automated Technical Data Tracking numbers shall be included, as appropriate, for all data used/or cited in the deliverable. The deliverable shall be submitted to YMSCO in accordance with QAP 5.1Q.

WOB 11/14/95 QR

RBK 11/14/95 11/14/95 11/13/1995

P&S Account No. - 1.2.3.12.1 TR -Chem. & Mineral. Properties of the Waste Package

DELIVERABLES

Deliv ID	Description/Completion criteria	Due Date
MOL305	chapters, and the "Outcomes" section for each reference Summary Account as stated in the FY1996 Annual Project Implementation Plan: Chapter 1 - Summary Account TR3C2EB6 ~ not active in FY96, not in PACS. Chapter 2 - Summary Account TR3C3EB6 /3 WJS 11/14/95 DB/RAK 11/15/95 Chapter 3 - Summary Account TR3C1EB1, TR3C1EB2, TR3C1EB3 11/14/95 Chapter 4 - Summary Account TR3C3EB1 and TR3C3EB5 Chapter 6 - Summary Account TR3C5EB1 dlw 11/15/1995 In addition, at a minimum, input from the following Summary Accounts shall be included in Revision 1 of Volume II of the Near-Field Environment Report: Summary Account TR32112EB1 - WBS 1.2.3.2.1.1.2 Summary Account TR32122EB2 - WBS 1.2.3.2.1.2.2 Summary Account TR3A2EB1 - WBS 1.2.3.10.2 Summary Account TR3231EB1 - WBS 1.2.3.10.3.1	

Approvals

Preparer - print name	Date	Technical Reviewer - print name	Date	QA Reviewer - print name	Date
THOMAS STATTON	11/13/95	DENNIS R WILLIAMS	11/13/1995	Richard A Kettell	11/13/95
Preparer - Signature		Technical Reviewer - Signature		QA Reviewer - Signature	Date
				Richard A. Kettell	11/13/95